Laboratoire Kastler Brossel - Université Pierre et Marie Curie

ACQAO - Department of Quantum Science - The Australian National University

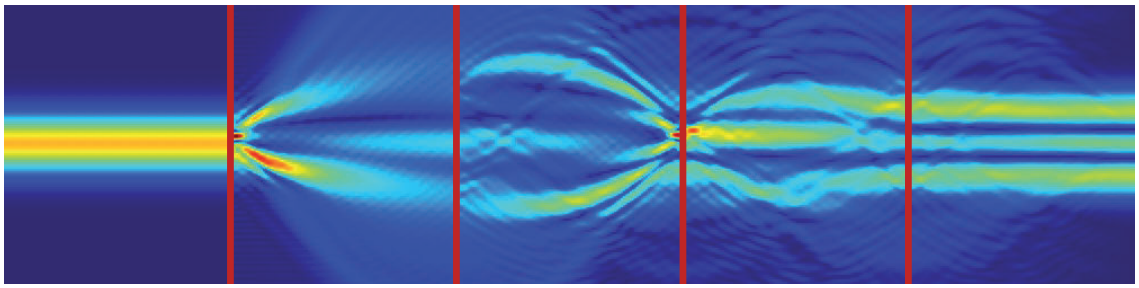

Quantum protocols with transverse spatial modes

Author:
Jean-François Morizur

Supervisors:
Prof. Hans Bachor
Dr. Nicolas Treps

A co-tutelle thesis submitted for the degree of
Doctor of Philosophy
of the Australian National University
and the Université Pierre et Marie Curie

June 2011

Pour Elise

Declaration

This thesis is an account of research undertaken between September 2007 and June 2011 in the Department of Quantum Science, Faculty of Science, Australian National University, Canberra, Australia, and the Laboratoire Kastler Brossel, Université Pierre et Marie Curie, Paris, France. Except where acknowledged in the customary manner, the material presented in this thesis is, to the best of my knowledge, original and has not been submitted in whole or part for a degree in any university.

Personal contribution

This manuscript presents the results of a cotutelle thesis undertaken in collaboration between the Australian National University in Canberra, Australia, and the Université Pierre et Marie Curie in Paris, France. I worked at the interface between the two teams.
Prof. Bachor's team in Australia, and Prof. Treps and Prof. Fabre's team in Paris have had a fruitful collaboration over several years studying the quantum properties of higher order spatial modes of laser light. My work is a natural continuation of these studies with a strong bias towards using the higher order modes as tools for quantum protocols.

I started this project in 2007 in France. After a few months of theoretical and bibliographical studies in Paris, I flew to Canberra, and began my experimental work with the characterization of a small teaching experiment built by Dr M. Colla. I reported on this experiment in the American Journal of Physics(Morizur 08). Then, I started building a first version of the squeezing cavities we would later use for the squeezed modes superposition experiment. At the same time, helped by Anais Dréau, a MSc intern from France, I designed a new digital data acquisition system able to replace the spectrum analyser in our experiments. We used this new data acquisition system along with quadrant detectors to study entanglement between co-propagating spatial modes. To perform this experiment, Dr Jiri Janousek built a degenerate optical parametric oscillator, and I set up the measurement system. I participated in the first experimental runs, and then returned to France in June 2008. This work led to a publication later on, in Nature Photonics(Janousek 08a).

From July 2008 to February 2009, my PhD project took place in France. I worked on two things. First, I assisted Benoit Chalopin, a PhD applicant working on a fully degenerate optical parametric amplifier. At the same time, I worked on a way to formalize theoretically the relationship between general spatial transformations and the ability to build complex multimode entanglement. In February, thanks to this theoretical work, I was able to relate a mathematical solution to the problem of general spatial transforms: I found out that a succession of deformable surfaces and propagation can perform any possible spatial transform of the field, which allows to build any entangled state. We named such a system a Unitary Programmable Mode Converter.
In January and February 2009, I worked closely with the electronics department at LKB to design the first version of a 8-channel multipixel photodiode, which we wanted to use to build a multimode homodyne detection.

I came back to Australia in February 2009. I first simulated the UPMC, using both normal and mainframe computers. I then built it at ANU with a deformable mirror bought specifically for that purpose. I was helped in that work by MSc student Pu Jian (from ENS, Paris, at ANU for a 5 months internship) and honors student Lachlan Nicholls (from ANU).
I first characterized the UPMC in the classical domain. Then, with the help of an optical parametric amplifier built by Dr Janousek and Seiji Armstrong, I characterized the ability of the UPMC to transfer squeezing.
Simultaneously, we tested the electronics from LKB designed for the 8-channel multipixel photodiode. We found it fragile and unstable. Dr Boris Hage improved on the original design and built a second version of the multipixel detector, overcoming the deficiencies of the first version. This work provided us with a fully functional multipixel homodyne detection.

Back in France in January 2010, I wrote two articles. The first one reporting about the classical characterization of the UPMC (Morizur 10c), the second one about its quantum performances (Morizur 10a). I also worked on a new method to optimize the UPMC. After talking to Dr Treps and the Université Pierre et Marie Curie intellectual property office, we decided to proceed to a patent filing to protect this method. I came back to Australia in September 2010 for a last month of measurements. This month allowed me to help Dr Jiri Janousek and Seiji Armstrong take very interesting data using multimode squeezed light and the new 8 channels multipixel homodyne detection.

Abstract

English

We present in this thesis a study of the spatial properties of light at the quantum level. More specifically, we focus on techniques to manipulate the quantum fluctuations of different degrees of freedom in a beam's transverse plane, and on the quantum protocols we can implement using these specific fluctuations.

We begin by providing an experimental characterization of different methods to manipulate the quantum fluctuations of multiple transverse profiles, or modes, in one beam. While manipulating the quantum fluctuations of a mode, a process known as squeezing, for a single mode beam can be performed very efficiently using a conventional optical parametric oscillator, we present implementations of different, less conventional techniques able to generate a beam carrying multiple squeezed modes.

Conventionally, the squeezed modes we can generate using these techniques are fixed by the optical design. We present a new optical system, called a Unitary Programmable Mode Converter (UPMC), able to reshape these modes at will. We show theoretically that such a UPMC can in principle perform any desired reshaping of the modes. We present the performances of an experimental implementation of the UPMC, both in a classical and quantum context. We find that the UPMC performs as predicted, and we present a method to optimize the UPMC settings taking into account experimental restrictions.

The UPMC, combined with a technique to build a beam carrying multiple squeezed modes, allows us to generate a beam with squeezing in any desired set of spatial modes. In order to detect these fluctuations, we built a multipixel homodyne detection, a detection system able to record simultaneously the quantum fluctuations in all these modes. We provide in this thesis our solutions to overcome the electronic challenges associated with such a device, and present an experimental characterization of the performances of our multipixel homodyne detection.

Finally, we combine these experimental characterizations to discuss how these techniques help us implement different quantum protocols involving multiple spatial modes, more specifically quantum enhanced detections and cluster states quantum computation.

French

Nous présentons dans cette thèse une étude des propriétés spatiales de la lumière au niveau quantique. Nous nous attachons plus particulièrement aux fluctuations quantiques des différents degrés de libertés qui caractérisent le profil spatial transverse d'un rayon lumineux, et à différentes manières de les manipuler et de les utiliser.
Manipuler des fluctuations quantiques d'un profil transverse, un mode, à l'aide d'un OPA (amplificateur paramétrique optique) est un procédé bien connu, appelé squeezing. L'OPA nous permet de réduire les fluctuations quantiques d'un degré de liberté. Mais afin de générer un faisceau laser dont plusieurs modes sont squeezés, il nous faut utiliser des techniques moins conventionnelles. Nous présentons dans cette thèse des résultats expérimentaux pour trois d'entre elles. Nous montrons que la technique la plus simple, qui consiste à utiliser des OPA conventionnels et à superposer les modes produits au sein du même faisceau, est la technique la plus fiable.
Les faisceaux ainsi produits contiennent plusieurs modes spatiaux squeezés. Ces modes sont cependant fixés par la méthode choisie pour créer le faisceau. Nous introduisons donc un nouvel outil, l'UPMC (Unitary Programmable Mode Converter). Ce système optique programmable est capable de réaliser n'importe quelle transformation spatiale du champs lumineux, donc de transformer les modes spatiaux squeezés en n'importe quels autres modes. Nous avons construit un tel UPMC et nous présentons dans cette thèses les résultats de nos tests. Ces résultats confirment que l'UPMC est bien capable de transférer les fluctuations quantiques d'un mode à un autre.
A partir d'un faisceau contenant de multiple modes squeezés et d'un UPMC, nous sommes donc capable de générer un faisceau dont n'importe quel ensemble de modes serait squeezé. Afin de détecter ces fluctuations quantiques, nous avons mis au point une détection homodyne multipixel. Ce système de détection est capable d'enregistrer simultanément les fluctuations de tous les modes transverses du faisceau. Nous présentons tout d'abord les solutions techniques aux défis électroniques soulevés par ce type de détecteur, et nous le caractérisons ensuite expérimentalement.
Pour finir, nous combinons nos résultats expérimentaux pour deux études de cas. Nous étudions tout d'abord la capacité de notre système combinant production, manipulation et détection à améliorer la mesure d'un paramètre spatial quelconque en réduisant le bruit quantique correspondant. Puis nous utilisons ces mêmes résultats pour évaluer à quel point notre système peut constituer une alternative à des ensembles de faisceaux pour l'implémentation de protocoles de calcul quantique.

Contents

Chapter 1

Introduction

The particle and wavelike behaviors of light at the quantum level are a fundamental evidence of quantum theory (Cohen-Tannoudji 06). The wavelike behavior is a well understood phenomenon, formalized in Maxwell's equations(Siegman 86). These classical equations fully predict the spatial transformations the light undergoes throughout its propagation through air, through lenses, or through any complex optical system (Yee 66). Armed with these models, we can design optical tools able to reshape the light, such as microscopes or telescopes for optical investigation (Török 07; Herschel 61), or even corrective glasses to correct myopia or astigmatism (Eames 49).

While at the classical level the discreet nature of light can be neglected, its particle behavior has clear manifestations at the quantum level(Gleyzes 07). One of these manifestations is the quantum noise: because it is composed of photons, the light cannot be a perfect continuous wave(Morizur 08). This discreet nature adds a fundamental noise to any continuous signal. It sets a limit to the signal to noise ratio of any optical communication(Gallion 09). Thus, in the case of a conventional laser beam, on top of the technical noise resulting from the different classical processes involved in the generation of the light, which could be reduced to zero with enough care, the quantum noise is an ever present reminder of the quantum properties of the light (Glauber 65).

While we cannot completely remove this noise, we can manipulate it using devices such as optical parametric amplifiers. These manipulations allow us to transfer noise from one property of the light field to another (Slusher 84; Wu 86), thus creating a beam with specific quantum fluctuations. This noise manipulation is called squeezing.

Our work focuses on the spatial evolution of these quantum properties. We study how they change with propagation, and how we can use optical elements to engineer desired changes. Our main investigative tool to study this spatial evolution are quantum fluctuations (Grynberg 10). We use specific quantum fluctuations, such as squeezed light, as an unforgeable signature of the quantum properties we are following, allowing us to track their evolution with propagation. Studying their spatial evolution allows us to confront our theoretical understanding of this evolution to experimental results. Moreover, gen-

erating, reshaping and detecting quantum fluctuations is at the core of several protocols based on the quantum properties of a beams transverse profile.

In this thesis, we develop techniques to generate squeezing in specific spatial profiles, to manipulate these profiles and finally to detect the quantum fluctuations. We build on previous studies, from very early results, which described the spatial evolution of quantum fields in relation to the classical models of light propagation (Grynberg 10), to more recent ones which introduced techniques to generate beams carrying a complex set of quantum fluctuations (Lassen 07; Delaubert 06), or which described ways to measure simultaneously these fluctuations in different parts of a beam (Beck 01; Dawes 01).

The first part of this thesis provides an overview of the relevant theoretical aspects of the spatial evolution of quantum fluctuations. We first present the classical models for propagation, and the notion of spatial mode, a solution of Maxwell's equations. We then introduce the notion of quantum fields and how they relate to this classical notion of modes. We finally present how the quantum fluctuations of the fields are described by their quantum states.
We finish this part with the description of two applications of our study of the spatial properties of quantum fluctuations. We first present how the quality of a measurement system can be improved by using squeezing to reduce the quantum noise in the spatial profile most relevant to the quality of this measurement. We show that in order to bring forth this improvement (first presented in (Treps 03)) for any detection, we need to be able to reshape at will the mode carrying the reduced quantum fluctuations (Treps 05).
Another application of our study is quantum computation. Indeed, while conventional quantum computation protocols are designed for a set of separate beams (Aoki 09b; Yukawa 08b), they can be replaced by the multiple spatial modes carried simultaneously in a single beam. Such a replacement has obvious scalability advantages, since the manipulation of additional beams requires an ever increasing amount of resources. But we show that on the other hand such a replacement requires an efficient method to generate a beam carrying these multiple spatial modes, a flexible method to manipulate these modes and a scalable detection system.

In the second part of the thesis, we first present an experimental implementation of different methods to produce a beam carrying multiple squeezed modes. We use these different implementations to assess the experimental advantages and drawbacks of each methods, and we find that the simplest and most scalable one is simply to generate the squeezed modes independently and then superpose them.
We then present the experimental characterization of a multipixel homodyne detection, a device able to detect the fluctuations in multiple transverse profiles of the beam simultaneously. After a theoretical overview of the capabilities of such a device, we present the technical challenges we overcame to build it. While the idea of a multipixel homodyne detection is not new (Beck 01), its implementation to detect simultaneously the quantum

fluctuations in different complex modes was a completely new challenge.

The third part brings in recent developments in optical engineering, namely deformable mirrors, to fully control the spatial evolution of our quantum fields. We show that, theoretically, a succession of deformable mirrors and optical Fourier transform can generate any possible spatial transformation of the beam of light. We call such a device a UPMC, Unitary Programmable Mode Converter. The UPMC allows us to expand the possible spatial manipulations of the quantum fields beyond what was available with conventional optical elements. Instead of being limited to rather simple modes, we can now theoretically reshape quantum fluctuations into any spatial profile. Moreover, we can manipulate different modes simultaneously, thus providing us with as much freedom to manipulate transverse modes as we would have with separate beams.
We test this new result experimentally, both in a classical and quantum context. We show that even if the theoretical result calls for a large number of reflections, a limited number of reflections coupled with an optimization algorithm to perform the desired transform as well as possible gives us good results. We show experimentally that we can change the transverse profile of a squeezed mode, and benchmark the efficiency of such a process.

Finally, we tie up this thesis by applying our different experimental results to two case studies, examples of the two applications we proposed in the first part. We first show that the combination of an optical parametric amplifier to generate squeezing, a UPMC to reshape it and multipixel homodyne detection allows for the improvement of any measurement of small fluctuations of a light field. We quantify this improvement in a practical case, combining our experimental characterizations of all these devices.
A second case study presents how with a UPMC and a multipixel homodyne detection on a beam carrying multiple squeezed modes we can implement a specific kind of quantum computations. Similarly, we also present for this case quantitative prediction on the quality of such a computation.

Part I

Fundamentals

Chapter 2

A quantum description of light

Quantum optics is the field of physics that studies light at the quantum level. In this thesis we focus more specifically on the relationship between quantum mechanics and the spatial properties of the light. We begin here with a brief overview of the theoretical concepts underlying these issues. We first deal with the concept of spatial mode in a classical context. This concept is at the core of a significant proportion of the theoretical subtleties in this thesis, and can be understood without quantum mechanics. We then introduce the quantization of the light, and describe more specifically the Gaussian states, the class of quantum states we work with.

2.1 Classical wave optics

2.1.1 Maxwell's equations

The classical description of light as a wave is governed by Maxwell's equations. These equations successfully explain the full behavior of any field of light when its quantum properties are neglected. Let us name the electromagnetic field $\vec{E}(x, y, z, t)$. In the absence of electric charges and currents, $\vec{E}$ is solution of the homogeneous equation:

$$\left(\Delta - \frac{1}{c^2}\frac{\partial^2}{\partial t^2}\right)\vec{E} = 0 \tag{2.1}$$

where Δ is the Laplacian operator, and c the speed of light. For a given set of boundary conditions, the homogeneous equation has a unique solution.

In our work, we focus specifically on the spatial properties of the light. We consider only the case of monochromatic light, when $\vec{E}$ is oscillating constantly in time, at a frequency ν_0. We restrict ourselves to the cases when the light is propagating in a beam, and call the direction of propagation the z axis.
We can write

$$\begin{aligned}\vec{E}(x, y, z, t) = \quad & \vec{x}\left(\mathcal{E}_x(x, y, z)e^{-i2\pi\nu_0(t-\frac{z}{c})} + \mathcal{E}_x^*(x, y, z)e^{i2\pi\nu_0(t-\frac{z}{c})}\right) \\ & +\vec{y}\left(\mathcal{E}_y(x, y, z)e^{-i2\pi\nu_0(t-\frac{z}{c})} + \mathcal{E}_y^*(x, y, z, t)e^{i2\pi\nu_0(t-\frac{z}{c})}\right)\end{aligned} \tag{2.2}$$

where $\mathcal{E}_x$ and $\mathcal{E}_y$ are the electric field envelopes for the two orthogonal polarizations $\vec{x}$ and $\vec{y}$, respectively. The term $e^{-i2\pi\nu_0(t-\frac{z}{c})}$ is the carrier for a wave propagating in vacuum along $\vec{z}$. $\vec{x}$ and $\vec{y}$ are the two transverse directions of polarization. For the sake of simplicity, we consider only the polarization $\vec{x}$, and rename $\mathcal{E}_x$ in $\mathcal{E}$, with the understanding that all the results we develop can be applied to the polarization $\vec{y}$.

Since the light is propagating in a beam, the variations of $\mathcal{E}$ along the z axis can be neglected compared to the variations of $e^{i2\pi\nu_0 t - ik_0 z}\mathcal{E}$ ($\frac{\partial \mathcal{E}}{\partial z} \ll k_0 \mathcal{E}$). This is called the paraxial approximation, and it assumes that no part of the field $\vec{E}$ deviates significantly from the propagation axis z. It leads to the reduced propagation equation on the envelope field $\mathcal{E}$ (Siegman 86):

$$\frac{\partial \mathcal{E}}{\partial z} = -\frac{\Delta_\perp \mathcal{E}}{2ik} \tag{2.3}$$

Here $\Delta_\perp$ is the transverse Laplacian operator, in this case $\Delta_\perp = \frac{\partial^2}{\partial x^2} + \frac{\partial^2}{\partial y^2}$.

Equation 2.3 describes the evolution of the spatial shape of a beam of light, as we travel along the propagation axis in vacuum. If, for a given position z_0 along the propagation axis, we know the full transverse profile of the envelope $\mathcal{E}(x, y, z_0)$, we can use 2.3 to compute directly the envelope $\mathcal{E}$ at any other position (x_1, y_1, z_1) (Yee 66). Optical components, such as lenses, curved mirrors or more complex structures, affect the evolution of the spatial shape of the beam. Taking these components into account in the propagation of $\mathcal{E}$ simply requires additional computing resources (Sterkenburgh 97).

A specific kind of propagation, of particular importance for us, is the unitary propagation. It is the class of propagation in which we do not add nor subtract light. It corresponds to propagation through transparent media. In this case, the light power remains constant throughout the propagation.

As it can be noticed in equation 2.3, the three directions $\vec{x}$ and $\vec{y}$ and $\vec{z}$ do not play equivalent roles: $\vec{z}$ is singled out as the direction of propagation. We adapt our notation to this situation, by replacing (x, y, z) by $(\vec{\rho}, z)$, where $\vec{\rho} = (x, y)$.

2.1.2 Spatial Modes

Let us consider a solution $\mathcal{E}(\vec{\rho}, z)$ to the equation 2.3. It is uniquely defined by giving its transverse profile at any given position along the z axis: for any $z_0 \in \mathbb{R}$, defining $\mathcal{E}(\vec{\rho}, z_0)$ in the transverse plane (for all $\vec{\rho} \in \mathbb{R}^2$) fully specifies $\mathcal{E}(\vec{\rho}, z)$. Moreover, since equation 2.3 is linear, if $\mathcal{E}_1$ and $\mathcal{E}_2$ are both solutions, then any linear combination $\mathcal{E}_3 = \alpha\mathcal{E}_1 + \beta\mathcal{E}_2$, where $(\alpha, \beta) \in \mathbb{C}^2$, is also a solution of equation 2.3.
A spatial mode is a normalized solution of equation 2.3. We denote it $u(\vec{\rho}, z)$. On any given plane $z = z_0$

$$\iint_{\vec{\rho}\in\mathbb{R}^2} u^*(\vec{\rho}, z_0) u(\vec{\rho}, z_0) d^2\vec{\rho} = 1 \tag{2.4}$$

If the propagation is unitary, if a given envelope is normalized at a position z_0, it remains normalized throughout its propagation.

Let us consider two modes u_1 and u_2. We say that they are orthogonal when

$$\iint_{\vec{\rho}\in\mathbb{R}^2} u_1^*(\vec{\rho}, z_0) u_2(\vec{\rho}, z_0) d^2\vec{\rho} = 0 \tag{2.5}$$

The left term of equation 2.5 is the scalar product of the two modes. It is kept constant by a unitary propagation: calculating the scalar product at z_0 or z_1 gives the same result.

2.1.3 Mode basis

Let us now introduce a set of modes u_k, $k \in K$. This set of modes is a basis if and only if the modes are orthogonal to each other, and linear combinations of these modes span the set of all the possible envelopes. This last property is known as the completeness of the basis. It is part of the definition of a basis in a mathematical context, but in an experimental context arbitrarily complex fields are not achievable. We can relax the completeness condition to consider that a set of modes is a basis when they span all the modes our optical system deals with. In most of the basis we consider, K is either $\mathbb{N}$ or $\mathbb{N}^2$. But if we only consider a finite basis (using a relaxed definition for the completeness) K can be $K = [1, 2, ..., N]$, with N the number of modes in the basis.

Let us consider the basis u_k. The modes are defined by their transverse profiles in the plane $z = z_0$: $u_k(\vec{\rho}, z = z_0)$. Because the u_k are complete, any envelope $\mathcal{E}$ can be decomposed in

$$\mathcal{E} = \sum_{k\in K} \mathscr{e}_k u_k \tag{2.6}$$

Where the coefficients $\mathscr{e}_k \in \mathbb{C}$ are the scalar products between the envelope $\mathcal{E}$ and the modes u_k:

$$\mathscr{e}(k) = \iint_{\vec{\rho}\in\mathbb{R}^2} u_k^*(\vec{\rho}, z_0) \mathcal{E}(\vec{\rho}, z_0) d^2\vec{\rho} \tag{2.7}$$

A property of the $\mathscr{e}_k$ is that they have the same norm as the envelope considered:

$$\sum_{k\in K} \mathscr{e}_k^* \mathscr{e}_k = \iint_{\vec{\rho}\in\mathbb{R}^2} \mathcal{E}^*(\vec{\rho}, z_0) \mathcal{E}(\vec{\rho}, z_0) d^2\vec{\rho} \tag{2.8}$$

The decomposition 2.6 simplifies the process of computing how a given field profile $\mathcal{E}(\vec{\rho}, z = z_0)$ propagates through transparent media. Indeed, if we know the transverse profiles of the modes $u_k(\vec{\rho}, z)$, we can begin by projecting the field profile onto the $u_k(\vec{\rho}, z = z_0)$. Then, the spatial shape of $\mathcal{E}$ evolves simply as a linear combination of the spatial shapes of the u_k. This method can prove easier to implement than the direct computation of the propagation if we consider specific modes u_k, chosen so that their propagation through the transparent media considered is easy to calculate. (Fleck 80)

Let us now present two specific mode basis of particular importance to us. We provide here a limited set of properties, for a more in depth presentation, please see (Siegman 86).

Hermite Gaussian modes

First of all, a very important spatial mode basis is the Hermite Gaussian basis. This basis is of particular interest to us as it is the basis of the spatial modes resonant in optical cavities. The basis elements, denoted TEM_{mn}, are defined as

$$TEM_{mn}(\vec{\rho}, z) = \frac{C_{mn}}{w(z)} H_m\left(\frac{\sqrt{2}x}{w(z)}\right) H_n\left(\frac{\sqrt{2}y}{w(z)}\right) e^{-\frac{x^2+y^2}{w(z)^2} + ik_0\frac{x^2+y^2}{2R(z)} - i(n+m+1)\Phi_G(z)} \tag{2.9}$$

with

$$\begin{aligned} C_{mn} &= \frac{1}{\sqrt{\pi 2^{n+m+1} n! m!}} \\ z_R &= \frac{\pi w_0^2}{\lambda_0} \\ R(z) &= z + \frac{z^2}{z_R} \\ w(z) &= w_0\sqrt{1 + \left(\frac{z}{z_R}\right)^2} \\ \Phi_G(z) &= \arctan\left(\frac{z}{z_R}\right) \end{aligned} \tag{2.10}$$

where λ_0 is the wavelength of the light, w_0 is the beam waist, z_R is the beam Rayleigh range, $R(z)$ is the radius of curvature, $\Phi_G(z)$ is the Gouy phase shift with regard to the fundamental mode and H_n is the Hermite Polynomial of n-th degree. A planar wavefront only occurs for $z = 0$. A useful definition of H_n is given by the recurrence relation

$$H_0(x) = 1,\ H_1(x) = 2x \text{ and } H_{n+1}(x) = 2xH_n(x) - 2nH_{n-1}(x) \tag{2.11}$$

The quantity $w(z)$ is independent of m and n. In the case where $n = m = 0$, it corresponds to the beam radius. When m and n are not 0, the spatial extension of the mode increases. A TEM_{mn} mode has m zeros along the $\vec{x}$ axis, and n zeros along $\vec{y}$. This means that it has $m + 1$ and $n + 1$ lobes along the $\vec{x}$ and $\vec{y}$ axis respectively. The position of the furthest lobe from the center scales with $\vec{\rho} = (\sqrt{m}w(z), \sqrt{n}w(z))$. Fig. 2.1 presents transverse profiles of a few of these modes at $z = 0$.

This mode basis is particularly convenient to describe the effects of propagation and Gaussian optical components such as spherical lenses and spherical mirrors. Indeed, the shape of the mode remains unchanged by free space propagation: its size $w(z)$ and the radius or curvature $R(z)$ change, but the overall transverse profile of the mode, defined by H_m and

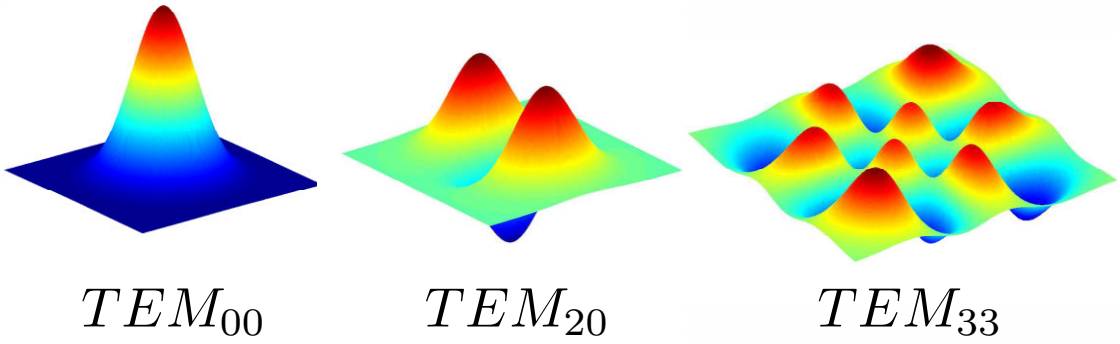

Figure 2.1: Transverse profile of TEM modes, at $z = 0$

H_n remains the same. In the case of Gaussian optical components, the change in waist size and position induced by the curvature of the lenses and mirrors does not change the orders m and n either.

Binary modes and pixel modes

Let us now define another basis of modes, that we call binary modes, or flip modes. This basis, less conventional, is particularly useful to describe the effect of a deformable surface or phase plate on a light beam.

It is first based on a TEM_{00} mode, defined by w_0 at the position $z = 0$. We then define higher order binary modes by introducing localized π phase shifts on the spatial profile of this mode at $z = 0$. For example, the flip-mode, presented in Fig. 2.2 is a TEM_{00} with a π phase shift for $x < 0$. As presented in Fig. 2.2, we add additional phase shifts to build the other higher order modes. The spacing between the phase shifts is set so as to ensure orthogonality, taking into account the beam waist w_0 of the TEM_{00}.

This family of modes can be made a basis. These mode do not keep their shapes with propagation but are nonetheless very useful to describe the effect of a phase plate on a beam.

A final family of interest are the pixel modes. They are of particular interest to describe how light is detected by an array of pixels. These spatial modes are defined in a similar fashion as the binary mode: we consider a TEM_{00} mode, defined by w_0 at $z = 0$, and we then define the pixel modes at $z = 0$ by:

$$\begin{aligned} v_{m,n}(\vec{\rho}, z = 0) &= TEM_{00}(\vec{\rho}, z = 0) && \text{if } \vec{\rho} \in S_{m,n} \\ v_{m,n}(\vec{\rho}, z = 0) &= 0 && \text{if } \vec{\rho} \notin S_{m,n} \end{aligned} \tag{2.12}$$

with the surfaces $S_{m,n}$ corresponding to square pixels. These modes, like the binary modes,

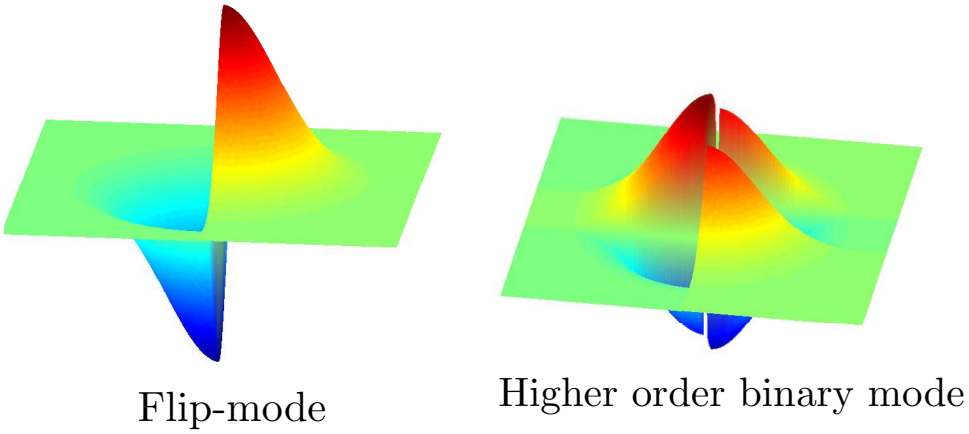

Figure 2.2: Transverse profile of binary modes, at $z = 0$

do not retain their shapes as they propagate. For a pixel array of a given size, the number of surfaces $S_{m,n}$ is finite. Therefore the family of the $v_{m,n}$ can only be a basis if we relax the completeness condition. Indeed, if the pixels have a given size, any feature below this size cannot be distinguished by this family. We can only consider that the $v_{m,n}$ form a basis of modes if none of the fields we consider has any feature smaller than the pixel size.

2.1.4 Basis change

Let us now consider two different mode basis: u_k and u'_l, with $(k, l) \in K^2$. A given envelope $\mathcal{E}$ can either be decomposed on the modes u_k, with the coefficients e_k or on the modes u'_l, with the coefficients e'_l. The coefficients e_k and e'_l are linked by the linear relation:

$$e_k = \sum_{l \in K} \iint_{\vec{\rho} \in \mathbb{R}^2} u_k^*(\vec{\rho}, z) u'_l(\vec{\rho}, z) d^2\vec{\rho} e'_l \tag{2.13}$$

with z any position along the propagation axis.

When we can consider that the mode basis are finite, we can define the matrix U_{kl} of this transformation:

$$U_{kl} = \iint_{\vec{\rho} \in \mathbb{R}^2} u_k^*(\vec{\rho}, z) u'_l(\vec{\rho}, z) d^2\vec{\rho} \tag{2.14}$$

If we turn the coefficients e_k into the vector $\vec{e}$ and the coefficients e'_l into $\vec{e}'$ with:

$$\vec{e} = \begin{pmatrix} e_1 \\ e_2 \\ \dots \end{pmatrix} \tag{2.15}$$

and

$$\vec{e}' = \begin{pmatrix} e'_1 \\ e'_2 \\ \dots \end{pmatrix} \tag{2.16}$$

the matrix U is defined so that

$$\vec{e} = U\vec{e}' \tag{2.17}$$

Since the coefficients e'_l and e_k relate to the same envelope $\mathcal{E}$ we have:

$$\sum_{k\in K} e_k^* e_k = \sum_{l\in K} e_l'^* e_l \tag{2.18}$$

This means that U preserves the norm. It belongs to the group of the unitary matrices (Serre 02).
Let us now describe two specific kinds of basis changes, which we will use extensively in the rest of this work.

Basis change induced by an optical system

When we consider a field envelope $\mathcal{E}$, the evolution of the transverse shape of $\mathcal{E}$ with the propagation along the z axis takes into account all the different media the beam is going through. It takes into account the lenses, curved mirrors or interfaces that we set in the beam path. Here we want to characterize the effect of a given unitary optical system on the beam, as presented in Fig. 2.3.

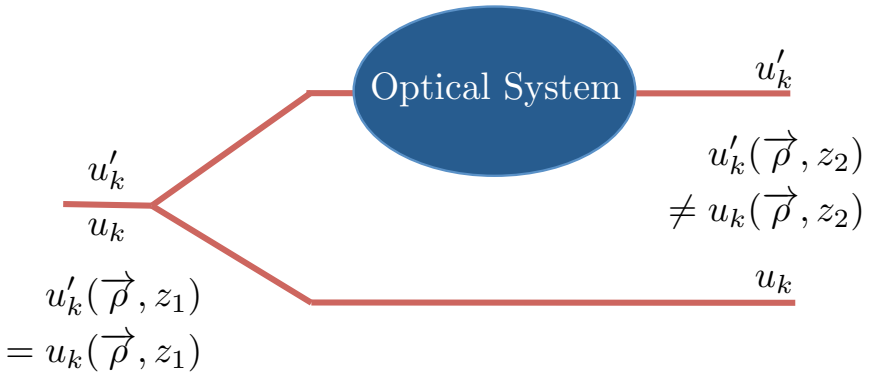

Figure 2.3: Schematic of the basis change induced by an optical system

To do so, a conventional method is to introduce two mode bases: the first basis is u_k, it is the reference basis in the absence of optical system. A second basis is u'_k: for any z_1 before the optical system we want to study, we set $u_k(\vec{\rho}, z_1) = u'_k(\vec{\rho}, z_1)$ for any $k \in K$. Then the modes u'_k propagate through the optical system we want to characterize. At a position z_2 after the optical system, $u'_k(\vec{\rho}, z_2)$ is now different from the original $u_k(\vec{\rho}, z_2)$. We can calculate the basis change matrix U defined above in equation 2.14 between the profiles $u_k(\vec{\rho}, z_2)$ and $u'_k(\vec{\rho}, z_2)$. This matrix fully describes the unitary optical system by

describing its effect on a basis of modes: the addition of the unitary optical system turns the modes u_k into the modes u'_k.

The unitary optical system we want to characterize can be a lens, a deformable reflective surface, simple propagation through different transparent media or a combination thereof. An interesting property of this matrix representation of the optical systems is that we are able to compose them. Indeed, if our beam goes through a first unitary system A, which applies the basis change matrix matrix U_A and a second unitary system B with the basis change U_B, going through both system sequentially applies the basis change $U_B U_A$, described by the product of these two unitary matrices.

Beamsplitters

Finally, let us focus on a different basis change, one which we use extensively in this work. A beamsplitter is a simple half reflecting mirror. We align two beams so that the transmitted part of a beam is superposed with the reflected part of another, as presented in Fig 2.4. Consider first that the beamsplitter has a perfect reflectivity $R = 1$. In this case we have two independent beams A and B, never superposed. An imperfect reflectivity lets some light through, and parts of beam A and B are swapped. Still, the transverse shapes of the spatial modes are untouched by the beamsplitter. If we introduce two identical mode bases (u_{Ak} and u_{Bk}), on the two beams A and B respectively, we find that a beamsplitter defined by the reflectivity $R = \cos(\theta)^2$ transforms the modes u_{Ak} and u_{Bk} in:

$$\begin{pmatrix} u'_{Ak} \\ u'_{Bk} \end{pmatrix} = \begin{pmatrix} \cos(\theta) & \sin(\theta) \\ -\sin(\theta) & \cos(\theta) \end{pmatrix} \begin{pmatrix} u_{Ak} \\ u_{Bk} \end{pmatrix} \tag{2.19}$$

This relationship applies to all the spatial modes $k \in K$.

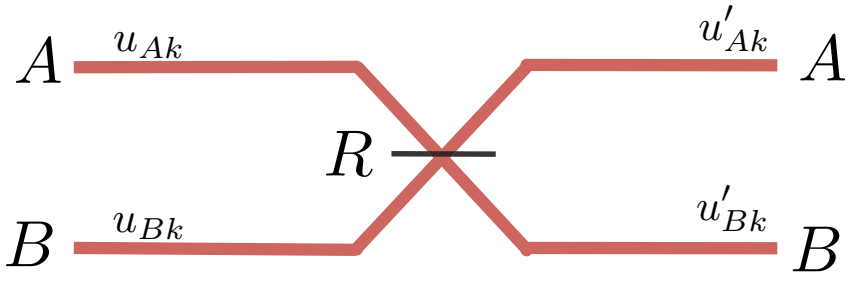

Figure 2.4: Schematic of a beamsplitter, with reflectivity R

2.2 Quantization of the electro-magnetic field

After this brief recall of important classical properties of the electro-magnetic field, let us now focus on the theoretical framework underlying the justification of this work: the

quantum nature of the light. Before introducing the necessary formalism, we first provide an experimental justifications for the quantization, developed as a teaching experiment as part of this work. Then, after having presented the Hamiltonian for the electromagnetic field, we finish with the Heisenberg picture of the evolution of field observables.

2.2.1 Why quantization?

Maxwell's equations are extremely successful at describing the dynamics of the average value of an electro-magnetic field. Teaching the quantization of the electro-magnetic field is made easier when we can exhibit phenomena which reach the limits of these equations. To do so we either need to detect very weak fields, or consider the smallest fluctuations of the electro-magnetic field. In the first case, using photomultiplier tubes or avalanche photodiode, the discreet nature of the energy of the electromagnetic field can be made clear to students.
Another justification can be found in the quantum noise, the fluctuations of an intense electro-magnetic field arising from its quantum nature. We present here a teaching publication (Morizur 08), written during the course of this work. It presents a classroom experiment built using a low cost commercial laser and electronics, able to demonstrate the existence of a quantum noise.

The teaching experiment is based on a simple laser beam, split in two by an edged mirror. We detect both the outputs using good quality photodiodes. We then use either an oscilloscope or a computer to analyse the two signals we detect on the photodiodes. With this set-up, the laser intensity noise originating from the laser is shared between the two detectors, and we detect a strong correlation of the two traces. Modulating the laser intensity increases this correlation between the channels.
On the other hand, when we increase the intensity of the beam, we find that the anti-correlated noise increases too. This shows that there is an added light related noise source, and that this other noise source introduces intensity anti-correlations. Moreover, we show that the variance of this anti-correlated noise scales as the light intensity. These are clear manifestations of quantum noise.

Quantum noise detection: A portable and educational system

Jean-François Morizur[a)]
ACQAO, The Australian National University, Canberra ACT, 0200 Australia and Laboratoire Kastler Brossel, Université Pierre et Marie Curie, Case 74, 75252 Paris cedex 05, France

Massimiliano Colla[b)]
ACQAO, The Australian National University, Canberra ACT, 0200 Australia and Centre for Quantum Technologies, National University of Singapore, Singapore

Hans-A. Bachor[c)]
ACQAO, The Australian National University, Canberra ACT, 0200 Australia

(Received 8 April 2008; accepted 22 July 2008)

Quantum noise is a key feature of laser beams. It is both a limiting effect in contemporary optical measurements and a manifestation of the quantum nature of light. Its properties distinguish it from classical noise. We demonstrate a simple, reliable, and portable apparatus using low cost commercial lasers and electronics that provides evidence of these properties. © *2008 American Association of Physics Teachers.*

[DOI: 10.1119/1.2969722]

I. INTRODUCTION: THE PROPERTIES OF OPTICAL QUANTUM NOISE

The quantum properties of light are often associated with wave-particle duality.[1,2] By using modern photodetectors it is possible to record the arrival of each photon in a beam as an individual event, if the photon flux is relatively low. This ability can be used to demonstrate some quantum effects, such as single particle interference.[3] The quantum nature of light also has consequences for the properties of much stronger beams.[4] Shot noise or optical quantum noise is the result of quantum fluctuations of the intensity of a laser beam. The formalism of quantum optics has been spectacularly successful in describing the quantum state of a laser beam, using the coherent state or Glauber state.[5] This formalism has been well tested and extended to include nonclassical or squeezed states of light[6] in which quantum noise is lowered for one property, for example, the phase, while increased for another, the amplitude; the total amount of uncertainty is kept constant.

In recent years many optical instruments have been perfected so that optical quantum noise, or shot noise as it has been called, is the dominant remaining source of noise. Quantum noise thus limits the signal-to-noise ratio for many optical tools such as absorption spectrometers,[7] interferometers,[8,9] and even laser pointers.[10] In brief, optical quantum noise is important as a fundamental consequence of quantum mechanics and as a limiting effect in the development of modern instruments.

In this paper we describe a method of detecting quantum noise in a teaching context and describe a convincing demonstration of the properties of quantum noise. The emphasis is on a simple, reliable, and low-cost apparatus using, whenever possible, readily available components.

There are three defining features of quantum noise[1,4] that allow a clear distinction between classical noise and quantum noise:

1. The quantum fluctuations of the intensity of a laser beam have a specific noise spectrum. The noise power is independent of the frequency at which it is detected. Such a spectrum is called white noise, and differs from many other noise sources which increase for lower frequencies, for example with a $1/f$ dependence.
2. Another property of quantum noise is the scaling of the noise variance with the intensity. For quantum noise the variance V_{qn} scales as

$$V_{\mathrm{qn}}(P) \sim P. \tag{1}$$

In contrast the standard deviation $\sqrt{V_{\mathrm{cl}}}$ of classical noise is a fixed percentage of the total power. Hence,

$$V_{\mathrm{cl}}(P) \sim P^2. \tag{2}$$

Likewise, the scaling law resulting from a modulation of the laser intensity is

$$V_{\mathrm{mod}}(P) \sim P^2. \tag{3}$$

3. A feature of quantum noise is its behavior in relation to beam splitting. The classical fluctuations and modulations of the beam intensity are shared between the reflected and the transmitted beams, equivalent to Kirchoff's law in electrical circuits, and result in two perfectly correlated beams hitting the detectors. In contrast, quantum noise introduces uncorrelated noise. One way to understand this property is to remember that quantum noise comes from the random arrival of photons. The photons are not split in half by the beam splitter, but have a 50% probability to be transmitted or reflected. This randomness gives rise to uncorrelated noise in the detectors. If a laser beam is quantum noise limited and the classical noise is negligible, the noise in the two output beams from the beam splitter is completely uncorrelated.

In our experiment we demonstrate properties (2) and (3). The spectral properties (1) can be demonstrated using an electronic spectrum analyzer, but this kind of device is outside the scope of most teaching laboratories. To demonstrate the scaling and correlation properties, a light source with as little classical noise as possible is necessary. Such a source is readily available as a low-cost diode laser. Detectors and amplifiers that contribute less electronic noise than quantum noise are also required. For this purpose we use photodetectors with custom-made preamplifiers and commercial low noise amplifiers.[11,12] A conventional oscilloscope is used to

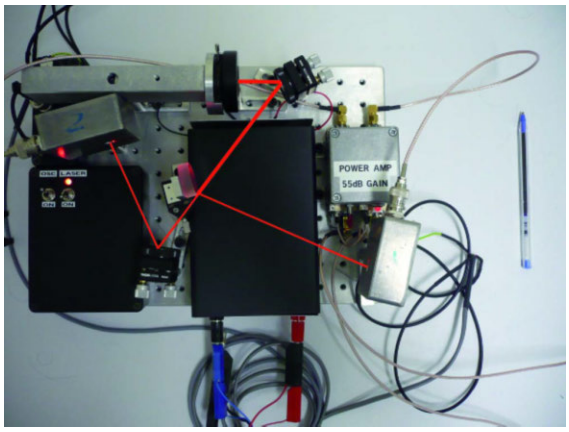

(a)

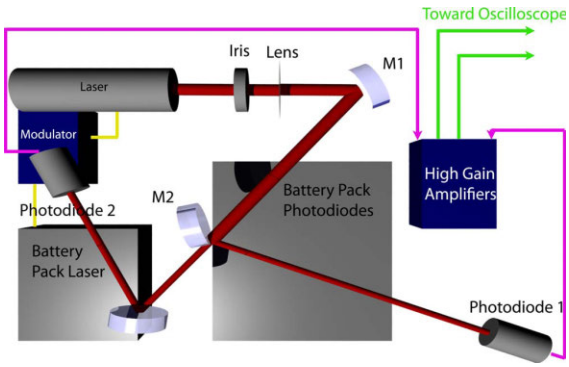

(b)

Fig. 1. The total laser beam power is adjusted using an aperture in front of the laser source. The laser intensity is modulated using a custom-built amplified crystal oscillator which produces a sinusoidal modulation at 2 MHz. The two beams are simultaneously detected by photodiodes 1 and 2 and the amplified signals are displayed on an oscilloscope in x-y mode.

detect the output signal, and a straightforward analysis method is available using an oscilloscope with an x-y display.

The apparatus shown in Fig. 1 enables us to measure both the correlation and scaling properties of optical quantum noise and to demonstrate some quantum features of light. Most optical experiments either focus on the frequency domain using spectrum analyzers and measure the noise spectrum of intense beams.[13] Alternatively, they focus on counting the clicks from individual photons with avalanche photodiodes[14] to study the correlations between the clicks from one or more detectors. Our design allows us to investigate correlations in an intense beam using a continuous noise signal.

II. THE EXPERIMENT

Because the goal is to design a teaching and demonstration experiment, our emphasis is on simplicity. Accordingly, the apparatus is small (the entire experimental setup fits on a 210 mm $\times$ 300 mm breadboard) and uses a conventional oscilloscope. The trick is to use an oscilloscope as a detector for correlations. The laser beam is split into two beams 1 and 2 of equal power by sliding mirror M2 half-way across the beam. Each beam is detected separately and the photocurrents are amplified and displayed simultaneously on the x and y axis of the oscilloscope. If the two photocurrents, which are proportional to the intensities $I_1(t)$ and $I_2(t)$ of the beams, are correlated, the display will be on the diagonal axis. That is, correlated noise will be seen as fluctuations along the diagonal axis, at 45° to the x and y axes, if the intensities and gains in the two beams are the same. Uncorrelated noise will lead to independent fluctuations in both the x and y axes and produce a fuzzy area on the screen. For equal intensity and gain this area will be circular. The oscilloscope displays all frequencies up to its cutoff frequency or the detector's or the amplifier's. To demonstrate quantum noise we have to be very careful to avoid any extraneous noise, for example from stray magnetic fields. Reducing extraneous noise can be achieved by good design and electromagnetic shielding.

The apparatus employs a relatively low power laser diode pointer (~8 mW) emitting a beam at 632 nm with a slightly elliptical shape. The laser is housed in an aluminium casing secured to the custom-made aluminium breadboard. The laser beam intensity can be changed by adjusting the diameter of an aperture mounted directly outside the diode laser. The laser beam is then focussed by a lens (200 mm focal length) on the detectors to maximize the detection efficiency. After the lens the beam is reflected by mirror M1 and split into equal parts by a second mirror M2. One half of the beam is redirected onto the first photodetector while the other half misses the mirror and proceeds to the second photodetector. The beamsplitting mirror is mounted on a miniature translational stage (Thorlab MR 1.4) which allows it to move in and out of the beam and the splitting ratio to be adjusted. The mirror M2 could also be replaced by a half-silvered mirror, at the expense of loosing the ability to adjust the splitting ratio.

The two detectors are custom made and are matched to produce very similar outputs when exposed to the same power. The aim is to create the largest quantum noise signal and suppressing the electronic noise from the first amplifier inside the detector is critical. The direct current (dc) signals from the detectors are monitored to ensure that the power P is equally split between the photodiodes; the alternating current (ac) signals are connected to a pair of high-gain/low noise commercial amplifiers (MITEQ, frequency 1–100 MHz). Several rechargeable battery packs make this system completely portable and reduce noise inputs from power supply. A picture and the layout of the system can be found in Fig. 1.

The laser intensity can be modulated with the electronic voltage created by the amplified crystal oscillator (IQXO-350). The degree of modulation is adjusted by the user. The modulation frequency must be high enough so that the modulated signal is not affected by low-frequency noise sources, including the $1/f$ noise resulting from the electronics, and is above the lower cutoff frequency of the amplifiers (1 MHz). The frequency also must not exceed either the maximum modulation frequency of the laser or push to the limits the low-noise amplifiers inside the detectors. For this reason an intermediate value of 2 MHz was chosen. Because the evidence of quantum noise that we seek does not depend on this modulation frequency, it remains fixed throughout the experiments.

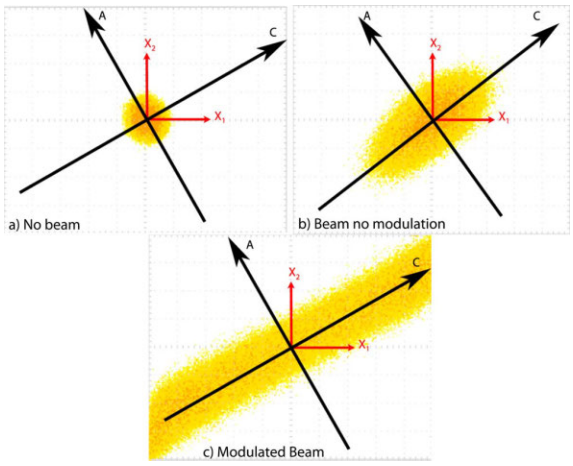

Fig. 2. Display of the oscilloscope used for measuring the noise and correlation. The x and y axis display the photocurrent generated by detectors 1 and 2, respectively. Any correlated noise will appear on the diagonal axis labeled C; any uncorrelated noise will appear equally on the A and C axes. (a) The laser is turned off, (b) the laser beam at 8 mW without modulation, and (c) the laser beam at 8 mW and maximum modulation.

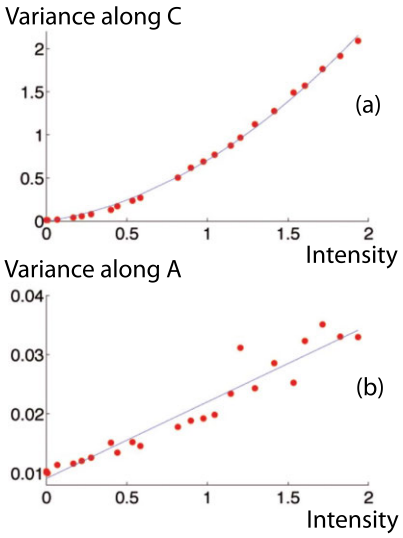

Fig. 3. Variance of the intensity fluctuations as a function of the average intensity of the beam in photocurrent units. (a) The variance along the correlated axis with a quadratic dependence on the intensity. (b) The variance along the anti-correlated axis with a linear dependence on the intensity.

III. RESULTS

With the two photodiodes aligned and the laser turned on, the two signals originating from the photodetectors are displayed in x-y mode. Different investigations are possible by varying the intensity of the beam and the modulation amplitude.

The electrical noise, that is, dark noise, of the detectors and amplifiers is first measured by turning the laser off. This noise calibration is critical because we need the quantum noise to be significantly larger than the dark noise.

By turning on the laser without introducing any modulation, the beams create additional fluctuations. They are the result of the optical quantum noise for which the two signals from photodiode 1 and 2 are uncorrelated and the residual classical noise in the laser. This classical noise introduces correlations between the two photodiode channels. Figures 2(a) and 2(b) show oscilloscope traces of the signal for no beam, that is, dark noise, and for an 8 mW beam, respectively.

Noise along the C axis is correlated noise, and noise along the A axis is anticorrelated. The C axis is not perfectly at 45° because the gains of the amplifiers are not perfectly balanced. Both dark noise and quantum noise, because they produce noncorrelated signals on the two detectors, introduce fluctuations equally on the A and C axes. In contrast, classical noise and modulation of the laser intensity introduce correlations between the two signals and give fluctuations only on the C axis. Thus, a comparison of Figs. 2(a) and 2(b) makes it easy to evaluate the different components of the noise encountered. Along the A axis the difference of the noise level between Figs. 2(a) and 2(b) can be attributed to quantum noise. This simple comparison provides us with a first demonstration of the uncorrelated nature of quantum noise and a clear assessment of the quality of the detectors. We show a ratio of 3.5 between the variance of the noise from a 8 mW beam and the variance of the electrical noise, without filtering the output signal. Using bandpass filters in the 3–5 Mhz range improves the ratio to 5.5, and introduces phase differences between the two output signals. These phase differences do not allow for a clear linear shape when introducing modulation and thus were not used in our measurements. Second, comparing the noise levels along the C and A axes in Fig. 2(b) emphasizes the correlated nature of the classical noise of the beam.

Further analysis is possible by using the modulator, which introduces strong classical fluctuations. Their correlated nature is obvious in Fig. 2(c), with overextended fluctuations along the C axis, while fluctuations along A remain similar to Fig. 2(b). Thus, the analysis of several oscilloscope traces demonstrates the uncorrelated nature of quantum noise. By setting the modulation amplitude to the maximum value below the amplifier's saturation and changing the average beam intensity, it is possible to observe the scaling laws. Figure 3 shows the variance of the fluctuations as a function of the beam intensity. We observe both the linear scaling of the quantum noise and the quadratic scaling of the classical noise.

Finally, recording the trace is possible, either by using a digital oscilloscope with relevant connectivity (for example a Tektronix TDS 2004 B) or a USB oscilloscope (Voltcraft DSO-220 USB). The distribution of the data points recorded with a modulated beam provide further confirmation of the correlated nature of classical fluctuations. As can be seen in Fig. 4 the shape of the distribution is clearly non-Gaussian along the C axis because it is the result of the sinusoidal modulation of the intensity. In contrast, along the A axis, the distribution remains Gaussian, thus indicating that no fluctuations on the A axis result from the modulation. The A axis is thus truly uncorrelated noise, that is, dark noise and quantum noise. If we consider that the total fluctuations of the signal are a result of the modulation, classical noise, dark noise, and quantum noise, the fit of the theoretical distribution to the data gives very accurate results.

In conclusion, our simple experiment provides evidence of

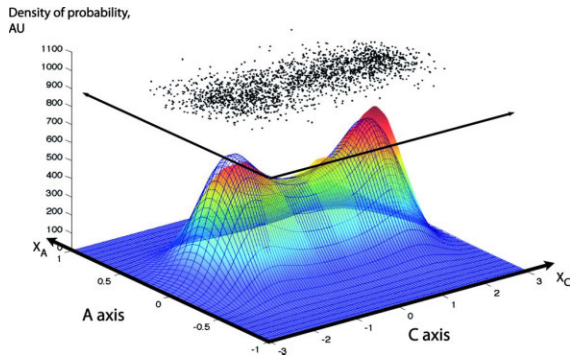

Fig. 4. The distribution of the measurements is non-Gaussian as a result of the sinusoidal modulation. The black dots are the measurements results (only one fifth of the actual sample is shown), and the full surface is the measurement's density. The wired surface is a theoretical distribution which accounts for all the noise terms discussed in the text.

the properties of quantum noise in intense beams. It can also be used as a benchmark to compare the performance of equipment to the quantum noise limit.

ACKNOWLEDGMENTS

The authors would like to thank Neil Hintchey and Caroline Christenson for their great technical support. This work was supported by Centre of Excellence for Quantum-Atom Optics of the Australian Research Council.

[a]Electronic mail: jean-francois.morizur@anu.edu.au
[b]Electronic mail: max.colla@nus.edu.sg
[c]Electronic mail: hans.bachor@anu.edu.au

[1]Rodney Loudon, *The Quantum Theory of Light*, 3rd ed. (Oxford U.P., Oxford, 2004), pp. 117–123.
[2]Claude Cohen-Tannoudji, Bernard Diu, and Frank Laloe, *Quantum Mechanics* (Wiley-Interscience, Malden, MA, 2006).
[3]C. H. Holbrow, E. Galvez, and M. E. Parks, "Photon quantum mechanics and beam splitters," Am. J. Phys. **70**, 260–265 (2002).
[4]Hans-A. Bachor and Timothy Ralph, *A Guide to Experiments in Quantum Optics*, 2nd ed. (Wiley, Malden, MA, 2003).
[5]R. J. Glauber, "Coherent and incoherent states of radiation field," Phys. Rev. **131**, 2766–2788 (1963).
[6]D. F. Walls, "Squeezed states of light," Nature (London) **306**, 141–146 (1983).
[7]F. Marin, A. Bramati, V. Jost, and E. Giacobino, "Demonstration of high sensitivity spectroscopy with squeezed semiconductor lasers," Opt. Commun. **140**, 146–157 (1997).
[8]A. F. Pace, M. J. Collet, and D. F. Walls, "Quantum limits in interferometric detection of gravitational-radiation," Phys. Rev. A **47**, 3173–3189 (1993).
[9]C. M. Caves, "Quantum-mechanical noise in an interferometer," Phys. Rev. D **23**, 1693–1708 (1981).
[10]N. Treps, N. Grosse, W. P. Bowen, C. Fabre, H.-A. Bachor, and P. K. Lam, "A quantum laser pointer," Science **301**, 940–943 (2003).
[11]See EPAPS Document No. E-AJPIAS-76-013810 for the design of the amplifiers. For more information on EPAPS, see http://www.aip.org/pubservs/epaps.html.
[12]M. B. Gray, D. A. Shaddock, C. C. Harb, and H.-A. Bachor, "Photodetector designs for low-noise, broadband, and high-power applications," Rev. Sci. Instrum. **69**, 3755–3762 (1998).
[13]A. Furusawa, J. L. Sorensen, S. L. Braunstein, C. A. Fuchs, H. J. Kimble, and E. S. Polzik, "Unconditional quantum teleportation," Science **282**, 706–709 (1998).
[14]R. Short and L. Mandel, "Observation of sub-Poissonian photon statistics," Phys. Rev. Lett. **51**, 384–387 (1983).

2.2.2 Formalism

Quantization

A complete introduction of the quantization process is out of the reach of this work, it can be found in (Grynberg 10) or (Mandel 95). Rather, this section aims at emphasizing the role of observables in our approach of quantum optics (Balian 88) while introducing the notations used in the rest of the work.

Quantifying the electric field means considering that $\vec{E}.\vec{e_x}$ is not a defined value anymore, but the result of an observation on a quantum state. The mean value of these observations is of course the classical $\vec{E}.\vec{e_x}$, but additional fluctuations of these observations arise due to the quantum nature of the state considered. To explain the fluctuations recorded experimentally, we replace the classical envelope field $\mathcal{E}$ by the operator $\hat{\mathcal{E}}$, and we introduce $\hat{a}(\vec{\rho}, z)$, the photon annihilation operator at the position $(\vec{\rho}, z)$ defined by

$$\hat{\mathcal{E}}(\vec{\rho}, z) = \sqrt{\frac{\hbar 2\pi\nu_0}{2\epsilon_0 cT}}\hat{a}(\vec{\rho}, z) \tag{2.20}$$

with T an integration time. $\hat{a}(\vec{\rho}, z)^\dagger\hat{a}(\vec{\rho}, z)$ is homogeneous to a number of photons (an integer) per square meter, incident at position $(\vec{\rho}, z)$, detected during a time interval $[t, t+T]$.

Our work focuses on spatial properties of the quantum fluctuations. We work with stationary fields. Thus we can write $\hat{a}(\vec{\rho}, z)$ without the dependency in the time t: the expectations for the results of any given measurement in our system does not depend on the time at which we take this measurement. The value of T is set depending on the detection system. It corresponds to the inverse of the sampling rate.

Creation and annihilation operators

The operator $\hat{a}(\vec{\rho}, z)$ is the annihilation operator. Its conjugate, $\hat{a}^\dagger(\vec{\rho}, z)$ is the photon creation operator. These two operators are not Hermitian, so they cannot be observables. However, they are the building blocks of quantum optics, and to that extend have a few interesting physical properties. First of all, as a consequence of the definition 2.20, the local electric field can be decomposed using these two operators:

$$\hat{\vec{E}}(\vec{\rho}, z, t).\vec{e_x} = \sqrt{\frac{\hbar 2\pi\nu_0}{2T\epsilon_0 c}}\left(\hat{a}(\vec{\rho}, z)e^{-i2\pi\nu_0(t-\frac{z}{c})} + \hat{a}^\dagger(\vec{\rho}, z)e^{i2\pi\nu_0(t-\frac{z}{c})}\right) \tag{2.21}$$

The number of photon crossing a given surface S in our integration time T can also be expressed using $\hat{a}(\vec{\rho}, z)$ and $\hat{a}^\dagger(\vec{\rho}, z)$:

$$\hat{N}(z, S) = \iint_{\vec{\rho}\in S} \hat{a}^\dagger(\vec{\rho}, z)\hat{a}(\vec{\rho}, z)\, d^2\vec{\rho} \tag{2.22}$$

This quantity can for example be detected using a photon counter. The commutator of these two operators has a simple expression when we consider annihilation and creation operators on the same propagation plane defined by $z = z_0$:

$$\left[\hat{a}(\vec{\rho_1}, z_0), \hat{a}(\vec{\rho_2}, z_0)^\dagger\right] = \delta^2(\vec{\rho_1} - \vec{\rho_2}) \tag{2.23}$$

When they are not in the same propagation plane, these two operators are not independent anymore, and their commutator depends on the optical system between them.

The observables amplitude and phase

Let us name amplitude $\hat{x}(\vec{\rho}, z)$ and phase $\hat{p}(\vec{\rho}, z)$ the observables defined by:

$$\begin{aligned} \hat{x}(\vec{\rho}, z) &= \hat{a}^\dagger(\vec{\rho}, z) + \hat{a}(\vec{\rho}, z) \\ \hat{p}(\vec{\rho}, z) &= i\left(\hat{a}^\dagger(\vec{\rho}, z) - \hat{a}(\vec{\rho}, z)\right) \end{aligned} \tag{2.24}$$

These two observables, also named quadratures of the electro-magnetic field at the position $(\vec{\rho}, z)$ are closely related to the the observable $\vec{\hat{E}}(\vec{\rho}, z, t).\vec{e_x}$. Indeed, the expression 2.21 can be rewritten using $\hat{x}(\vec{\rho}, z)$ and $\hat{p}(\vec{\rho}, z)$ as:

$$\vec{\hat{E}}(\vec{\rho}, z, t).\vec{e_x} = \sqrt{\frac{\hbar 2\pi\nu_0}{T\epsilon_0 c}}\left[\cos\left(2\pi\nu_0\left(t - \frac{z}{c}\right)\right)\hat{x}(\vec{\rho}, z) + \sin\left(2\pi\nu_0\left(t - \frac{z}{c}\right)\right)\hat{p}(\vec{\rho}, z)\right] \tag{2.25}$$

This formulation of $\vec{\hat{E}}(\vec{\rho}, z, t)$ shows that depending on the phase of $2\pi\nu_0(t - \frac{z}{c})$, the electro-magnetic field is either proportional to the amplitude $\hat{x}(\vec{\rho}, z)$ or the phase $\hat{p}(\vec{\rho}, z)$.

These two observables describe the electro-magnetic field, and detecting a quantum state can result in any value in $\mathbb{R}$, depending on the state. As opposed to $\hat{a}(\vec{\rho}, z)^\dagger\hat{a}(\vec{\rho}, z)$, which can only lead to discreet values (a number of photons) in a detection volume, they are continuous. In this thesis, we only deal with this kind of observable: we remain in the continuous variable regime.

The commutator of $\hat{x}(\vec{\rho_1}, z_0)$ and $\hat{p}(\vec{\rho_2}, z_0)$ is

$$[\hat{x}(\vec{\rho_1}, z_0), \hat{p}(\vec{\rho_2}, z_0)] = 2i\delta^2(\vec{\rho_1} - \vec{\rho_2}) \tag{2.26}$$

When they are not in the same propagation plane, as for the creation and annihilation operators, their commutator depends on the optical system between the planes.

Finally, let us introduce $\hat{x}^\theta(\vec{\rho}, z)$ and $\hat{p}^\theta(\vec{\rho}, z)$. We define them as rotations of $\hat{x}(\vec{\rho}, z)$

and $\hat{p}(\vec{\rho}, z)$:

$$\hat{x}^\theta(\vec{\rho}, z) = \cos(\theta)\hat{x}(\vec{\rho}, z) + \sin(\theta)\hat{p}(\vec{\rho}, z) \tag{2.27}$$

$$\hat{p}^\theta(\vec{\rho}, z) = \sin(\theta)\hat{x}(\vec{\rho}, z) - \cos(\theta)\hat{p}(\vec{\rho}, z) \tag{2.28}$$

We call $\hat{x}^\theta(\vec{\rho}, z)$ and $\hat{p}^\theta(\vec{\rho}, z)$ the θ-quadratures of the electro-magnetic field, and we have

$$[\hat{x}^\theta(\vec{\rho_1}, z_0), \hat{p}^\theta(\vec{\rho_2}, z_0)] = 2i\delta^2(\vec{\rho_1} - \vec{\rho_2}) \tag{2.29}$$

The θ-quadratures of the electro-magnetic field correspond to the original $\hat{x}(\vec{\rho}, z)$ and $\hat{p}(\vec{\rho}, z)$ with a θ phase shift in $\hat{\vec{E}}(\vec{\rho}, z, t).\vec{e_x}$:

$$\hat{\vec{E}}(\vec{\rho}, z, t).\vec{e_x} = \sqrt{\frac{\hbar 2\pi\nu_0}{T\epsilon_0 c}} \left[\cos\left(2\pi\nu_0\left(t - \frac{z}{c}\right) - \theta\right)\hat{x}^\theta(\vec{\rho}, z) + \sin\left(2\pi\nu_0\left(t - \frac{z}{c}\right) - \theta\right)\hat{p}^\theta(\vec{\rho}, z)\right] \tag{2.30}$$

In the literature, the notations for the amplitude and phase quadratures of the electro-magnetic field are not consistent. We can find $\hat{X^+}$ and $\hat{X^-}$ (Delaubert 06; Grosse 06), $\hat{x}$ and $\hat{y}$ (Beck 01), or $\hat{X}$ and $\hat{X}^\perp$ (Hage 10). Our choice, $\hat{x}$ and $\hat{p}$, also used in (Adesso 06; Aoki 09a; Duan 00; Grosshans 01; Hage 08), is more traditional. Still, confusions may arise between the spatial coordinate x and the field amplitude quadrature $\hat{x}$. In this work, both the notations and the context will provide a disambiguation.

Modal operators

Local operators, such as $\hat{a}(\vec{\rho}, z)$ or $\hat{x}(\vec{\rho}, z)$ are defined at a given, localized position. This kind of localization, while theoretically useful, is not physically sound. Instead, let us introduce modal operators: for a given spatial mode u defined by its transverse profile $u(\vec{\rho}, z = 0)$ in the plane $z = 0$, we define the modal operators $\hat{a}_u$, $\hat{x}_u$ and $\hat{p}_u$ as:

$$\begin{aligned}
\hat{a}_u &= \iint_{\vec{\rho}\in\mathbb{R}^2} \hat{a}(\vec{\rho}, z = 0)u(\vec{\rho}, z = 0)^* \, d^2\vec{\rho} \\
\hat{x}_u &= \iint_{\vec{\rho}\in\mathbb{R}^2} \hat{x}(\vec{\rho}, z = 0)u(\vec{\rho}, z = 0)^* \, d^2\vec{\rho} \\
\hat{p}_u &= \iint_{\vec{\rho}\in\mathbb{R}^2} \hat{p}(\vec{\rho}, z = 0)u(\vec{\rho}, z = 0)^* \, d^2\vec{\rho}
\end{aligned} \tag{2.31}$$

For these new operators, the commutation relations are now simply

$$[\hat{a}_u, \hat{a}_u^\dagger] = 1 \tag{2.32}$$

and

$$[\hat{x}_u, \hat{p}_u] = 2i \tag{2.33}$$

Because the commutator of $\hat{x}_u$ and $\hat{p}_u$ is not 0, there is a fundamental limit to the

simultaneous measurement of $\hat{x}_u$ and $\hat{p}_u$. Indeed, Heisenberg' uncertainty principle states that, for any two observables $\hat{A}$ and $\hat{B}$

$$\left\langle \Delta^2 \hat{A} \right\rangle \left\langle \Delta^2 \hat{B} \right\rangle \geq \frac{1}{4} | \left\langle [\hat{A}, \hat{B}] \right\rangle |^2 \tag{2.34}$$

Hence, the uncertainty relation between $\hat{x}_u$ and $\hat{p}_u$ is simply:

$$\left\langle \Delta^2 \hat{x}_u \right\rangle \left\langle \Delta^2 \hat{p}_u \right\rangle \geq 1 \tag{2.35}$$

Whatever the nature of the quantum state, 2.35 means that the variances of the measured values of $\hat{x}_u$ and $\hat{p}_u$ are related. There is a minimum to the product of these variances.

States which variances $\left\langle \Delta^2 \hat{x}_u \right\rangle$ and $\left\langle \Delta^2 \hat{p}_u \right\rangle$ satisfy $\left\langle \Delta^2 \hat{x}_u \right\rangle \left\langle \Delta^2 \hat{p}_u \right\rangle = 1$ are called quantum limited states. Furthermore, the equal repartition of the fluctuations between $\left\langle \Delta^2 \hat{x}_u \right\rangle$ and $\left\langle \Delta^2 \hat{p}_u \right\rangle$ gives $\left\langle \Delta^2 \hat{x}_u \right\rangle = \left\langle \Delta^2 \hat{p}_u \right\rangle = 1$, and the limit $\left\langle \Delta^2 \hat{x}_u \right\rangle = 1$ is called the quantum noise limit for $\hat{x}_u$. Similarly, $\left\langle \Delta^2 \hat{p}_u \right\rangle = 1$ is the quantum noise limit for $\hat{p}_u$.

Propagation of modal operators

In the above definition of the operators $\hat{a}_u$, $\hat{x}_u$ and $\hat{p}_u$, we did not not use the fact u is an electro-magnetic field mode. The transverse profile of u evolves with the propagation to satisfy Maxwell's equations. This property is reflected in the quantization: for any other position z_1, the same operators $\hat{a}_u$ $\hat{x}_u$ and $\hat{p}_u$ can be expressed as:

$$\begin{aligned} \hat{a}_u &= \iint_{\vec{\rho} \in \mathbb{R}^2} \hat{a}(\vec{\rho}, z_1) u(\vec{\rho}, z_1)^* \, d^2\vec{\rho} \\ \hat{x}_u &= \iint_{\vec{\rho} \in \mathbb{R}^2} \hat{x}(\vec{\rho}, z_1) u(\vec{\rho}, z_1)^* \, d^2\vec{\rho} \\ \hat{p}_u &= \iint_{\vec{\rho} \in \mathbb{R}^2} \hat{p}(\vec{\rho}, z_1) u(\vec{\rho}, z_1)^* \, d^2\vec{\rho} \end{aligned} \tag{2.36}$$

Conversely, if we now consider a basis of modes u_k, $k \in K$ and name the corresponding operators $\hat{a}_k$ we have

$$\begin{aligned} \hat{a}(\vec{\rho}, z) &= \sum_{k \in K} u_k(\vec{\rho}, z) \hat{a}_k \\ \hat{x}(\vec{\rho}, z) &= \sum_{k \in K} u_k(\vec{\rho}, z) \hat{x}_k \\ \hat{p}(\vec{\rho}, z) &= \sum_{k \in K} u_k(\vec{\rho}, z) \hat{p}_k \end{aligned} \tag{2.37}$$

Another way to understand these operators is to consider the envelope coefficients $\boldsymbol{e}_k$ resulting from the decomposition of a classical field in a mode basis u_k presented in 2.6. The quantization transformed the value of the envelope $\boldsymbol{\mathcal{E}}(\vec{\rho}, z)$ into an observable $\hat{\boldsymbol{\mathcal{E}}}(\vec{\rho}, z)$. Similarly, the quantization transforms the coefficients $\boldsymbol{e}_k$ into the observables $\hat{\boldsymbol{e}}_k$.

And we find that:

$$\hat{\boldsymbol{e}}_k = \sqrt{\frac{\hbar 2\pi\nu_0}{2\epsilon_0 cT}}\hat{a}_k \tag{2.38}$$

The position dependence of the quantum operators is entirely transferred to the mode basis $u_k(\vec{\rho}, z)$. This gives us the ability to propagate our operators through optical systems. And we have the commutators

$$[\hat{a}_{u_k}, \hat{a}^\dagger_{u_l}] = \delta_{kl} \tag{2.39}$$

$$[\hat{x}_{u_k}, \hat{p}_{u_l}] = i\delta_{kl} \tag{2.40}$$

Basis change

Like in the classical case, we introduce $\hat{a}_k$ and $\hat{a}'_l$, two sets of modal operators which correspond to the two mode basis u_k and u'_l, respectively. The operators $\hat{a}_k$ and $\hat{a}'_l$ are not independent. Indeed, using the same relation as in the classical case, only this time with the modal operators, we have

$$\begin{aligned} \hat{a}(\vec{\rho}, z) &= \textstyle\sum_{l\in K} u'_l(\vec{\rho}, z)\hat{a}'_l \\ &= \textstyle\sum_{k\in K} u_k(\vec{\rho}, z)\hat{a}_k \end{aligned} \tag{2.41}$$

Thus, by defining the same transfer matrix U as in the classical case (see equation 2.14), we find a direct relationship between the modal operators:

$$\hat{a}_k = \sum_{l\in K} U_{kl}\hat{a}'_l \tag{2.42}$$

If we introduce the notations $\vec{\hat{a}}$ and $\vec{\hat{a}}'$, which denote the vectors of operators $\hat{a}_k$ and $\hat{a}'_l$, we can write simply:

$$\vec{\hat{a}} = U\vec{\hat{a}}' \tag{2.43}$$

Even if U acts on quantum operators, it is completely defined by the classical equation 2.14. We have seen classically that transparent media and beamsplitters produce specific unitary transforms U on the classical envelope coefficients $\boldsymbol{e}_k$. Similarly, in a quantum context, these optical elements apply the same unitary transform U to the quantum operators $\hat{a}_k$.

2.2.3 Quantum states

Quantum observables are hermitian operators within the space of the quantum states. We have presented relationships between these properties, such as equation 2.35. These relations are true independently from the quantum state measured. But observables correspond to physical measurements of properties of an underlying quantum state. Let us now present a few properties of the quantum states we deal with in the course of this work.

Generalities

The quantum state of a physical system is represented by a vector in a Hilbert space. We call it $|\psi\rangle$, and its conjugate $|\psi\rangle^\dagger = \langle\psi|$. This vector represents the complete physical state of the experimental apparatus. In our case, if we limit our experiment to a single mode, $|\psi\rangle$ represents the quantum state of the light in this spatial mode. If the experiment is more complex and deals with multiple modes and beams, $|\psi\rangle$ represents the state of the light in all these beams.

Schrödinger's description of quantum mechanics is based on the idea of an evolving quantum state (Cohen-Tannoudji 06; Haroche 06). In this picture, we start from a specific quantum state $|\psi_0\rangle$ and the experimental apparatus makes this state evolve. This evolution is described by a unitary operation in the Hilbert space U so that after the evolution we have the state $|\psi_1\rangle = U|\psi_0\rangle$. We then use observables to detect the output state $|\psi_1\rangle$. For example, the mean of the detection of observable $\hat{A}$ is then:

$$\left\langle \hat{A} \right\rangle = \langle\psi_1|\hat{A}|\psi_1\rangle = \langle\psi_0|U^\dagger \hat{A} U|\psi_0\rangle. \tag{2.44}$$

This description of quantum mechanics is best suited to systems for which we can prepare a well-defined starting state $|\psi_0\rangle$. It is especially well suited to describe Rydberg atoms for example (Guerlin 07). In quantum optics, such a precise state preparation is crucial when dealing with protocols based on single photon states (Hübel 10; Knill 01).

On the other hand, Heisenberg's description of quantum mechanics is based on the evolution of observables (Grynberg 10; Mandel 95). Indeed, instead of letting the state evolve under U, we choose to represent the same evolution by letting all the observables evolve: $\hat{A} \to U^\dagger \hat{A} U$, keeping the state fixed at $|\psi_0\rangle$. This means that instead of focusing on the quantum state itself, we describe our physical apparatus by how it changes the operators. For example, this is what we did in equation 2.43 where we described the effect of a beamsplitter or transparent media by their effect on a set of operators. Heisenberg's description is widespread in quantum optics, especially when dealing with continuous variable systems, i.e. with observables with a continuous spectrum of results, which is our case (Duan 00; Loock 07b; Janousek 08a).

Gaussian states

We only deal with a specific family of quantum states: the Gaussian states, sometimes referred to as a "Gausson" (Simon 88), in the continuous variable regime. The Gaussian states are fully specified by giving, for all the observables $\hat{x}_u$ and $\hat{p}_u$ (for all the modes u considered), their means and all their covariances. For example, if we consider a two mode Gaussian state, (the modes being u and v), it can be fully defined by measuring

their mean:

$$\begin{pmatrix} \langle \hat{x}_u \rangle \\ \langle \hat{x}_v \rangle \\ \langle \hat{p}_u \rangle \\ \langle \hat{p}_v \rangle \end{pmatrix} \tag{2.45}$$

and their covariance matrix:

$$C = \begin{pmatrix} \mathrm{cov}\left(\hat{x}_u, \hat{x}_u\right) & \mathrm{cov}\left(\hat{x}_u, \hat{x}_v\right) & \mathrm{cov}\left(\hat{x}_u, \hat{p}_u\right) & \mathrm{cov}\left(\hat{x}_u, \hat{p}_v\right) \\ \mathrm{cov}\left(\hat{x}_v, \hat{x}_u\right) & \mathrm{cov}\left(\hat{x}_v, \hat{x}_v\right) & \mathrm{cov}\left(\hat{x}_v, \hat{p}_u\right) & \mathrm{cov}\left(\hat{x}_v, \hat{p}_v\right) \\ \mathrm{cov}\left(\hat{p}_u, \hat{x}_u\right) & \mathrm{cov}\left(\hat{p}_u, \hat{x}_v\right) & \mathrm{cov}\left(\hat{p}_u, \hat{p}_u\right) & \mathrm{cov}\left(\hat{p}_u, \hat{p}_v\right) \\ \mathrm{cov}\left(\hat{p}_v, \hat{x}_u\right) & \mathrm{cov}\left(\hat{p}_v, \hat{x}_v\right) & \mathrm{cov}\left(\hat{p}_v, \hat{p}_u\right) & \mathrm{cov}\left(\hat{p}_v, \hat{p}_v\right) \end{pmatrix} \tag{2.46}$$

with $\mathrm{cov}\left(\hat{x}_v, \hat{x}_u\right) = \frac{1}{2}\left\langle \hat{x}_v\hat{x}_u + \hat{x}_u\hat{x}_v \right\rangle - \left\langle \hat{x}_v \right\rangle \left\langle \hat{x}_u \right\rangle$ and $\mathrm{cov}\left(\hat{x}_v, \hat{p}_u\right) = \frac{1}{2}\left\langle \hat{x}_v\hat{p}_u + \hat{p}_u\hat{x}_v \right\rangle - \left\langle \hat{x}_v \right\rangle \left\langle \hat{p}_u \right\rangle$.

Combinations of moments can be calculated from the results of these measurements in a fashion similar to the computation of moments of Gaussian distributions. These properties make Gaussian states easier to characterize using the observables $\hat{x}_u$ and $\hat{p}_u$: measuring the means and the covariance matrix fully defines the state.

Let us now discuss further two specific, single mode, Gaussian states: the coherent state and the squeezed state.

Coherent state

The coherent state is a Gaussian state first introduced by Glauber in his seminal paper (Glauber 65). A thorough description of the state can be found in (Zhang 90). If we consider a single mode u, a coherent state in mode u is an eigenstate of the annihilation operator $\hat{a}_u$. This means that there is a complex number α so that the coherent state $|\psi\rangle$ has the property

$$\hat{a}_u|\psi\rangle = \alpha|\psi\rangle \tag{2.47}$$

We name these states by their eigenvalues α, so that the coherent state with the eigenvalue α is simply written $|\alpha\rangle$. These state have a few interesting properties. First of all, they are the states generated by a perfect, noiseless, laser. If the laser cavity is resonant in the mode u, at its output there is a coherent state $|\alpha\rangle$ in mode u.

A second property of the coherent state is that it is quantum noise limited, with specific variances: $\left\langle \Delta^2\hat{x}_u \right\rangle = \left\langle \Delta^2\hat{p}_u \right\rangle = 1$. Both of its variances are at the quantum noise limit. Let us introduce the phasor representation (the "ball on stick" picture). It is presented in Fig 2.5. The "stick" represent the means of the observables $\hat{x}_u$ and $\hat{p}_u$, while the sizes of the ball represent the variances $\left\langle \Delta^2\hat{x}_u \right\rangle$ and $\left\langle \Delta^2\hat{p}_u \right\rangle$. Since $\left\langle \Delta^2\hat{x}_u \right\rangle = \left\langle \Delta^2\hat{p}_u \right\rangle = 1$, we also have $\left\langle \Delta^2\hat{x}_u^\theta \right\rangle = 1$ for all the values of θ.

A final interesting property of the coherent state is that the vacuum is, by definition,

a coherent state: $\hat{a}_u|0\rangle = 0$. The vacuum is an eigenstate of $\hat{a}_u$. The vacuum has the same noise properties as the other coherent states. It is presented in Fig. 2.5, and we have $\langle \Delta^2 \hat{x}_u \rangle = \langle \Delta^2 \hat{p}_u \rangle = 1$. The quantum noise limit is the vacuum noise.

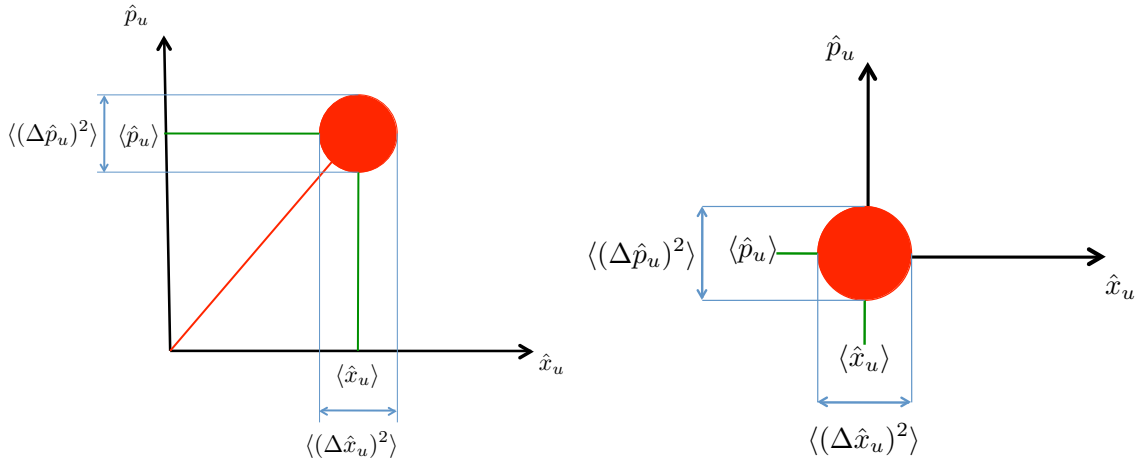

Figure 2.5: Phasor diagrams of a coherent state and of the vacuum state

Squeezed states

Another class of single mode Gaussian states that we can experimentally generate are the squeezed states (Walls 83; Davidovich 96). They were first experimentally reported in (Slusher 84).
A single mode Gaussian state in mode u is fully specified by its means:

$$\begin{pmatrix} \langle \hat{x}_u \rangle \\ \langle \hat{p}_u \rangle \end{pmatrix} \tag{2.48}$$

and its covariance matrix

$$C = \begin{pmatrix} \mathrm{cov}\,(\hat{x}_u, \hat{x}_u) & \mathrm{cov}\,(\hat{x}_u, \hat{p}_u) \\ \mathrm{cov}\,(\hat{p}_u, \hat{x}_u) & \mathrm{cov}\,(\hat{p}_u, \hat{p}_u) \end{pmatrix} \tag{2.49}$$

This covariance matrix can be diagonalized by rotating $\hat{x}_u$ and $\hat{p}_u$. Indeed, if we consider the observables $\hat{x}_u^\theta$ and $\hat{p}_u^\theta$, the means are changed to:

$$\begin{pmatrix} \langle \hat{x}_u^\theta \rangle = \cos(\theta)\,\langle \hat{x}_u \rangle + \sin(\theta)\,\langle \hat{p}_u \rangle \\ \langle \hat{p}_u^\theta \rangle = \sin(\theta)\,\langle \hat{x}_u \rangle - \cos(\theta)\,\langle \hat{p}_u \rangle \end{pmatrix} \tag{2.50}$$

and we can find θ to that the covariance matrix becomes

$$C' = \begin{pmatrix} \langle \Delta^2 \hat{x}_u^\theta \rangle & 0 \\ 0 & \langle \Delta^2 \hat{p}_u \rangle \end{pmatrix} \tag{2.51}$$

We know that $\left\langle \Delta^2 \hat{x}_u^\theta \right\rangle \left\langle \Delta^2 \hat{p}_u^\theta \right\rangle \geq 1$. For a coherent state, we have $\left\langle \Delta^2 \hat{x}_u^\theta \right\rangle = \left\langle \Delta^2 \hat{p}_u^\theta \right\rangle = 1$. Any state with $\left\langle \Delta^2 \hat{x}_u^\theta \right\rangle < 1$ or $\left\langle \Delta^2 \hat{p}_u^\theta \right\rangle < 1$ is called a squeezed state. Without loss of generality, let us assume that we have $\left\langle \Delta^2 \hat{x}_u^\theta \right\rangle < 1$. In that case the state is squeezed along the quadrature $\hat{x}_u^\theta$. We necessarily have $\left\langle \Delta^2 \hat{p}_u^\theta \right\rangle > 1$. $\hat{p}_u^\theta$ is the anti-squeezed quadrature.

Fig. 2.6 presents the phasor diagram of such states.

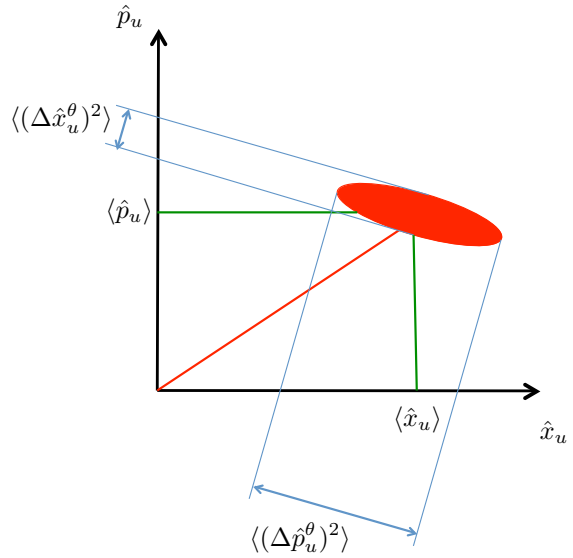

Figure 2.6: Phasor diagrams of a squeezed state

Typical values of squeezing are given in dB compared to the quantum noise limit:

$$s = 10 \log \left(\left\langle \Delta^2 \hat{x}_u^\theta \right\rangle \right) \tag{2.52}$$

s is the squeezing level. The best experiment currently report $s = -11.5dB$ of squeezing (Mehmet 10), and in this thesis we typically work with $s = -5dB$ (Wagner 08; Morizur 10b). The anti-squeezing level a defined as $a = 10 \log \left(\left\langle \Delta^2 \hat{p}_u^\theta \right\rangle \right)$ is above $-s$. Indeed, Heisenberg inequality correspond to $a + s \geq 0$. A pure squeezed state is a state for which $a + s = 0$.

An interesting property of the squeezed state is its sensitivity to losses. Indeed, if we consider a squeezed state in mode u, with a squeezing s and anti-squeezing a, applying a loss of R can be modelled as a beamsplitter of reflectivity R, as presented in Fig. 2.4 , with a vacuum state for second input. The output state is still squeezed but with different ratios:

$$s' = 10 \log \left(R + (1 - R) 10^{\frac{s}{10}} \right) \tag{2.53}$$

$$a' = 10 \log \left(R + (1 - R) 10^{\frac{a}{10}} \right) \tag{2.54}$$

$$\tag{2.55}$$

These expressions for the new squeezing and anti-squeezing s' and a' show that whatever the input squeezing, the amount of squeezing is now limited by $10\log(R)$. For example, if we have 50% loss in the system, the output squeezing is limited to $-3dB$. Squeezing is extremely sensitive to losses.

Chapter 3

Quantum protocols with transverse spatial modes

Conventionally, quantum protocols are implemented using the fundamental spatial mode of one or more beams. However, higher order modes also carry information, and our vision is that we can use them, instead of multiple beams, to perform quantum protocols.

In this chapter, we present two situations for which we can achieve more with multiple transverse modes than with multiple beams, and we introduce the tools we need to build these protocols. The first situation is quantum imaging, where we reduce the quantum noise related uncertainty for the measurement of a parameter in a light field. The second problem, more general, deals with the implementation of general continuous variable quantum computing protocols.

3.1 Quantum enhanced detection

3.1.1 Quantum noise and parameter estimation

Measuring a physical parameter using an optical system with the best achievable precision is a common imaging problem (Treps 03; Török 07; Treps 05; Fade 08).

Let us introduce an example: a cell under the objective of a microscope. We want to estimate its diameter. To do so, we record the image at the output of the microscope using a photographic plate or a camera. Then, using this image, we determine its diameter. The precision of our diameter estimation depends on the resolution of the image, and on how truthful the image is to the actual parameter. For example, a defocus or a jitter of the cell decrease the accuracy of the diameter estimation. While these sources of inaccuracy can be eliminated, quantum noise will remain as a fundamental source of uncertainty (Delaubert 08).

The light intensity measured by the camera or the photographic plate is proportional

to the number of photons that hits each of its pixels. In the limit of small number of photons, there is not enough signal on the camera to even see the cell, let alone measure its diameter, and the image is completely dominated by the quantum noise. When the photon flux increases, the quantum noise becomes less and less dominant, but still remains as a fundamental source of noise, due to the nature of the light.

3.1.2 Single mode sensitivity of a parameter estimation

Let us introduce a field envelope $\mathcal{E}(\vec{\rho})$ which evolves with a parameter p as $\mathcal{E}(\vec{\rho}, p)$. We want to estimate p from a measurement of the field, with minimal uncertainty. Without loss of generality, we can decompose p as $p = p_0 + \delta p$, where we have $\overline{\delta p} = 0$. With this decomposition, in the first order, we have

$$\mathcal{E}(\vec{\rho}, p) = \mathcal{E}(\vec{\rho}, p_0) + \delta p \left.\frac{\partial \mathcal{E}(\vec{\rho}, p)}{\partial p}\right|_{p=p_0} \tag{3.1}$$

We introduce the spatial mode $u(\vec{\rho})$ defined by

$$u(\vec{\rho}) = \frac{\left.\frac{\partial \mathcal{E}(\vec{\rho},p)}{\partial p}\right|_{p=p_0}}{\left\| \left.\frac{\partial \mathcal{E}(\vec{\rho},p)}{\partial p}\right|_{p=p_0} \right\|} \tag{3.2}$$

This mode carries all the information about δp.
It has been shown in (Delaubert 08) and (Fade 08) that all the quantum related uncertainty on the evaluation of p comes from quantum noise in the spatial mode u. To increase the precision on the estimation of p, one needs to reduce the quantum noise in u. Such a reduction can be achieved using squeezing.

An example of such a quantum noise reduction can be found in (Delaubert 06). This experiment, part of the foundations behind our work, proves that introducing squeezing in a specific transverse mode can improve the measurement of a beam's deflection. The transverse profile of a laser beam is a TEM_{00} mode, with a waist of w_0. We want to detect d the lateral displacements of this beam. In this case, the relevant spatial mode u which carries all the information about d is the TEM_{10} mode, as presented in Fig. 3.1. In (Delaubert 06), amplitude squeezing in the TEM_{10} mode was superposed to a bright beam, and the detection of a lateral displacement p was thus improved.

It is worth noting that the conjugate quadrature of the amplitude of the TEM_{10}, i.e. the phase of the TEM_{10}, corresponds to small tilts of the TEM_{00} beam. This implies that reducing the quantum noise variance on the lateral displacement of the TEM_{00} increases the noise variance of its tilt.

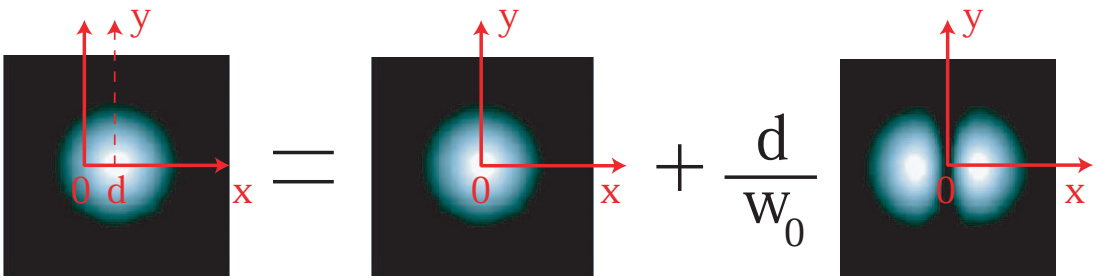

Figure 3.1: Lateral displacements d of a beam in the TEM_{00} mode are proportional, in the first order, to the amplitude of the TEM_{10} mode. Quantum fluctuations in the TEM_{10} mode are the source of quantum noise related uncertainty on the evaluation of d. Squeezing in the TEM_{10} mode reduces this uncertainty.

3.1.3 Squeezing a complex mode

As a conclusion, information about a system can be carried in complex spatial modes. Using squeezed light improves our ability to detect this information, but the quantum noise reduction needs to be in the specific detection mode. In the case of the displacement of a TEM_{00}, this mode is the rather simple TEM_{10} mode. But if we aim at more complex parameter estimations, for example measuring the diameter of a cell or the displacement of a complex structure, we need squeezed light in complex modes, specific to each detection problem.

Producing complex squeezed modes is a challenging task. A first way to do it is to produce the squeezed light directly in the desired complex mode (Lassen 07; Wagner 08). But, as we will describe later in II, squeezed light is most often produced in the resonant mode of a cavity (Vahlbruch 08; Takeno 07; Suzuki 06). Thus, with this method, we can only produce squeezing in a limited set of modes, and we cannot achieve quantum enhanced detection for any parameter.

An alternative approach is to produce the best squeezed light possible (typically in the TEM_{00} mode), and then convert the spatial mode of the beam into the desired complex mode. This conversion needs to be performed losslessly in order to retain squeezing in the desired mode: the conversion needs to be unitary. This means that only a unitary mode converter allows general quantum enhanced detection. We invented such a device during the course of this work, and we present it in 6.2.2.

3.2 Quantum information protocols

Quantum information protocols use the properties of quantum mechanics to secure or process information more efficiently than classical protocols (Childs 10). Quantum key distribution focuses on sharing secret keys in a protected way: the fact that no eavesdropper has intercepted these keys is guaranteed by quantum mechanics (Ekert 91; Shor 00;

Grosshans 01). On the other hand, quantum computing uses the properties of entanglement and superposition to solve specific mathematical problems faster than classical computers. For example, Shor's Algorithm (Shor 94; Shor 97), which necessitates a quantum computer, computes the prime factors of a large integer in a time that scales as $O((\log N)^3)$, where $\log N$ is the bit size of the integer. The best public algorithm that runs on a classical computer computes the prime factors in a time that scales as $O(\exp^{(\log N)^{1/3}(\log\log N)^{2/3}})$ (Lenstra 93). The significant improvement between the classical sub-exponential time and the quantum polynomial time derives from the efficiency of the quantum Fourier Transform.

3.2.1 Continuous variable quantum computing

Quantum information protocols were originally developed with discreet physical systems in mind (Shor 94; DiVincenzo 95; Childs 10), especially two-level systems (Mooij 99) for which the Bloch sphere description allows for an intuitive understanding of the protocol. Later on, these discreet protocols were generalized to continuous variable systems by showing that continuous variables could be used in a discreet way (Gottesman 01). More than that, quantum protocols were developed specifically for continuous variable systems (Lloyd 99; Menicucci 06).

Entanglement: the fundamental resource

The strength of quantum computing over classical computing resides in entanglement. Entanglement is a property of the quantum state of a physical system with two or more subsystems. It occurs when measurements on the subsystems are linked so that we cannot adequately describe a subsystem independently from the others. A very simple example of an entangled state is:

$$|\psi\rangle = \frac{1}{\sqrt{2}}\left(|0\rangle_A|\alpha\rangle_B + |\alpha\rangle_A|0\rangle_B\right) \tag{3.3}$$

with A and B the two subsystems. The state of the subsystem A alone is a statistical superposition of either the vacuum state or the coherent state $|\alpha\rangle$. This statistical superposition means that A alone is not in a pure state, while the complete system A and B is. Assuming α is real, detecting the amplitude $\hat{x}_A$ gives statistically either 0 or α, while detecting the sum $\hat{x}_A + \hat{x}_B$ systematically gives the result α (with the quantum noise around it, of course). Thus, we can say that these two subsystems are entangled.

In continuous variables, especially when performing detections in noisy environments, it can be difficult to prove that two subsystems are entangled. This is the reason why entanglement criteria are introduced. When we find a set of observables on the two subsystems which satisfy a given inequality, they are deemed entangled for this criterion. Criteria are chosen to reflect a specific quantum property of entanglement. Of course, perfectly entangled subsystems satisfy all these criteria, but for specific protocols, some criteria can be more important than others. In the course of this work, we used two com-

mon entanglement criteria: Duan's inseparability (Duan 00), a very general criterion, and the Einstein-Podolsky-Rosen (EPR) paradox inequality (Reid 89), which is very important in teleportation protocols.

First of all, consider two pairs of non-commuting observables $(\hat{x}_1, \hat{p}_1)$ and $(\hat{x}_2, \hat{p}_2)$ so that $[\hat{x}_1, \hat{p}_1] = 2i$ and $[\hat{x}_2, \hat{p}_2] = 2i$ on two different beams.
For Duan's inseparability criterion, we introduce two operators, linear combinations of these $\hat{x}_i$ and $\hat{p}_i$ so that

$$\hat{x} = \frac{1}{\sqrt{2}} \left(|a| \hat{x}_1 + \frac{1}{a} \hat{x}_2 \right) \tag{3.4}$$

$$\hat{p} = \frac{1}{\sqrt{2}} \left(|a| \hat{p}_1 - \frac{1}{a} \hat{p}_2 \right) \tag{3.5}$$

If there exists an $a \in \mathbb{R}$ for which

$$\left\langle \Delta^2 \hat{x} \right\rangle + \left\langle \Delta^2 \hat{p} \right\rangle < a^2 + \frac{1}{a^2} \tag{3.6}$$

then the state measured by the system is inseparable: it means that a measurement on a part of the system allows the experimentalist to predict the outcome of a measurement on another part of the system better than the quantum noise limit. The quantum description of the system cannot be limited to describing each of its parts independently. The state is inseparable.

The EPR paradox, of the "spukhafte Fernwirkung", "spooky action at a distance" in Einstein's words, underlines the strange nature of quantum mechanics. Consider the same two pairs of non-commuting observables $(\hat{x}_1, \hat{p}_1)$ and $(\hat{x}_2, \hat{p}_2)$. When the conditional variances of $\hat{x}_1$ knowing $\hat{x}_2$ and of $\hat{p}_1$ knowing $\hat{p}_2$ satisfy the relationship:

$$\sqrt{\left\langle \Delta^2 \hat{x}_1 | \hat{x}_2 \right\rangle \left\langle \Delta^2 \hat{p}_1 | \hat{p}_2 \right\rangle} < 1 \tag{3.7}$$

the EPR paradox occurs. Indeed, Einstein Podolsky and Rosen assume that if we can predict with certainty the outcome of a measurement, then there is a physical reality corresponding to this outcome. They also assume that there is no action at a distance: measuring in 2 does not affect the system in 1.
If by measuring either $\hat{x}_2$ or $\hat{p}_2$ we can predict the outcome a measurement of $\hat{x}_1$ or $\hat{p}_1$ (respectively) then there must be an element of physical reality that carries that information in the system in 1. But the system in 1 has not been detected yet, and a precise measurement of the conjugate observable ($\hat{p}_1$ or $\hat{x}_1$, respectively) is possible. This contradicts the non-commuting nature of the observables $\hat{x}_1$ and $\hat{p}_1$ that limits the precision of a simultaneous measurement of $\hat{x}_1$ and $\hat{p}_1$ to

$$\left\langle \Delta^2 \hat{x}_1 \right\rangle \left\langle \Delta^2 \hat{p}_1 \right\rangle > 1 \tag{3.8}$$

As a result, either quantum mechanics is incomplete, and there is a better description

of the physical system which would not limit the precisions to $\left\langle \Delta^2 \hat{x}_1 \right\rangle \left\langle \Delta^2 \hat{p}_1 \right\rangle > 1$ or we cannot assume there is an element of physical reality in 1 which carries the information about the measure we performed in 2. As a result, we need to consider both pairs of observables $(\hat{x}_1, \hat{p}_1)$ and $(\hat{x}_2, \hat{p}_2)$ when we describe the system.

Our ability to build and detect entangled systems reflects our ability to perform quantum protocols. This makes detecting entanglement an important indicator of the performance of a given physical system for quantum computation.

Continuous variables quantum protocols

A first kind of protocol is quantum teleportation (Furusawa 98; Yonezawa 04; van Loock 00; Zhang 08). The main resource of a teleportation protocol is a pair of two entangled beams. The first beam of the pair is combined with the state to be teleported, and measurements of the amplitude $\hat{x}$ and phase $\hat{p}$ of this combination are performed. The results of this measurements are carried by classical channels and used to correct the other beam of the entangled pair, in a process called feed-forward. This recreates the original state.
The quality of the teleportation, defined as the fidelity between the input state and the output state, is limited by the quality of the entanglement. An imperfect entanglement introduces noise in the system, which reduces the fidelity.

Another possible application of continuous variable entanglement is quantum computing. The conventional way to envision quantum computing (the evolution of qbits undergoing a succession of linear operations and projections (Childs 10)) does not apply well to beams of light: their continuous nature and the difficult coupling between different beams make this conventional method impractical. One-way computing, on the other hand, is far more adapted to beams of light. Introduced in 2001 in (Raussendorf 01), it sets forth a succession of measurements on a set of entangled systems. In this method, the quantum resource for the computation comes originally from a specific entangled state, the cluster state (Nielsen 06), with a large number of entangled systems. Then, a measurement is performed on the first system, and depending on the classical result of this measurement and the desired computation, a different measurement is performed on the second system. It is the complete succession of these measurements, as well as their classical results, that provides the result of the quantum computation.

In 2006, this scheme of computing was generalized to continuous variables in (Menicucci 06). A method to build a specific kind of continuous variable cluster states, the Gaussian cluster states, using optical parametric oscillators and linear optical elements was later developed in (Loock 07b). In this scheme, the qbits of the original one-way quantum computer are replaced by continuous variable systems, such as beams of light. Similar entanglement relations between the systems are required, and the computation itself is still performed using a succession of different measurements.

Some examples of possible Gaussian cluster states computations can be found in (Loock 07a; Menicucci 07), but there are practical limitations to implement these theoretical propositions. First, it remains difficult to generate a big enough cluster state: apart from proposals of cluster states computation using frequency combs (Menicucci 08), it seems that the only option to generate a Gaussian cluster state with N entangled states is to use N input squeezed states and combine them (Yukawa 08a; Ukai 10; Aoki 09a). A second issue is the difficulty to build and integrate in this system a non-Gaussian measurement. Indeed, cluster-state computation is based on a succession of measurements (Loock 07a). Any Gaussian measurement can be performed using an homodyne detection, but non-Gaussian measurements such as photon counting require different devices (Menicucci 06).

Multimode Gaussian states: building a covariance matrix

In general, multimode Gaussian states are Gaussian quantum states carried by multiple modes. Gaussian cluster states are but one example of this class of states. Gaussian states are fully described by their mean and covariance matrices.

An interesting question is on what condition a given symmetric matrix M is a covariance matrix, and how can we produce a Gaussian state which has this covariance matrix. The symplectic group (de Gosson 06) is a mathematical tool which provides a formalism to answer this question. Since a complete demonstration of the following can be found in the literature, we focus on the main results, and give references whenever needed.

Symplectic matrices describe how a quadratic hamiltonian affects a covariance matrix. Quadratic hamiltonians include interferences between modes, squeezing production, down-conversion (Arvind 95) (Braunstein 05)... Let us assume that M is a $2N \times 2N$ symmetric matrix, which would correspond to a N mode state. Let us introduce a matrix Ω defined as

$$\Omega = \begin{pmatrix} 0_{N\times N} & 1_{N\times N} \\ -1_{N\times N} & 0_{N\times N} \end{pmatrix} \tag{3.9}$$

A real matrix S is symplectic if and only if $S\Omega S^* = \Omega$, where S^* denotes the conjugate of S, which here is equivalent to its transpose, because S is real.

Williamson's theorem states that any symmetric matrix M can be decomposed as $M = S^* D S$, where S is a symplectic matrix and D is a diagonal matrix composed of two identical diagonal blocks of size $N \times N$ with the same diagonal coefficients $D_i \geq 0$. The values of D_i are unique (to a reordering), and provide us with a lot of information on M. First of all, M is a physical covariance matrix if and only if all the D_i are above or equal to 1. Furthermore, M is the covariance matrix of a pure state if and only if $D_i = 1$ for all the coefficients. If one or more of the coefficients D_i is strictly above 1, M describes a

state which is not quantum limited: there is additional randomness.

We now focus on the second part of our inquiry: how can we build a given physical M. We begin with the covariance matrices M describing pure states. In this case, applying Williamson's theorem, we find that there is always a symplectic matrix S so that $M = S^*S$. The implications of this result can be understood physically. It means that if we apply the quadratic hamiltonian operation represented by S on N vacuum modes, we are able to produce N modes with the specified covariance matrix M. We now use Euler's decomposition presented in (Arvind 95). It can also be found, although without the symplectic formalism, in (Braunstein 05). It is related to the Block-Messiah reduction: any symplectic matrix S can be decomposed in the product $S = KDU$, where K and U belong to the n-dimensional unitary group, which represents the basis changes of the modes, and D is a diagonal matrix which represents squeezing operations. Physically, this decomposition implies that any covariance matrix M describing a pure state can be built from vacuum modes by applying a basis change U, squeezing, and another basis change K. The first basis change U, which acts on vacuum modes, is not important in the case of a pure state: even after a basis change, vacuum modes remain vacuum modes.

This means that any covariance matrix M describing the results of a set of observables $\hat{x}_u$ and $\hat{p}_u$ on a pure state can be built by producing a set of squeezed modes and applying a basis change on these modes. This result can be expanded to more complex, non-pure states, as can be found in (Arvind 95; Adesso 06). Still, additional noise is almost always detrimental in the quantum protocols we aim at. To that extend, we try to build quantum states which are as pure as possible, using only squeezers and basis changes.

This result means that in order to build any Gaussian multimode entangled state, and cluster states in particular, we need to be able to produce independent squeezed modes, and mix these modes in a basis change.

3.2.2 Higher order modes for multimode entanglement

The conventional approach

A conventional approach to continuous variable multimode entanglement consists in using multiple light beams as the carriers of the entangled systems (Yukawa 08a; Aoki 09a). Squeezed beams are first generated in the TEM_{00} mode using optical parametric oscillators. Then these beams are mixed together using beamsplitters: the output field operators $\hat{a}'_i$ and $\hat{a}'_j$ are linear combinations of the input field operators $\hat{a}_i$ and $\hat{a}_j$:

$$\begin{pmatrix} \hat{a}'_i \\ \hat{a}'_j \end{pmatrix} = \begin{pmatrix} \cos(\theta) & \sin(\theta) \\ -\sin(\theta) & \cos(\theta) \end{pmatrix} \begin{pmatrix} \hat{a}_i \\ \hat{a}_j \end{pmatrix} \tag{3.10}$$

The angle θ is related to the power reflectivity of the beamsplitter mirror by $R = \cos(\theta)^2$. The relative phase of these two modes at the position of the beamsplitter is another degree of freedom. Indeed, different path lengths for the two beams introduce different phase shifts:

$$\begin{pmatrix} \hat{a}'_i \\ \hat{a}'_j \end{pmatrix} = \begin{pmatrix} e^{\phi_i} & 0 \\ 0 & e^{\phi_j} \end{pmatrix} \begin{pmatrix} \hat{a}_i \\ \hat{a}_j \end{pmatrix} \tag{3.11}$$

A succession of beamsplitters with carefully controlled relative phases can apply any unitary transform to the array of beams (Serre 02; Reck 94). After the mixing is complete, and the desired unitary transform has been applied to the array of squeezed beams, the entanglement between the n outputs $\hat{a}'_1, \hat{a}'_2, \ldots \hat{a}'_n$ can be characterized by measuring the covariance matrix between the $\hat{x}$ or $\hat{p}$ quadratures of all these beams. This measurement can be performed using one homodyne detection per output beam. The covariance matrix gives a full characterization of the Gaussian entangled state.

Such a scheme is synthesized in Fig 3.2, where the production, mixing and detection phases are outlined.

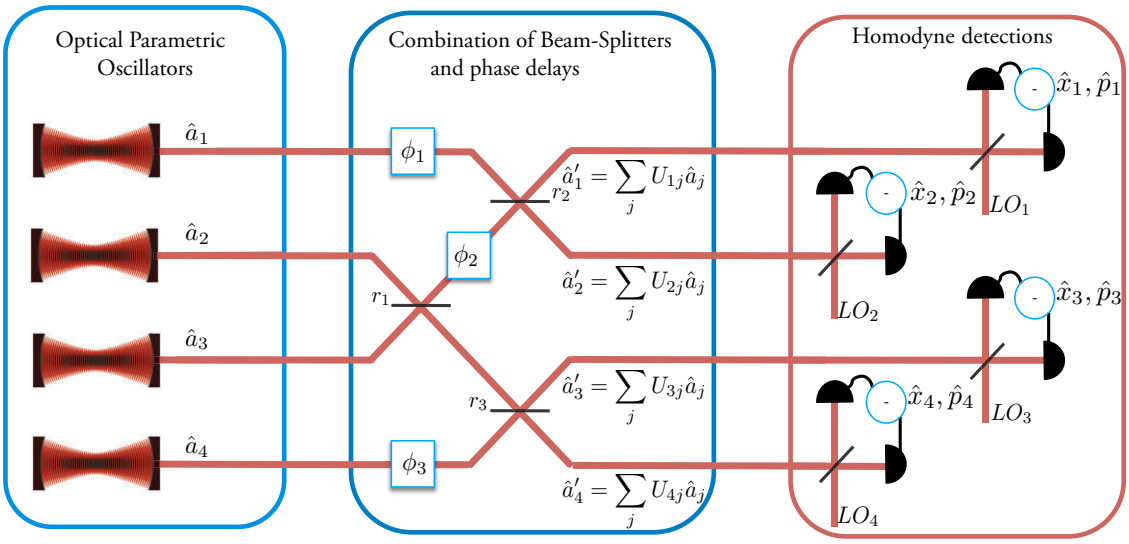

Figure 3.2: Conventional approach to create and characterize Gaussian multipartite entanglement. N independent optical parametric oscillators generate N TEM_{00} squeezed beams. These squeezed beams are then combined on beamsplitters with specific reflectivities which, in combination with controlled phase delays between the beams, control the Gaussian entanglement between the N outputs. The desired entanglement relation is then checked by measuring the covariance matrix of the observables $\hat{x}_i$ and $\hat{p}_i$.

After building a specific Gaussian entanglement between the beams and checking its covariance matrix, the entangled beams are then used to perform quantum information protocols.

This conventional procedure to build N entangled beams suffers a few drawbacks. First of all, all the interferences on the beamsplitters require a precise phase control. Any undesired relative phase changes dramatically the nature of the entanglement produced (Yukawa 08a). For all the interferences, there needs to be a control mechanism that measures the relative phase between the beams and adjusts it continuously to the desired position. While such a scheme can be simple for independent controls, here the feedback loops are nested: the first interference needs to be stabilized before the second one is.

This technical difficulty, as well as the ever increasing amount of resources needed to include more beams in the entangled output mean that such experiments with a high number of squeezed beams are extremely challenging.

Equivalence multiple beams / multiple modes

In the conventional approach the light is carried by a single transverse mode per beam (the TEM_{00} mode resonant with the optical parametric oscillator). The other transverse modes are vacuum. Thus, building a N-partite entanglement with this method requires N different output beams.

However, fundamentally, N-partite entanglement only requires N pairs of observables $\hat{x}'_i$, $\hat{p}'_i$ with some variance relations between them. These pairs of observables do not need to be all in different beams. Higher order modes within a single beam can carry these observables.

For example, instead of using N different beams, one can use the N transverse modes TEM_{i0} with $i = 1..N$ of the same beam. The pairs of observables are then $\hat{x}_{TEM_{i0}}$ and $\hat{p}_{TEM_{i0}}$. The main advantage of using copropagating transverse modes is that a single beam carries all the multipartite entanglement: since all the transverse modes go through the same optical media, the propagation does not change the relative phases between the modes.

Multipartite entanglement on a single beam of light

In this thesis, we provide the set of tools required to build and detect entanglement between multiple modes in a single beam. The idea of using multiple higher order modes within a beam to carry more quantum resources is not new (Lassen 07). Still, we demonstrate in this work that it is possible to produce within a beam the multimode Gaussian state necessary for one-way computation protocols. As an alternative to Fig. 3.2 we propose Fig 3.3, a method able to build and characterize any multimode Gaussian state required for the computation.

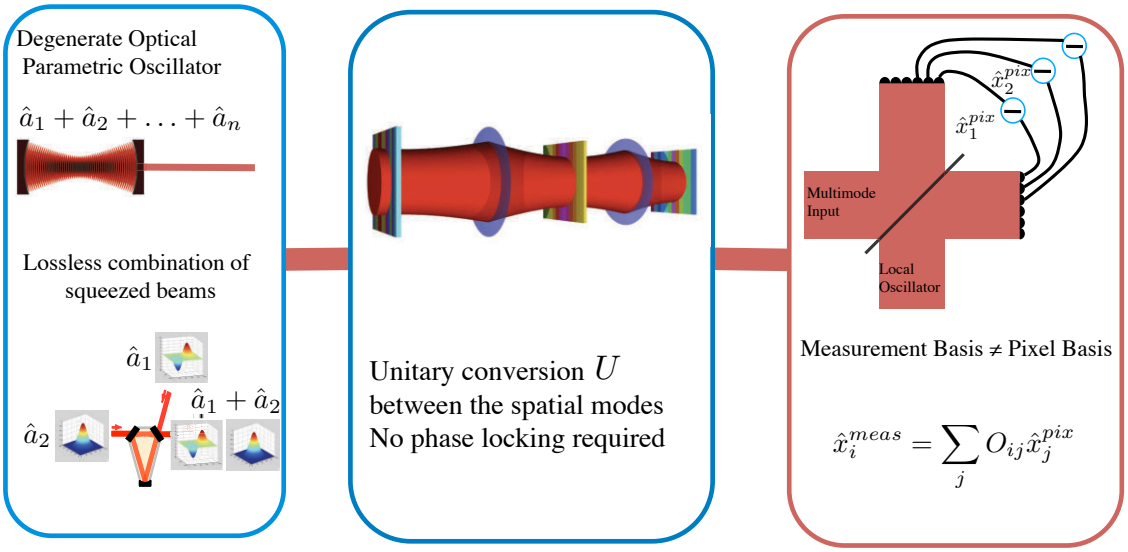

Figure 3.3: Practical method to build and characterize copropagating multipartite entanglement, in the form of entanglement between higher order modes in the same beam.

Our method requires the production and the detection of a beam carrying multiple squeezed modes, and the unitary manipulation of the modes in-between. While our approach of the production and the detection processes, detailed in the next part, is based on improvements of existing techniques, our unitary mode converter, presented in the last part of this work, is a completely new device.

Part II

Production and detection of copropagating squeezed modes

Chapter 4

Producing a multimode squeezed beam

We aim at building and detecting an entangled state between multiple spatial modes in a beam. The first step in creating such a state is producing a beam carrying multiple squeezed modes. These are the fundamental resources we then manipulate to build the desired multimode state. To produce the squeezed modes, we use optical parametric amplifiers (OPA). We begin this chapter with a brief presentation of the principles of squeezing generation in OPA. We then present our technical choices to achieve high levels of squeezing while retaining a good reliability of the OPAs. Finally we present different methods to produce a multimode squeezed beam.

4.1 Principles of squeezing generation

Optical parametric amplifiers are resonant cavities with a non-linear crystal set inside. Let us briefly describe here its theoretical principles. In the non-linear crystal, the quantum state evolve with the Hamiltonian (Walls 08):

$$\hat{H} = \chi_2 \left(\hat{a}_2 (\hat{a}_1^\dagger)^2 + \hat{a}_2^\dagger (\hat{a}_1)^2 \right) \tag{4.1}$$

where $\hat{a}_2$ is the annihilation operator at the frequency ν_2, $\hat{a}_1$ is the annihilation operator at the frequency ν_1 and χ_2 is the constant defining the strength of this process. It is a subtle process, and the spatial (Delaubert 07a; Delaubert 07b; Chalopin 09) and temporal properties (Hage 10) of optical parametric amplifiers have been discussed thoroughly in the literature (Walls 08; Bachor 03) and in previous thesis (Janousek 08b; Delaubert 07b; Bowen 03; Lam 98). We only present here the fundamental workings of the device. During the evolution of the field in the non-linear crystal, photons of the intense pump beam at ν_2 are down-converted to be replaced by two photons at frequencies close to $\nu_1 = \frac{\nu_2}{2}$. Actually, the frequencies of the two generated photons are so that $\nu_1 + \nu_1' = \nu_2$. Thus, this process generates a stream of photons in a single spatial mode with correlated frequencies. This correlation is the source of the noise reduction.

We use a cavity around the non-linear crystal to enhance this effect. The cavity selects a specific mode u resonant, and the squeezed state is produced in this mode. We can choose to seed the cavity: to introduce a coherent state in the mode u. In that case, the output of the optical parametric amplifier is a squeezed state with a non zero mean (Vahlbruch 08; Masada 10). On the other hand, non-seeded optical parametric amplifiers generate vacuum squeezing (Lam 99).

4.2 Technical description of the optical parametric amplifier

After this very brief explanation of the physical principles underlying the OPAs, let us present here different implementations of these devices, with different geometries, locking techniques and non-linear crystals. We present a set of experimental squeezing measurements for our few different set-ups.

4.2.1 Geometrical design

Let us begin with the common OPA geometrical designs: linear cavities and Bow-Tie cavities.

Linear cavity

The simplest design for an OPA is linear (Vahlbruch 08; Mckenzie 04; Lam 99; Wu 86). In this case, a resonant cavity is created by two reflective surfaces, and a non-linear crystal is added in the cavity to make it, with the addition of a pump beam, an OPA. A very conventional improvement consist in coating one side of the non-linear crystal so as to use it as one of the reflective surfaces. Such a cavity is presented in Fig 4.1.

The waist of the eigenmodes of the cavity is defined by the radii of curvature of the two surfaces. Fig 4.2 presents as an example the relation between the radius of curvature of one of the mirrors and the resulting waist of the eigenmode, for a very simple linear cavity of length $10cm$, the other reflective surface being flat. As can be noted on Fig 4.2, there is a stability region, outside of which there is no eigenmode. When the radius of curvature is in the stability region, all the modes TEM_{mn} with the right waist at the right position are possible eigenmodes of the cavity.

Now, a very fine length control of the cavity decides which of these modes will be resonant: because each of the TEM_{mn} accumulates a different Gouy phase shift by looping in the cavity (Siegman 86), and because a mode is resonant only if it interferes constructively in the cavity, a small change in the cavity length (less than a wavelength) allows to switch the resonance from one higher order mode to another.

One of the reflective surfaces is transparent to the pump beam, so that the eigenmode of the cavity and the pump beam enter both the non-linear crystal. Fig 4.1 presents such situation. We choose the pump beam shape depending on the TEM_{mn} eigenmode of the

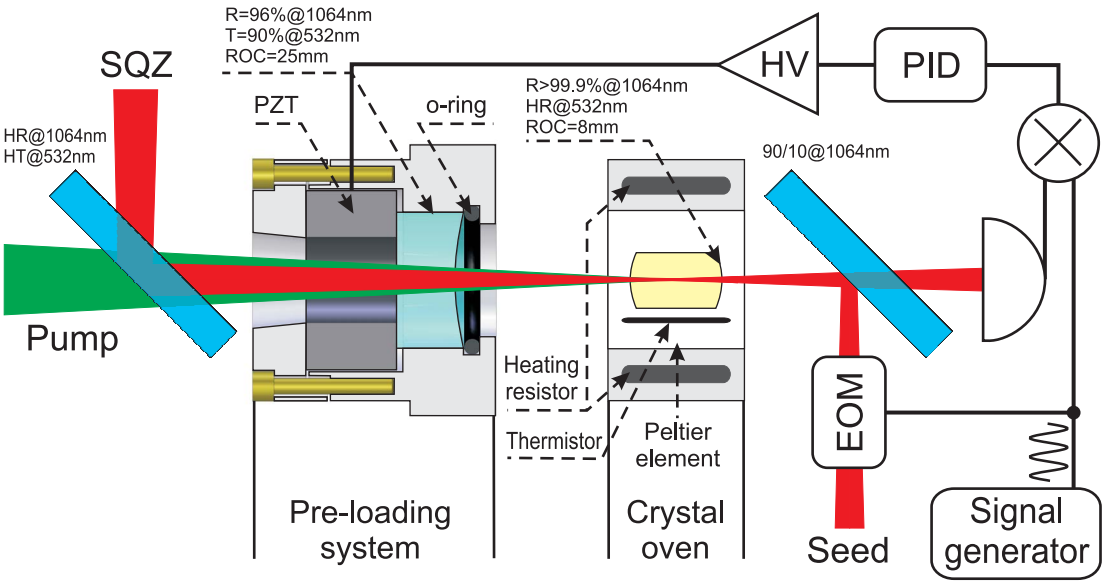

Figure 4.1: Detailed schematic of our linear cavity. The cavity is formed between a reflective surface on the non-linear crystal, and a curved mirror. The cavity is seeded with a phase modulated beam. Part of the seed is coupled into the cavity. Another part is reflected on the input mirror. Because of cavity properties, the phase modulation of the seed is transformed in the reflected beam into an amplitude modulation, which depends on the length of the cavity. This modulation is detected on the photodiode, and the signal is demodulated to produce an error signal. We use a proportional integrator derivator (PID) controller to integrate this error signal and produce a control signal, which, amplified, is used to drive the piezo-electric actuator (PZT). In order to achieve higher bandwidth, the PZT is pre-loaded using a rubber band. Source (Janousek 08b)

cavity we want to couple it with (Lassen 07). For example, the optimal waist size for the pump beam in the simple case when both the pump and the desired squeezed eigenmode are TEM_{00} is simply $w_{pump} = \frac{w_{sqz}}{\sqrt{2}}$ (Delaubert 07b).

One of the cavity mirror is not as highly reflective as the other. It is the output mirror of the cavity: the squeezed beam will exit the OPA from this mirror. The light that exits the other mirror is equivalent to loss in the cavity, and we use a highly reflective surface to avoid it.

A big advantage of this linear design is its stability. Today, the best squeezing results are achieved with linear designs (Mehmet 10; Vahlbruch 08), and they can be made very compact, even to the level of shaping and coating both sides of a non-linear crystal so that the cavity is contained within the crystal (monolithic cavity) (Yonezawa 10). In this particular case, locking the OPA cavity to the laser frequency is the main challenge.

Another advantage is its full cylindrical symmetry. Indeed, apart from the non-linear crystal, the rest of the optical components are fully invariant for any rotation around the

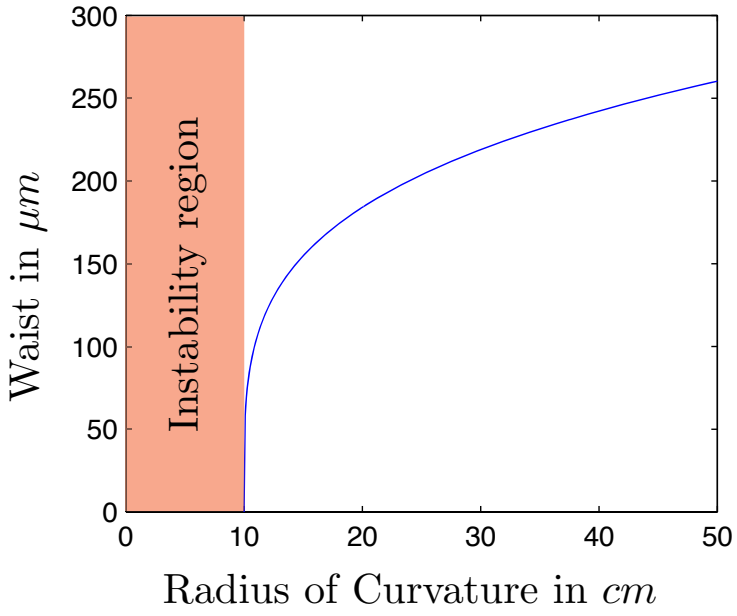

Figure 4.2: Waist of the eigenmodes of a simple linear cavity $10cm$ in length, as a function of the radius of curvature of one of its mirrors. The other mirror is set flat. Notice the instability region, in which there is no eigenmode.

propagation axis. We will detail further in 4.3.2 how this particular property can be used to achieve multimode squeezing.

We found that the main issue of the linear design for OPAs is the lack of independent input/output ports. It has an impact on the available locking techniques, and requires efficient dichroic mirrors to superpose and separate the pump and the seed/squeezed beams. Fig 4.1 details our layout for the input and output beams of our linear cavity.

Bow-Tie cavity

Another OPA design consist in having the beam propagating in a loop, instead of a back and forth motion in the case of a linear cavity. Such a loop can be implemented in a Bow-Tie shape (Masada 10; Takeno 07; Suzuki 06). See Fig. 4.3 for reference. This specific shape is chosen to minimize the reflection angles: when a beam hits a spherical mirror at an angle, the horizontal and vertical curvatures are different. These differences, on all the reflections, make the eigenmode of the cavity elliptic, which is difficult to correct.

The bow-tie design of the OPA means that the eigenmode has two different waists in the cavity, at two different positions. The non-linear crystal is located at the smallest of these waists, and the pump is superposed to the infrared beam in this crystal. Like in the

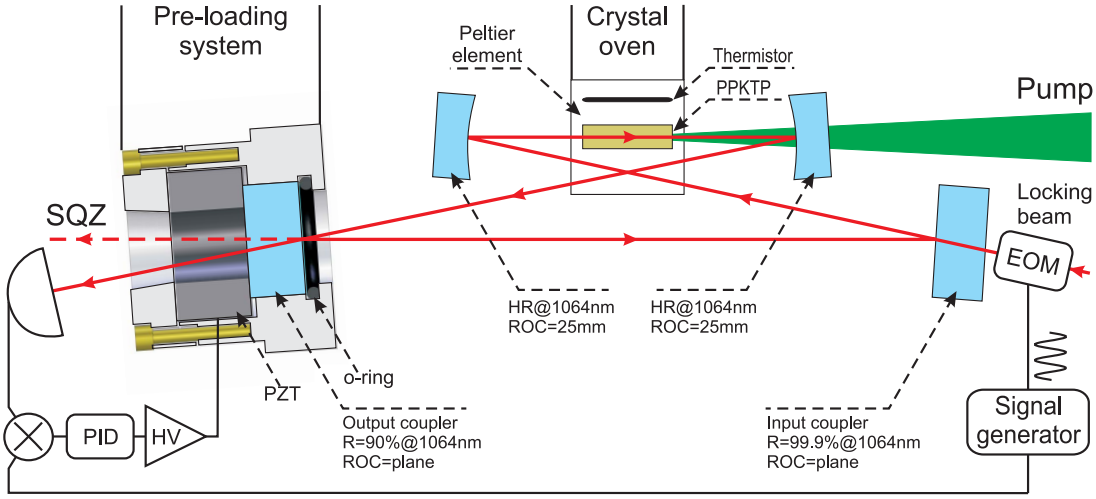

Figure 4.3: Detailed schematic of a Bow-Tie cavity. Unlike in the case of the linear cavity, in this case we do not detect the amplitude modulation on a reflected beam. Rather, we send a seed beam in a contra-propagating way (propagation in the other direction in the cavity as the squeezed mode), and we are able to detect the transmitted part of this modulated seed beam. This kind of lock is especially useful to achieve vacuum squeezing. We either use this technique, or use the more conventional locking in reflection. Source (Janousek 08b)

linear cavity situation, the optimum size of the pump depends on the desired eigenmode, and is given by $w_{pump} = \frac{w_{sqz}}{\sqrt{2}}$ in the simple case when both the modes are the fundamental TEM_{00}.

As can be seen in Fig. 4.3, the inputs and outputs do not share the same beam: because of the small reflection angle on the cavity mirrors, the beam that is coupled in the cavity is not superposed to the beam that is coupled out. This gives more options as far as locking techniques are concerned, and reduces the difficulties related to the superposition of the intense pump beam and the weak infrared beam. On the other hand, such a cavity design is less stable and compact, with more sources of loss (more reflections).

4.2.2 Locking

The geometrical design of a cavity defines its possible eigenmodes. For a mode to be resonant in the cavity, the cavity length must be precisely controlled so that after one loop, the field interferes constructively with itself. Air fluctuations, vibrations, make the cavity length change. Ensuring resonance requires an active feedback to compensate for these effects. We first present different locking techniques, required for different systems: cavities, OPAs, and simple interferences. Then we proceed to looking at new possible locking techniques, based on digital locking.

Locking cavities

A standard method to lock a cavity is to use a seed beam (also named probe beam (Takeno 07)). This infrared beam, which has the shape of the eigenmode we want to lock to, is first phase modulated at a relatively high frequency (in our set-ups between $2MHz$ and $16MHz$) using an electro-optic modulator. It is then injected into the cavity. On the injection mirror, a small part of the beam is reflected, and the intensity of this reflected beam is measured on a photodiode. The signal from the photodiode is demodulated at the frequency used for the phase modulation, which provides us with an error signal. A similar error signal can be obtained from the detection of the output of the cavity. See Fig. 4.3 for a design example with the relevant electronic components.

This method is called the Pound-Drever-Hall technique (Drever 83; Black 01). It is based on the fact that the two sidebands created by the phase modulation are reflected by the cavity. Recombining the reflected sidebands using the demodulation and the low pass filter performs the difference between the transfer function $2MHz$ above and $2MHz$ below the laser frequency (for a $2MHz$ phase modulation). Since the cavity transfer function is symmetric around its resonant frequency, when this difference is 0 the cavity is well tuned to the laser frequency, otherwise the sign of the difference tells us on which side of the resonance we are. We use a piezoelectric actuator (PZT) to control the cavity length based on the error signal.

Once the cavity length is controlled, one only needs to control the relative phase between the seed and the pump. Indeed, the squeezing conditions are optimal when the pump deamplifies the seed. To perform this lock, a piezo-electric actuator, located either on the seed beam or on the pump beam, is driven using a specific error signal. To produce this error signal, the pump beam is phase modulated, and the squeezed beam (or alternatively a beam leaked from the OPA cavity because of an imperfect reflection) is detected and demodulated using the same frequency. The error signal is then used to lock the actuator.

Another situation which requires locking is the stabilization of the relative phase of two interfering beams (to perform an homodyne detection for example). Depending on the relative phase that is needed, the phase locking method is different. When we need the two fields to have a different, fixed, phase, then the direct DC measurement is enough to produce an error signal: a small relative phase increase immediately translate into an increase (or a decrease, depending on the relative phase we want to lock to) of the interference intensity. On the other hand, when we need to lock the two fields in phase, then changing the relative phase in both directions from the optimal position changes the interference intensity in the same way. To solve this issue, a phase modulation is introduced on one of the two beams, and using demodulation, a similar approach to a Pound-Drever-Hall locking allows to stabilize the relative phases.

Digital locking

The feedback voltage is conventionally the result of an analog processing of the detected signal on the photodiode. It is based on a succession of a demodulator, a low pass filter, and a proportional-integrator system (PI). It is a well tested method, which does not introduce digitization noise (all the signals remain continuous) and that does not limit the speed of the system (the system is limited by the piezo-electric actuator bandwidth, typically $10kHz$). The two main issues of this scheme are the difficulty of its tuning (because everything is analog, the settings of the PI system need to be readjusted for every change in the optical conditions) and its scalability (every locking loop requires an additional demodulator, low pass filter and PI system, which can fail due to electrical stresses). Moreover, such a scheme cannot really be improved using more complicated processing (power fluctuation subtractions, nested locking loops).

An alternative system consists in using a digital locking process. In such a system, the signal is digitized and the desired output is computed using a digital signal processor (DSP) implemented on a field-programmable gate array (FPGA) chip. The FPGA solution is chosen because it gives us the ability to easily try different DSP designs. Because a typical FPGA chip involves 4 million gates, many PI systems can be implemented on the same chip. Moreover, it is possible to design logic circuits more complex than simple, single input - single output PIs, with automatic locking and optimization procedures.

Digital locking has limitations. First of all, except with very specialized high-end digitizers, recording the full output of the photodiode significantly faster than the modulation frequency is a challenge. A common method to avoid difficulties is simply to perform the demodulation using a demodulator and a low pass filter before the digitizer. This limits the flexibility of the logic circuit that can be implemented, but makes the digitizing and the data processing achievable.

Moreover, the digitization is limited to a certain number of bits. For example, for a 8 bit digitizer, this limitation is equivalent to introducing a digitization noise $24dB$ smaller than the signal maximums. It becomes really important to get rid of all the additional modulations that are irrelevant to the signal considered. Indeed, they do not help in the computation of the feedback voltage but their presence increase the digitization noise. This limitation of the digitization, while relevant for locking, is especially critical for detection, and we explain it further in 5.1.2.

Finally, it is necessary to use a dedicated DSP rather than a standard computer because of the delay induced by the processing. The time between the input arrives in the DSP and the feedback is sent out limits the frequency range of the locking. The delay can be really high in the case of a standard computer. In the case of our FPGA board (NI-7833R), we found it was typically on the order of $0.2ms$.

4.2.3 Single mode squeezing performances

Once the cavity and the relative phase between the pump beam and the seed are locked, the output of the OPA produces a squeezed beam on eigenmode resonant in the cavity. We now present our two different practical implementations (different geometries, different non-linear crystals).

Linear Cavity with a lithium niobate ($LiNbO_3$) crystal

Our first OPA is based on a lithium niobate crystal (a type I second order crystal) placed in a linear cavity. It is pumped with $532nm$ light from a frequency-doubled diode-pumped Nd:YAG laser operating at $1064nm$. The non linear crystal is a $2 \times 2.5 \times 6.5mm^3$ parallelepiped made from bulk $LiNbO_3$ doped with 7% of MgO. We stabilize the crystal temperature to $61°C$ to achieve the optimal phase matching conditions. We utilize the d_{31} non-linearity of the lithium niobate, with a non-linear coefficient of $d_{31} = 5.95pm/V$.

The OPA cavity is formed by the rear surface of the crystal and an external mirror. The rear surface of the crystal has a $8mm$ radius of curvature and is 99.9% reflective for the $1064nm$ light and fully reflective for the $532nm$ light. The external mirror has a $25mm$ radius of curvature and is 96% reflective at $1064nm$ while begin 10% reflective at $532nm$. The front surface of the crystal is antireflection-coated for both the wavelengths. The cavity is set so that its optical path length is $38mm$. It is this OPA which is presented in Fig. 4.1.

We locked this cavity to deamplification and measured a noise reduction on the amplitude quadrature $-4dB$ below the quantum noise limit in the frequency bandwidth $3MHz$ to $4MHz$. This OPA was used in a few different entanglement experiments. One them to entangle the transverse position and momentum of two beams (Wagner 08) and another one, using this OPA in a degenerate configuration (see 4.3.2), to generate two entangled modes within the same beam (Janousek 08a).

Bow-Tie Cavity with a periodically poled potassium titanyl phosphate ($PPKTP$) crystal

Our second OPA is based on a $PPKTP$ crystal in a Bow-Tie cavity. Likewise, this OPA is pumped with $532nm$ light from a frequency-doubled diode-pumped Nd:YAG laser operating at $1064nm$. The non-linear crystal is now a $1 \times 2 \times 10mm^3$ parallelepiped. When the crystal is grown, a periodic reversal of the optical domain orientation (using patterning electrodes) changes periodically the sign of the non linear coefficient. This process ensures quasi phase matching is retained even for long propagations within the crystal, enabling higher coupling between the $532nm$ pump and the $1064nm$ light. Thanks to the periodic poling, we can use the highest non-linearity, the d_{33}, for which all the fields polarizations are identical. We have $d_{33} = 16.9pm/V$.

Both the front and back surfaces of this crystal are flat, coated so as to be antireflective

both for the $532nm$ and the $1064nm$ light. The cavity's optical path length is $275mm$, and is formed by two mirrors of radius of curvature $25mm$ and two plane mirrors. The cavity forms a beam waist of radius $19\mu m$ between the curved mirrors, where the crystal is located. It is presented in Fig. 4.3.

When we lock the relative phase of the pump to deamplification, we can detect the amount of squeezing and anti-squeezing produced at a given frequency using a homodyne detection and scanning the local oscillator phase. We will explain further the homodyne detection in the next chapter. In order to reach the results presented in Fig. 4.4, we need to optimize the OPA.

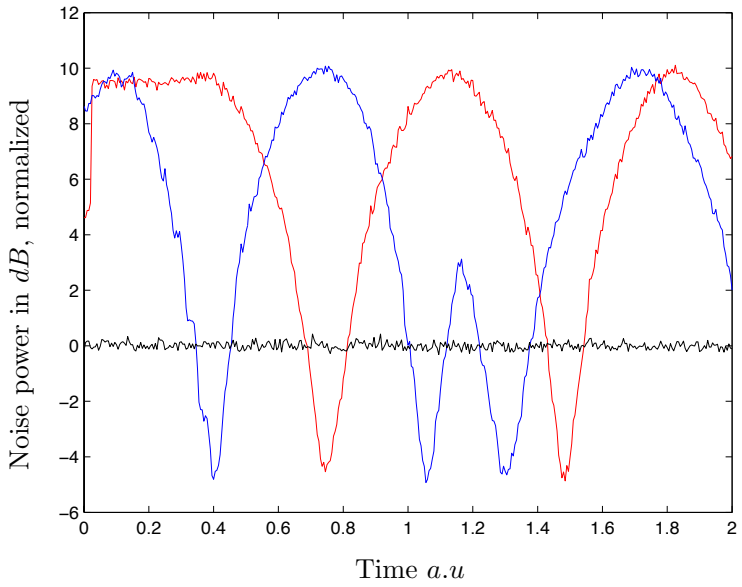

Figure 4.4: Experimental measures of the variance of the noise detected by an homodyne detection when we scan the local oscillator phase. We consider a frequency band of width $200kHz$ centered at $3.5MHz$. The spatial profile of the local oscillator is in the eigenmode of the Bow-Tie OPA. The OPA is pumped with a beam of $200mW$ of $532nm$ light, with a crystal temperature set at $32.75°C$.

We can optimize our PPKTP OPA by working on several parameters. First of all, in order to maximize the overlap between the $532nm$ pump and the eigenmode of the cavity, we optimize the amplification and deamplification. Fig. 4.5 presents an experimental measurements of amplification and deamplification as a function of the pump power. When we improve the overlap between the pump and the eigenmode of the cavity the amplification ratio increases for the same pump power.

A second parameter is the temperature of the non-linear crystal: for a range of temperatures from $25°C$ to $44°C$, we measure the amplification and deamplification of the $1064nm$ seed, for a fixed pump power of $200mW$. Fig. 4.6 presents these results. This figure confirms that the periodic poling allows for a wider range of efficient coupling than

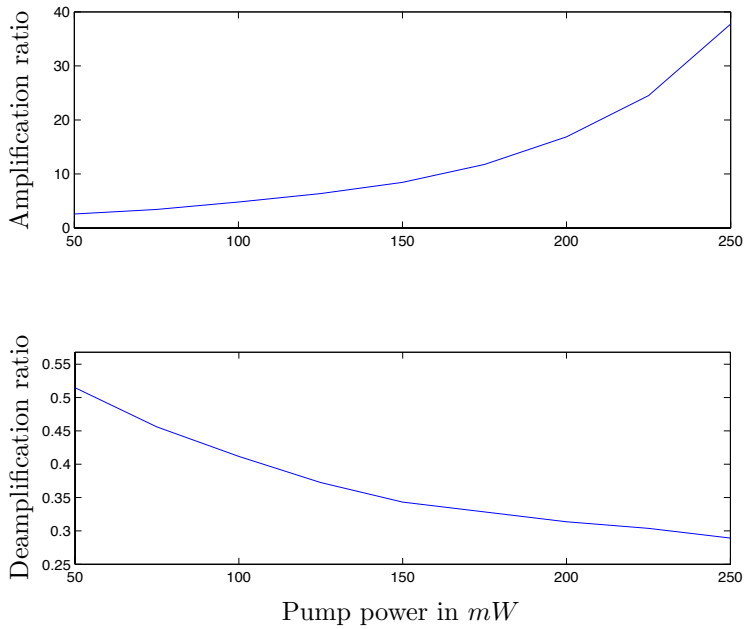

Figure 4.5: Amplification and deamplification as a function of the pump power, with a crystal temperature set at $32.75°C$.

the very narrow $2°C$ of the $LiNbO_3$.

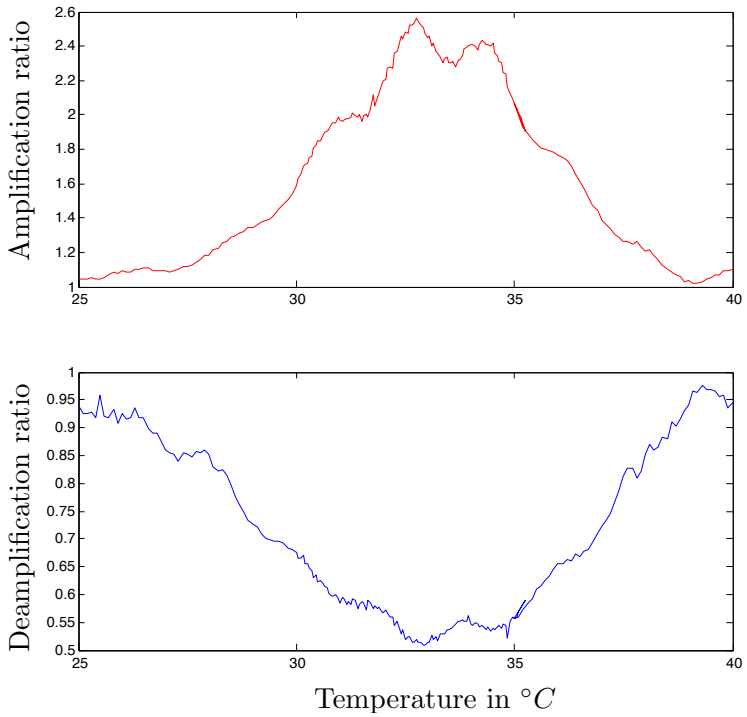

Figure 4.6: Amplification and deamplification as a function of the temperature, with a pump power set at $50mW$.

A third parameter is the pump power. While it would seem that a maximum pump

power would allow for the best squeezing results, we find that locking difficulties can deteriorate the squeezing above a certain pump power level. Typical traces such as Fig. 4.7 allow to adjust the pump power so as to maximize squeezing.

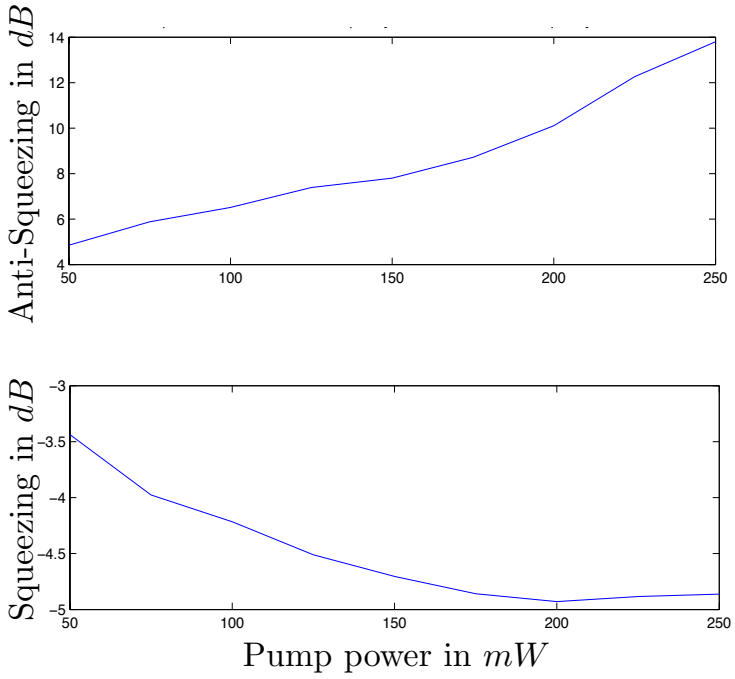

Figure 4.7: Squeezing and Anti-Squeezing measurements in a band of width $200kHz$ around $3.5MHz$, as a function of the pump power, with a fixed crystal temperature $32.75°C$.

The best squeezing results can always be improved, but using this PPKTP Bow-Tie OPA, we found we could reliably achieve $5.0dB$ of squeezing and $6.3dB$ of anti-squeezing every day for two months without much realignment. The results presented in Fig. 4.4 are typical.

4.3 Copropagating squeezed modes

The OPAs produce squeezed modes. We now focus on the different methods available to create a multimode squeezed beam using OPAs.

4.3.1 Superposing orthogonal modes on the OPA's cavities

A first, straight-forward method to produce a beam carrying multiple orthogonal squeezed modes is to produce them separately and then superpose them (Treps 03; Delaubert 06). We introduced an efficient and scalable way to do so: we use the OPA cavity as the method of superposition.

Geometrical set-up

Consider a squeezed beam, produced by a first OPA (OPA_1). Since the OPAs are more efficient when locked to the fundamental mode TEM_{00}, let us consider that the output of OPA_1 is a squeezed beam in a TEM_{00} mode. Consider now another OPA cavity (OPA_2). For the same reason as with OPA_1, we want OPA_2 to be locked to the fundamental mode TEM_{00}. It is not possible to superpose two TEM_{00} modes on the same beam: they are not orthogonal. We use a phase plate after OPA_1 to transform losslessly the output of OPA_1 into a mode orthogonal to the TEM_{00}. When this mode is sent on the output mirror OPA_2, it is fully reflected as it is orthogonal to the mode the cavity is locked to. After this reflection, both the outputs of OPA_1 and OPA_2 are superposed.

Such a scheme is detailed in Fig. 4.8. It is necessary to use increasingly complex phase plates to superpose many orthogonal modes. An interesting feature of this method is that the copropagating nature of the orthogonal modes is guaranteed by the coupling into the cavity. Indeed, when there is not phase plate after OPA_1, its output should be fully coupled into OPA_2, and scanning the length of OPA_2 should exhibit a single peak. When it is so, the positions, directions and sizes of the output of OPA_1 are fully identical to those of the output of OPA_2. The addition of a phase plate changes the profile of the mode to make it orthogonal but does not change its direction and position: the modes remain copropagating.

In order to control the relative phase between the two modes, a piezoelectric actuator is set between OPA_1 and OPA_2. We will detail further along (when we discuss the detection process) how this piezoelectric actuator is controlled to achieve a relative phase stabilization.

Experimental example: superposition of a TEM_{00} and a flip mode

We used two OPAs to test this superposition technique. Between the OPAs, the phase plate inserted was a simple flip plate, on a translation stage. This way, we can first make sure the output of OPA_1 is well coupled into OPA_2, and then slide in the phase plate until the peak corresponding to the TEM_{00} mode disappears.

After the reflection on OPA_2, we have a beam carrying two squeezed modes: a TEM_{00} squeezed mode, produced by OPA_2 and a flip mode, produced by OPA_1 and the phase plate. We use a multipixel homodyne detection (detailed in the next chapter) to detect the squeezing levels achieved. Fig. 4.9 presents the measurement results. We scan the local oscillator phase, so as to record the noise variances along different quadratures for the TEM_{00} mode and the flip mode. We record $-3.1dB$ of squeezing for the TEM_{00} mode, and $-2.6dB$ of squeezing for the flip mode. Since these OPAs produce the same squeezing

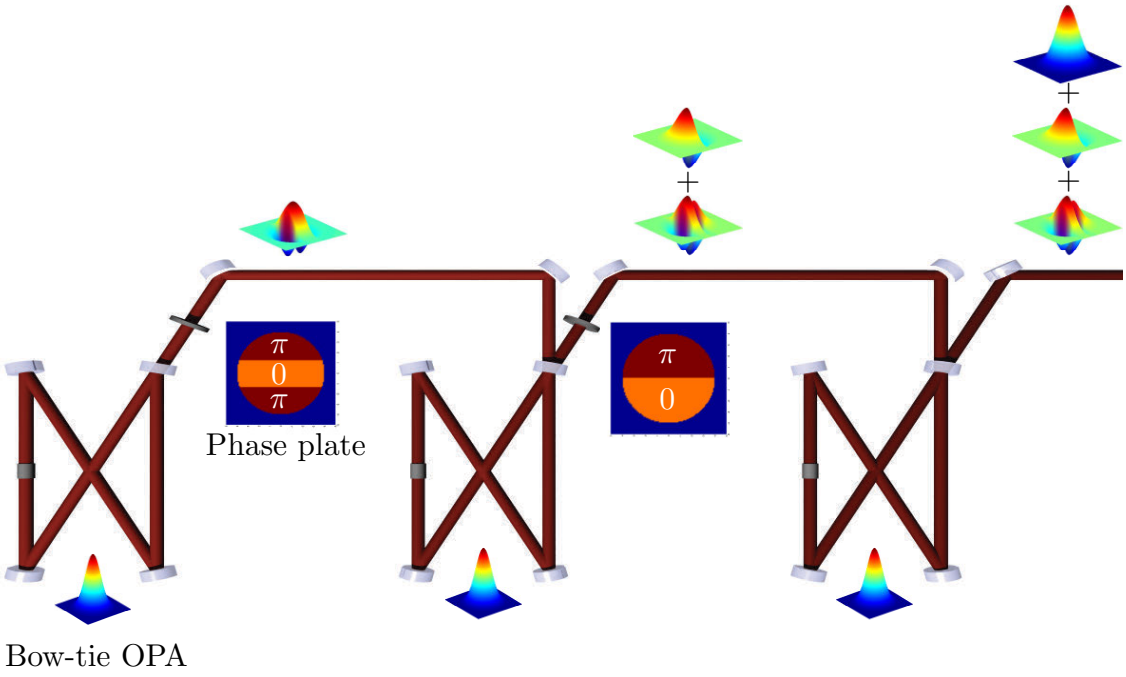

Figure 4.8: Representation of a general scheme to build a beam carrying several orthogonal squeezed modes. Each OPA is locked to produce a TEM_{00} squeezed mode, but phase plates placed along the beam make sure that each addition is orthogonal to the modes already carried in the beam. In the schematic are shown a few phase-plates, but many more are possible, as long as they produce orthogonal beams.

levels, and the detection apparatus is equivalent for the TEM_{00} and the flip-mode, this difference in squeezing values is due to losses on the order of 12% induced by the phase plate and the bouncing back of the flip-mode on OPA_2.

4.3.2 Partially degenerate cavities

Partially degenerate cavities present another option to generate multimode squeezed beams. Indeed, if several spatial modes are resonant at the same time in the OPA, all these modes are simultaneously squeezed.

Characteristics

We use the linear design detailed in Fig. 4.1. This design has a cylindrical symmetry: the TEM_{10} and TEM_{01} modes, images of each other by a 90° rotation should have the same coupling with the pump beam, and be resonant for the same cavity length. We begin by seeding the cavity with a TEM_{10} mode, locking the cavity to this mode, and recording the amplification as a function of the pump power. We then perform the same operation for the TEM_{01} mode. After a careful alignment of the pump, we record the same amplifications as a function of the pump power for the TEM_{10} and the TEM_{01} modes. This means that the pump beam is symmetrically aligned.

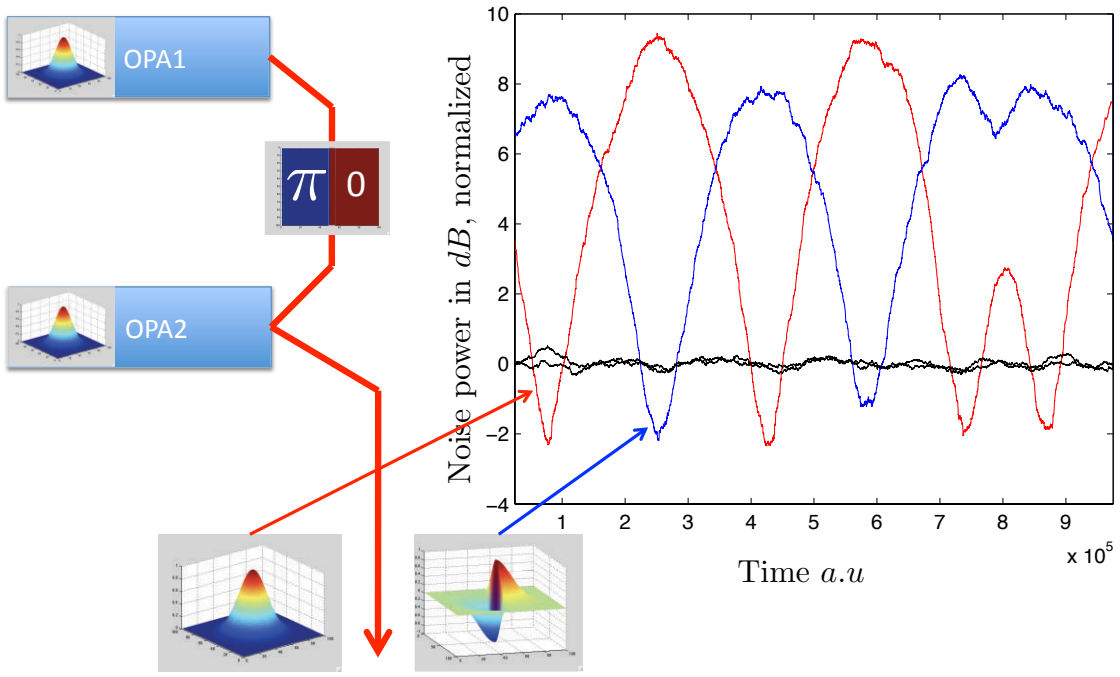

Figure 4.9: Experimental measures of the variance of the noise detected in two different spatial modes by an homodyne detection when we scan the local oscillator phase. We consider a frequency band of width $300kHz$ centered at $3MHz$, and the red curve represents the results for the TEM_{00}, while the blue curve represents the results for the flip mode. The black curves represent the quantum noise limit measurements.

We now seed this OPA with a TEM_{01} mode, and lock the cavity so that this mode is resonant. Because of the cylindrical symmetry, the TEM_{10} is also almost resonant. We optimize the crystal temperature to achieve a full degeneracy.

Simultaneous generation of squeezing in the TEM_{10} and TEM_{01} copropagating modes

This cavity generates squeezing on both the TEM_{10} and the TEM_{01} modes. We use a homodyne detection with a rotated local oscillator to measure the squeezing achieved in the two modes. The local oscillator has the shape of a TEM_{01} mode, and we use a dove prism to rotate the TEM_{01} around the propagation axis. When it is rotated 90°, the local oscillator is then a TEM_{10}. We measure squeezing for different angles of rotation, and we find we have achieved $4dB$ of squeezing and $6.5dB$ of anti-squeezing at $4.8MHz$ for all the detection angles. Fig. 4.10 presents these results, which can also be found in (Janousek 08a).

4.3.3 Fully degenerate cavity

Partially degenerate cavities achieve the simultaneous squeezing of several spatial modes. A fully degenerate cavity goes a step further. Its geometry makes it possible to achieve

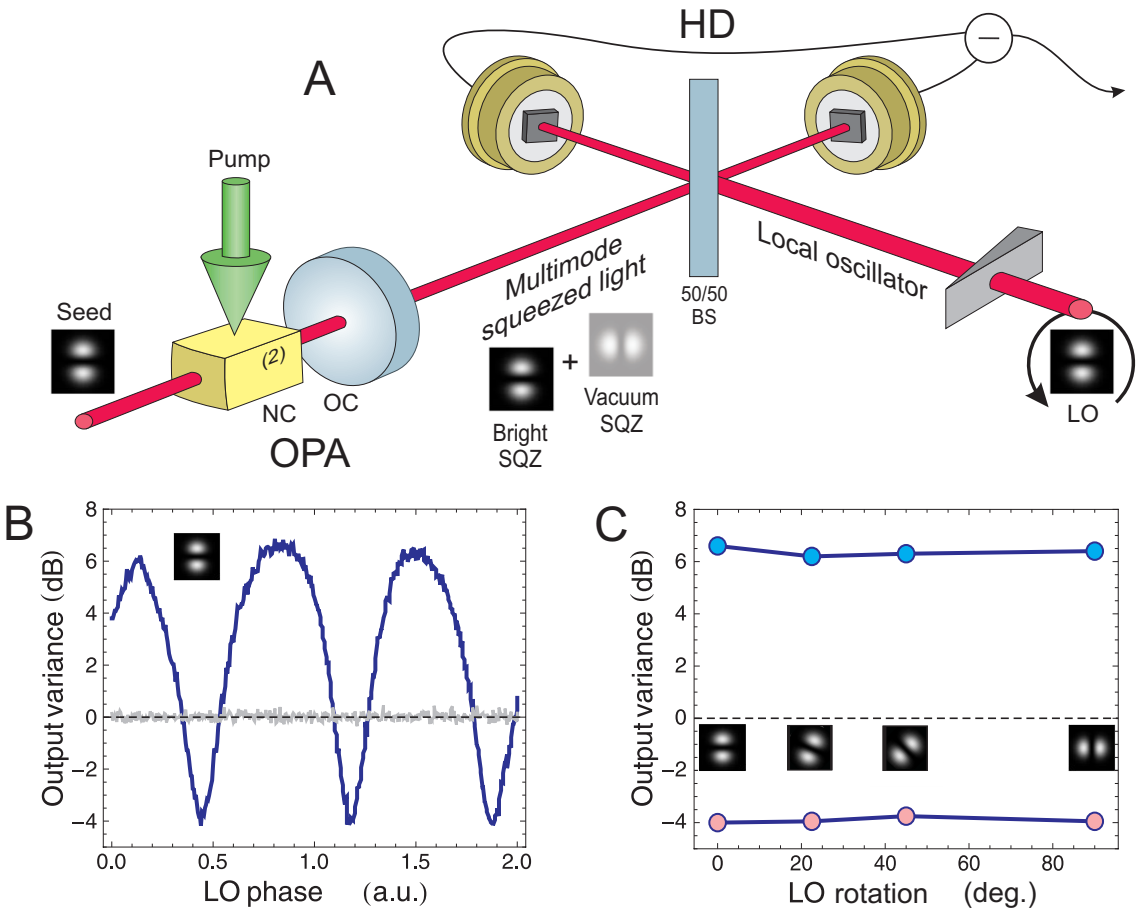

Figure 4.10: The cavity formed by the non-linear crystal NC and the output coupler OC produces a multimode squeezed beam. We use a homodyne detection to characterize the squeezing level of the different modes. We first send in a TEM_{01}, similar to the seed, and we measure $-4dB$ of squeezing. Rotating the local oscillator allows to measure the amount of squeezing in the TEM_{10} mode, again $-4dB$. This linear degenerate OPA, stabilized at $61°C$, created a beam carrying both a squeezed TEM_{10} and TEM_{01}.

resonance for all the transverse spatial modes (Chalopin 09). Depending on the spatial coupling between these transverse modes and the pump beam, each profile exhibits a different level of squeezing.

Building a spatially degenerate OPA is a complex process, mainly because such a degeneracy can only be achieved close to the instability region of the OPA cavity. In that region, any small change in the geometry of the cavity makes it unstable. For example, an increase of the pump power heats locally the non-linear crystal, which creates a local lens and can push the cavity out of stability. During the course of this thesis, some work was done to improve the reliability of spatially degenerate OPAs, in collaboration with Benoit Chalopin. The outcomes of this work can be found in (Chalopin 09) and in (Chalopin 11).

We found that the best method to create a reliable and efficient spatially degenerate OPA remains undecided. As such, while a fully degenerate OPA would be the resource of choice to produce a beam with several spatial modes simultaneously squeezed, it is not,

at the moment, a reliable candidate. The simplest and most reliable method remains the superposition of orthogonal modes on the OPA cavities.

Chapter 5

Multimode homodyne detection

In the previous chapter, we described how we can make a beam carrying multiple squeezed modes. We now focus on the detection of multiple co-propagating modes. Our goal is to achieve a complete analogy with the multiple beam set-up: we want to be able to perform the same kind of detection on orthogonal modes within a beam as can be performed on multiple beams.

When dealing with multiple beams, simple homodyne detections are sufficient to fully characterize the multimode Gaussian state of the system (Simon 88). Additionally, a significant portion of the quantum protocols involves these detections (Ukai 10). That is why our work focuses on this kind of detection. We do not consider photon counting techniques. This chapter presents the expansion of homodyne measurements to mutimode beams. We first start with a description of the conventional homodyne detections, including technical noise considerations and data acquisition. We then proceed to discuss multipixel homodyne detections, both from a fundamental and from a technical point of view.

5.1 Simple Homodyne Detection

Let us begin with conventional homodyne detections (Bachor 03). We start this description with a brief theoretical reminder. We explain the quantum measurement performed and its link to the output signal of the homodyne detection. We then have a look at some technical considerations important in the building of homodyne detections. Finally, we use a simple example to illustrate how useful these quantum detections can be.

5.1.1 Theoretical framework

Detecting a single mode

A simple homodyne detection consists in interfering a strong beam called a local oscillator (LO) with a beam which field we want to detect on a $50:50$ beamsplitter. We then mea-

sure the intensity of both outputs, and compute their difference. This process is detailed in Fig 5.1.

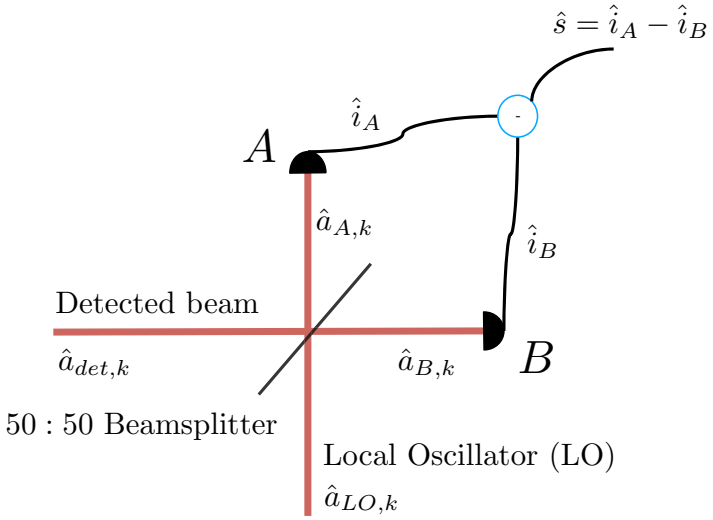

Figure 5.1: Simple schematic of a homodyne detection. The local oscillator and the detected beam are overlapped on a $50:50$ beamsplitter, and their intensities are detected on photodiodes A and B. We then make the difference of the output signals of the photodiodes.

Let us name the field operators $\hat{a}_{LO,k}$ and $\hat{a}_{det,k}$ respectively for the local oscillator beam and the beam we want to detect. The index k specifies which transverse mode of the considered beam the field operator applies to. For example, if the basis is the TEM_{mn} basis, the field operator $\hat{a}_{LO,20}$ is the annihilation operator on the TEM_{20} transverse mode on the local oscillator beam.

Without loss of generality, we can consider a basis defined so that the spatial mode of the local oscillator beam is the first transverse mode of this basis (see section 2.1.3). In this case, the operator $\hat{a}_{LO,0}$ applies to this intense mode. Since all the energy is concentrated in this mode, we have $\left\langle \hat{a}^\dagger_{LO,k} \hat{a}_{LO,k} \right\rangle = 0$ for all $k > 0$.

After the beamsplitter, we have two output beams:

$$\hat{a}_{A,k} = \frac{1}{\sqrt{2}} \left(\hat{a}_{LO,k} + \hat{a}_{det,k} \right) \tag{5.1}$$

$$\hat{a}_{B,k} = \frac{1}{\sqrt{2}} \left(\hat{a}_{LO,k} - \hat{a}_{det,k} \right) \tag{5.2}$$

Using the detectors, we measure the intensity of these two beams:

$$\hat{i}_A = \sum_{k\in\mathbb{N}} \hat{a}^\dagger_{A,k}\hat{a}_{A,k} \tag{5.3}$$

$$\hat{i}_B = \sum_{k\in\mathbb{N}} \hat{a}^\dagger_{B,k}\hat{a}_{B,k} \tag{5.4}$$

There are no terms in $\hat{a}^\dagger_{A,k}\hat{a}_{A,l}$, where $l \neq k$ because $\hat{a}_{A,k}$ and $\hat{a}_{A,l}$ are operators on orthogonal modes.

Finally we subtract the two intensities, so that the output signal $\hat{s}$ is

$$\hat{s} = \hat{i}_A - \hat{i}_B \tag{5.5}$$

We can decompose $\hat{s}$ in powers of $\hat{a}_{LO,0}$, and use the fact that the local oscillator is an intense beam:

$$\begin{aligned}\hat{s} \quad &= \tfrac{1}{2}\left(\hat{a}^\dagger_{LO,0}\hat{a}_{LO,0} - \hat{a}^\dagger_{LO,0}\hat{a}_{LO,0}\right) \\ &+ \left(\hat{a}^\dagger_{LO,0}\hat{a}_{det,0} + \hat{a}^\dagger_{det,0}\hat{a}_{LO,0}\right) \\ &+ \tfrac{1}{2}\left(\hat{a}^\dagger_{det,0}\hat{a}_{det,0} - \hat{a}^\dagger_{det,0}\hat{a}_{det,0}\right) \\ &+ \textstyle\sum_{k>0} \hat{a}^\dagger_{A,k}\hat{a}_{A,k} - \hat{a}^\dagger_{B,k}\hat{a}_{B,k} \end{aligned} \tag{5.6}$$

$$\tag{5.7}$$

gives us

$$\hat{s} = \hat{a}^\dagger_{LO,0}\hat{a}_{det,0} + \hat{a}^\dagger_{det,0}\hat{a}_{LO,0} \tag{5.8}$$

In the equation 5.8, we neglected the terms which do not contain $\hat{a}_{LO,0}$ or $\hat{a}^\dagger_{LO,0}$. Indeed, we choose a very strong local oscillator to make sure that the values $\left\langle \hat{a}^\dagger_{LO,0}\hat{a}_{det,0} \right\rangle$ and $\left\langle \hat{a}^\dagger_{det,0}\hat{a}_{LO,0} \right\rangle$ are far bigger than the other terms.

It is very important to notice the common noise cancellation. Indeed, in the complete equation of the difference, we have a term in $\left(\hat{a}^\dagger_{LO,0}\hat{a}_{LO,0} - \hat{a}^\dagger_{LO,0}\hat{a}_{LO,0}\right)$, that cancels out. In this term, each of the components $\hat{a}^\dagger_{LO,0}\hat{a}_{LO,0}$ are the intensity of the local oscillator measured in A or B. In order to be able to write 5.8, we need to make sure that these terms cancel out: they are dominant compared to 5.8. A significant part of the successful building of an homodyne detection is the achievement of this balancing between the channels A and B, to cancel out the local oscillator noise.

Once we have 5.8, we can simplify it further. Indeed, we use a local oscillator in the coherent state $|\alpha_0\rangle$. We decompose the local oscillator field operator in $\hat{a}_{LO,0} = \alpha_0 + \delta\hat{a}_{LO,0}$. Acting on the coherent state $|\alpha_0\rangle$, we find that the operator $\delta\hat{a}_{LO,0}$ can also be neglected

compared to α_0. Thus, if we introduce $\alpha_0 = |\alpha_0|e^{i\theta}$, we have:

$$\hat{s} = |\alpha_0| \left(e^{-i\theta} \hat{a}_{det,0} + e^{i\theta} \hat{a}^\dagger_{det,0} \right) \tag{5.9}$$

Basically, $\hat{s}$ is measuring the quadrature of the quantum state in the mode of $\hat{a}_{det,0}$ along the direction defined by the local oscillator phase: when we have $\alpha_0 \in \mathbb{R}$, $\hat{s} = \frac{\alpha_0}{\sqrt{2}} \hat{x}_{det,0}$ and when $\alpha_0 \in i\mathbb{R}$ then $\hat{s} = i\frac{\alpha_0}{\sqrt{2}} \hat{p}_{det,0}$. When we measure the variance of the observable $\hat{s}$, we are measuring the variance of $\hat{x}_{det,0}$ or $\hat{p}_{det,0}$, depending on the local oscillator phase. By changing the local oscillator phase, we can of course measure a combination of these observables: $\hat{x}^\theta_{det,0}$ is detected when we measure the local oscillator phase is θ.

The local oscillator phase needs to be stable relative to the beam we want to detect. Indeed, the quadrature of the detected beam ($\hat{x}_{det,0}$ or $\hat{p}_{det,0}$) that is measured by the observable $\hat{s}$ is simply set by this phase. To that extent, it is important to use the same coherent source of light (in our case a laser) for both beams. Then, by locking the local oscillator phase to the detected beam, we can ensure that we compensate for phase fluctuations arising from path differences between the local oscillator, and the beam carrying the quantum state that we want to detect.

A key idea to remember is that the transverse mode in the detected beam that is measured by the homodyne is the mode 0 defined as the mode carrying all the energy of the local oscillator. Thus, a simple homodyne detection can measure sequentially different spatial modes, simply by using different different local oscillator shapes (Lassen 07; Hsu 10).

If the mode of interest is not exactly the local oscillator mode u_0 but a different mode v_d, this mismatch is equivalent to losses. Indeed, the homodyne detection only measured a proportion α^2 of the mode (in power) where α^2 is the intensity overlap:

$$\alpha^2 = \left| \iint_{\vec{\rho} \in \mathbb{R}^2} v_d(\vec{\rho})^* u_0(\vec{\rho}) \, d^2\vec{\rho} \right|^2 \tag{5.10}$$

Measuring the covariance matrix of a multimode state

When we consider a single mode, an homodyne detection measures the observable $\hat{x}^\theta_u$, where u is the spatial mode of the Local Oscillator. In the simple case of a squeezed beam, measuring the average and the variance of $\hat{x}^\theta_u$ for a few values of θ provides a complete description of the state. Indeed, when we know or assume that the state is a squeezed coherent state, it is fully defined by its covariance matrix (Simon 88). The covariance matrix of a single mode state is given by:

$$C = \begin{pmatrix} \mathrm{cov}\,(\hat{x}_u, \hat{x}_u) & \mathrm{cov}\,(\hat{x}_u, \hat{p}_u) \\ \mathrm{cov}\,(\hat{p}_u, \hat{x}_u) & \mathrm{cov}\,(\hat{p}_u, \hat{p}_u) \end{pmatrix} \tag{5.11}$$

We find that $\mathrm{cov}\,(\hat{x}_u, \hat{x}_u) = \left\langle \Delta^2 \hat{x}_u \right\rangle$ and $\mathrm{cov}\,(\hat{p}_u, \hat{p}_u) = \left\langle \Delta^2 \hat{x}_u \right\rangle$. These two coefficients can be measured by setting the relative phase θ at 0 and $\frac{\pi}{2}$ respectively and detecting the

variance of the output signal. As far as the coefficients $\mathrm{cov}\left(\hat{x}_u, \hat{p}_u\right)$ and $\mathrm{cov}\left(\hat{p}_u, \hat{x}_u\right)$ are concerned, we simply need to measure the variance $\left\langle \Delta^2 \hat{x}_u^{\frac{\pi}{4}} \right\rangle$. Indeed we find

$$\mathrm{cov}\left(\hat{x}_u, \hat{p}_u\right) = \frac{1}{2}\left(\left\langle \Delta^2 \hat{x}_u^{\frac{\pi}{4}} \right\rangle - \frac{1}{2}\left(\left\langle \Delta^2 \hat{x}_u \right\rangle + \left\langle \Delta^2 \hat{p}_u \right\rangle\right)\right) \tag{5.12}$$

For a single mode, a few measurements with an homodyne detection are able to fully characterize a Gaussian state.

When we consider a multimode Gaussian state carried by multiple beams, a similar procedure can be applied to reconstruct the covariance matrix using homodyne detection measurements. In the case of two modes u and v carried by two different beams, the covariance matrix is

$$C = \begin{pmatrix} \mathrm{cov}\left(\hat{x}_u, \hat{x}_u\right) & \mathrm{cov}\left(\hat{x}_u, \hat{x}_v\right) & \mathrm{cov}\left(\hat{x}_u, \hat{p}_u\right) & \mathrm{cov}\left(\hat{x}_u, \hat{p}_v\right) \\ \mathrm{cov}\left(\hat{x}_v, \hat{x}_u\right) & \mathrm{cov}\left(\hat{x}_v, \hat{x}_v\right) & \mathrm{cov}\left(\hat{x}_v, \hat{p}_u\right) & \mathrm{cov}\left(\hat{x}_v, \hat{p}_v\right) \\ \mathrm{cov}\left(\hat{p}_u, \hat{x}_u\right) & \mathrm{cov}\left(\hat{p}_u, \hat{x}_v\right) & \mathrm{cov}\left(\hat{p}_u, \hat{p}_u\right) & \mathrm{cov}\left(\hat{p}_u, \hat{p}_v\right) \\ \mathrm{cov}\left(\hat{p}_v, \hat{x}_u\right) & \mathrm{cov}\left(\hat{p}_v, \hat{x}_v\right) & \mathrm{cov}\left(\hat{p}_v, \hat{p}_u\right) & \mathrm{cov}\left(\hat{p}_v, \hat{p}_v\right) \end{pmatrix} \tag{5.13}$$

The procedure to calculate the coefficients $\mathrm{cov}\left(\hat{x}_u, \hat{x}_u\right)$ or $\mathrm{cov}\left(\hat{p}_v, \hat{x}_v\right)$, are similar to the single mode case. For the coefficients involving the two different beams, such as $\mathrm{cov}\left(\hat{x}_v, \hat{p}_u\right)$, we simply set the corresponding local oscillator phase (here 0 for mode v and $\frac{pi}{2}$ for u), and measure simultaneously the two signals. We then compute the covariance. This procedure is made possible by our ability to control independently the local oscillator phase for the mode u and the mode$v$. This method can of course be generalized to systems of more than two beams.

Thus, when a multimode Gaussian state is carried by multiple beams, we can use a sequence of homodyne measurements to build the covariance matrix of the state, which fully characterizes it.

5.1.2 Technical considerations

After this fundamental discussion about homodyne detections and their theoretical capabilities, let us describe common technical difficulties arising when building such a device. This description is of particular importance since the real challenge to build a multipixel homodyne detection is not theoretical, but merely technical.

Photodiodes Electronics

After the interference on the beamsplitter, the intensity of the two superpositions of the local oscillator and the detected beam are measured by photodiodes. These devices convert the light intensity fluctuations into usable electronic signals.

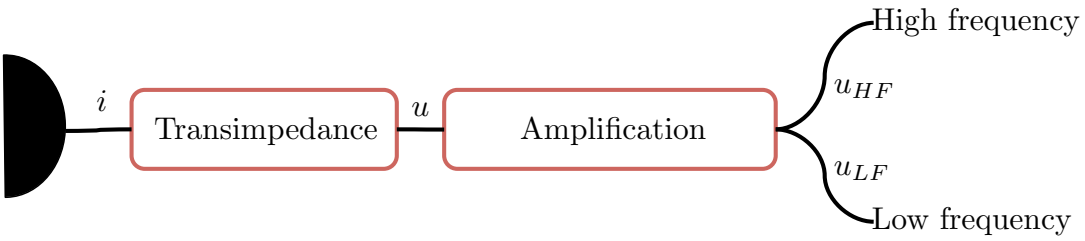

Figure 5.2: Overall schematic of the three stages of a photodiode electronics.

As described in Fig. 5.2, a photodiode is built in three stages. The first stage is the photodiode itself. We use ETX500 photodiodes. These are simple InGaAs photodiodes, selected for their high quantum efficiency (qe). The quantum efficiency is the average number of electrons the photodiode releases for each photon hitting it. It depends on the quality of the photodiode substrate, but can be found above 95%. It is sometimes necessary to test a few photodiodes in order to select the best. To maximize the quantum efficiency, the protective window is removed. We apply a very stable reverse bias voltage to the photodiode ($V_d = 5V$ for the ETX500). This way, when photons hit the diode, a current flows.

After the photodiode, the information on the light intensity is carried by an electronic intensity. We convert this intensity signal into a voltage signal using a transimpedance stage. Indeed, a voltage signal can be more easily amplified, carried and manipulated than an intensity signal. To do so, we could use a simple resistor R_s, straight at the output of the photodiode. In this case, the combination of the parasitic capacitance of the photodiode and the resistor form a low pass filter, and the bandwidth of the detection is limited. Instead we use a more complicated, active, circuit based on an operational amplifier (op-amp) to perform this conversion. Our transimpedance design is based on (C D Hobbs 99), adapted to match the performance of our photodiode. Fig. 5.3 presents such a circuit.

The transimpedance stage outputs a voltage signal. This signal could be used straight away, but we use an amplification stage to prepare it so as to simplify the data acquisition. We split the signal between a low-frequency part, which is amplified by another op-amp, and a high frequency part. This last part can be amplified again, or used as it is. We amplify again the low frequencies so as to limit the intensity draw on the transimpedance op-amp, which can limit its performances.

The combined transfer function of these three stages is complex, and there might not be a simple relation between the input light intensity and the output voltages. We use normalization techniques to avoid the need to reverse these transfer functions. Nonetheless,

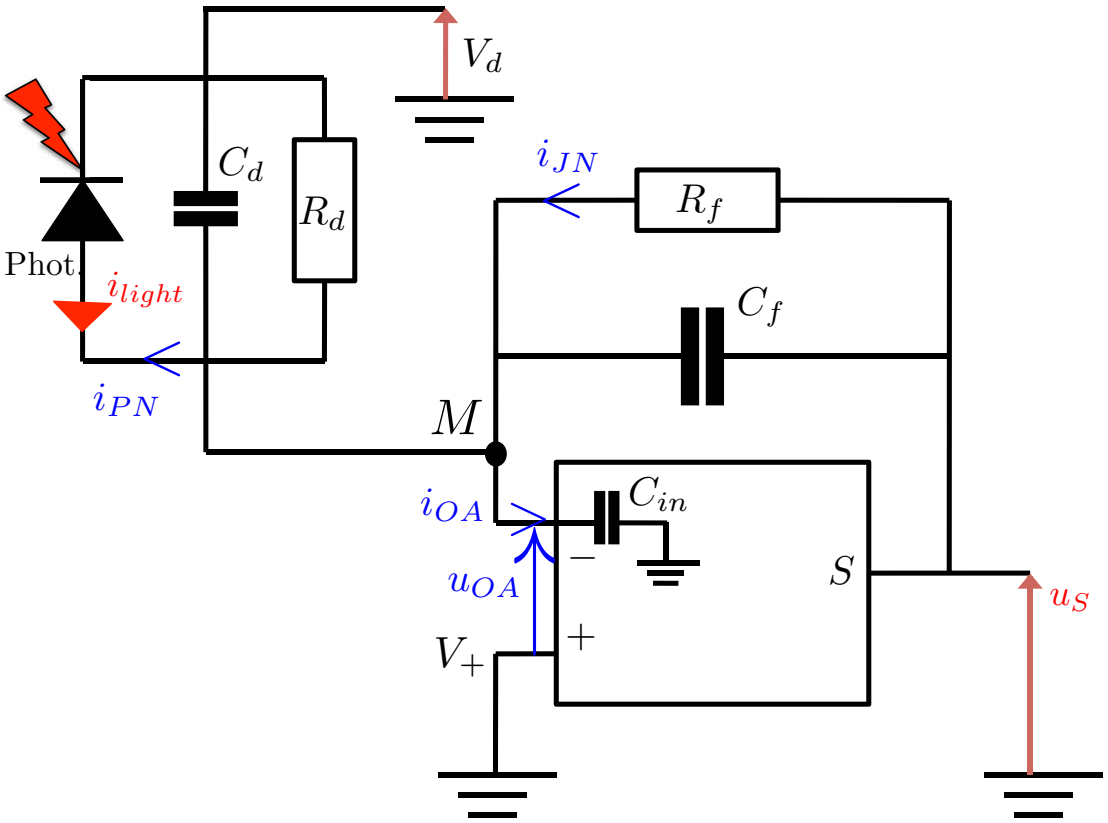

Figure 5.3: Electronic diagram of a transimpedance stage, with all the significant sources of noise: Op-Amp voltage and intensity noise (u_{OA} and i_{OA}), Johnson Nyquist noise of the transimpedance resistor (i_{JN}), Photodiode noise (i_{PN}). The transimpedance stage aims at converting the signal i_{light} into the voltage u_S

this system needs to remains linear: the selection of the electronics components takes into account the railing voltages of the different op-amps as well as the expected light spectrum.

Noise sources in the transimpedance stage

We want to measure the fluctuations of the light intensity hitting the detector. The conversion process is imperfect, and the electronic components introduce additional noise. The most critical processes take place before the transimpedance. Indeed, after the transimpedance, the voltage signal is high enough not to be too sensitive to additional noise sources.

Let us focus on the transimpedance stage. Fig. 5.3 presents a complete schematic of this stage, with the noise sources and some relevant properties of the photodiode (C D Hobbs 99). The different sources of noise can be divided in two categories: intensity noises and voltage noises. In the first category, we find the intensity noise of the op-amp , the Johnson-Nyquist noise and the intensity noise of the photodiode. In the second category, we have the op-amp voltage noise. The intensity noises superpose them-

selves on top of the intensity signal coming from the photodiode, while the voltage noise occurs because of the use of a op-amp.

The intensity noises of the op-amp and the photodiode are linked to small intensity leaks. They are specified by the manufacturers in $A/\sqrt{Hz}$. The Johnson-Nyquist noise is a thermodynamical noise arising from the use of a resistor: depending on the temperature, the flow of current fluctuates: $i_{JN} = \sqrt{4k_BT}$, with k_B the Boltzmann constant, and T the temperature in Kelvin.
The voltage noise of the op-amp is also specified by the manufacturer, and corresponds to a fluctuation of the difference between the positive and negative inputs of the op-amp. It is given in $V/\sqrt{Hz}$.

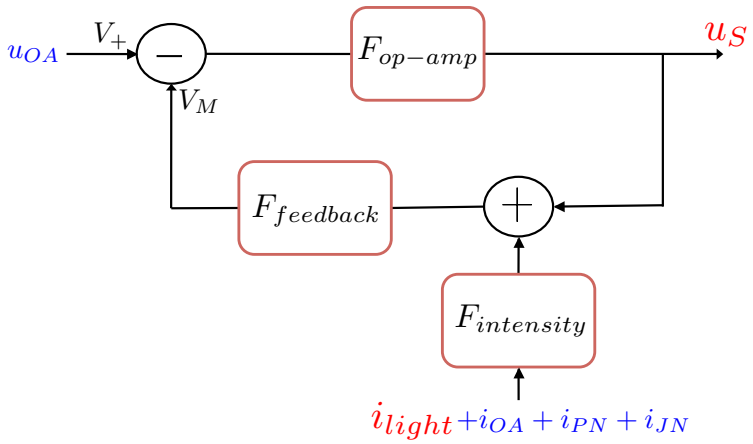

Figure 5.4: Block diagram of the full model of the transimpedance stage, with the significant sources of noise. The transimpedance stage transforms the intensity fluctuations i_{light} into the voltage signal u_S.

These values give us the predicted noise sources and their relative importance. But we need to consider a full model of the transimpedance stage to predict the different contributions to the output signal. Fig. 5.4 presents the block diagram of this system, with different transfer functions calculated using different theorems. In this diagram, the feedback function is computed using Millman's theorem at point M, and corresponds to the feedback from the output of the op-amp to M:

$$F_{feedback}(i\omega) = \frac{i\omega R_d R_f C_f + R_d}{i\omega R_d R_f (C_f + C_d + C_{in}) R_d + R_f} \tag{5.14}$$

where ω is the angular frequency of the signal.

We model the op-amp by a high gain with a double low pass filter (with cutting frequencies f_{dom} and f_2, f_{dom} being the lower one). The gain is the open-loop gain of the op-amp (specified by the manufacturer, G_{ol}) and f_{dom} is derived from the gain-bandwidth-product (GBP): $G_{ol} f_{dom} = GBP$. The second frequency f_2 is less important

and we derive it from the data-sheets of the op-amps. This gives:

$$F_{op-amp}(i\omega) = \frac{G_{ol}}{(i\omega f_{dom} + 1)(i\omega f_2 + 1)} \tag{5.15}$$

Finally, we derive the additional transfer function $F_{intensity}$ needed to take into account the intensity noises in Millman's theorem:

$$F_{intensity}(i\omega) = \frac{R_f}{i\omega R_f C_f + 1} \tag{5.16}$$

With this model, we can predict the output noise levels for different light input powers, for different components and op-amps. For example, Fig. 5.5 presents a noise variance measurement for the AD829 op-amp with $400mW$ of $1064nm$ light. The light produces an intensity noise of $\sqrt{2qI}$ with $q = 1.6 * 10^{-19}C$ the charge of the electron, and I the current intensity due to the $400mW$ of light hitting the detector. The values of the different parameters are presented in Table 5.1.

Table 5.1: Table of parameter values used to model the transimpedance stage of the photodiode

Components	Parameter	Value
Photodiode	Photodiode Capacitance (C_d)	$10^{-10}F$
	Photodiode Resistor (R_d)	$10^8\Omega$
	Photodiode intensity noise (i_{PN})	$1.36 * 10^{-14}A/\sqrt{Hz}$
	Conversion efficiency	$0.68A/W$
Op-amp	Open-loop Gain (G_{ol})	$6.5 * 10^4$
	First op-amp cut-off frequency (f_{dom})	$9.2 * 10^3Hz$
	Second op-amp cut-off frequency (f_2)	$5 * 10^7Hz$
	Op-amp voltage noise (u_{OA})	$1.7 * 10^{-9}V/\sqrt{Hz}$
	Op-amp intensity noise (i_{OA})	$1.5 * 10^{-12}A/\sqrt{Hz}$
	Op-amp input capacitance (C_{in})	$5 * 10^{-12}F$
Feedback	Feedback Capacitance (C_f)	$5.3 * 10^{-12}F$
	Feedback Resistor (R_f)	$5.1 * 10^3\Omega$
Other	Temperature (T)	$300K$

Using this kind of models, we can predict and optimize the noise clearance for a photodetector: the quantum noise clearance for a given power at a given frequency is the difference in dB between the noise variance of the signal when there is light and when there is no light. This noise clearance represents the signal to noise ratio induced by the detector. For example, from Fig. 5.5, we see that at $3MHz$ and for $400mW$ light power, the noise clearance is $8dB$.

All the op-amp and photodiode characteristics are provided by their manufacturer, and correspond to specific conditions of use. When away from these conditions, modelling the behavior of the system is not reliable. For example, when using non-unity gain stable op-amps (such as OPA657), low feedback resistors would lead to a ringing of the tran-

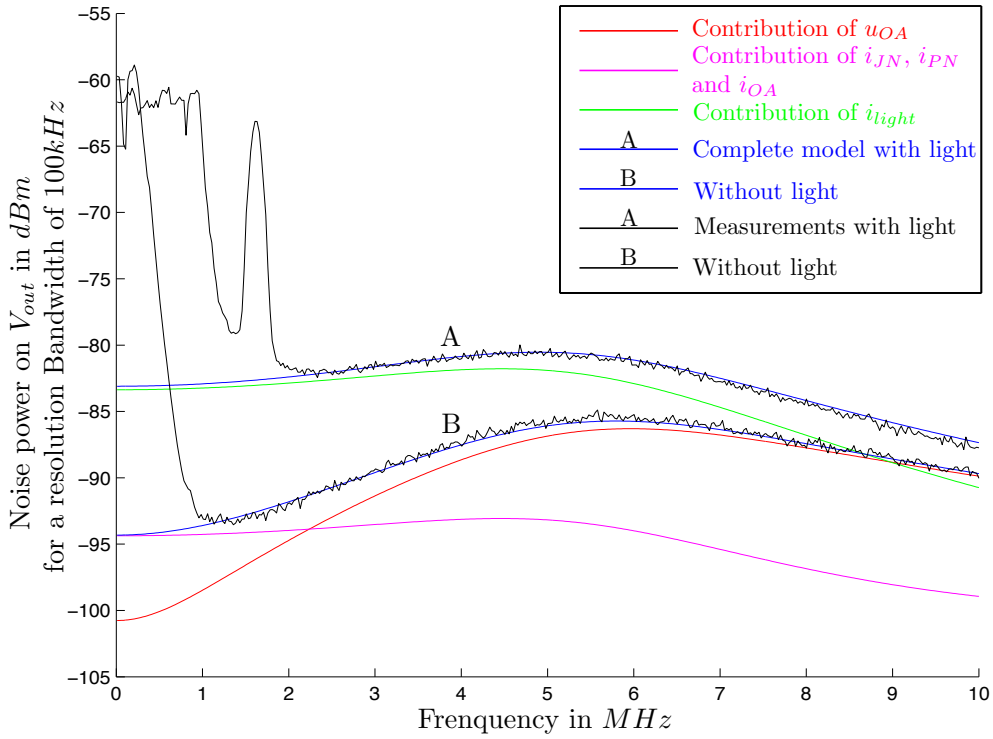

Figure 5.5: Comparison between the noise variances measured at different frequencies, with and without light, and the noise variances modelled (the model parameters are reported in 5.1). The light noise i_{light} is the noise that we want to be able to detect. The modelled and measured variances match very well. Low frequency mismatch appear because of low-frequency amplitude modulation of the light and $1/f$ electronic noise.

simpedance stage (strong oscillation generated by the op-amp that saturates it). In such a situation, the detector does not operate and noise models do not apply.

Local oscillator noise cancellation and data acquisition

After the detectors have converted the two output light intensities into two fluctuating voltage signals, the next step in the homodyne detection is the subtraction of these two signals. Indeed, it is this subtraction that removes the terms in $\hat{a}^{\dagger}_{LO,0}\hat{a}_{LO,0}$ from the final output (Abas 83). These terms are bigger than the term $(\hat{a}^{\dagger}_{LO,0}\hat{a}_{det,0} + \hat{a}^{\dagger}_{det,0}\hat{a}_{LO,0})$ we want to detect, so this subtraction is a necessary step to detect 5.8.

To do so, we use analog splitters, such as the ZSCJ-2-2 from Minicircuits. These splitters can be used in one direction, splitting a single signal into two outputs of opposite phases, or as we do, subtracting two input signals. For this difference, we found that the limiting factor is not the splitter itself, but balancing the two outputs. This is the reason why we try to match as closely as possible the electronics of the detectors, and we use a variable attenuators (LAV-50-B-L from RLC electronics) to attenuate the strongest

output. We can make sure the two detector outputs are matched by checking that an amplitude modulation is fully cancelled.

Using a variable attenuator does not suppress the need for matching electronics. The attenuation achieved by a LAV is flat: if the two gain functions have different shape they cannot be matched for all frequencies, and cancelling a specific amplitude modulation only ensures that the two detectors are matched for that modulation frequency.

After the subtraction, we need to record the signal. We use two main methods: a first way is to use a completely analog system. If needed, we amplify the signal with an analog amplifier (ZFL-500LN+ from Minicircuits). Then, we measure the variance of this signal on a Spectrum Analyser. We can either sweep the detection frequency, as we can find in 5.5 or keep the detection frequency fixed, as presented in 4.4. In both cases, the Spectrum Analyser presents the variance of the noise in a frequency band around the detection frequency, defined by the resolution bandwidth (typically $100kHz$ or $200kHz$).

The Spectrum Analyser provides us with the variance of the signal on a single output. When we only want to characterize a single mode state, using a single homodyne detection, it is a very efficient method. If we want to characterize multimode states, we use multiple adders and subtracters to build a linear combination of the outputs and we measure the variance of linear combination. From a sufficient number of variance detection, it is possible to build the covariance matrix.

An alternative method consists in recording digitally the outputs of the homodyne detections. We can then compute the sums and differences of the multiple outputs more easily, and derive their variances, or compute the covariance matrix directly. This more convenient method presents a challenge: the limited number of bits we can use to record the output of the homodyne detection adds noise to the signal. For example, if we are recording a signal between $-1V$ and $1V$ on $8bits$ the smallest voltage step is $0.78mV$. Recording our signal on $8-bits$ means that any feature smaller than $-24dB$ below our maximum signal cannot be recorded.

For example, if we are recording the squeezing ($-5dB$) and anti-squeezing levels ($9.5dB$) of a beam, using a single homodyne detection, we find that $8-bits$ are sufficient. But if some additional modulation is also recorded (relative phase modulation between the Local Oscillator and the detected beam for example), we may find ourselves either saturating the analog-to-digital converter or hiding the squeezing level because of the digitization.

To avoid such a difficulty, we prepare the signal before the computer data-acquisition. We use a frequency mixer (ZP-3, Minicircuits) and a low-pass filter (BLP-1.9+, Minicircuits) to select a frequency band devoid of any modulation. We then use amplifiers and attenuators to match the signals to the range of the analog-to-digital converters. Using

a mixer and low-pass filter also has the advantage of reducing the frequency we want to record. At lower frequencies, data acquisition cards perform better, with higher number of bits. We use a National Instrument PXI-5105 controlled with Matlab to perform the data acquisition.

For both these methods, we normalize to the quantum noise (vacuum noise) by blocking the detected beams on all the homodyne detections. The signals then reflect the noise variances of the vacuum. We use them as normalization to compute the covariance matrix.

5.1.3 Example: Bias entanglement

A simple experiment we set-up is a good example of how homodyne detections are used to characterize the quantum state of a set of beams. We use a single optical parametric amplifier to generate an amplitude squeezed beam ($-2.9dB$ of squeezing, $5.3dB$ of anti-squeezing). This beam is then split into two beams on a polarizing beamsplitter, and we add losses on one of the two outputs, using a wave-plate and a polarizing beamsplitter. We finally detect both the outputs using homodyne detections. See Fig. 5.6 for details. This very simple experiment allowed us to test counter-intuitive results about asymmetric entanglement.

The detectors have two outputs. A low frequency one (sampled at $1MHz$), that we use to measure the intensity of the light hitting the detectors, and a high frequency output. A ZSCJ-2-2 splitter performs the difference of the two high frequency outputs, and we use a PXI-5122 data acquisition card from National Instrument to records the two differences with a 14-bits depth, sampled at $100MHz$. This high depth, coupled with the absence of strong modulation on the output beams, allows us to record the outputs of the homodyne detections straight away, without demodulation.
We then apply numerically a 6th order butterworth pass band filter centered at $4.5MHz$ with a frequency window of $1MHz$. We focus on this frequency band because the effect of the optical parametric amplifier is at its strongest there.

The low frequency outputs are used for two independent purposes. First of all, we use them to derive the amount of losses induced by the polarizing beamsplitters: when the local oscillators are all blocked, summing the two detectors in a homodyne detection gives the power of the light in the detected beam. We derive the losses by comparing this measure with the total light power. A second purpose of the low frequency outputs is the locking of the local oscillator phases. Indeed, because of air fluctuations, the relative phases between the local oscillators and the detected beams do not remain stable. We use the difference of the two low frequency outputs to drive a piezo-electric actuator to stabilize this relative phase.

For different angles of the wave-plates, i.e. different levels of losses, the quantum state

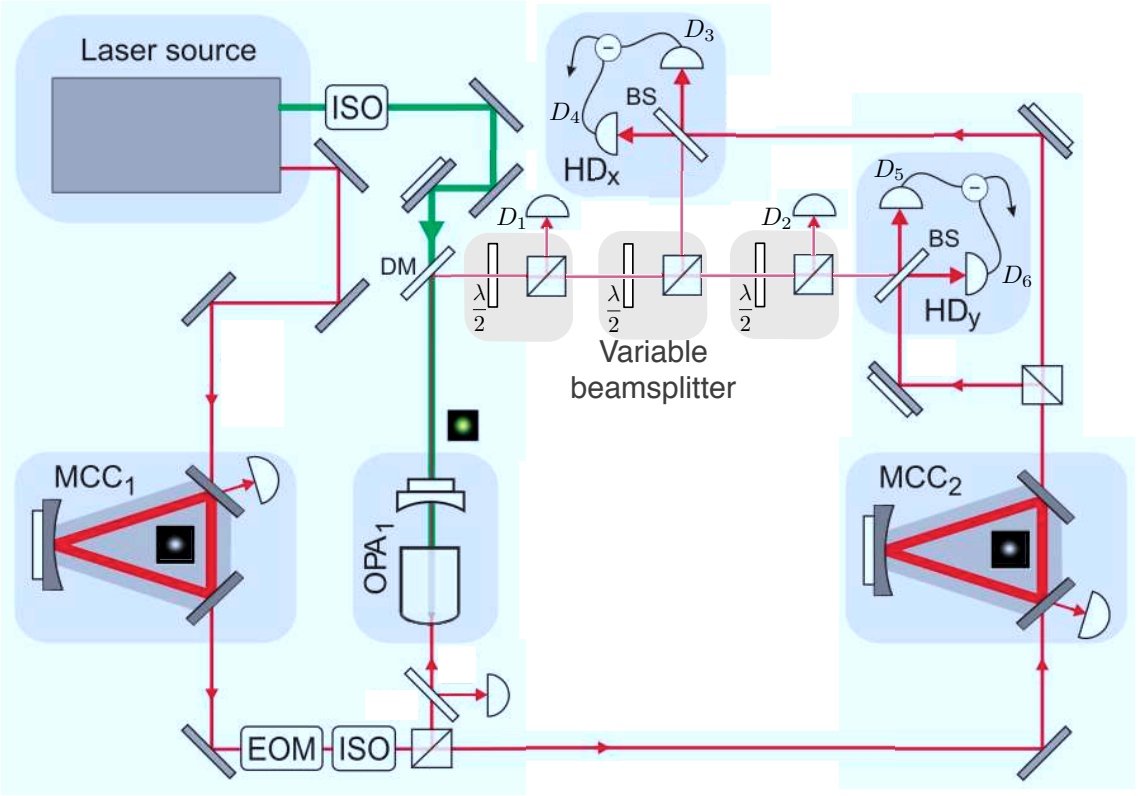

Figure 5.6: Schematic of the bias entanglement experiment. A squeezed beam is produced by the optical parametric amplifier OPA_1. We can then add losses using a first set of a $\frac{\lambda}{2}$ wave-plate and a polarizing beamsplitter (PBS). We then use a second set of $\frac{\lambda}{2}$ and PBS to split the beam into two beams, x and y, and we add a third set to introduce additional losses on beam y. The two homodyne detections HD_x and HD_y record the fluctuations of the phase or the amplitude of beams x and y respectively. We lock the local oscillator phase to measure a specific quadrature. We use a first mode cleaning cavity MCC_1 to shape the infrared beam before it is used as a seed in the OPA. We then use a second mode cleaning cavity to MCC_2 to optimize the shape of the local oscillator.

of the output beams is different. We use the two homodyne detections to characterize the state, recording fluctuations along the amplitude or phase quadratures for each beam simultaneously. In this case, we are interested in the conditional variances $\langle \Delta^2 \hat{x}_x | \hat{x}_y \rangle$, $\langle \Delta^2 \hat{p}_x | \hat{p}_y \rangle$, $\langle \Delta^2 \hat{x}_y | \hat{x}_x \rangle$ and $\langle \Delta^2 \hat{p}_x | \hat{p}_y \rangle$ between the beams x and y. We record a set of traces for different local oscillator phases. By doing so, we assume that the quantum state does not change between the recordings.

In the specific case when we transmit 80% of the light through the variable beamsplitter, these measurements exhibit an interesting phenomenon, called bias entanglement: if we compute the conditional variances of beam x having measured the beam y, and the

conditional variances of the beam y having measured beam x, we find that:

$$\sqrt{\langle \Delta^2 \hat{x}_x | \hat{x}_y \rangle \langle \Delta^2 \hat{p}_x | \hat{p}_y \rangle} = 0.48 \pm 0.01 \tag{5.17}$$

$$\sqrt{\langle \Delta^2 \hat{x}_2 | \hat{x}_1 \rangle \langle \Delta^2 \hat{p}_2 | \hat{p}_1 \rangle} > \frac{1}{2} \tag{5.18}$$

We find that this quantum state can violate the EPR paradox by measuring the beam y and predicting the measurement on beam x but cannot do the opposite. This result is especially important in quantum communication schemes, where asymmetric losses are common (one part of the state is carried to the receiver, while the other part remains with the sender).

This simple example shows that homodyne detections are sufficient to characterize the quantum state of a complex, multipartite system. We found that the characterization relies on our ability to record simultaneously the fluctuations of several homodyne detections outputs and that the phase of each local oscillator needs to be stabilized.

5.2 Multipixel Homodyne Detection

Instead of using separate beams to carry the interesting quantum state we want to characterize or use, we built this state within a single beam using the orthogonal transverse spatial modes just like as many separate beams. We have seen previously that preparing a beam carrying multiple squeezed modes can be done either by using spatially degenerate optical parametric amplifiers, or by superposing the outputs of conventional amplifiers.

On the detection side, our aim is to be able to detect the multiple transverse spatial modes with the same efficiency and flexibility as we can measure separate beams using several homodyne detections. In this section we detail the use of multipixel photodiode to build a multimode homodyne detection.

5.2.1 Theoretical presentation

Let us begin with a brief presentation of the principles of a multimode homodyne detection.

Multipixel homodyne detection

A multimode homodyne detection is based on the same components as the single mode homodyne detection presented earlier. The difference is that we replace the two photodiodes by two arrays of adjacent photodiodes, as detailed in Fig. 5.7.

Consider there are N_{pix} pixels in each of the photodiode arrays. The two photodiode arrays both have N_{pix} intensity outputs, proportional to the light intensity hitting the relevant pixels. For each of these channels, we build an independent transimpedance and

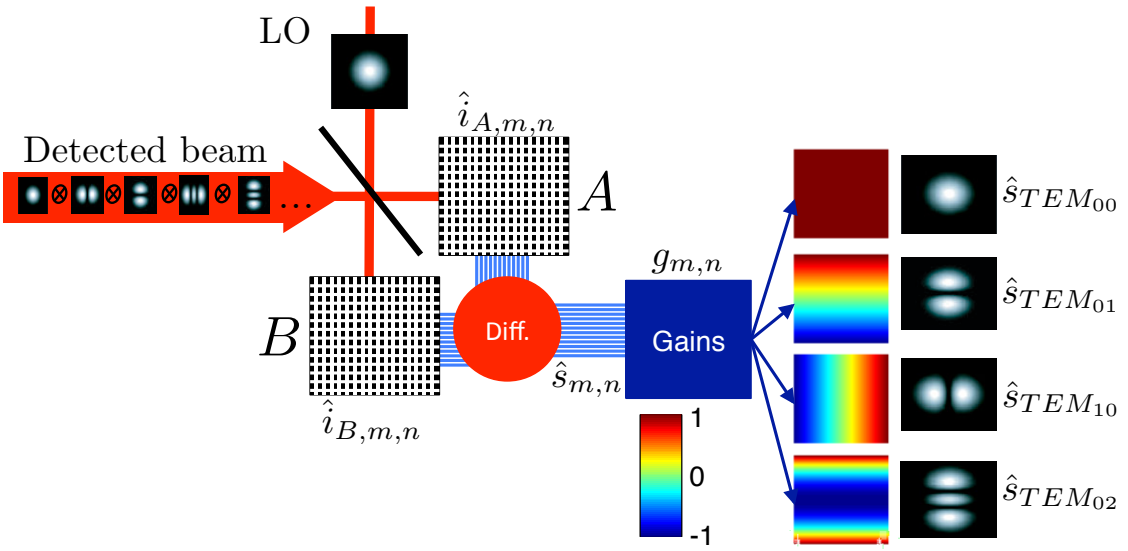

Figure 5.7: Schematic of the multimode homodyne detection: the detected beam is superposed with a local oscillator LO on a 50 : 50 beamsplitter. The two superpositions are then detected using the two arrays of photodiodes (A and B). We make the difference of each pair of corresponding pixels: $\hat{s}_{m,n} = \hat{i}_{A,m,n} - \hat{i}_{B,m,n}$, and we recombine these outputs to measure a specific spatial mode.

amplification stage, to convert the intensity outputs into voltage outputs.

Then, as indicated in Fig. 5.7, we subtract pixel per pixel the outputs from photodiode array B from the outputs of photodiode array A. After theses N_{pix} subtractions, we have N_{pix} new outputs, corresponding to as many small homodyne detections signals.

Mathematically, we find that we now have N_{pix} signals each corresponding to a specific spatial location on the beam. To be more precise, we need to consider the local field operators $\hat{a}_A(\vec{\rho})$ and $\hat{a}_B(\vec{\rho})$ respectively. Because one beam has been reflected and the other one has not, it is convenient to consider that the positions $(\vec{\rho})$ of the operators are relative to the detector surface, so that the positions $(\vec{\rho})$ on detectors A and B correspond to the same part of the beam before the beamsplitter.

Each of the detectors measures the intensity of the light hitting a specific area. For pixel (m, n) on detector A, which area is defined by $S_{m,n}$, we find:

$$\hat{i}_{A,m,n} = \iint_{(\vec{\rho})\in S_{m,n}} \hat{a}_A(\vec{\rho})^\dagger \hat{a}_A(\vec{\rho})\, d^2\vec{\rho} \tag{5.19}$$

We find the same expression on detector B, and the signal resulting from the difference is

$$\hat{s}_{m,n} = \hat{i}_{A,m,n} - \hat{i}_{B,m,n} \tag{5.20}$$

Using the same decomposition as presented for the single mode homodyne detection, we

decompose the detected beam and the local oscillator beam into a sum of orthogonal transverse modes, with the first mode of the basis being the mode that contains all the energy of the local oscillator. As opposed to the single mode homodyne detection, the shape of these modes is now relevant. Let us name their spatial profiles $u_k(\vec{\rho})$. We know that we have

$$\hat{a}_A(\vec{\rho}) = \sum_{k\in\mathbb{N}} \hat{a}_{A,k} u_k(\vec{\rho}) \tag{5.21}$$

or that, conversely,

$$\hat{a}_{A,k} = \iint_{\vec{\rho}\in\mathbb{R}^2} \hat{a}_A(\vec{\rho}) u_k(\vec{\rho})^* \tag{5.22}$$

We use this decomposition to express the signal $\hat{s}_{m,n}$ in terms of the incident field operators $\hat{a}_{det,k}$ and $\hat{a}_{LO,k}$. We have:

$$\hat{a}_{A,k} = \frac{\sqrt{2}}{2}\left(\hat{a}_{LO,k} + \hat{a}_{det,k}\right) \tag{5.23}$$

$$\hat{a}_{B,k} = \frac{\sqrt{2}}{2}\left(\hat{a}_{LO,k} - \hat{a}_{det,k}\right) \tag{5.24}$$

We find that $\hat{s}_{m,n}$ becomes

$$\begin{aligned}\hat{s}_{m,n} &= \tfrac{1}{2}\textstyle\sum_{(k,l)\in\mathbb{N}^2}\left(\hat{a}^\dagger_{LO,k}\hat{a}_{LO,l} - \hat{a}^\dagger_{LO,k}\hat{a}_{LO,l}\right)\iint_{(\vec{\rho})\in S_{m,n}} u_k(\vec{\rho})^* u_l(\vec{\rho})\, d^2\vec{\rho} \\ &+\tfrac{1}{2}\textstyle\sum_{(k,l)\in\mathbb{N}^2}\left(\hat{a}^\dagger_{LO,k}\hat{a}_{det,l} + \hat{a}^\dagger_{det,k}\hat{a}_{LO,l}\right)\iint_{(\vec{\rho})\in S_{m,n}} u_k(\vec{\rho})^* u_l(\vec{\rho})\, d^2\vec{\rho} \\ &+\tfrac{1}{2}\textstyle\sum_{(k,l)\in\mathbb{N}^2}\left(\hat{a}^\dagger_{det,0}\hat{a}_{det,0} - \hat{a}^\dagger_{det,0}\hat{a}_{det,0}\right)\iint_{(\vec{\rho})\in S_{m,n}} u_k(\vec{\rho})^* u_l(\vec{\rho})\, d^2\vec{\rho}\end{aligned} \tag{5.25}$$

This rather complex expression can be simplified using the same approximations as in the case of the single mode homodyne detection. We begin by selecting only the terms in the expression of $\hat{s}_{m,n}$ which involve $\hat{a}_{LO,0}$. This approximation comes from the assumption that the local oscillator is far more intense than all the other modes. We will detail this approximation after the derivation of a simple expression for $\hat{s}_{m,n}$. The expression of $\hat{s}_{m,n}$ is now

$$\begin{aligned}\hat{s}_{m,n} &= \textstyle\sum_{k\in\mathbb{N}} \hat{a}^\dagger_{LO,0}\hat{a}_{det,k}\iint_{(\vec{\rho})\in S_{m,n}} u_0(\vec{\rho})^* u_k(\vec{\rho})\, d^2\vec{\rho} \\ &+ \textstyle\sum_{k\in\mathbb{N}} \hat{a}^\dagger_{det,k}\hat{a}_{LO,0}\iint_{(\vec{\rho})\in S_{m,n}} u_k(\vec{\rho})^* u_0(\vec{\rho})\, d^2\vec{\rho}\end{aligned} \tag{5.26}$$

$$\tag{5.27}$$

We can go a step further, as in the single homodyne case, and consider the average value of the local oscillator coherent field α_0. We find the expression:

$$\begin{aligned}\hat{s}_{m,n} &= \textstyle\sum_{k\in\mathbb{N}} \alpha_0^*\hat{a}_{det,k}\iint_{(\vec{\rho})\in S_{m,n}} u_0(\vec{\rho})^* u_k(\vec{\rho})\, d^2\vec{\rho} \\ &+\hat{a}^\dagger_{det,k}\alpha_0\iint_{(\vec{\rho})\in S_{m,n}} u_k(\vec{\rho})^* u_0(\vec{\rho})\, d^2\vec{\rho}\end{aligned} \tag{5.28}$$

The sum over all the values of k makes this expression complex. It can be better understood by introducing a new set of transverse spatial modes, the pixel modes. These modes, named $v_{m,n}$ with the same labelling as the pixels, have the same shape as the local oscillator in the pixel (m,n), and are 0 otherwise. We do not use them as a basis, but rather as an efficient description of our detection apparatus. We have:

$$v_{m,n}(\vec{\rho}) = u_0(\vec{\rho}) \quad \forall(\vec{\rho}) \in S_{m,n} \tag{5.29}$$

$$v_{m,n}(\vec{\rho}) = 0 \quad \forall(\vec{\rho}) \notin S_{m,n} \tag{5.30}$$

We name the annihilation operators on these new modes $\hat{a}_{det,v_{m,n}}$. With these new modes, the expression for $\hat{s}_{m,n}$ becomes:

$$\hat{s}_{m,n} = \left(\alpha_0^* \hat{a}_{det,v_{m,n}} + \hat{a}^\dagger_{det,v_{m,n}} \alpha_0\right) \iint_{(\vec{\rho})\in S_{m,n}} |u_0(\vec{\rho})|^2 \, d^2\vec{\rho} \tag{5.31}$$

This means that each pixel performs a homodyne detection on a specific transverse mode. In the single mode homodyne detection case, this mode was the local oscillator mode u_0. When we use pixels, each does not capture all the local oscillator light. Each pair of pixels (A,m,n) and (B,m,n) performs a homodyne detection on the spatial mode $v_{m,n}$.

As we have seen, we neglected all the terms which do not involve $\hat{a}_{LO,0}$ in the general expression of $\hat{s}_{m,n}$. This assumption is only valid when for each pixel the power of the local oscillator light is significantly larger that the average power of the detected beam. For example, this means that if we use a local oscillator with a Gaussian shape, we have to be careful for the pixels on the edge, where the approximation will not be as valid as for the pixels in the center, which receive more light.

Signal recombination

We have described the outputs $\hat{s}_{m,n}$ of the N_{pix} parallel channels of the multimode homodyne detections. We can use these outputs directly. In this case, the modes of the multimode homodyne detection are the $v_{m,n}$. But it is also possible to recombine these N_{pix} parallel outputs.

Consider a set of gains $g_{m,n} \in \mathbb{R}^{N_{pix}}$ and consider now the output $\hat{s}_g = \sum g_{m,n}\hat{s}_{m,n}$. This new combination can be expressed with:

$$\hat{s}_g = \alpha_0^* \hat{a}_{det,v_g} + \hat{a}^\dagger_{det,v_g} \alpha_0 \tag{5.32}$$

With the mode v_g defined by

$$v_g(\vec{\rho}) = \sum g_{m,n} v_{m,n}(\vec{\rho}) \tag{5.33}$$

If we take the gains $g_{m,n}$ in $\mathbb{R}^{N_{pix}}$ without constraint, v_g as defined above is not necessarily normalized. But without loss of generality, we can scale up or down the gains $g_{m,n}$ to bring back v_g's norm to 1, and satisfy our definition of a mode.
The observable $\hat{s}_g$ is the result of the homodyne detection on a new specific transverse mode, defined by the gains $g_{m,n}$. Since the pixels do not overlap, we can define a function $g(\vec{\rho})$ which associate the value of the gain $g_{m,n}$ associated to each position $(\vec{\rho})$ (If $(\vec{\rho}) \in S_{m,n}$ then $g(\vec{\rho}) = g_{m,n}$). The shape of v_g is simply:

$$v_g(\vec{\rho}) = g(\vec{\rho})u_0(\vec{\rho}) \tag{5.34}$$

Thus, with recombinations, it is possible to detect complex spatial modes instead of the original local oscillator mode u_0.

Finding the values of $g(\vec{\rho})$ to detect a specific mode is straight-forward: we simply divide the mode we want to detect by the local oscillator mode u_0. But this continuous solution for $g(\vec{\rho})$ does not apply when the number of pixels is limited. In this case, we choose the $g_{m,n}$ to maximize the overlap between the desired mode v_d and the normalized mode $g(\vec{\rho})u_0(\vec{\rho})$. This maximization corresponds to maximizing a scalar product:

$$\iint_{(\vec{\rho})\in\mathbb{R}^2} v_d(\vec{\rho})^* g(\vec{\rho})u_0(\vec{\rho})\, d^2\vec{\rho} = \sum_{m,n} \left(g_{m,n} \iint_{\vec{\rho}\in S_{m,n}} v_d(\vec{\rho})^* u_0(\vec{\rho})\, d^2\vec{\rho} \right) \tag{5.35}$$

taking into account the constraint that the norm of v_g must remained 1.

We find that the best values for $g_{m,n}$ are

$$g_{m,n} = \frac{1}{N} \frac{\iint_{\vec{\rho}\in S_{m,n}} v_d(\vec{\rho})^* u_0(\vec{\rho})\, d^2\vec{\rho}}{\iint_{\vec{\rho}\in S_{m,n}} u_0(\vec{\rho})^* u_0(\vec{\rho})\, d^2\vec{\rho}} \tag{5.36}$$

where N is a normalization constant. For example, Fig. 5.8 presents the optimal modes v_g we can use to detect a TEM_{00}, a TEM_{10} and a TEM_{20} when we the local oscillator is a wide TEM_{00} mode and we have 16 pixels to apply gains on.

The gains $g_{m,n}$ are all in $\mathbb{R}$. Indeed, introducing a complex gain is equivalent to changing the local oscillator phase for this pixel (and measuring a different quadrature): it cannot be done after the measurement, i.e. when we recombine electronically the different signals. This introduces a limit to the transverse modes we can detect with the multipixel homodyne detection. Indeed, while the amplitude of $v_g(\vec{\rho}) = g(\vec{\rho})u_0(\vec{\rho})$ can be changed by $g(\vec{\rho})$, the phase is fixed by the phase of u_0.

As a result, we can use the different gains to increase the intensity overlap α^2 between the mode v_d and v_g, but we can be limited by their phase difference. Shaping the phase of the local oscillator, i.e. matching the transverse phase profile of u_0 to the one of v_d can solve this issue.

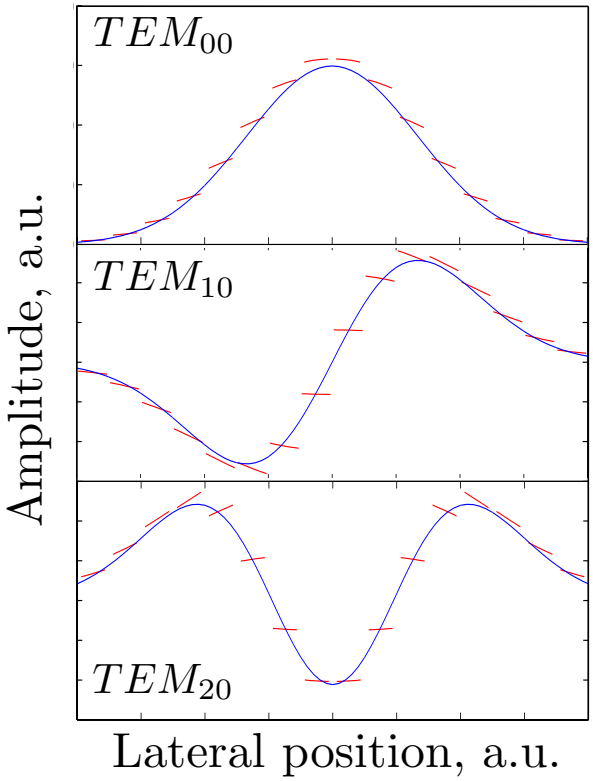

Figure 5.8: Optimal modes v_g (in red) to detect a TEM_{00}, a TEM_{10} and a TEM_{20} (in blue) with a wide TEM_{00} local oscillator and an array of 16 pixels.

Basis change

We have seen we can recombine the different outputs of the multimode homodyne detection into the result of a virtual, single mode homodyne detection on a new transverse mode, different from the local oscillator. We can expand this idea to multiple modes: the signals are voltages, they can be read digitally and we can perform easily multiple simultaneous recombinations on a computer. Instead of limiting ourselves to a single mode, we decide to detect multiple modes at the same time, by performing multiple different recombinations of the output signals.

In order to be equivalent to as many separate beams, the recombined modes we want to measure need to be orthogonal. Let us define a matrix formulation of these recombinations: if we rename the pixels with a single index (so that $\hat{s}_{m,n} \to \hat{s}_i$), we can define the matrix $O \in O_{N_{pix}}(\mathbb{R})$ as the matrix of the recombination. Detecting the recombined mode i corresponds to performing the combination $\hat{s}_i = \sum O_{i,j}\hat{s}_j$. We want the N_{pix} recombined modes to be orthogonal. Because the pixel modes are all orthogonal, it entails that O belongs to $O_{N_{pix}}$, the group of the orthogonal matrices.

Using a multimode homodyne detection, we are able to measure simultaneously a set of observables $\hat{s}_i$. While these observables measure orthogonal transverse spatial modes, they share the same local oscillator. Because of the sharing of the local oscillator, there is a limitation to the nature of the observables $\hat{s}_i$.

Let us begin with an example: measuring a TEM_{00} and a TEM_{10} mode, using a TEM_{00} local oscillator. Obviously, the gains are unity to detect the TEM_{00}, and linear to detect the TEM_{10}. We can measure $\hat{x}_{TEM_{00}}$ and $\hat{x}_{TEM_{10}}$ simultaneously, by setting the right local oscillator phase. We can also measure $\hat{p}_{TEM_{00}}$ and $\hat{p}_{TEM_{10}}$ at the same time. But can we measure $\hat{x}_{TEM_{00}}$ and $\hat{p}_{TEM_{10}}$ simultaneously? Since these two modes are orthogonal, they are equivalent to two independent beams, for which such a combination of observables is not an issue. But measuring these two transverse modes with the same multimode homodyne detection introduces a limitation. Indeed, measuring $\hat{x}_{TEM_{00}}$ means measuring on all the pixels the quadratures $\hat{x}_i$, while measuring $\hat{p}_{TEM_{10}}$ conversely imply measuring the quadratures $\hat{p}_i$. And measuring $\hat{x}_i$ and $\hat{p}_i$ simultaneously cannot be done because of the non-commutative nature of these observables.

This example shows the limits of the multimode homodyne detection: it is not fully equivalent to an array of separate homodyne detection, measuring different beams. For separate homodyne detections, measuring the $\hat{x}$ quadrature of a beam and the $\hat{p}$ quadrature of another is possible, while performing the same task on copropagating modes within a beam is not always achievable.

A complete description of a multimode homodyne detection takes into account this limitation. Depending on the spatial profile of the phase of the local oscillator, each pixel measures an observable $\hat{x}_i^{\theta_i}$. The complete set of achievable basis of observables is then defined by $\hat{s}_j = \sum O_{i,j}\hat{x}_i^{\theta_i}$ with O an orthogonal matrix.

5.2.2 Electronics

Arrays of detectors have been used to measure quantum noise for some time, either in the form of quadrant detectors (Janousek 08a; Treps 03), or of bigger arrays (Beck 01; Dawes 01; Dawes 03). Our multimode homodyne detection was specifically designed to be able to record quantum fluctuations in multiple transverse modes.
We built our multimode homodyne detection using a pair of multipixel photodiodes. After a brief description of the properties of the photodiodes, we focus on the specific electronic requirements they entail, and the practical solutions we implemented.

Multipixel Photodiode

Multipixel photodiodes are specialty equipments. They can be built with custom requirements (i.e. pixel sizes, shapes, connections...), but without guarantee on their physical properties (noise levels, photodiode capacitance). Off-the-shelf multipixel photodiodes,

with reliable data-sheets, are mainly designed for spectroscopy applications: their pixels are arranged in a single line. As a proof of concept, a line of pixels is enough, and our multimode homodyne detection was built using two such arrays.

We selected our photodiode array on a set of criteria: we need a photodiode array without any electronic processing on the chip, so as to be able to design a specific transimpedance stage, optimized for our light power and detection frequencies. We need the lowest photodiode noise, and the lowest photodiode capacitance achievable. Finally, we need the quantum efficiency as high as possible.

We chose the G7150-16 produced by Hamamatsu. It is composed of 16 adjacent InGaAs photodiode. These photodiodes share the same cathode, and we have a pin for each anode. Hence, all the photodiode share the same bias voltage ($5V$), but the intensity released when light hits them can be detected separately. The quantum efficiency of each of these diodes is 80%, which includes the losses induced by the protective window. Measurements of its quantum efficiency as a function of the wavelength can be found in Fig. 5.9. After taking away the protective window, we measured the quantum efficiency at 92%. This means that the protective window introduced a significant loss of 13%. This is due to the absence of coating of this glass. The 92% quantum efficiency measured at $1064nm$ is not as high as what we found for simple photodiodes, but the extra challenge of building a line of pixels close together explains the difference.

The 16 pixels of the G7150-16 are all $0.45 \times 1mm^2$. They are separated by a $0.05mm$ gap. In total, the length of the array is $8mm$, with a width of $1mm$. A picture of this array can be found in Fig. 5.10. The gaps between the pixels is equivalent to losses: here 10% of the light power does not hit an active surface.

Specific electronic requirements

The G1750-16 photodiode array does not have any electronic processing. Apart from the shared cathodes, which require a stabilized $5V$ voltage, the 16 parallel outputs behave exactly like as many independent photodiodes. They all require independent transimpedance and amplification stages, and we select the components for each transimpedance stage depending on the expected local oscillator power hitting each pixel. Indeed, since we use a Gaussian local oscillator, the pixels on the edge receive less light than the center pixels. To begin with, we choose to use only eight pixels to simplify the data acquisition. All the pixels have the same transimpedance Op-Amp, the AD 829. For a Gaussian local oscillator of $10mW$ in the TEM_{00} mode, table 5.2 presents a list of optimum optical components:

A first design for the electronic stage of the photodiodes was based on a single electronic board. This design, chosen for the simplicity of its connections, turned out to be disastrous for the prototyping stage: changing any electronic component resulted in damages to the electronic connections of neighboring components. As a result we developed

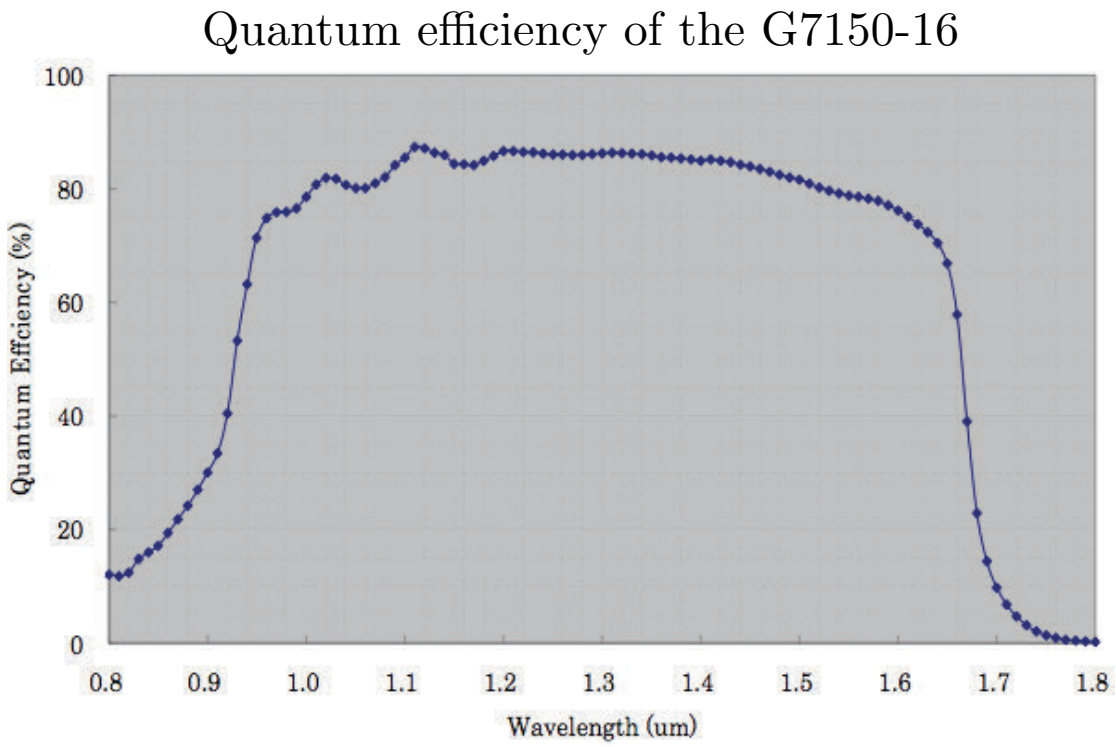

Figure 5.9: Quantum efficiency at $25°C$ of the InGaAs photodiodes which compose the G7150-16 array. At $1064nm$ the efficiency is 80%. This data was provided by Hamamatsu Corp.

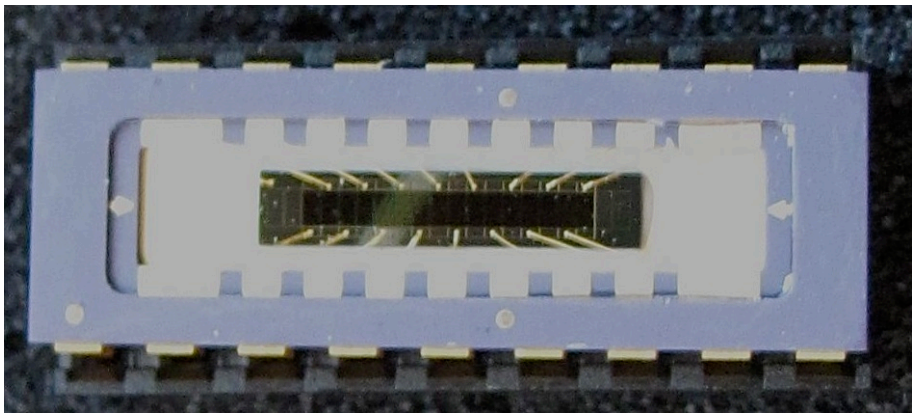

Figure 5.10: Picture of the G7150-16 InGaAs photodiode array.

a different design, based on modular transimpedance stages. A picture of the photodiode can be found in Fig 5.11. This design is based on multiple small boards, each carrying a single transimpedance and amplification stage, all connected to a transverse board on which the photodiode and the supply voltages are centralized. We use low noise micro-miniature connectors between the boards so as to minimize noise addition while still being able to detach the boards to change components without damaging other pixels' electronics. Moreover, being able to remove boards allows us to prepare multiple transimpedance stages and switch from one to another depending on the local oscillator power.

Table 5.2: Values of the different circuit components

Pixel Name	Pixel 1	Pixel 2	Pixel 3	Pixel 4	Pixel 5	Pixel 6	Pixel 7	Pixel 8
Power in μW	250	750	1600	2400	2400	1600	750	250
R_f in Ω	8000	6800	3200	2150	2150	3200	6800	8000
C_f in pF	6.36	6.36	9	11	11	9	6.36	6.36
Clearance at 2 MHz	8.3	12.4	13.5	13.6	13.6	13.5	12.4	8.3
at 5 MHz (in dB)	4.1	7.7	9.8	10.6	10.6	9.8	7.7	4.1

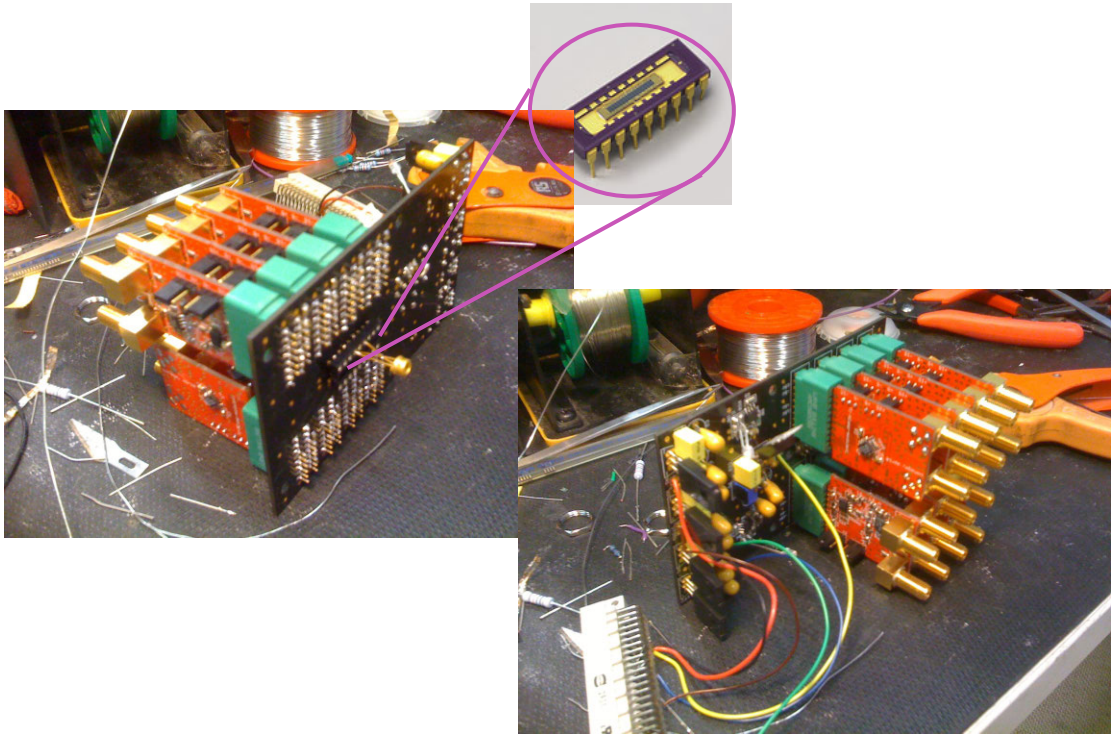

Figure 5.11: Photographs of the multiboard design for the electronics of the photodiode array. The main board carries the detectors and the supply circuit. The smaller boards, attached perpendicularly, perform the transimpedance and amplification stages.

We use these two photodiode arrays to build a multimode homodyne detection. For each pair of pixels, we use variable attenuators (LAV-50-B-L) and power splitters (ZSCJ-2-2) to cancel out the local oscillator intensity noise. We then amplify the resulting 8 signals using ZP-3 amplifiers, and we use additional attenuators to match the output powers so as to maximize the use of the range of the data acquisition card. The data acquisition card is a NI PXI 5105, 8-channels, 12-bits digitizer, with a sampling frequency of $60MHz$.

5.2.3 Entanglement within a beam

Let us now present experimental results achieved using the multimode homodyne detection. The goal of this experiment is to build and characterize entanglement within a single beam in a universal and potentially scalable way. We begin by producing a beam carrying two transverse squeezed modes with the method presented in Fig. 4.9.

The beam carries an amplitude squeezed TEM_{00} and a phase squeezed flip mode. This beam is then detected on the multimode homodyne detection. We recombine the signals into a set of specific spatial modes, we show that these modes are entangled, and that the multimode homodyne detection can achieve this characterization.

Since the way we produce the beam carrying the two squeezed transverse modes has already been discussed extensively in section 4.3.1, and our experimental multimode homodyne detection in section 5.2.2, we focus here on the data processing stage, specific to this experiment. We then present the experimental outcomes and a theoretical generalization of this system.

Data processing: a general overview

Our multimode homodyne detection has 8 outputs, corresponding to the 8 differences between the output voltages of pairs of corresponding pixels. We amplify the resulting signals to match them to the ranges of the data acquisition card. In this experimental set-up, the locking of the squeezing cavities with the Pound-Drever-Hall technique resulted in two phase modulations: a first modulation at $7MHz$ only in the flip-mode, and a second modulation at $16MHz$ both in the TEM_{00} and the flip-mode.

Each one of the 8 outputs of the multimode homodyne detection has a different overall transfer function. This transfer function depends on the transimpedance stages, amplification stages, and on the final attenuation before the data acquisition. In order to measure the amplitude or phase of a specific spatial mode, we need to recombine the 8 outputs $s_i(t)$, taking into account these different transfer functions.

A straight forward method to do so would be to measure the transfer functions and correct the signals based on this measurement. This method requires a calibrating procedure, involving a specific, well controlled modulated beam hitting one pixel at a time. Since we tweak the amplification stages and attenuations between each measurement to maximize the signal to noise ratio, we would need to perform this calibration before every data acquisition.

Our method consists in focusing on the data processing, and deriving the needed corrections from the 8 signal traces. This method is based on the a-priori knowledge we have about the noise content of each spatial mode.

Exploiting the covariance matrix on modulations

In our experiment, the two OPAs are locked using the Pound-Drever-Hall technique. This results in the addition of a $7MHz$ phase modulation in the flip mode, and a $16MHz$ modulation in the flip-mode and the TEM_{00} mode. We use these phase modulations to derive the optimal gains to detect these modes.

We begin the data analysis process with the strong modulation at $7MHz$. We filter the data in a frequency band of width $300kHz$ around $7MHz$. The output signals can then be expressed as $s_i(t) = a_i \cos(2\pi f_{mod} t + \phi_i) + \delta s_i(t)$, with $a_i \cos(2\pi f_{mod} t + \phi_i)$ the modulation at $f_{mod} = 7MHz$, and $\delta s_i(t)$ the additional signal. Experimental data is presented in Fig. 5.12.

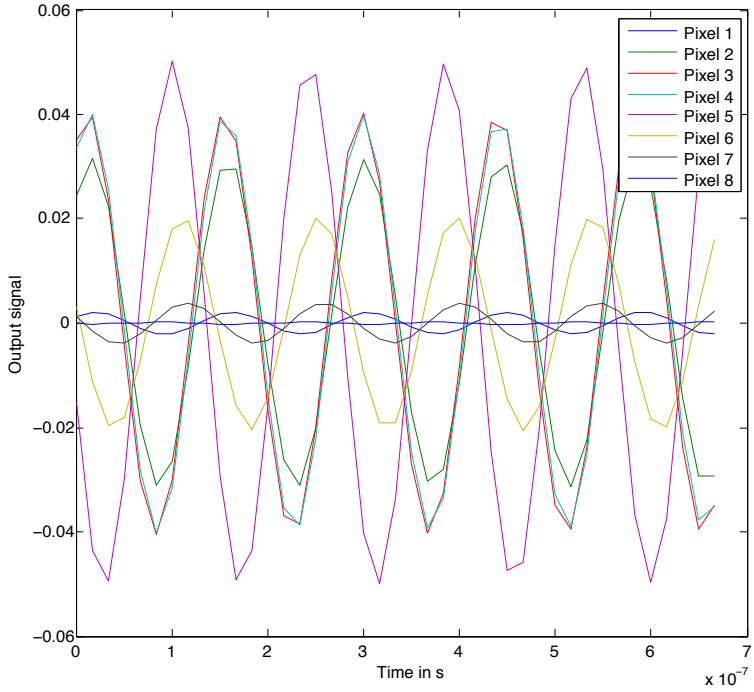

Figure 5.12: Short sample of the output signals $s_i(t)$ filtered around the $7MHz$ modulation frequency

We consider the covariance matrix C_{ij} between these signals. Since they all have a 0 average, $C_{ij} = \int_{t_{begin}}^{t_{end}} s_i(t) s_j(t)\, dt$. Our sample is far longer than $1/f_{mod}$, and since we selected a narrow band around the modulation frequency, the term $\delta s_i(t)$ is small compared to the modulation. This means that we have $C_{ij} = a_i a_j \cos(\phi_i - \phi_j)/2$. For the

experimental data presented in Fig. 5.12, the covariance matrix is:

$$C = 10^{-4} \begin{pmatrix} 0.0164 & 0.2219 & 0.2984 & 0.2907 & -0.3584 & -0.1040 & -0.0083 & 0.0018 \\ 0.2219 & 3.5041 & 4.9100 & 4.6145 & -4.0482 & -0.7179 & -0.0032 & 0.0130 \\ 0.2984 & 4.9100 & 7.0169 & 6.5131 & -5.0348 & -0.6216 & 0.0558 & 0.0126 \\ 0.2907 & 4.6145 & 6.5131 & 6.1232 & -5.2457 & -0.8863 & 0.0061 & 0.0165 \\ -0.3584 & -4.0482 & -5.0348 & -5.2457 & 9.8955 & 3.8493 & 0.4493 & -0.0607 \\ -0.1040 & -0.7179 & -0.6216 & -0.8863 & 3.8493 & 1.9210 & 0.2642 & -0.0289 \\ -0.0083 & -0.0032 & 0.0558 & 0.0061 & 0.4493 & 0.2642 & 0.0538 & -0.0036 \\ 0.0018 & 0.0130 & 0.0126 & 0.0165 & -0.0607 & -0.0289 & -0.0036 & 0.0008 \end{pmatrix} \tag{5.37}$$

Let us now assume that the signals are all perfectly synchronized. In that case, $\phi_i = 0$ and $C_{ij} = \frac{a_i a_j}{2}$. We diagonalize this symmetric matrix: we find an orthogonal matrix O, which is a basis change, and a diagonal matrix D, so that $C = O^{-1}DO$. By recombining the signals $s_i(t)$ according to the coefficients of O, we find that the variance of the last recombination is maximal, while all the other variances are close to 0. In the experimental case presented above, with $\phi_i = 0$, we find:

$$D = 10^{-4} \begin{pmatrix} 0.0003 & 0 & 0 & 0 & 0 & 0 & 0 & 0 \\ 0 & 0.0003 & 0 & 0 & 0 & 0 & 0 & 0 \\ 0 & 0 & 0.0094 & 0 & 0 & 0 & 0 & 0 \\ 0 & 0 & 0 & 0.0121 & 0 & 0 & 0 & 0 \\ 0 & 0 & 0 & 0 & 0.0135 & 0 & 0 & 0 \\ 0 & 0 & 0 & 0 & 0 & 0.0148 & 0 & 0 \\ 0 & 0 & 0 & 0 & 0 & 0 & 0.1002 & 0 \\ 0 & 0 & 0 & 0 & 0 & 0 & 0 & 25.2288 \end{pmatrix} \tag{5.38}$$

The last recombination, with a high variance, corresponds necessarily to the spatial mode of the $7MHz$ modulation. This recombination is our flip mode. The coefficients are:

Pixel 1	Pixel 2	Pixel 3	Pixel 4	Pixel 5	Pixel 6	Pixel 7	Pixel 8
0.0115	0.3197	0.4538	0.4508	-0.5934	-0.3273	-0.1711	-0.0045

consistent with the $[+ + + + - - - -]$ pattern we were expecting. Their different absolute values compensate for the different transfer functions.

As can be seen in Fig. 5.12, the modulations on the different signals are not synchronised: the different transfer functions of the pixels introduce different phases on the signals. We want to correct the effect of these different phases by synchronizing the traces. Since the highest value of D reaches a maximum when the traces are synchronized, we can use D to find this synchronization point. We delay the traces relative to each other, and for each set of delay we compute D. We use an interpolation method to be able to delay traces less than the sampling time.

Fig. 5.13 presents signals after their synchronization and their recombination using O. All the modulation is now carried by a single signal, which corresponds to the flip-mode.

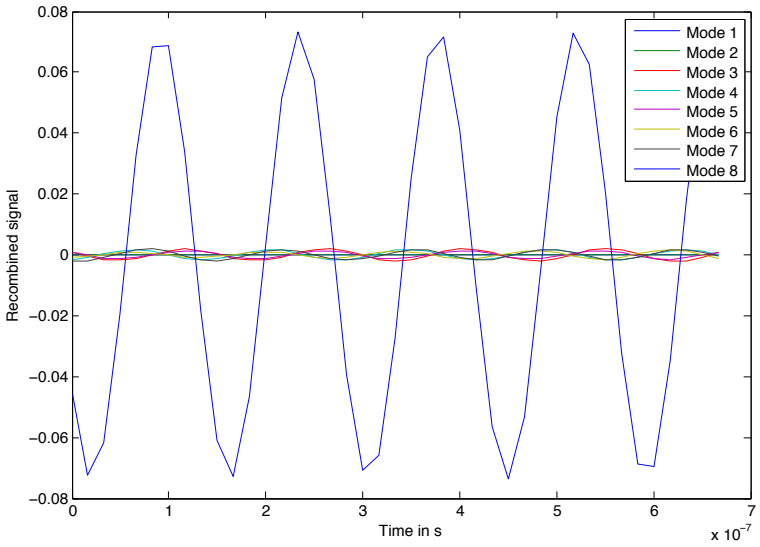

Figure 5.13: Recombined signals. All the modulation is now concentrated in one signal, which correspond to the detection of the flip-mode.

By using the $7MHz$ modulation we find the recombination corresponding to the flip-mode. We then use the $16MHz$ modulation to find, among the recombinations orthogonal to the flip-mode's, the one corresponding to the TEM_{00}. We now filter the signals $s_i(t)$ in the frequency range of interest, between $2.85MHz$ and $3.15MHz$, and we use the two orthogonal sets of gains to derive the signals $s_{flip-mode}(t)$ and $s_{TEM_{00}}(t)$. After an averaging which corresponds to a video bandwidth of $2.4kHz$, the result is presented in Fig. 5.14.

Such a high video bandwidth is necessary because of the speed at which we scan the local oscillator phase: since we want at least a complete turn of the local oscillator phase within our recording time ($16ms$), we need to scan at typically $f_{LO} = 100Hz$. A $2.4kHz$ video bandwidth is a compromise: the higher the bandwidth, the higher the imprecision on our evaluation of the squeezing, while when we lower the bandwidth, we average out the time window when the local oscillator phase is optimal, thus reducing the squeezing value.

We detect $-2.6dB(\pm 0.3dB)$ of squeezing in the flip-mode, and $-3dB(\pm 0.4dB)$ in the TEM_{00} mode.

Direct optimization in specific time intervals

The results presented in Fig. 5.14 are based upon the assumption that the gains computed at $7MHz$ and $16MHz$ are still valid at $3MHz$. Using the trace in Fig. 5.14, we can refine

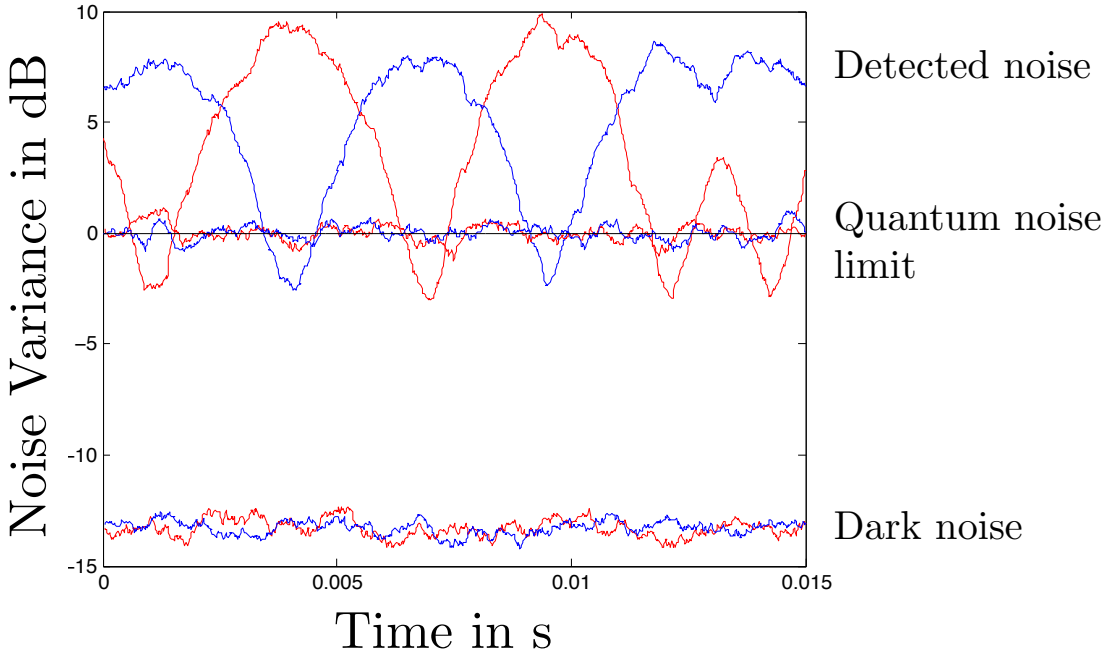

Figure 5.14: Noise variances in dB of $s_{flip-mode}(t)$ (blue) and $s_{TEM_{00}}(t)$ (red) as we scan the local oscillator phase. We consider the variance of the noise in a $300kHz$ frequency band around $3MHz$, and the variances are measured with a video bandwidth of $2.4kHz$. We normalize this variance to the quantum noise limit, the noise detected in the absence of detected beam. We also present the dark noise (DN), the noise originating from the electronics.

our gain combinations to avoid making this assumption. To do so, we select two time windows when there is a clear hierarchy of variances, as presented in Fig. 5.14. In these time windows, we can perform the same covariance computations, and selecting the modes with the highest variance, find simply the optimal recombinations.

On the other hand, correcting for the different phases resulting from the different transfer functions is a more challenging task in this context. Indeed, around $3MHz$ we do not have any strong modulation which would provide a clear synchronization. Instead, we choose to base our optimization on the amount of squeezing we detect. The optimization takes place in several steps: we first choose a delay d_i for each pixel. Then we apply these delays on the traces. Using the delayed traces, we compute the covariance matrices in the two interesting time windows. The highest variance corresponds in one time window to the flip mode, in the other to the TEM_{00}. We record the corresponding recombinations, and apply them to the delayed traces. We then measure the amount of squeezing in the two spatial modes. Our goal is to maximize the amount of squeezing detected: we optimize the delays d_i so as to get the best squeezing values. We find that the best optimization method is sequential: move d_1, find its best position, then move d_2 ... And then start over again at d_1. In the end, when we move the delays away from their optimum values, the squeezing levels should always be reduced. Fig. 5.15 shows the reduction in squeezing

when the delays are taken away from their optimal values.

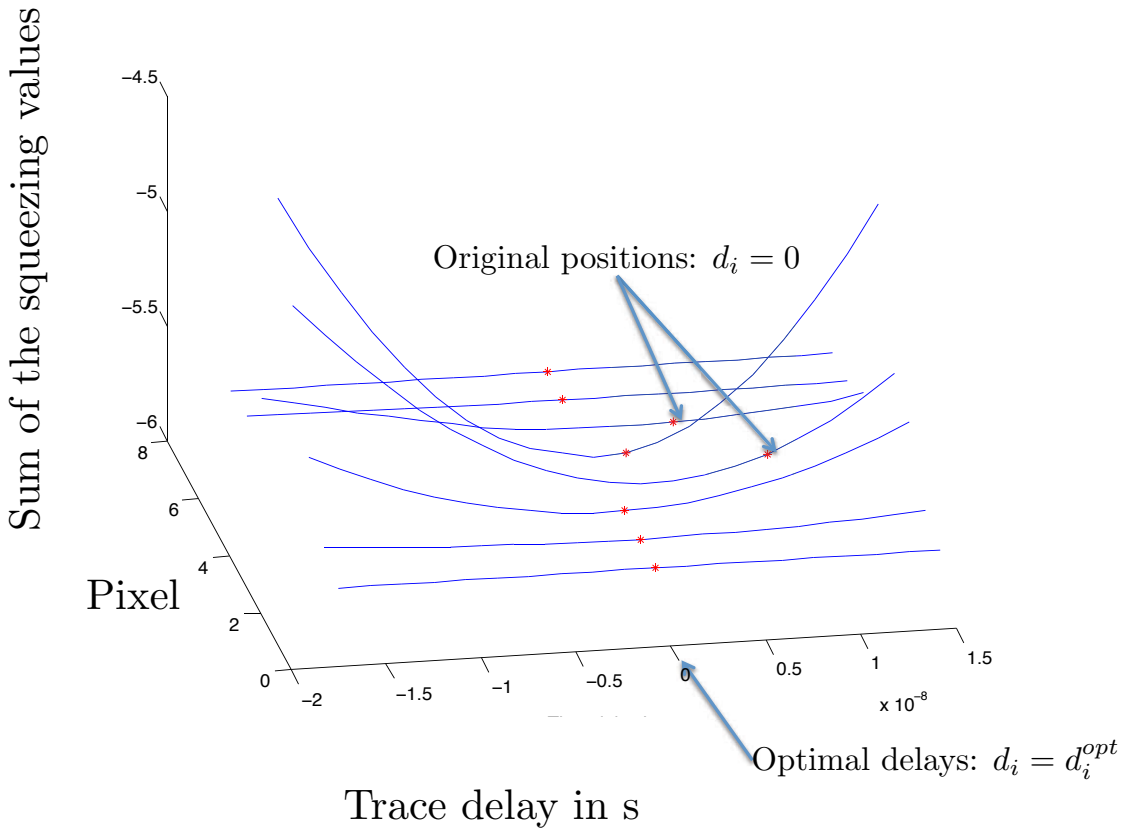

Figure 5.15: Influence of the delays on the squeezing levels. For each pixel, we delay the signal around its optimal position, and measure the squeezing values in $s_{flip-mode}(t)$ and $s_{TEM_{00}}(t)$. This diagram presents the sum of the measured squeezing as a function of the delay. The red dots correspond to the original signals, without the delay optimization. It is clear that uncorrected delays can be very detrimental, but in our case the optimal values are very close to the situation where we do not apply any delay.

In the end, we find $-2.6dB(\pm 0.3dB)$ of squeezing in the flip-mode and $-3.1dB(\pm 0.4dB)$ of squeezing in the TEM_{00} mode (see Fig. 5.16). These results are close to the squeezing levels obtained when using the gains derived with the modulations, but show nonetheless a slight improvement. The dark noise traces, presented both in 5.14 and 5.16, are $13dB$ below the quantum noise. This means that our measured squeezing is not significantly influenced by the detector noise.

Entanglement within an image

The experimental results presented in Fig. 5.16 can also be interpreted as the entanglement between two other spatial modes. Indeed, if we consider the two orthogonal spatial modes "up" and "down" which are the result of the sum and the difference of the TEM_{00} and the flip-mode (respectively), as pictured in Fig. 5.17, the same experimental data

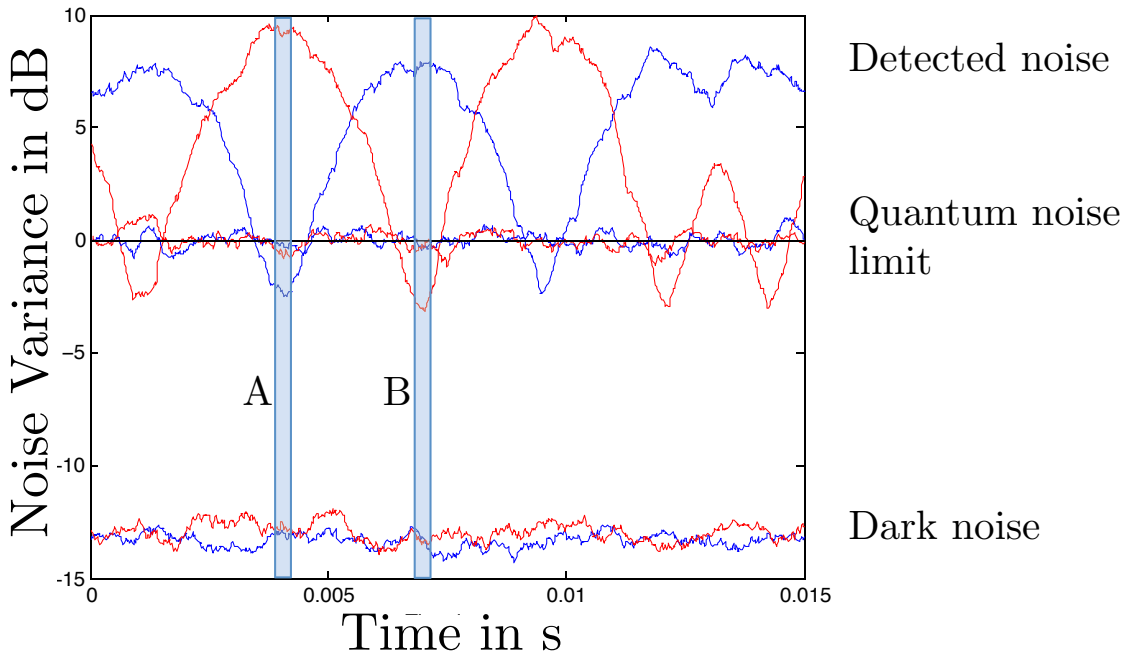

Figure 5.16: Noise variances in dB of $s_{flip-mode}(t)$ (blue) and $s_{TEM_{00}}(t)$ (red) as we scan the local oscillator phase. In this case, the recombinations where optimized by computing the covariances in the time frames A and B, where there is a clear variance hierarchy. This method allows for a direct derivation of the necessary gains, instead of using the modulations frequencies. We also represent the dark noise traces.

proves their entanglement.

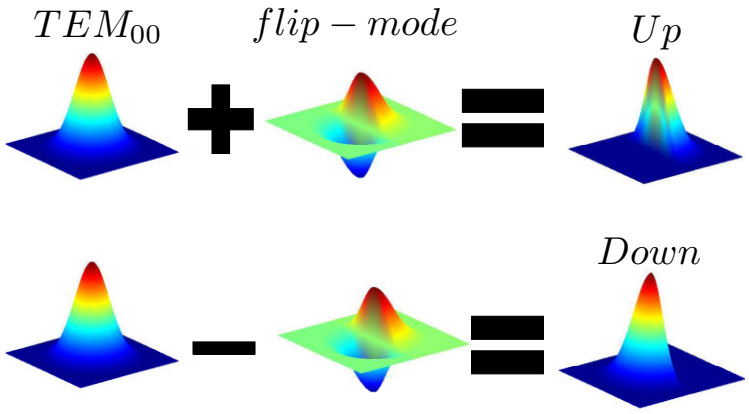

Figure 5.17: Entangled modes "Up" and "Down", linear combinations of the squeezed TEM_{00} and flip-mode.

We have

$$\hat{x}_{up} = \frac{\sqrt{2}}{2}\left(\hat{x}_{TEM_{00}} + \hat{x}_{FM}\right) \tag{5.39}$$

$$\hat{p}_{up} = \frac{\sqrt{2}}{2}\left(\hat{p}_{TEM_{00}} + \hat{p}_{FM}\right) \tag{5.40}$$

and

$$\hat{x}_{down} = \frac{\sqrt{2}}{2}\left(\hat{x}_{TEM_{00}} - \hat{x}_{FM}\right) \tag{5.41}$$

$$\hat{p}_{down} = \frac{\sqrt{2}}{2}\left(\hat{p}_{TEM_{00}} - \hat{p}_{FM}\right) \tag{5.42}$$

We can calculate Duan's inseparability criterion between the two sets of observables $\hat{x}_{up}, \hat{p}_{up}$ and $\hat{x}_{down}, \hat{p}_{down}$. We define two operators $\hat{u}$ and $\hat{v}$ so that :

$$\hat{u} = \frac{1}{\sqrt{2}}(\hat{x}_{up} + \hat{x}_{down}) \tag{5.43}$$

$$\hat{v} = \frac{1}{\sqrt{2}}(\hat{p}_{up} - \hat{p}_{down}) \tag{5.44}$$

We find that $\left\langle \Delta^2 \hat{u} \right\rangle = \left\langle \Delta^2 \hat{x}_{TEM_{00}} \right\rangle$ and $\left\langle \Delta^2 \hat{v} \right\rangle = \left\langle \Delta^2 \hat{p}_{FM} \right\rangle$. From the experimental measurements presented in Fig. 5.16, we know that $\left\langle \Delta^2 \hat{x}_{TEM_{00}} \right\rangle$ is $-3.1dB$ below the quantum noise limit, while $\left\langle \Delta^2 \hat{p}_{FM} \right\rangle$ is $-2.6dB$ below the quantum noise limit. Since the quantum noise limit it 1, in the convention $[\hat{x}, \hat{p}] = 2i$ which we used to write this criterion, we have

$$\left\langle \Delta^2 \hat{u} \right\rangle + \left\langle \Delta^2 \hat{v} \right\rangle = 0.55 + 0.49 < 2 \tag{5.45}$$

The two modes "up" and "down" are inseparable.

Theoretical limitations

This simple experiment shows that is it possible to produce and detect entanglement between transverse spatial modes within a beam. Squeezing more of the beam's transverse modes does not involve any fundamental difficulty. The number of modes simultaneously detected by the multimode homodyne detection is also not fundamentally limited: increasing this number simply requires additional pixels. This set of techniques could be expanded to higher number of modes to perform quantum algorithms. On a technical point of view, it allows a more compact system, and makes the system resistant to air fluctuations.

On the other hand, on a fundamental point of view, the system composed of a succession of optical parametric amplifiers and a multimode homodyne detection is limited. If we want to use this system as a tool for quantum computation, we need to be able to build and detect any state. This system does not allow this universality.

As we have previously discussed in 3.2.1, it is possible to build any Gaussian state using a set of squeezers and general unitary mixing $U_{general} \in U(N_{modes})$ of the modes. With this general description, the phase of the local oscillator is included in the general unitary mixing, and without loss of generality all the modes share the same local oscillator phase.

In our system, the multiple optical parametric amplifiers produce squeezing in orthog-

onal modes. The relative phase of these modes can be set at will. The beam is then detected on the multimode homodyne detection. If we limit ourselves to cases where we cannot change the phase profile of the local oscillator, we can apply the mixing $OU_T D_r$, where $O \in O(N_{pix})$ is the orthogonal matrix of the pixel recombination, chosen at will in $O(N_{pix})$, the group of the orthogonal matrices. $U_T \in U(N_{pix})$ is the basis change matrix between the transverse profiles of the squeezed modes and the pixel modes $v_{m,n}(\vec{\rho})$ as presented in 2.1.3. Without loss of generality, we have set $N_{modes} = N_{pix}$. And finally, D_r is the diagonal matrix of the phase differences we lock the superposition of squeezed modes to. The phases can be chosen at will. The addition of a variable local oscillator phase profile in the multimode homodyne detector expands the mixing to $O\ D_{LO}\ U_T\ D_r$: the phase profile of the local oscillator is equivalent to a spatial phase shift on the beam we want to detect.

If we aim at being able to create any multimode Gaussian state, we need to be able to apply any unitary transform $U_{general} \in U(N_{modes})$ to the original squeezed modes. This cannot be achieved using only the transform $O\ D_{LO}\ U_T\ D_r$. Indeed, a simple consideration of the degrees of freedom available shows that $U_{general}$ cannot be fully covered by $O\ D_{LO}\ U_T\ D_r$. Depending on the spatial profiles of the squeezed modes, which define $U_{transfer}$, specific examples of $U_{general}$ unachievable can be found.

Part III

Manipulation of copropagating modes

We have presented efficients methods to generate and detect copropagating squeezed modes. The detection process is particularly flexible: a simple coefficient change in the data processing allows for the detection of different sets of observables. This allows to measure simply different kinds of entanglements with the same resources. Still, as pointed out previously, gain changes in the data processing does not give access to all the unitary manipulations on the input squeezed modes, manipulations which are a requirement to be able to build any desired entanglement relationship within a set of observables. Therefore, manipulating the spatial modes before detection seems necessary. This next part deals with the challenges of such a manipulation, first from a theoretical point of view, then by focusing more precisely on the experimental device we built, the Unitary Programmable Mode Converter (Morizur 10c).

Chapter 6

Theoretical point of view

Building a specific entanglement within a set of observables carried by spatially separated beams can be achieved using beam-splitters. We have presented this result in 3.2.1. On the other hand, there is no such conventional method in the case of copropagating modes. In this theoretical chapter, we present a new procedure able to provide as much freedom for copropagating modes manipulations as separate beams manipulations. We begin this presentation by framing the problem of modes manipulation: we compare the manipulation of spatially separate beams and copropagating modes. We then use group theory to show that using a succession of specific optical transforms, one has the same freedom of manipulation with copropagating modes as with separate beams (Morizur 10c). Finally, we introduce simulations of an experimental implementation of these optical transforms.

6.1 Comparison between the manipulation of separate beams and copropagating modes

In this first section, we study two similar experiments we built, a first one which involves manipulating separate beams (Wagner 08), and another that uses copropagating beams (Janousek 08a). We underline the similarities and the difficulties arising from trying to manipulate copropagating higher order spatial modes with conventional optical elements.

6.1.1 Unitary manipulations of separate beams

When using separate beams to produce multipartite entanglement, each beam is first independently squeezed using an optical parametric oscillator, see 3.2.1. Straight after the oscillators, the quantum properties of the different beams are all independent: there is no cross-correlation between separate beams. In order to create entanglement, the beams need to be mixed together, with unitary manipulation. We begin by studying the properties of this mixing on an example, and then generalize these properties.

Example: entangling the position and momentum of two laser beams

In order to study the use of higher order modes to carry entanglement, we built an experiment to entangle the TEM_{10} mode of two separate beams (Wagner 08; Hsu 05). In this experiment, the quantum information is carried by a single transverse mode per beam. Often, the transverse mode used to do so would be the TEM_{00}, the fundamental Gaussian mode. In this particular case, a higher order mode was used (TEM_{10}). Nonetheless, the configuration chosen here was one of a single squeezed mode per beam.

Two optical parametric oscillators produce two beams in which the first higher order mode TEM_{10} is amplitude squeezed ($3.8dB$ below the quantum noise limit, in a frequency band from $3MHz$ to $4MHz$). These two beams are then mixed on a 50:50 beamsplitter. This beamsplitter lets 50% of the light power go through, while 50% is reflected. It does not change the spatial distribution of the light: the light in the TEM_{10} mode remains in the TEM_{10} mode after the beamsplitter.

If we name the two beams operators $\hat{a}_{11}$ and $\hat{a}_{21}$ just before the beamsplitter, and the two beams operators $\hat{a}_A$ and $\hat{a}_B$ after the beamsplitter, the 50:50 ratio entails that:

$$\begin{pmatrix} \hat{a}_A \\ \hat{a}_B \end{pmatrix} = \begin{pmatrix} \frac{\sqrt{2}}{2} & \frac{\sqrt{2}}{2} \\ -\frac{\sqrt{2}}{2} & \frac{\sqrt{2}}{2} \end{pmatrix} \begin{pmatrix} \hat{a}_{11} \\ \hat{a}_{21} \end{pmatrix} \tag{6.1}$$

This means that the amplitude quadratures are $\hat{x}_A = \frac{\sqrt{2}}{2}\hat{x}_{11} + \frac{\sqrt{2}}{2}\hat{x}_{21}$ and $\hat{x}_B = \frac{\sqrt{2}}{2}\hat{x}_{11} - \frac{\sqrt{2}}{2}\hat{x}_{21}$. If both the input amplitude quadratures $\hat{x}_{11}$ and $\hat{x}_{21}$ were squeezed $3.8dB$ below the quantum noise limit before the beamsplitter, then so are the amplitudes $\hat{x}_A$ and $\hat{x}_B$: the two beams can still be considered independent, and so are not entangled.

In order to produce two entangled beams, a key parameter is the relative phase between the two modes when they reach the beamsplitter. Indeed, if we consider now that we apply a $\frac{\pi}{2}$ phase delay on the second mode compared to the first one, then we can write:

$$\begin{pmatrix} \hat{a}_A \\ \hat{a}_B \end{pmatrix} = \begin{pmatrix} \frac{\sqrt{2}}{2} & \frac{\sqrt{2}}{2} \\ -\frac{\sqrt{2}}{2} & \frac{\sqrt{2}}{2} \end{pmatrix} \begin{pmatrix} 1 & 0 \\ 0 & i \end{pmatrix} \begin{pmatrix} \hat{a}_{10} \\ \hat{a}_{20} \end{pmatrix} \tag{6.2}$$

Where the operators $\hat{a}_{10}$ and $\hat{a}_{20}$ are the beams operators straight after the optical parametric oscillators, as presented in Fig. 6.1. In this situation, the output amplitude quadratures become $\hat{x}_A = \frac{\sqrt{2}}{2}\hat{x}_{10} + \frac{\sqrt{2}}{2}\hat{p}_{20}$ and $\hat{x}_B = \frac{\sqrt{2}}{2}\hat{x}_{10} - \frac{\sqrt{2}}{2}\hat{p}_{20}$ so that separately their variance is higher than the quantum noise limit, but their sum $\frac{\sqrt{2}}{2}(\hat{x}_A + \hat{x}_B) = \hat{x}_{10}$ has a variance $3.8dB$ below the quantum noise limit. Likewise, the difference of the phase quadratures is $3.8dB$ below the quantum noise limit. This is a signature of entanglement, as we previously developed in 3.2.1.
We can conclude that a proper manipulation of two beams implies both a beamsplitter and a phase control.

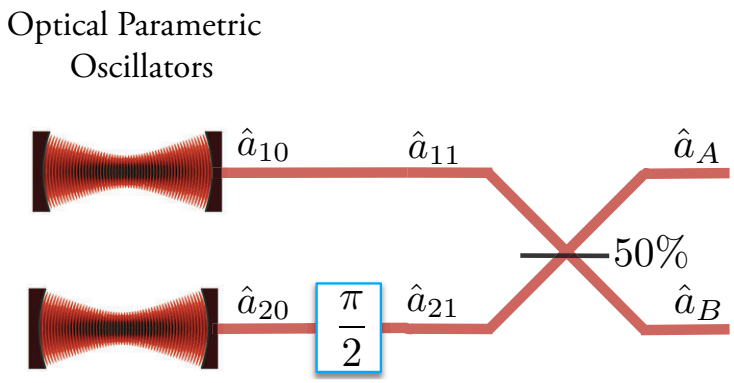

Figure 6.1: Presentation of a simple mixing operation. The relative phase between the beams interfering on the 50 : 50 beamsplitter is set at $\frac{\pi}{2}$

In (Wagner 08) a bright, classical TEM_{00} was superposed to one of the two input beams, as is described in Figure 6.2. Since any lateral displacement or tilt of this bright TEM_{00} corresponds, in the first order, to coupling light into the TEM_{10} amplitude of phase (respectively), measuring the amplitude or phase quadrature of the TEM_{10} mode is equivalent to measuring small displacement and tilts of this bright beam. This idea was previously developed in the quantum enhanced detection section 3.1.1, and is also developed in (Delaubert 06).

This means that entangling the pairs of observables $(\hat{x}_A, \hat{p}_A)$ and $(\hat{x}_B, \hat{p}_B)$ corresponds to entangling the lateral displacement (X) and tilt (θ) of the two output beams A and B. We measured the variance relations between the observables $(\hat{x}_A, \hat{p}_A)$ and $(\hat{x}_B, \hat{p}_B)$ so as to characterize the entanglement, and the results are presented in Figure 6.3.

Duan's inseparability criterion can be reduced for a symmetric system to (Duan 00)

$$I = \left\langle \Delta^2(X_A + X_B) \right\rangle \left\langle \Delta^2(\theta_A - \theta_B) \right\rangle \tag{6.3}$$

We find $I = 0.51 \pm 0.02$ for a frequency band of $300kHz$ centered around $3.3MHz$. This result $(I < 1)$ indicates that the system is indeed inseparable.

As a conclusion, mixing independent, separate squeezed beams on a beamsplitter produces two entangled beams, provided that the relative phase between the two inputs to the beamsplitter is well controlled.

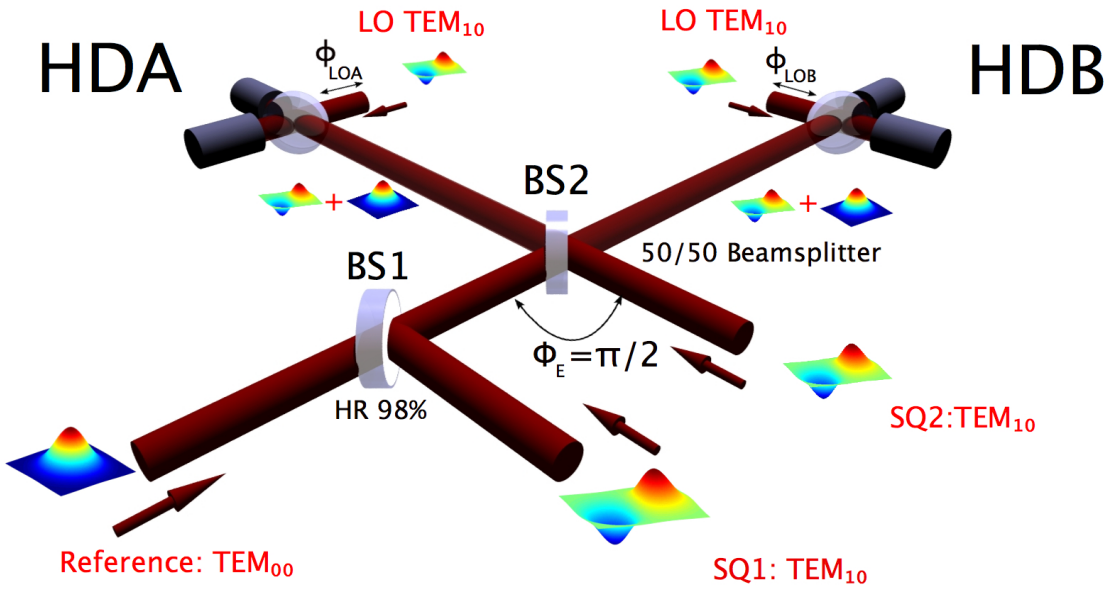

Figure 6.2: Schematic of the experiment. A bright reference TEM_{00} beam is first superposed with a squeezed TEM_{10} mode (SQ1) using beamsplitter BS1 (high reflectivity 98%). It is then entangled with a second squeezed TEM_{10} mode on a 50:50 beamsplitter BS2. A phase control loop ensures that the relative phase between the two TEM_{10} modes is fixed at $\Phi_E = \frac{\pi}{2}$. The two entangled beams are detected separately with two homodyne detectors (HDA and HDB) using local oscillator (LO) beams in the TEM_{10} mode. The local oscillator phase is changed to detect the amplitude of the phase quadrature of the TEM_{10} mode.

Generalization: any unitary manipulation

Using the previous example, let us now derive a more general statement about mixing separate beams. Indeed, when manipulating multiple beams, it is possible to apply a succession of beamsplitters of varying ratios θ_k between the beams. The angle θ is related to the power reflectivity of the beamsplitter mirror by $R = \cos(\theta)^2$. For each beamsplitter, a piezo-electric actuator can control the relative phase ϕ_k between the two interfering beams. This relative phase can be set to any value.

Such a general scheme is represented in 6.4. Let us now introduce a matrix representation of these manipulations to understand what is the set of all such transforms: consider a general description of a N-beam system. We can define a vector of beam operators

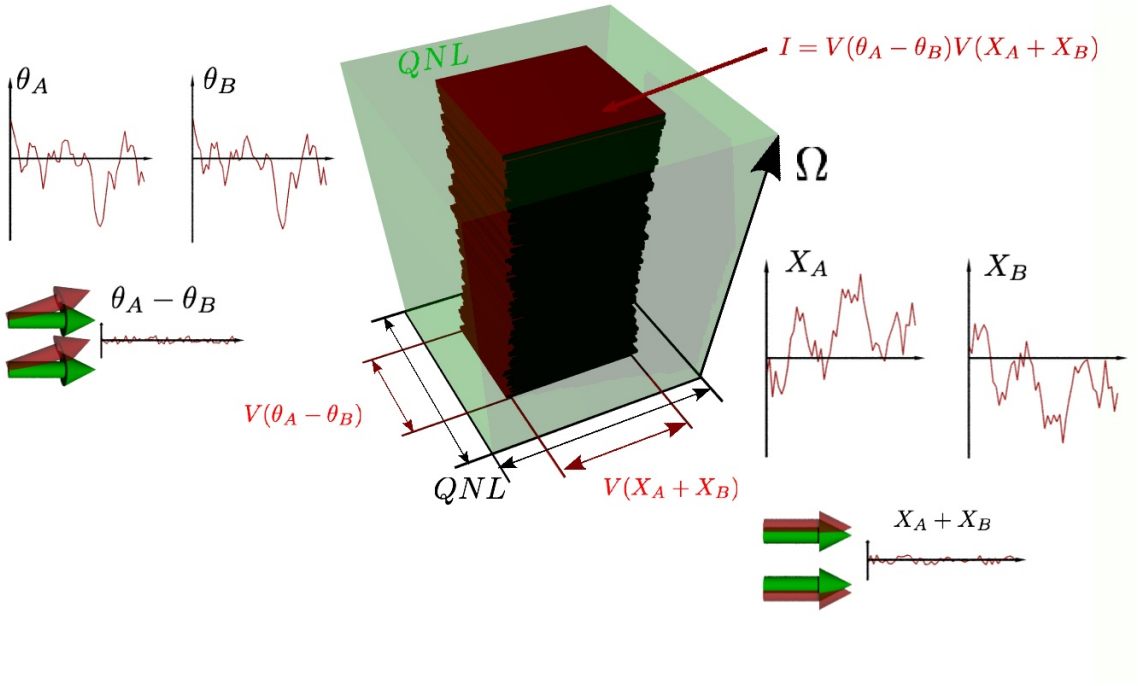

Figure 6.3: Spatial entanglement manifests itself as a strong quantum correlation between the position and direction of two beams, A (blue) and B (red). On the left, this illustration shows the fluctuating directions θ_A and θ_B of the two beams, which are correlated, and on the right, it shows the positions X_A and X_B, which are anti-correlated. For perfectly entangled beams, the differences (θ_A–θ_B) and sum (X_A+X_B) would both be zero. Real entangled beams have a small residual differential movement. The variances $\langle \Delta^2(X_A + X_B) \rangle$ and $\langle \Delta^2(\theta_A – \theta_B) \rangle$ are calibrated against their respective quantum noise limits (QNL), which corresponds to the minimum differential movement of two laser beams with independent quantum noise. A good measure of entanglement is Duan's inseparability, which (for a symmetric system) comes down to the product $I = \langle \Delta^2(X_A + X_B) \rangle \langle \Delta^2(\theta_A – \theta_B) \rangle$. This is shown as the area of the filled rectangles in the center of this figure. Each slice of the tower represents one measurement, and the comparison of the area with the QNL (green box) directly shows the degree of inseparability.

between each beamsplitter:

$$\vec{\hat{a}}_k = \begin{pmatrix} \hat{a}_{1k} \\ \dots \\ \hat{a}_{ik} \\ \dots \\ \hat{a}_{jk} \\ \dots \\ \hat{a}_{Nk} \end{pmatrix} \tag{6.4}$$

Where $\vec{\hat{a}}_k$ is the vector of all the fields operators after beamsplitter k. We study here all the transformations of $\vec{\hat{a}}_0$ achievable using only beamsplitters. A beamsplitter between the beams i and j performs the linear operation $T_{i,j}(\theta)$:

$$\vec{\hat{a}}_{k+1} = T_{i,j}(\theta)\vec{\hat{a}}_k \tag{6.5}$$

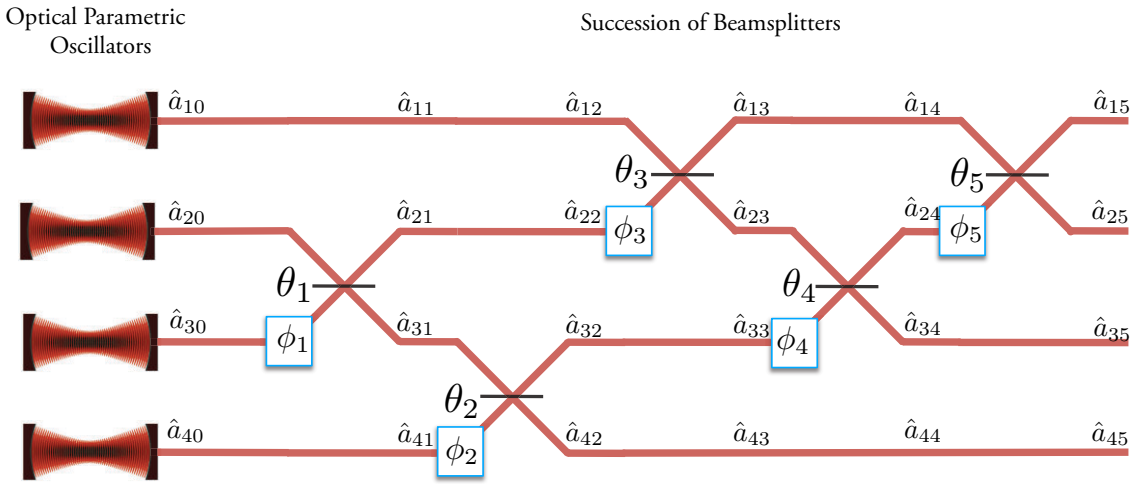

Figure 6.4: Representation of an entanglement production scheme. N separate beams are generated by N independent optical parametric oscillators. Originally there is no cross-correlation between the beams, and the system is fully separable. The set of beams undergoes a mixing process: pairs of beams are superposed on a succession of beamsplitters of varying ratios. The relative phase between the beams is set to a given value for each beamsplitter.

with

$$T_{ij}(\theta) = \begin{pmatrix} 1 & 0 & \dots & 0 & \dots & 0 & \dots & 0 \\ 0 & 1 & \dots & 0 & \dots & 0 & \dots & 0 \\ \dots & \dots & \dots & \dots & \dots & \dots & \dots & \dots \\ 0 & 0 & \dots & \cos(\theta) & \dots & \sin(\theta) & \dots & 0 \\ \dots & \dots & \dots & \dots & 1 & \dots & \dots & \dots \\ 0 & 0 & \dots & -\sin(\theta) & \dots & \cos(\theta) & \dots & 0 \\ \dots & \dots & \dots & \dots & \dots & \dots & \dots & \dots \\ 0 & 0 & \dots & 0 & \dots & 0 & \dots & 0 \\ 0 & 0 & \dots & 0 & \dots & 0 & \dots & 1 \end{pmatrix} \tag{6.6}$$

where the $\sin(\theta)$ are in the i-th line and j-th column. Additionally, a piezo-electric actuator controls the relative phase between the inputs of the beamsplitter. This relative phase control is equivalent to applying the matrix $P_j(\phi)$:

$$P_j(\phi) = \begin{pmatrix} 1 & 0 & \dots & 0 & \dots & \dots \\ 0 & 1 & \dots & 0 & \dots & \dots \\ \dots & \dots & \dots & 0 & \dots & \dots \\ 0 & 0 & 0 & e^{i\phi} & 0 & 0 \\ \dots & \dots & \dots & 0 & 1 & 0 \\ \dots & \dots & \dots & 0 & 0 & 1 \end{pmatrix} \tag{6.7}$$

A well known linear algebra result states that the group of all the $T_{i,j}(\theta)$ and all the $P_j(\phi)$ is the unitary group $\mathbb{U}(N)$. The demonstration of this result can be found in (Serre 02). A succession of beam mixing on beamsplitters with carefully controlled relative phases

performs any unitary combination U of the beams. Such a general recombination or basis change is one of the two necessary elements to be able to build any multimode Gaussian pure state, as we discussed in 3.2.1, the other element being the production of the desired level of squeezing in the input modes.

Moreover, if we restrict ourselves to passive linear elements (no addition of energy), this result can be expanded to encompass all the possible transforms which can be performed on the beams, including losses. Indeed, according to the singular value decomposition theorem, any linear manipulation $M \in \mathbf{M}_N(\mathbb{C})$ can be decomposed in $M = UDV$, where U and V are unitary matrices ($U, V \in \mathbb{U}(N)$), and D is a non-negative diagonal matrix. By definition, U and V belong to the unitary group, and thus can be decomposed as we previously described. Since there is no addition of energy, the coefficients of D are bounded by 0 and 1. A coefficient less than 1 describes losses on the beam considered. We model these losses by the conventional beamsplitters and additional vacuum beams. Formally, we can write:

$$M' = \begin{pmatrix} U & 0 \\ 0 & U \end{pmatrix} \begin{pmatrix} D & \sqrt{1-D^2} \\ -\sqrt{1-D^2} & D \end{pmatrix} \begin{pmatrix} V & 0 \\ 0 & V \end{pmatrix} \tag{6.8}$$

we find that the matrix M' is unitary, and its restriction to the subspace defined by the first N modes is M. Adding the vacuum modes allowed us to describe a general linear optical transformation using unitary transforms. Since these unitary transforms can be decomposed into a sequence of mixing on beamsplitters, we can conclude that such a sequence can perform any passive linear manipulation of the beams.

6.1.2 Copropagating modes

Let us now focus on copropagating modes. Like in the case of separate beams, we begin with an experiment. This experiment exemplifies how copropagating mode manipulation is limited when we restrict ourselves to conventional optical elements.

Example: generating entanglement within a single beam

In order to study copropagating modes manipulation, we built a device capable of generating and detecting entanglement between the two higher order modes TEM_{10} and TEM_{01} of the same beam (Janousek 08a). The symmetries between these two modes play a pivotal role in this device. We will first discuss the experiment itself, and then focus on the difficulties arising from the use of copropagating modes.

An optical parametric oscillator is set in a degenerate setting: using the temperature in the crystal, we make sure that both the TEM_{10} and the TEM_{01}, eigenmodes of the cavity, are resonant for the same cavity length. The oscillator is seeded with a beam in the TEM_{01} mode and locked so that this mode is resonant. When pumped with an intense

green beam, this cavity produces both an amplitude squeezed, relatively bright TEM_{01} and a vacuum squeezed TEM_{10} mode. This cavity and its outputs have already been discussed and presented in 4.3.2.

We then perform the same operations on the two squeezed modes as discussed in the previous pages for the separate beams. First of all, a $\frac{\pi}{2}$ phase shift needs is applied between the two modes. Then, a mixing operation produces two entangled modes. In order to apply a $\frac{\pi}{2}$ phase delay between the copropagating TEM_{10} and TEM_{01}, we use a geometrical property of these two modes. Indeed, when going through a succession of two vertical cylindrical lenses of focal $f = 250mm$ separated by a distance of $\sqrt{2}f$, the Gouy phase of the TEM_{01} remains constant while the lenses impart a $\frac{\pi}{2}$ to the Gouy phase of the TEM_{10} mode (Alekseev 98). For clarity sake, let us call $\hat{a}_{x0}$ and $\hat{a}_{y0}$ the annihilation operators on the modes TEM_{10} and TEM_{01} respectively, straight after the optical parametric oscillator. We name the mode operators after the two cylindrical lenses $\hat{a}_{x1}$ and $\hat{a}_{y1}$ (for the TEM_{10} and TEM_{01} respectively). The two cylindrical lenses transform the input mode operators $\hat{a}_{x0}$ and $\hat{a}_{y0}$ so that:

$$\begin{pmatrix} \hat{a}_{x1} \\ \hat{a}_{y1} \end{pmatrix} = \begin{pmatrix} i & 0 \\ 0 & 1 \end{pmatrix} \begin{pmatrix} \hat{a}_{x0} \\ \hat{a}_{y0} \end{pmatrix} \tag{6.9}$$

Then, in a fashion similar to the separate beams case, we mix these two modes to produce two sets of entangled observables. To perform this mix, we use again the symmetry properties of the spatial profiles TEM_{10} and TEM_{01}. Indeed, a TEM_{10} mode rotated with an angle θ around the propagation axis can be easily expressed in terms of the original TEM_{10} and TEM_{01}: $TEM_{10}^{\theta} = \cos(\theta)TEM_{10} + \sin(\theta)TEM_{01}$. This means that a rotation transforms the mode operators the mode operators $\hat{a}_{x1}$ and $\hat{a}_{y1}$ into the operators $\hat{a}_{x2}$ and $\hat{a}_{y2}$ with:

$$\begin{pmatrix} \hat{a}_{x2} \\ \hat{a}_{y2} \end{pmatrix} = \begin{pmatrix} \cos(\theta) & \sin(\theta) \\ -\sin(\theta) & \cos(\theta) \end{pmatrix} \begin{pmatrix} \hat{a}_{x1} \\ \hat{a}_{y1} \end{pmatrix} \tag{6.10}$$

This very specific relationship occurs only because the two modes considered are the TEM_{10} and the TEM_{01} modes: they have the same order, and they are the only two modes of this order in the basis. Other pairs of higher order modes would behave differently.

The rotation of angle $\theta = 45°$ is performed by rotating the detection basis, as presented in **c** of Fig:6.5. It is equivalent to a rotation of the beam, and easier to implement. We then use a quadrant detector and a bright TEM_{00} local oscillator to build an homodyne detection. The eigenmodes of this homodyne detection are not exactly the entangled TEM_{10} and TEM_{01} because of the discreet nature of the quadrants: with four quadrants, the closest achievable eigenmodes of detection are the horizontal and vertical flip-modes (respectively), which have a 64% detection efficiency, as presented in **b** of Fig:6.5. The quadratures of these flip-modes are detected by performing a different linear combination

of the outputs of the quadrant detector. The phase of the local oscillator is scanned so as to be able to detect in succession both $\hat{x}_{x2}$ and $\hat{x}_{y2}$ and then $\hat{p}_{x2}$ and $\hat{p}_{y2}$. This scheme is summarized in Fig 6.5.

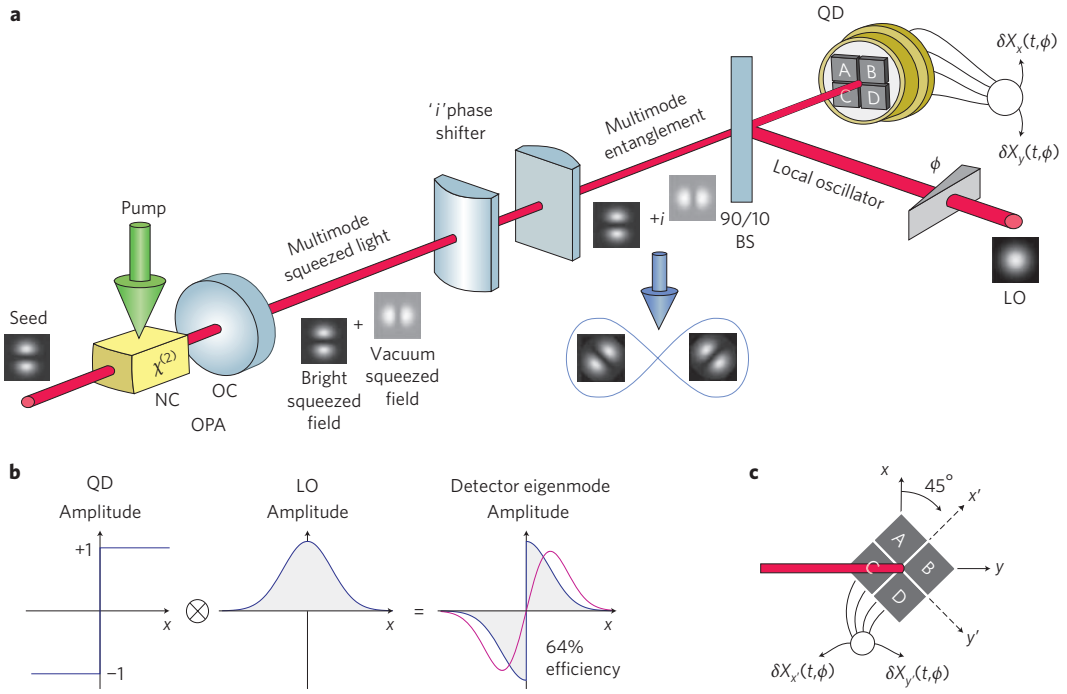

Figure 6.5: Schematic of the experimental setup. **a**, The time trace $\delta X_x(t,\Phi)$ is calculated from the difference $\delta X_x(t,\Phi) = (X_A + X_C - X_B - X_D)(t,\Phi)$ and $\delta X_y(t,\Phi)$ is given by $\delta X_y(t,\Phi) = (X_A + X_B - X_C - X_D)(t,\Phi)$. OPA, optical parametric amplifier; NC, nonlinear crystal; OC, output coupling mirror; BS, beamsplitter; LO, local oscillator; QD, quadrant detector. **b**, Principle of the split-detection technique. The eigenmode of a split-detector is a flipped mode, resulting in 64% detection efficiency in the TEM_{10} basis. **c**, A spatial 50:50 beamsplitter is introduced by carrying out a measurement in a 45° rotated basis.

Let us consider now the time traces given by $\delta X_x(t,\Phi) = (X_A + X_C - X_B - X_D)(t,\Phi)$ and $\delta X_y(t,\Phi) = (X_A + X_B - X_C - X_D)(t,\Phi)$: for a varying local oscillator phase, the variance of these traces changes. We focus on the bandwidth where the squeezing is most intense, a band of width $300kHz$ centered at $3.3MHz$. This allows us to consider the variance of the two time traces (one for each detected mode) as a function of the local oscillator phase. The results are presented in Figure **??**. They present the variances of the time traces for different stages of the experiment.

First, in **a**, we find the variance of the time traces $\langle \Delta^2 \delta X_{x0}(t,\Phi) \rangle$ and $\langle \Delta^2 \delta X_{y0}(t,\Phi) \rangle$, when there are no cylindrical lenses. These correspond to the outputs of the optical parametric oscillator. An important result that can be derived from these variance traces is that the variance is not minimum for the same local oscillator phase Φ depending on the detection considered: there is a $\frac{\pi}{7}$ difference between the minimum of $\langle \Delta^2 \delta X_{x0}(t,\Phi) \rangle$ and

the minimum of $\left\langle \Delta^2 \delta X_{y0}(t,\Phi) \right\rangle$. This means that the two squeezed modes TEM_{10} and TEM_{01} are not squeezed along the same quadrature. Such an effect is probably related to our crystal's properties, but we did not find any way to correct it.
In **b**, the beams have gone through the two cylindrical lenses, and the traces represent $\left\langle \Delta^2 \delta X_{x1}(t,\Phi) \right\rangle$ and $\left\langle \Delta^2 \delta X_{y1}(t,\Phi) \right\rangle$. There is now a $\frac{\pi}{2} + \frac{\pi}{7}$ phase difference between the minimum of $\left\langle \Delta^2 \delta X_{x1}(t,\Phi) \right\rangle$ and $\left\langle \Delta^2 \delta X_{y1}(t,\Phi) \right\rangle$. This tells us that the two cylindrical lenses introduced the expected $\frac{\pi}{2}$ phase shift.
Finally, the traces **c** present the variances of the two modes after the 45° rotation of the detection basis. These variances $\left\langle \Delta^2 \delta X_{x2}(t,\Phi) \right\rangle$ and $\left\langle \Delta^2 \delta X_{y2}(t,\Phi) \right\rangle$, are now both above the quantum noise limit for all the values of the local oscillator phase Φ. This is an expected behaviour, and to check that the two pairs of observables $(\hat{x}_{x2}, \hat{p}_{x2})$ and $(\hat{x}_{y2}, \hat{p}_{y2})$ are truly entangled, we can compute Duan's inseparability criterion:

$$I = \left\langle \Delta^2 \delta X_{x2}(t,0) + \delta X_{y2}(t,0) \right\rangle \left\langle \Delta^2 \delta X_{x2}(t,\frac{\pi}{2}) - \delta X_{y2}(t,\frac{\pi}{2}) \right\rangle \tag{6.11}$$

It is the same reduced criterion as previously introduced in the separate beams cases. In this case, $I = 0.62 \pm 0.04$, and since $I < 1$, the system that consists in the two modes TEM_{10} and TEM_{01} rotated can be deemed inseparable.

As a conclusion, it is possible to generate entanglement between modes within the same beam. To do so, we must be able to manipulate the relative phase between these modes, and mix them. For the pair of modes TEM_{10} and TEM_{01}, such manipulations can be engineered using ad-hoc solutions, a rotation along the propagation axis to perform the mixing, and cylindrical lenses to introduce a relative phase. Still, even in this particularly simple case, we were not able to correct a phase difference which appeared because of the optical parametric oscillator. To that extend, ad-hoc solutions are limited. Furthermore, for more complicated mode combinations, there is no general way to use Gaussian optical elements to perform the desired mixing and phase shifting of the modes.

General copropagating modes manipulations

In the case of separate beams, we found that a succession of beam mixing on beamsplitters with carefully controlled relative phases can perform any unitary manipulation U on the input beams. In the case of co-propagating modes, the example just developed illustrates that we can build and detect entanglement within a beam, simple optical elements are not always enough to perform the necessary manipulations. Let us generalize now this statement.

Consider the TEM basis. While the diameter and the radius of curvature of the TEM_{nk} modes can be changed at will using Gaussian optical elements (lenses, curved mirrors, propagation), their orders n and k along the $\vec{x}$ and $\vec{y}$ axis remain the same. This entails, for example, that there cannot be coupling between any odd order mode and even number mode (for parity reason). As a result, Gaussian optical elements cannot allow for the same range of manipulations as a succession of beamsplitters on separate beams.

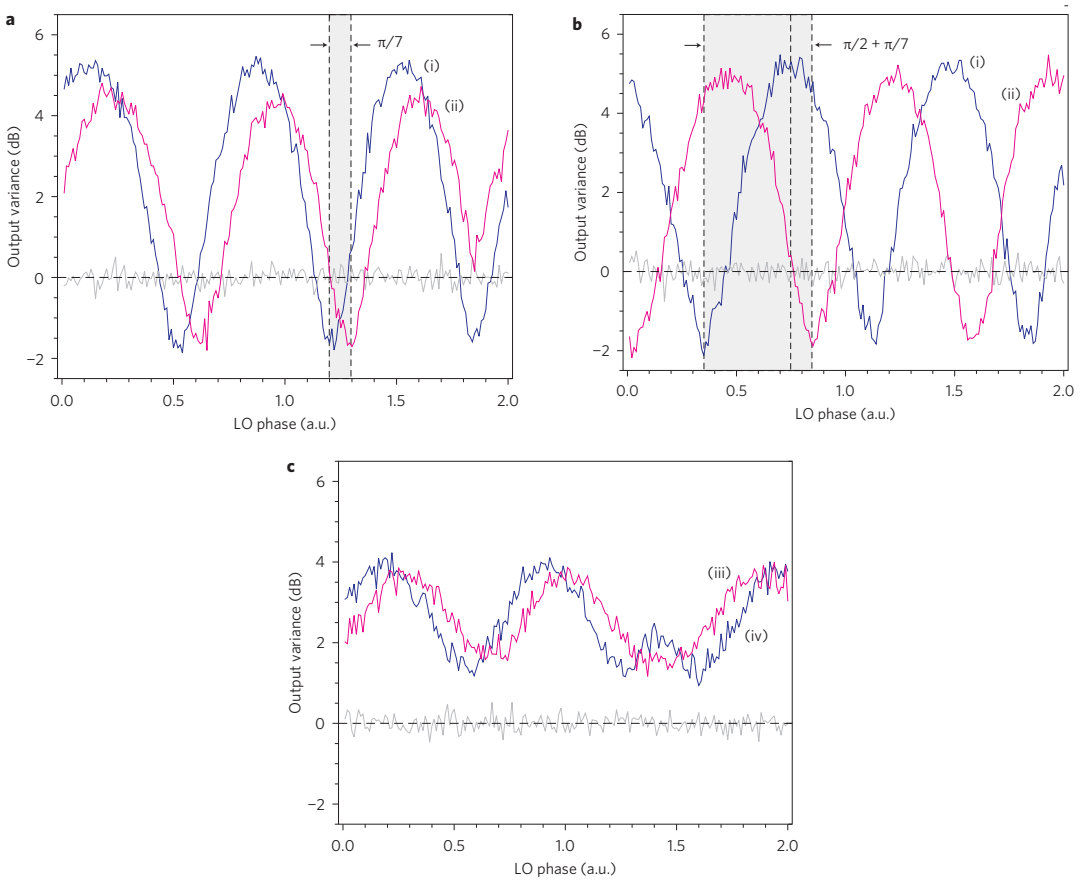

Figure 6.6: Variances of the detected time traces, signature of entanglement within a single beam: **a**, Variance of the outputs of the degenerate optical parametric oscillator, without the cylindrical lenses, measured using the quadrant detector and scanning the local oscillator phase Φ. Trace (i) represents $\langle \Delta^2 \delta X_{x0}(t,\Phi) \rangle$, and trace (ii) $\langle \Delta^2 \delta X_{y0}(t,\Phi) \rangle$. **b**, The same setup as **a**, but with the cylindrical-lens system included: traces (i) and (ii) now represent $\langle \Delta^2 \delta X_{x1}(t,\Phi) \rangle$ and $\langle \Delta^2 \delta X_{y1}(t,\Phi) \rangle$ respectively. **c**, Output variances $\langle \Delta^2 \delta X_{x2}(t,\Phi) \rangle$ (iii) and $\langle \Delta^2 \delta X_{y2}(t,\Phi) \rangle$ (iv) for the 45° rotated fields using a quadrant detector and scanning the local oscillator phase.

If we want to be able to perform any unitary manipulation U on the copropagating modes within a beam, non-Gaussian optical elements are needed. But any attenuation at any stage in the transform destroys the unitary nature of the transform. This discards all the optical elements which would introduce losses in the beam.

A very general non-Gaussian optical element which does not introduce loss is the deformable mirror, or phase only spatial light modulator. In the next section, we describe how using a succession of these elements separated by spatial Fourier transforms can perform any unitary transform on the copropagating transverse modes of a beam.

6.2 Theoretical solution

Conventional optical elements are not sufficient to perform any unitary transform on copropagating transverse modes within a single beam. In this section, we present an optical tool, the unitary programmable mode converter (UPMC), theoretically capable of such a feat. After setting up a theoretical framework, we demonstrate using group theory results that any unitary manipulation can be built using this device.

6.2.1 Theoretical framework: basis and transforms

Before focusing on the mathematical demonstration that the UPMC can perform any manipulation, let us first define the mathematical framework for the optical processes that needs to be considered to well understand this device.

Transverse basis decomposition

As we previously developed in 2.1.1, we limit ourselves to a beam of monochromatic, linearly polarized light of wavelength λ propagating along the $\vec{z}$ axis. The spatial distribution of the beam in the plane $(\vec{x}, \vec{y}, z = 0)$ is the transverse profile, or transverse mode, of the beam: $E(\vec{\rho}, z = 0) = A(\vec{\rho})\, e^{i\phi(\vec{\rho})}$, where $A(\vec{\rho})$ is the magnitude of the transverse profile, while $\phi(\vec{\rho})$ is its phase. As we already discussed in 2.1.3, different transverse mode basis can be used to decompose this profile. For example, in the TEM basis:

$$E(\vec{\rho}) = \sum_{m\in\mathbb{N}, n\in\mathbb{N}} a_{mn} TEM_{mn}(\vec{\rho}) \tag{6.12}$$

The a_{mn} are the complex coefficients of the decomposition of $E(\vec{\rho})$ in the TEM basis, and they are given by

$$a_{mn} = \iint_{x\in\mathbb{R}, y\in\mathbb{R}} TEM_{mn}(\vec{\rho})^* A(\vec{\rho}) e^{i\phi(\vec{\rho})}\, d^2\vec{\rho} \tag{6.13}$$

Any basis of transverse modes provides a decomposition of the field profile.

Any optical system transforms an input field $I(\vec{\rho})$ into an output field $O(\vec{\rho})$. Any linear optical system is fully characterized by its action in a transverse basis: the output of each mode of the basis through the optical system can be decomposed in the same basis, thus providing a matrix description of the transform. For example, the transform defined by

$$U_1 = \begin{pmatrix} \frac{\sqrt{2}}{2} & \frac{\sqrt{2}}{2} & 0 & 0 & \dots \\ -\frac{\sqrt{2}}{2} & \frac{\sqrt{2}}{2} & 0 & 0 & \dots \\ 0 & 0 & 1 & 0 & \dots \\ 0 & 0 & 0 & 1 & \dots \\ \dots & \dots & \dots & \dots & \dots \end{pmatrix} \tag{6.14}$$

in the TEM basis acts as a two mode beamsplitter wherein the spatial modes TEM_{00} and TEM_{10} are mixed together, while all the other modes in TEM_{mn} remain unaffected.

In another basis, this transform would have a different matrix representation. Let us define the transfer matrix P that converts a field decomposition from the basis $\{u_k(\vec{\rho}), k \in \mathbb{N}\}$ to the basis $\{v_l(\vec{\rho}), l \in \mathbb{N}\}$ (we use a single index for the transverse mode basis for simplicity). P is defined as:

$$P_{kl} = \iint_{x\in\mathbb{R},y\in\mathbb{R}} u_k(\vec{\rho})^* v_l(\vec{\rho})\, d^2\vec{\rho} \tag{6.15}$$

If a transform is defined by the matrix U_T in the basis $\{u_k(\vec{\rho}), k \in \mathbb{N}\}$, then it is defined by $P^{-1}U_T P$ in the basis $\{v_l(\vec{\rho}), l \in \mathbb{N}\}$. The matrix representation of the same optical transform changes dramatically depending on the decomposition basis considered.

These results apply to all linear transforms. In the specific case of unitary transforms, they can themselves also be construed as a basis change. They transform an input basis into another basis. Such a description is particularly intuitive when dealing with optical systems: these are often described by the outputs they offer to different inputs, rather than decomposing them on a basis.

A particular set of modes is of heightened interest to us: the pixels, that we presented in 2.1.3. With the assumption that no feature in the fields considered is smaller than the pixel size Δ_{pix}, we can approximate this set of modes to a basis. Let us define $E_{ij} = E(x_i, y_j)$ where x_i and y_j are the $(\vec{\rho})$ coordinates of pixel (i, j) with $i \in \mathbb{Z}$ and $j \in \mathbb{Z}$. When the size of the pixel Δ_{pix} is small compared to the variations of the transverse field $E(\vec{\rho})$ along the $\vec{x}$ and $\vec{y}$ axis, the transverse profile $E(\vec{\rho})$ is adequately described by its discretization E_{ij}. Moreover, since the transverse extension of a physical beam is finite, $E(\vec{\rho})$ is adequately described by E_{ij} with $|i| \leq N_{pix}/2$ and $|j| \leq N_{pix}/2$ for a large enough N_{pix}. The table of E_{ij} can be reorganized row by row into a single vector $\mathbf{E}_k = E_{ij}$ with $k \in A$ ($A = \{1, 2, ..., n = N_{pix}^2\}$).

Optical transform of a deformable surface

With this description of the field profile in the pixel basis $\mathbf{E}_k$, let us now describe the action of a deformable surface on this field profile. A programmable deformable mirror is a surface whose topography $z(\vec{\rho})$ can be defined by the user. When the beam hits the mirror, the continuous field profile $E(\vec{\rho})$ is transformed into

$$E(\vec{\rho}) \to e^{i\phi_{DM}(\vec{\rho})} E(\vec{\rho}) \tag{6.16}$$

with $\phi_{DM}(\vec{\rho}) = 2\pi\frac{z(\vec{\rho})}{\lambda}$. In the pixel basis, the deformable mirror transform becomes $\mathbf{E} \rightarrow U_{DM}(\phi)\,\mathbf{E}$ with

$$U_{DM}(\phi) = \begin{pmatrix} e^{i\phi_1} & 0 & 0 & ... & 0 \\ 0 & e^{i\phi_2} & 0 & ... & 0 \\ 0 & 0 & e^{i\phi_3} & ... & 0 \\ ... & ... & ... & ... & ... \\ 0 & 0 & 0 & ... & e^{i\phi_n} \end{pmatrix} \tag{6.17}$$

For all the phases ϕ chosen, the transforms $U_{DM}(\phi)$ are all unitary. All the pixels change the phase of the incoming field, but its amplitude remain constant. We name such a transform U_{DM} but here is no restriction on the method to apply this phase profile. A phase only spatial light modulator would apply the same transform to the field.

Fourier Transform

Since the amplitude profiles of any incoming field remain constant when hitting a deformable mirror, reflections on deformable mirrors cannot obviously perform all optical transforms. Thus it is necessary to introduce another kind of transform, one that changes the field's amplitudes.
Let us consider more specifically the unitary transform performed by the combination of a lens of focal length f_0 and free-space propagation before and after the lens of a distance f_0. These elements perform a Fourier transform on the spatial profile of the beam, and a rescaling of the profile: for an input beam with transverse size parameter ω_{in}, the typical transverse size of the output is $\omega_{out} = 2\pi\lambda f_0/\omega_{in}$.

Let us name the unitary matrix of this Fourier transform in the pixel basis U_{FT}; $\mathbf{E} \rightarrow U_{FT}\mathbf{E}$. We choose Δ_{pix} small enough and N_{pix} large enough such that a profile of transverse size $\omega_{in} = \Delta_{pix}$ is transformed by the Fourier transform into an output of size $\omega_{out} = N_{pix}\Delta_{pix}$. Typically, this condition is satisfied for $\Delta_{pix}^2 N_{pix} = 2\pi\lambda f_0$. This choice of discretization ensures that U_{FT} is as close as possible to the discrete Fourier transform matrix.
While the matrix representation of the Fourier transform is close to a discreet Fourier transform in the pixel basis, in the TEM basis, in the specific case when the fundamental mode TEM_{00} has the waist $w_0 = \sqrt{2\pi\lambda f_0}$, the Fourier transform is diagonal: $U_{FT,TEMbasis}TEM_{mn} = i^{m+n}TEM_{mn}$.
With this decomposition, it is easy to see that when a Fourier transform is applied twice, the result is a 180° rotation of the beam profile around the propagation axis. This is easily derived from the parity of the different TEM_{mn} modes. Hence, when a Fourier transform is applied four times, it does not change the beam profile at all.

6.2.2 Demonstration: group theory

We have described in the previous paragraphs a few specific unitary transforms that are performed by some optical elements. Using group theory, we demonstrate now that a succession of these specific transforms can build any desired unitary transform.

A specific transform: $T_{ij}(\theta)$

In the pixel basis, the transform defined by the matrix $T_{ij}(\theta)$ performs a beamsplitter operation between the pixels i and j:

$$T_{ij}(\theta) = \begin{pmatrix} 1 & 0 & ... & 0 & ... & 0 & ... & 0 \\ 0 & 1 & ... & 0 & ... & 0 & ... & 0 \\ ... & ... & ... & ... & ... & ... & ... & ... \\ 0 & 0 & ... & \cos(\theta) & ... & \sin(\theta) & ... & 0 \\ ... & ... & ... & ... & 1 & ... & ... & ... \\ 0 & 0 & ... & -\sin(\theta) & ... & \cos(\theta) & ... & 0 \\ ... & ... & ... & ... & ... & ... & ... & ... \\ 0 & 0 & ... & 0 & ... & 0 & ... & 0 \\ 0 & 0 & ... & 0 & ... & 0 & ... & 1 \end{pmatrix} \tag{6.18}$$

For example, the matrix $T_{23}(\pi/3)$ mixes the amplitudes and phase of the field in pixel 2 with the amplitude and phase of the field in pixel 3:

$$T_{23}(\pi/3) = \begin{pmatrix} 1 & 0 & 0 & 0 & ... \\ 0 & \frac{1}{2} & \frac{\sqrt{3}}{2} & 0 & ... \\ 0 & -\frac{\sqrt{3}}{2} & \frac{1}{2} & 0 & ... \\ 0 & 0 & 0 & 1 & ... \\ ... & ... & ... & ... & ... \end{pmatrix} \tag{6.19}$$

This set of transforms is a mathematical building block. We use the group generated by this set as a tool in our demonstration.

Theoretical result

In a pixel basis of size N, the set of all possible U_{DM} forms the subgroup $D\mathbb{U}$ of the unitary group $\mathbb{U}(N)$. Let us name H the subgroup of $\mathbb{U}(N)$ generated by $D\mathbb{U}$ and U_{FT}, the matrix representing the Fourier transform in the pixel basis. We know that H is included in $\mathbb{U}(N)$, we want to show that $H = \mathbb{U}(N)$. Since the pixel basis has been chosen so that U_{FT} resembles a discrete Fourier transform, all the coefficients of U_{FT} are non zero: $\forall i, j\ U_{FT}(ij) \neq 0$. This is of high importance as we want to use U_{FT} as a building block. Indeed, if we can create a matrix M by performing a product of many U_{FT} and diagonal matrices in U_{DM}, then M belongs to the group H.

Let us consider another group, the group formed by $D\mathbb{U}$ and all the matrices $T_{ij}(\theta)$ for all i, j, and θ. It is a well known result from linear algebra (Serre 02) that such a group is actually $\mathbb{U}(N)$. We will show that all the $T_{ij}(\theta)$ can be found in H, which implies that $H = \mathbb{U}(N)$. Let us choose a specific matrix $T_{i_0 j_0}(\theta_0)$. We know that $U_{FT}(i_0 j_0) \neq 0$. Lemma 2 in (Borevich 81) ensures that $T_{i_0 j_0}(\theta_0)$ can be built using U_{FT} and $D\mathbb{U}$. This entails that $T_{i_0 j_0}(\theta_0)$ is in H. No restriction was put on i_0 and j_0, since $U_{FT}(i_0 j_0) \neq 0$ for any pair of indices i_0 and j_0. This means that all the $T_{i_0 j_0}(\theta_0)$ belong to H.

We find that H is a subgroup of $\mathbb{U}(N)$ that contains $D\mathbb{U}$ (by definition) and all the $T_{ij}(\theta)$ (by construction). We know that such a subgroup is $\mathbb{U}(N)$ (Serre 02) so $H = \mathbb{U}(N)$.

This result means that any unitary transform M can be built using a succession of U_{DM} and U_{FT}. Any desired unitary transform has a systematic decomposition in terms of reflections on specific topographies and Fourier transforms. It means that any spatial optical transform that does not introduce loss or amplification of the light can be built. We name such a succession of reflections and optical Fourier transforms a Unitary Programmable Mode Converter (UPMC).

A finite sequence of U_{DM} and U_{FT} sufficient to build any $T_{ij}(\theta)$ is presented in (Borevich 81). When U_{FT} is exactly a discreet Fourier transform, it is possible to show that such a systematic construction requires 17 reflections on deformable mirrors, separated by FTs. Being able to potentially perform any unitary manipulation on spatial transverse modes within a beam makes the co-propagating modes equivalent on that level to sets of separate beams. And while there are technical difficulties to build any unitary manipulation in both cases, both cases have the potential to achieve a general manipulation of the modes.

This result can be generalized to include polarization manipulation by adding a $\lambda/2$ phase plate between each reflection, and using a spatial light modulator that addresses polarization.

6.3 Simulations

Our theoretical study showed that any kind of unitary transform can be performed using a finite succession of reflections on deformable mirrors and Fourier transforms. However, experimentally the number of reflections on deformable mirrors is limited. We need to evaluate the expected performances of a UPMC in such a situation. In this section, after presenting a numerical model of the UPMC, we show its expected performances, both for single mode and multiple modes manipulations.

6.3.1 Modelling a UPMC

The limits of the theoretical construction

The systematic approach to build a unitary transform M using the theoretical results presented above is: decompose M in a finite number of $T_{ij}(\theta)$, then decompose each $T_{ij}(\theta)$ in a finite succession of U_{FT} and U_{DM}. Consequently, for any unitary transform M, we can find a finite sequence of reflections on deformable mirrors separated by Fourier transforms which produces M.

This systematic method can be particularly resource hungry: when the number of pixels N increases (the number of matrices $T_{ij}(\theta)$ required to build a general unitary matrix increases as $O(N_{pix}^4)$ (Ikramov 84)). Moreover, this method is also clearly not optimal for whole ranges of transforms. For example, consider the simple Fourier transform. Decomposing it in $T_{ij}(\theta)$ to then find a succession of U_{FT} and U_{DM} to perform a single U_{FT} does not make sense. And when the transform could be performed with Gaussian optical elements (telescope, microscope), it is better to use Gaussian profiles on the deformable mirrors rather than decompose it in $T_{ij}(\theta)$.

A high number of reflections can be difficult to achieve because of limited resources or complex engineering. Moreover, each reflection or transmission on an optical device is imperfect: they all introduce loss. For these reasons, we need to limit the number of reflections, which means that we need to find an alternative, approximate solution instead of the theoretical construction. In this section, we first introduce a measure of how well the UPMC performs a desired transform. We then use a stochastic algorithm to find the best topography to perform a desired manipulation, with a set number of reflections.

Alternative solutions

Let us consider that the desired unitary transform D is defined by its N orthonormal input modes $I_i(\vec{\rho})$ and their N orthonormal corresponding output field modes $O_i(\vec{\rho})$ (with $i \in K$, $K = \{1, 2, ..., N\}$). For example, when $N = 1$, D is defined on a single mode. In this case we want a specific output $O_1(\vec{\rho})$ for a specific input $I_1(\vec{\rho})$, but the action of D for any other input mode is not important. Or D could be defined on some or all the modes of a transverse basis. In the latter case, the desired transform matrix is then completely specified. Fig. 6.7 provides a diagram of these specifications.

Consider now the actual optical system (the UPMC) that we wish to sue to realize D. Like any other lossless optical system, it is defined by its unitary transform A. For the input modes $I_i(\vec{\rho})$, A has the outputs $O'_i(\vec{\rho})$. When D is defined on a single mode, a conventional measure of how closely A approximates D is the intensity overlap between

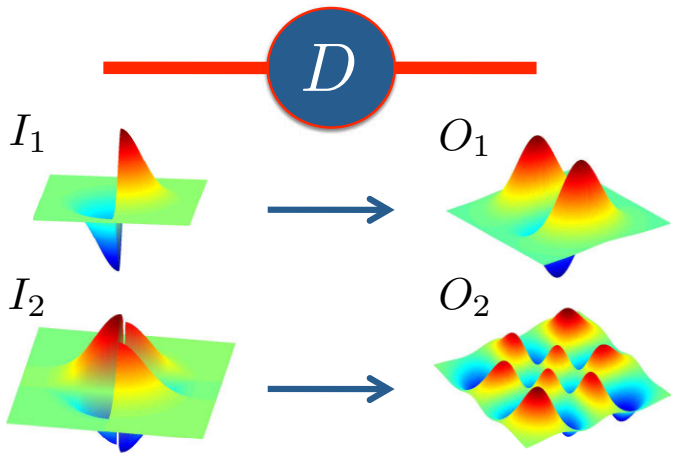

Figure 6.7: Diagram of the definition a a specific transform: a desired transform D is specified by giving a set of orthonormal input modes I_1 and I_2 and their respective output modes O_1 and O_2. The unitary nature of D imposes that O_1 and O_2 are orthonormal.

the mode $O_1(\vec{\rho})$ and the mode $O'_1(\vec{\rho})$:

$$\alpha = \left| \iint_{(\mathbf{x},\mathbf{y})} O_1(\vec{\rho})^* O'_1(\vec{\rho}) \right| \tag{6.20}$$

It is the modulus of the scalar product of these two modes. We generalize this coefficient α to all unitary transforms. It combines all the output overlaps, and is sensitive to the phase between the overlaps:

$$\alpha = \left| \sum_{i \in K} \iint_{(\mathbf{x},\mathbf{y})} O_i(\vec{\rho})^* O'_i(\vec{\rho}) \right| \tag{6.21}$$

If we decompose

$$O_i(\vec{\rho}) = \sum_{m \in \mathbb{N}, n \in \mathbb{N}} o_{i,m,n} TEM_{mn}(\vec{\rho}) \tag{6.22}$$

and

$$O'_i(\vec{\rho}) = \sum_{m \in \mathbb{N}, n \in \mathbb{N}} o'_{i,m,n} TEM_{mn}(\vec{\rho}) \tag{6.23}$$

α can be written as

$$\alpha = \left| \sum_{i \in K} \sum_{m \in \mathbb{N}, n \in \mathbb{N}} o^*_{i,m,n} o'_{i,m,n} \right| \tag{6.24}$$

In this last notation, α is the scalar product between the unitary matrices representing D and A in the TEM basis.

When $N = 1$, α^2 is the mode conversion efficiency: it is the fraction of power effectively transferred from the input mode into the desired output. For multimode transformations, i.e. higher values of N, we introduce the transform quality $\alpha_N^2 = \frac{\alpha^2}{N^2}$, a generalization of the mode conversion efficiency. α_N^2 is normalized to compare transforms with different in-

put mode numbers on the same 0 to 1 scale. When $\alpha_N^2 = 1$, there is no difference between A and D in the subspace defined by the N input modes $I_i(\vec{\rho}), i \in K$. The two optical transforms can still be different; they just differ outside of the considered input modes. α_n^2 was chosen as the measure of the difference between the transforms because it gives the same importance to all the considered modes and coefficients. For a specific purpose, another measure of distance could be more appropriate. For example, when the relative phases between the output modes are irrelevant, the quantity $\beta = \sum_{i \in K} \left| \iint_{(\mathbf{x},\mathbf{y})} \bar{O}_i(\vec{\rho}) O'_i(\vec{\rho}) \right|$ is more appropriate.

For a given desired transform D, finding the optimal achievable transform A within the experimental constraints is an optimization problem. When a large number of reflections on deformable mirrors is possible, we can use the systematic decomposition sequence of D in U_{FT} and $U_{DM}(\phi)$ presented above to perform the transform perfectly. However when the number of reflections is a constraint, there is no algebraic solution (Wyrowski 91). The problem then comes down to the optimization of a finite set of parameters (here the topographies of the deformable mirrors).

We did not find any analytical method to derive an optimal topography for the deformable surfaces. On the other hand stochastic optimization, using α_N^2 as the optimization criterion, performs well at the task of optimizing the topographies for a set number of reflections on deformable surfaces with a defined resolution.

Propagation model

First of all, we choose a model for the UPMC. This model simulates the effect of a succession of Fourier transforms and reflections on deformable surfaces of a light profile. The light profile is represented by a M values vector if we consider only one dimension, of by a $M \times M$ matrix if the full transverse plane is manipulated. The Fourier transform is performed as a normalized and centered Fast Fourier Transform algorithm, either a 1D or a 2D FFT (depending on the light profile representation).

We model the reflection on a deformable surface by a phase change of the light profile, based on the topography of the surface. We rotate the phase of each element of the vector or matrix representing the light. The values for the phase rotations are stored in a M value vector (or a $M \times M$ matrix) and rotating the phases simply corresponds to a product, element by element, of this phase vector (or matrix) with the light profile vector (or matrix). The phase rotations take into account the limited resolution of the deformable surface: we consider a smaller number of actuators, and derive from their positions and the smoothness of the surface the phase rotation values. A schematic of this process is shown in Fig. 6.8.

With this model for the propagation of the field in the system, we compute the outputs

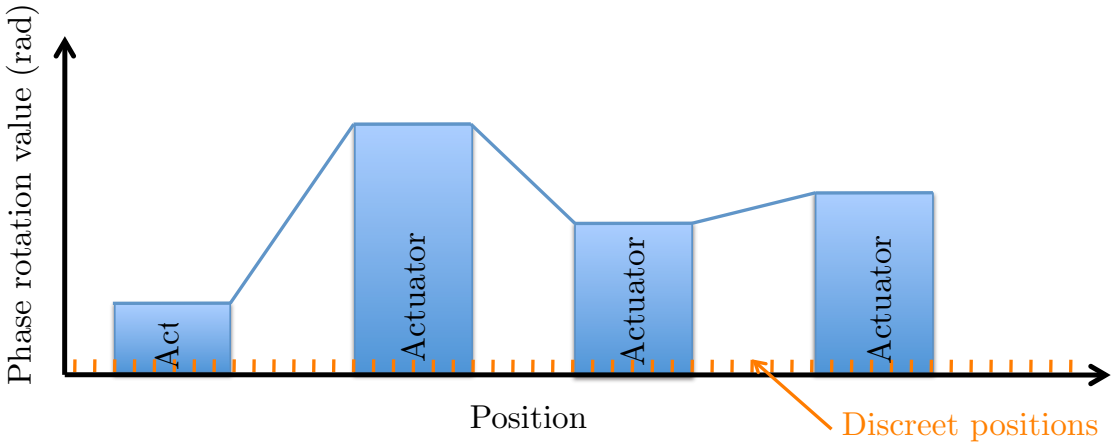

Figure 6.8: Model of the deformable surface. From a small number of actuator positions, taking into account the smoothness of the surface, we can derive the phase rotation values induced by the reflection on the surface for all the light profile elements. The discreet positions in orange represent the computational mesh. We work with a number M of phase elements significantly larger than the number of actuators in order to describe the surface accurately.

$O'_i(\vec{\rho})$ corresponding to the inputs $I_i(\vec{\rho})$. We then compare these outputs to the outputs $O_i(\vec{\rho})$ of the transform we actually want to perform. And we compute the transform quality α_N^2.

The combination of the model and the input $I_i(\vec{\rho})$ and desired outputs $O_i(\vec{\rho})$ allows to build a function that converts a list of L actuator positions (all the actuators positions, for all the different reflections) into a transform quality α_N^2. Let us introduce a few notations. We name the positions of the L actuators p_i $i \in \{1, 2, ..., L\}$, thus forming a vector $\vec{p}$. We name $f_{model,I,O}$ the function that converts these positions into a transform quality:

$$f_{model,I,O} : \vec{p} \rightarrow f_{model,I,O}\,(\vec{p}) = \alpha_N^2 \tag{6.25}$$

$f_{model,I,O}$ has values between 0 and 1, and takes in arguments a vector of L values of actuator positions. Without loss of generality, we can re-normalize the positions so that they are bounded by 0 and 1 too. Thus, we need to optimize this L parameter function.

Simulated Annealing

We use stochastic optimization, and more specifically simulated annealing. Simulated annealing is an optimization method that performs well for optimizing high number of variables. Indeed, a systematic mapping of the space of parameters requires too many evaluations of the function, and we found that direct optimizations based on Newton's method did not reach the global maxima we found with simulated annealing. Simulated annealing is a random walk: from a position $\vec{p}$, we test neighboring positions for higher

valuer of $f_{model,I,O}(\vec{p})$. If any of these neighboring position is better then the original position, we jump there, and continue the process of testing new positions.

In the specific case of simulated annealing, the random walk is controlled by two parameters. A temperature T, and a boundary b. These two parameters evolve during the optimization process, in order to match efficiently the annealing process in metallurgy: the system starts with a very high temperature T, which is then brought down gradually. As such, it is an improved Metropolis-Hastings algorithm: a standard Markov chain is computed for a fixed temperature.

The process of simulated annealing is performed as follows. To begin with, the temperature is chosen high ($T = 1$ is often a good starting point, this value is to be compared to the boundaries of the function $f_{model,I,O}$), and b is chosen big ($b = \sqrt{L}$ is a good starting point, since b is to be compared to the norm of $\vec{p}$). A starting position $\vec{p_0}$ is also chosen, either randomly or at the origin, and we compute the value $s_0 = f_{model,I,O}(\vec{p_0})$. Then, a first sequence of trials is performed with these values of T and b. Each trial consists in choosing a new $\vec{p'}$ so that $\left\|\vec{p'} - \vec{p_0}\right\| \leq b$. Then we compute $s' = f_{model,I,O}(\vec{p'})$. If $s' > s_0$, a jump occurs, and $\vec{p'}$ replaces $\vec{p_0}$ and we start a new trial. If $s' < s_0$ then we compute the value $e^{(s'-s_0)/T}$ which is the jump probability, and we choose a random number between 0 and 1. If this number is smaller than $e^{(s'-s_0)/T}$, then a jump occurs, and we replace $\vec{p_0}$ by the new $\vec{p'}$. This optimization process is synthesized in Figure 6.9.

Such a probabilistic approach to jumps allows for the optimization procedure to get out of a local maximum. Indeed, if the jumps would only occur when $s' > s_0$, once $\vec{p_0}$ is a local maximum, and provided that b is small enough, there is no possibility for the optimization to jump anymore. Introducing probabilistic jumping allows to overcome this difficulty.

This kind of trials (and jumps) is repeated a high number of times, say N_{trials}. N_{trials} is chosen depending on the number of variables, the nature of the problem and the computing resources available. In any case, the higher the better. At the end of the N_{trials}, we count the number of jumps that occurred during these trials, and we reduce T if there was more than $N_{trials}/2$ jumps, or reduce b if there was less than $N_{trials}/2$ jumps. There are many different approaches to reduce T and b. We achieved our best results when using a geometric sequences for T: $T' = T/constant$ and an arithmetic decrease for b: $b' = b - constant$. In any case, it is the fact that b and T remain matched to a number of jumps of $N_{trials}/2$ which ensures a nice simulated annealing procedure. After changing T, b or both, we restart a sequence of N_{trials}, and continue this process until both T and b are below preset limit values.

Adjusting b and T so as to maintain the 1/2 ratio is important: indeed, if b is reduced, the variations of $f_{model,I,O}(\vec{p})$ for all the $\vec{p}$ with $\|\vec{p} - \vec{p_0}\| \leq b$ become smaller. This means that for a smaller value of b, if T does not change, the likelihood to jump for any $\vec{p}$ gets

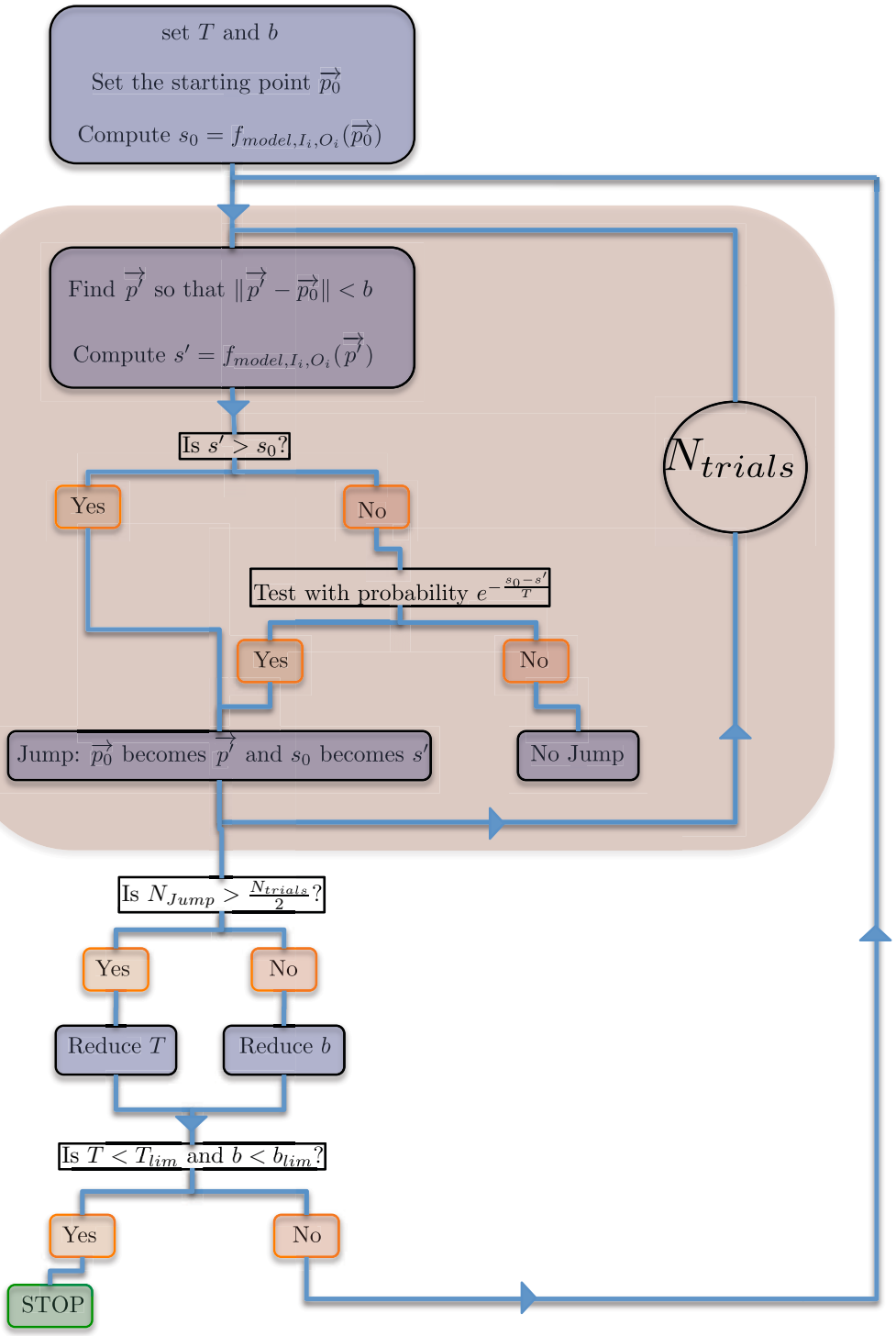

Figure 6.9: Process diagram of the simulated annealing optimization method.

higher, and the probabilistic behaviour of the optimization, introduced so as to get away from local maxima, gets in the way of optimizing at small scales. Maintaining a fixed

ratio in the number of jumps ensures that the behaviour of the optimization at small scales remain balanced. Other ratios can be used, but the 1/2 ratio is put forward in the literature, and we found that it indeed gave us our best results.

This optimization process gave us the best actuator position it could find to perform a desired optical transform with a system defined by a specific number of reflections and number of actuators.

6.3.2 Simulation results

We now focus on a specific implementation of the UPMC: a succession of reflections on deformable surfaces which topography are controlled by a line of twelve actuators each. Indeed, as we will develop further in this thesis, our experimental system has twelve actuators per line. The light profile manipulations performed by this UPMC are limited to a single transverse direction. A schematic of this UPMC model can be found in Fig. 6.10.

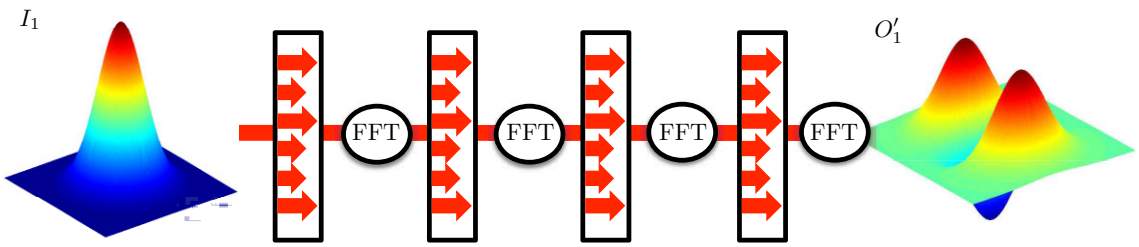

Figure 6.10: Schematic of our UPMC model. The light profile undergoes a succession of reflections on deformable surfaces controlled by 12 actuators. These reflections are separated by Fast Fourier Transforms, which represent an optical Fourier transform. From a given input I_1, we computed the output O'_1 of the system. We optimize the actuator positions to bring O'_1 as close as possible to O_1, the desired output.

Single mode transforms

We first perform a sequence of optimizations to study how well such a UPMC would convert a single mode into another. We are not considering here a complete unitary matrix applied on many modes, but rather the simple problem of turning one mode into another. While this simple problem does not allow for the building or the manipulation of multimode entanglement, it is a first step to check that the concept of substituting a limited number of reflections instead of the theoretical construction sequence is meaningful. Moreover, it has important applications in quantum enhanced detection, as we have shown previously. These computational tests involve typically 10^6 to 10^7 trials each.

Fig. 6.11 presents simulated mode conversion efficiencies for single mode transforms. For these transforms, we only considered the output profile O'_1 of a single input profile I_1.

This profile was compared to a desired profile O_1. The mode conversion efficiency α^2 is the proportion of the output power of the output profile O_1' actually in the desired profile O_1. For all these transforms we considered from one to four reflections on the deformable surfaces, separated by Fourier transforms. We mainly considered transforms between TEM_{mn} modes, with the exception being a flip mode (a TEM_{00} with a π phase shift in the middle).

We find that the efficiency consistently increases with the number of reflections allowed, for all the transforms considered. The results for single reflections match the theoretical maximums (modulus overlap). Comparing the results of d. and e. to c. and a. respectively show that the difference between the shape of the input and the shape of the desired output has a stronger impact on the overlap than the complexity of the profiles themselves.

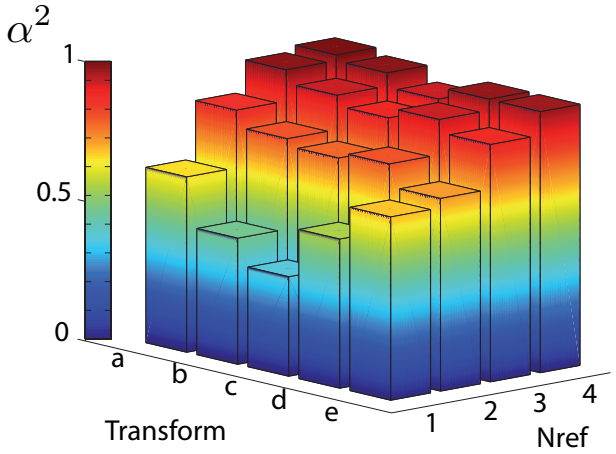

Figure 6.11: Presentation of the mode conversion efficiency α^2 as a function of the transform considered and the number of reflections N_{ref} allowed. The transforms are: a. $TEM_{00} \rightarrow TEM_{10}$; b. $TEM_{00} \rightarrow TEM_{20}$; c. $TEM_{00} \rightarrow TEM_{30}$; d. $TEM_{10} \rightarrow TEM_{30}$ and e. TEM_{10} to flip mode

Fig. 6.12 presents the magnitude and phase evolution in the conversion process: $TEM_{00} \rightarrow TEM_{20}$. This simulation details the spatial process that the light undergoes. On each surface, the intensity profile is not changed, but a phase is printed onto the light field. The propagation of the phase profile is then responsible for the change in the intensity profile of the beam.

These results are encouraging. Not only do they validate the idea of replacing the theoretical construction sequence based on $T_{ij}(\theta)$ with limited number of reflections optimized stochastically, but the results show that the conversion efficiency remains high even for complex modes, and that, as expected, the number of reflections is a determining factor to how close the optimized transforms perform the desired mode conversion.

It should be noted that our design overcomes the boundaries set in (Lüpken 92; Krackhardt 92; Wyrowski 91; Zhou 00) for the conversion efficiency with deformable sur-

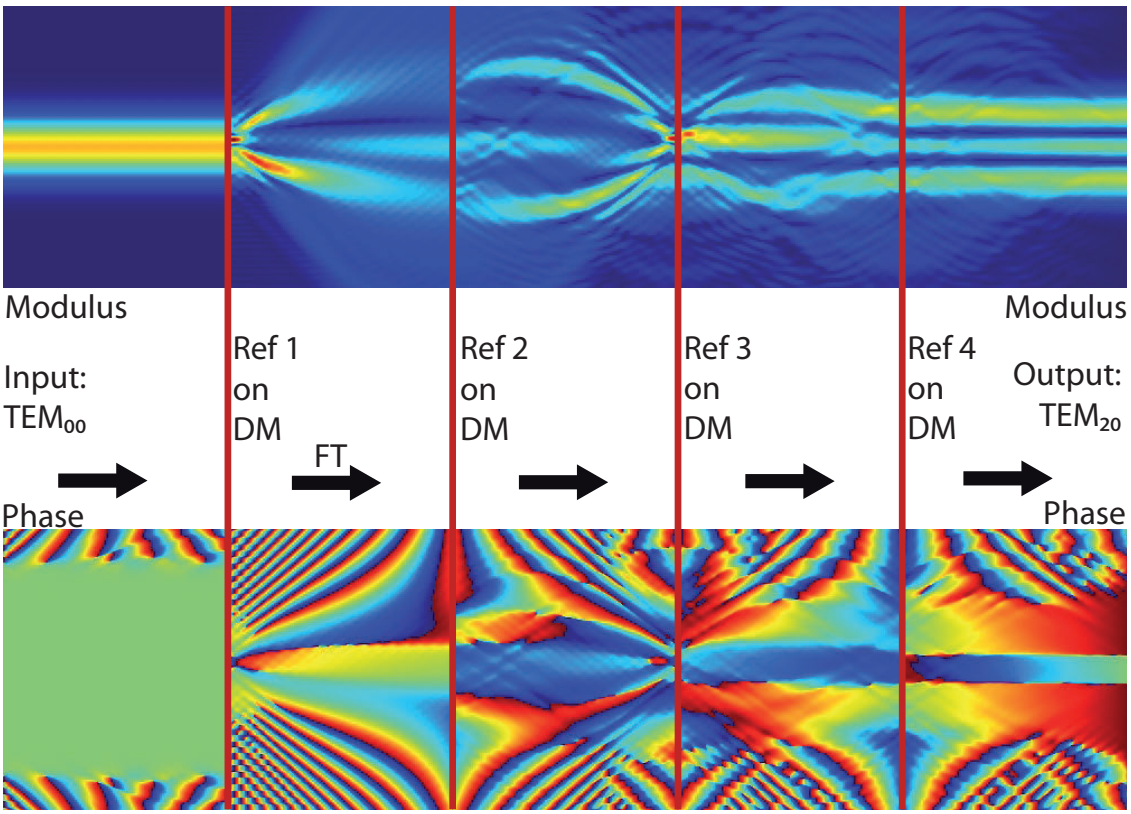

Figure 6.12: Transverse profiles of the magnitude of the field when undergoing a succession of Fourier transforms (FT) and reflections on deformable mirrors (DM). The transverse profile of the magnitude remains constant at the reflection surfaces while the phase has a sharp discontinuity. The transverse axis is re-normalized for all planes to keep the profile of TEM_{00} constant throughout propagation.

faces or phase masks. Indeed, these earlier designs limited themselves to two reflections (one controlling the amplitude, the over one the phase of the output mode), while, as we show in 6.11, it is a higher number of reflections which can allow for a perfect conversion efficiency.

Multiple mode transforms

After simulating single mode transforms, we can now introduce multiple modes. Similarly to the single mode case, we set our optimization procedure so that each optimization requires 10^6 to 10^7 trials. Multimode manipulations can take many forms. We focus here on two families of transforms: phase operators; and beamsplitters. Two mode transforms between the first two TEM modes will be considered - TEM_{00} and TEM_{10}. The beamsplitter transform is the matrix

$$U_{BS}(r) = \begin{pmatrix} r & t \\ t & -r \end{pmatrix} \tag{6.26}$$

with the relationship $t = \sqrt{1-r^2}$. This means that we want to transform the TEM_{00} mode into $rTEM_{00} + tTEM_{10}$ and the TEM_{10} mode into $tTEM_{00} - rTEM_{10}$. $U_{BS}(r)$ is the beamsplitter matrix for a mirror of reflectivity r^2. We chose to consider U_{BS} instead of $T_{12}(\theta)$ because of the sign relation. Both these matrices describe a beamsplitting operation between the modes, but with different sign conventions: when $\theta = 0$, i.e. $r = 1$, $T_{ij}(0)$ is the identity matrix, while $U_{BS}(1)$ carries a minus sign on the second line. This is equivalent to swapping the names of the two outputs of the beamsplitter. We choose to study $U_{BS}(r)$ instead of $T_{ij}(\theta)$ so that all the transforms considered are "difficult": for all the transforms considered, increasing the number of reflections improves the conversion efficiency.

The phase operator is defined by the matrix

$$U_P(\phi) = \begin{pmatrix} 1 & 0 \\ 0 & e^{i\phi} \end{pmatrix} \tag{6.27}$$

and corresponds to introducing a phase shift between the two copropagating modes: the TEM_{00} is left untouched, while the TEM_{10} becomes $e^{i\phi}TEM_{10}$

Fig. 6.13 presents the best transform quality achieved, α_n^2 (here with $n = 2$), when the system is optimized to perform the transforms $U_{BS}(r)$ and $U_P(\phi)$. We present α_n^2 as a function of r and ϕ and the number of reflections allowed. In the single reflection case, we can derive easily the analytical maximum for the transform quality, assuming the topography is fully controllable (i.e. not limited to a twelve actuators control). Comparing the performances of the realistic implementation to the theoretical maxima shows that the limited number of actuators has an impact on the transform quality. On the other hand, when higher number of reflections are allowed, our system outperforms the single reflection theoretical maxima. With increased number of reflections, the efficiency improves for all values of r and ϕ: this validates the multiple reflection scheme as a way to perform unitary transforms.

In a) of Fig. 6.13, the value $r = 0$ corresponds to a swapping of the modes TEM_{00} and TEM_{10}. All the light in the first mode is transferred into the second one, and vice versa. Comparing these results to transform a of Fig. 6.11, which simply considers the transfer of light from the mode TEM_{00} to the TEM_{10} mode shows that while it is obviously simpler to perform a single mode transform, the quality of the two mode transform is similar to the single mode transform quality when we increase the number of reflections.

The high α_n^2 values obtained both for the beamsplitters and the phase operators for 3 and 4 reflections, especially compared to the single mode transforms in Fig. 6.11 tends to show that the limiting factor is the complexity of the modes manipulated, rather than the number of manipulated modes. This means that this realistic UPMC can efficiently manipulate multiple copropagating modes, mixing them or introducing phase shifts between

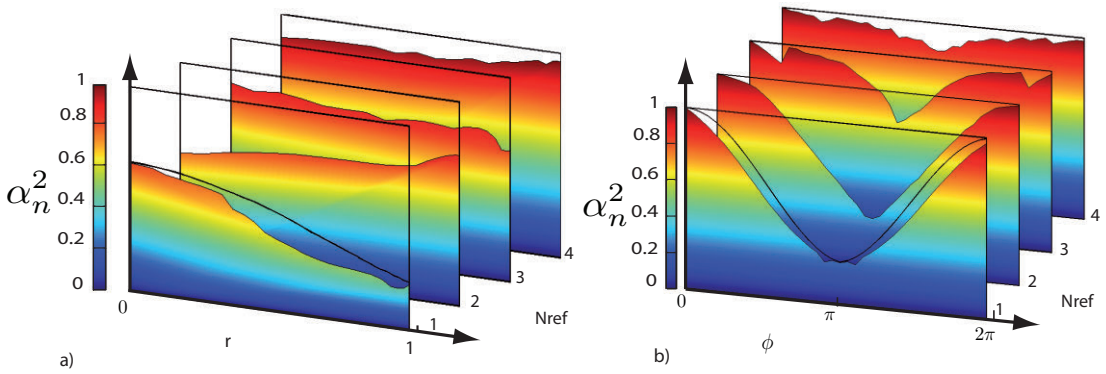

Figure 6.13: Transform quality α_n^2 when the realistic implementation is optimized to perform a beamsplitter U_{BS} (a) and a phase operator U_P (b). They are plotted as a function of their respective parameters r and ϕ and the number of reflections. The black curve represents the single reflection theoretical maximum. The overlap is perfect for $\alpha_n^2 = 1$. Additional simulations with the same number of trials for a constant transform presented similar small fluctuations in the case of three and four reflections. These are artifacts of the optimization process.

them.

As the constraints include more modes, the transform quality gets lower, but the tendency remains: with more reflections allowed, the unitary transform performed by the system approaches the desired one. This statement is in agreement with the theoretical result, and shows empirically that even for a limited number of resources (i.e. reflections and actuators), efficient transforms are possible.

As a conclusion, theoretical results indicate that it is possible to perform any desired unitary optical transform of the spatial modes within a beam, using a sequence of reflections on deformable surfaces, separated by optical Fourier transforms. We found that any unitary optical transform can be constructed in a systematic way, but this systematic decomposition can be highly inefficient. We introduced a model for the propagation of the field through the sequence of reflections and Fourier transforms, and designed an algorithm to optimize the shape of the surfaces so as to make the propagation perform a desired unitary optical transform. These optimizations provide us with simulated efficiencies for a realistic implementation of the sequence of reflections.

Chapter 7

Implementation: building and characterizing a Unitary Programmable Mode Converter

We built a UPMC to validate experimentally its ability to manipulate spatial modes. This device consists in an implementation of a sequence of up to three reflections on deformable surfaces separated by Fourier transforms.
We begin by describing the UPMC itself, its optical components (the deformable mirror, cylindrical and spherical lenses, polarization beamsplitters) and the complete optical set-up procedure. We then focus on classical results: we send in a given input profile, and we optimize the UPMC to output another profile. We compare the efficiency of this process to the efficiencies computed through simulation. Finally, we transform a squeezed input mode into another, and characterize the noise properties of this transform.

7.1 The Unitary Programmable Mode Converter

Our UPMC is based on a succession of three reflections on deformable surfaces separated by an optical Fourier transform. Let us first describe the physical properties of the deformable surface. We will then proceed to explain the optical set-up that performs the Fourier transform and ensures that the beam hits three independent surfaces.

7.1.1 The deformable surface

The deformable surface we use is a Thorlabs Multi-DM. We begin with a precise description of its physical properties, before discussing alternative technologies for spatial phase modulation and the reasons behind our choice. We then describe the way our Multi-DM is driven and the influence of the membrane's elasticity on its shape. Finally, because we limit ourselves to a single Multi-DM, we explain how we can use different parts of the same membrane for different reflections.

Thorlabs Multi-DM

We chose to use a deformable mirror to introduce a spatial phase modulation on the beam. These devices are mainly adaptive optics tools, used in combination with a wavefront sensor for wavefront control and optical aberrations correction. The shape of a deformable mirror is controlled by mechanical actuators. We chose a Thorlabs multi-DM (DM140-35-UM01). This device is a square continuous membrane of $20mm^2$ with a gold coating, controlled by 140 electrostatic actuators (laid out in a 12 by 12 square without the 4 corners). The center-to-center actuator spacing is $400\mu m$, and their maximum displacement is $3.5\mu m$. They are controlled by a 14-bit drive electronics: the smallest step of the actuators is $0.21nm$. The actuators are computer controlled, with a settling time of 10ms.
A picture of the deformable mirror mounted can be found in Figure 7.1.

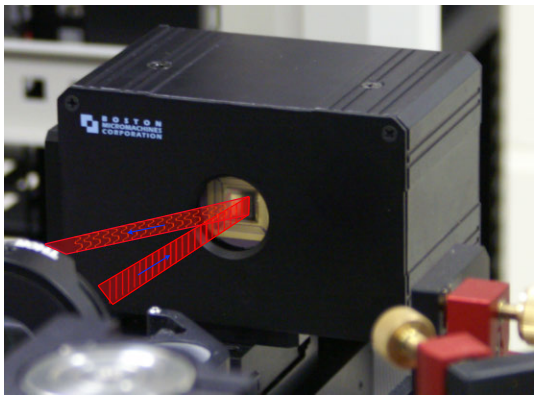

Figure 7.1: Picture and 3-dimensional representation of the deformable mirror used. The light hits the multi-DM and its spatial phase profile is changed, while its amplitude remains constant

Around the $20mm^2$ of continuous membrane lying on top of the actuators, there is a flat gold surface for another $10mm$. This extra surface ensures that even if the beam is slightly misaligned, the beam is still reflected. A protective window lies on top of the deformable mirror. This window is tilted at an angle of 6° so as to forbid multiple reflections: a Fabry-Perot cavity is not possible. This window has a broadband anti-reflection coating to transmit efficiently in the wavelength range $400nm$ to $1100nm$, see Fig. 7.2. We found that this window can be particularly lossy, especially when the beam hits it at an angle.

Alternative technologies for spatial phase modulation

The Multi-DM performs a spatial phase modulation. Other kind of devices can also apply such a modulation on a beam of light (Shirai 02; Bagnoud 04; Potsaid 08; Roorda 02).
There are two main methods to introduce a spatial phase shift in a beam. The first method is the one chosen by the Multi-DM, and involves a deformable surface. While in our case we chose a smooth, continuous surface, it is possible to find segmented surfaces, see Figure

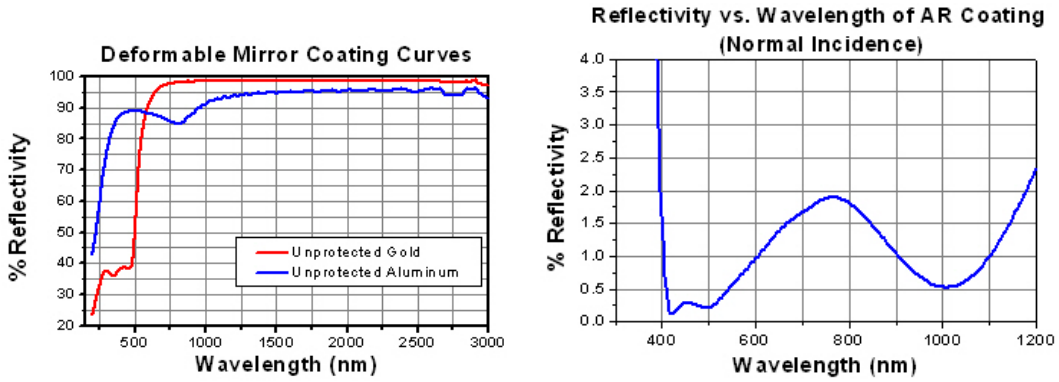

Figure 7.2: Reflectivity of the gold surface and of the protective window as a function of the wavelength. Source: Thorlabs corporation

7.3. Segmented surfaces suppress the inter-actuator coupling, making possible very sharp phase differences between adjoining pixels. The issue with such a surface is that between the actuators, a small gap exists. This gap does not reflect the light, and this reduces the proportion of the surface that reflects the light. This proportion is called fill factor, and while the fill factor for our Multi-DM is above 0.99, the fill factor for the equivalent device with a segmented surface is 0.95 (Boston Micromachine DM140 segmented).

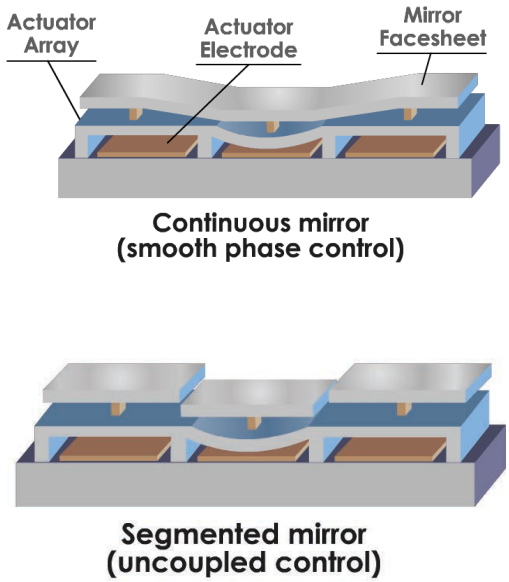

Figure 7.3: Schematic of different kind of deformable mirror surfaces. On the top, a continuous surface, such as our chosen Multi-DM. On the bottom, a segmented surface. Source: Boston Micromachine corporation

Another method to perform light modulation is to use a liquid crystal on silicon spatial light modulators (LCOS SLM). In this technology, a layer of parallel-aligned nematic liquid crystals performs the spatial phase modulation. Applying a voltage between a front and a back electrode change the alignment of the crystals, which in turn change the phase

of the reflected field. A schematic can be found in Figure 7.4.

Using liquid crystals allows these device to have resolutions comparable to computer screens. We tested a Hamamatsu model (X10468) with a resolution of 800 by 600 pixels. In spite of these high resolutions, we found we could not use these devices. Indeed, the alignment of the crystals is set by pulses, and after each pulses the liquid crystals relax and loose their alignment. We found that our model exhibited a strong spatial phase modulation at $300Hz$, which corresponds to the refreshing rate of the device. Such a modulation changes continuously the phase of the output field. Even if the average phase is correct, such a modulation would require extensive data post processing to select the right time window during which the phase profile is exactly the one expected. Such a modulation was also documented in (Tay 09).

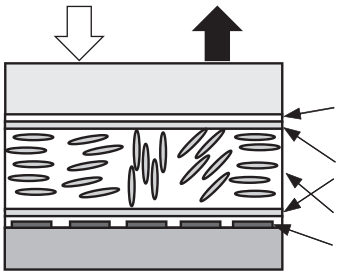

Figure 7.4: Schematic of a liquid crystal on silicon spatial light modulator. Source: Hamamatsu corporation

Lately, LCOS SLM manufacturers (Holoeye, Hamamatsu, Boulder Nonlinear) have come to recognize this relaxation modulation as an issue, and have increased their refreshing rate so as to reduce it. Figure 7.5 presents the improvement, in the case of a LCOS SLM from Boulder Nonlinear. We were not able to use these devices for this work and they show promising performances for future improvements of the UPMC.

Controlling the shape of the membrane

The Multi-Dm deformable mirror is controlled by a driver box. This box translates the digital requests originating from the laboratory computer into 140 analog voltages. These voltages are then carried to the actual deformable mirror using a bundle of independent wires. This design allows for a very stable setting of the actuators: when there is no change in the actuator position, the DC voltages on the wires are kept constant. Moreover, the 140 parallel wires make possible very fast switching between actuators positions: the switching speed is only limited by the inertia of the deformable surface.

When switching from a position of the actuators $\vec{p_1}$ (where $\vec{p}$ represents the vector of

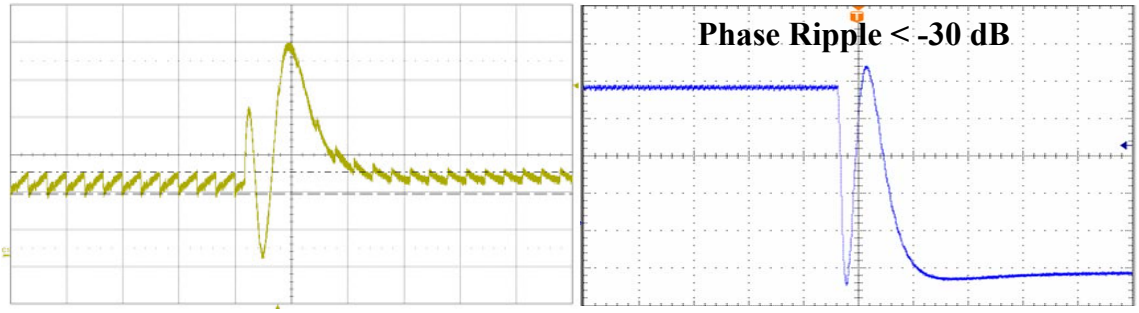

Figure 7.5: Liquid crystal on silicon spatial light modulators addressed at different rates. The left trace shows a strong ripple that is synchronous with the video rate addressing period. The right trace shows the ripple being suppressed by sub-millisecond refresh rates. Source: Boulder Nonlinear Systems corporation

the positions of all the actuators) to a new position $\vec{p_2}$, we found that there was a succession of steps. First of all, the new position is sent to the driver box. Then, we see the first changes in the phase profile. Less than $0.2ms$ later, the phase profile is settled. Finally, the driver box sends back a signal to the computer validating the change. We found that the first stage of this process can take up to $0.2ms$, depending on the state of the computer (we are not using a real time operating system), and that the last stage was generally quite shorter, around $0.1ms$. As a result, we limit ourselves to $1ms$ switching speeds.

We use the Matlab driver of the deformable mirror. This allows us to integrate both the action on the actuator positions and the read-out of the transform quality (which will be detailed further in the thesis) in the same computing environment.

The relationship between the positions of the actuators $\vec{p}$ and the actual membrane shape is difficult to derive. Indeed, each pixel has a different gain, and there is a significant cross-coupling between the actuators. We found that a linear relation between the membrane shape and $\vec{p}$ could not account for the changes in the membrane shape when we changed $\vec{p}$. We detected these changes as modifications of the interference visibility between a reference beam and a beam hitting the deformable mirror. As a result, we developed a second order model to explain these variations. It is presented in Figure 7.6. While we found that this model made possible visibility prediction with an accuracy of 10%, it is still not good enough to derive the right $\vec{p}$ so as to print out a desired spatial phase modulation.

As a result, we found that the control of the deformable mirror required adaptive optics techniques: in such a scheme, $\vec{p}$ is optimized to maximize a given output measurement, and the deformable mirror is considered as a black box.

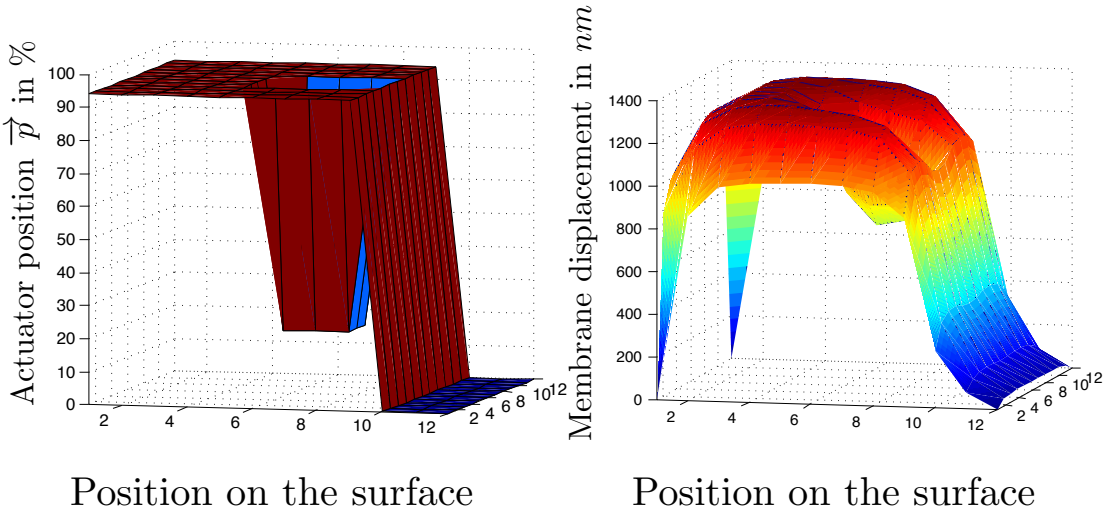

Figure 7.6: Position signals (on the left) and the corresponding simulated displacement of the membrane (on the right). This model for the behavior of the deformable mirror is consistent with interference measurements.

Using the same deformable mirror several times

For this UPMC, we utilize a single deformable mirror. In order to satisfy the requirement of having multiple reflections on deformable surfaces, we choose to designate three separate areas of the deformable mirror, allowing for three successive independent reflections. We choose to use a highly elliptic beam; the topography of the deformable mirror along the vertical axis is controlled by 12 actuators, while the horizontal axis for each reflection remains flat (see Figure 7.7).

We choose this highly elliptic configuration so as to use the full resolution of the deformable mirror at least in one direction. The generalization of the UPMC's performances to the full transverse plane would then require the use of three deformable mirrors.

We choose to perform only three reflections at maximum. This way, the three distinct reflection areas are truly independent, with a minimal cross-coupling. It is likely that the same set-up would be capable of performing four reflections equally well. But when the number of reflections increases, the cross-coupling on the membrane makes finding the optimal actuator position difficult: each change of a position has an influence on several reflections.

7.1.2 Optical set-up

The UPMC is based on a succession of optical Fourier transforms and reflections on a deformable mirror. Let us now discuss the optical requirements of the set-up, and then the alignment procedure we designed to build such a set-up.

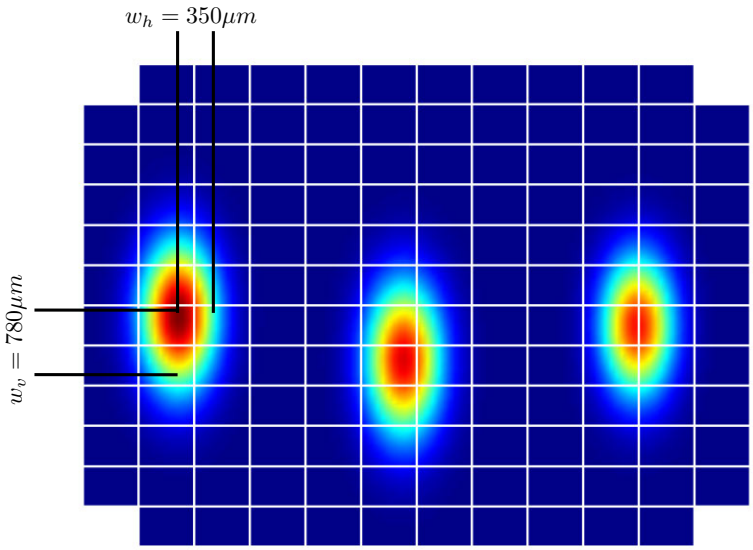

Figure 7.7: Pixel layout and measured positions and sizes of the beam for the three reflections, when the beam is a fundamental Gaussian mode. Manipulations of the beam makes the spatial profile bigger than the simple Gaussian, hence the small footprint of the mode compared to the size of the deformable mirror.

A vertical Fourier transform and a small lateral displacement

Between each reflection on the deformable mirror, the transverse profile of the beam needs to undergo a Fourier transform. Moreover, the choice of using a single deformable surface requires a small and controllable lateral displacement of the beam between each reflection, so as to hit independent surfaces.

Since we limit ourselves to transforms along a single axis, the vertical axis, we choose to only perform a vertical Fourier transform. On the other direction, the horizontal one, there is no need to do any specific transform, except for the small lateral displacement. The deformable mirror sets the typical transverse sizes of the beam at the reflection. We find that, in order to optimize the use of the deformable mirror resolution while limiting the losses on the edges, the transverse vertical size of a TEM_{00} mode should be on the order of $w_v = 0.78mm$. Secondly, we want the transverse horizontal size to be small so as to allow three independent reflections. We choose $w_h = 0.35mm$.

We want to perform a vertical Fourier transform of the profile that hits the deformable surface. Moreover, if an incoming TEM_{00} mode has the typical vertical size $w_v = 0.78mm$, the output of the Fourier transform should be the same TEM_{00} mode, with the same transverse size. In a single lens system, such a constraint would set the focal length of the lens. We found that in this specific case, the focal length would be $3.6m$ which precludes it for practical reasons. A solution consists in using a first lens to perform a Fourier transform, so that the transverse size is reduced. In our case, we chose a lens of focal $f_{SL} = 300mm$. Then, another Fourier transform performed by a lens of focal $f_{CL} = 50mm$ keeps the diameter constant, and finally a third Fourier transform, identical to the first one, restores

the diameter size. In total, the transverse profile undergoes a succession of three Fourier transforms.

We choose to use a cylindrical lens to perform the second Fourier transform. This way, on the horizontal axis, the beam only undergoes a pair of Fourier transforms, which leave it unchanged. Moreover, a small tilt in a reflective mirror in the Fourier plane of the deformable mirror allows for an easy lateral displacement.
A schematic of this design can be found in Figure 7.8.

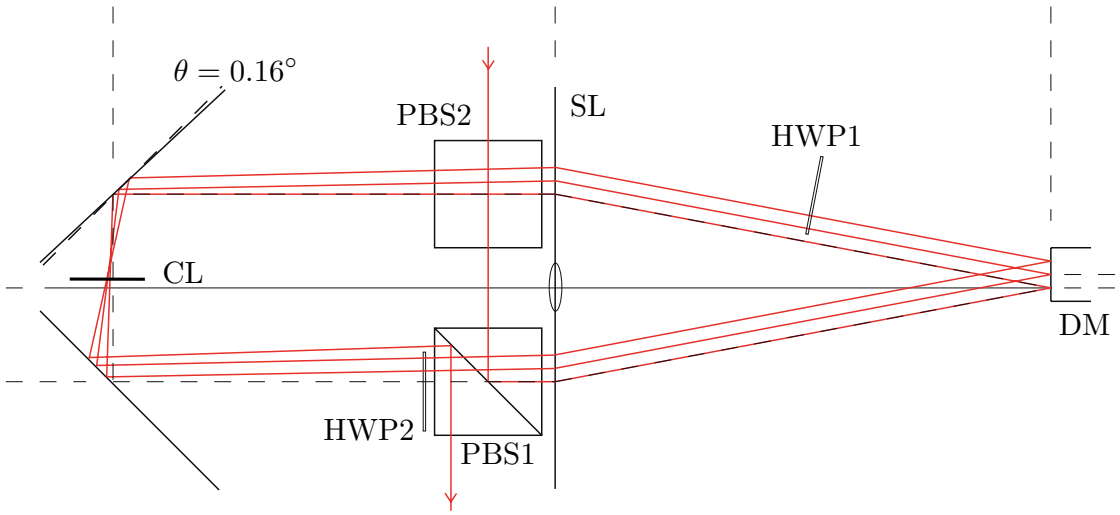

Figure 7.8: The Beam is coupled into the UPMC by a reflection on the polarizing beamsplitter PBS1. It is then focused on to the deformable mirror DM. The beam first undergoes a 2D Fourier transform through the 2" spherical lens SL (focal length $f_{SL} = 300mm$), followed by a vertical FT going through the cylindrical lens CL ($f_{CL} = 50mm$), and finally another 2D FT going back through SL. The optical path length between DM and SL is $300mm$ and between SL and CL $350mm$. The sliding half wave plates HWP1 and HWP2 are used to choose the number of reflections on the DM before being coupled out on PBS1. The angle θ is 0.16° to allow for three reflections on the deformable mirror.

As it can be seen in Figure 7.8, we use polarization beamsplitters and half wave plates to steer the beam. The half wave plates need to be able to distinguish between two adjacent beams. We use micro-metric translations and specially cut mounts so that we can change the polarization of a beam without touching its neighbour.

Alignment procedure

The alignment procedure is made easy by the use of polarization beamsplitters and the fact that the UPMC is designed as a misaligned cavity. To begin with, we build a beam of waist $w_v = 0.78$ using two lenses so that the waist is located on the deformable mirror. Then, we put in place the other components of the UPMC, without the half wave plates, and with a spherical lens of focal f_{CL} instead of the cylindrical lens. We set $\theta = 0$. At

that point, the beam only goes through the UPMC once, and goes out the polarization beamsplitter PBS1. We change the incoming polarization. At the output, we have two beams: one is coming straight through the polarization beamsplitter PBS1, and the other beam is reflected by PBS1. We oscillate the piezo electric actuator attached to one of the mirrors of the UPMC so as to get an interference signal between those beams (using another half wave plate and a polarizer). We can then optimize the interference signal by optimizing the UPMC. When the overlap is 1, i.e. when the two output beams are exactly identical, the UPMC is perfectly aligned.

Then, we put the cylindrical lens in place of its spherical replacement, and we put in cylindrical lenses in the incoming beam so that when the beam hits the deformable mirror, its waist is $w_h = 0.35mm$.
Finally, we need to perform the three reflections. We put in the half wave plate HWP2. This makes sure that the beam hits the deformable mirror twice. We tilt the mirror so that the second reflection is located in the center of the deformable mirror. Then, we introduce HWP1 and we slide HWP2 slightly so that after the third reflection the beam is allowed out of the UPMC.
This alignment procedure, designed to be performed step after step, makes the construction of the UPMC quite straightforward.

7.2 Classical characterization

A first test to characterize the UPMC is to consider classical transforms. In this case, we do not consider fluctuations, and we test whether the UPMC is able to convert the average transverse spatial mode of a beam of light. Basically, we measure how much of the energy of the light beam is transferred by the UPMC from a given mode to another.

7.2.1 Characterization method

We begin by discussing the assessment method chosen to evaluate the performances of the UPMC. We use mode cleaning cavities to produce modes in very well defined shapes, and we evaluate how close the UPMC's output is to the desired mode by measuring the visibility of their interference.

Mode cleaning cavities as references

Assessing how well the UPMC performs a desired single mode unitary transform requires the stable production of both the input mode (to send into the UPMC) and of the desired output mode (in order to measure the strength of its overlap with the output of the UPMC). The mode conversion efficiency, α_1^2, is derived from the intensity overlap measurements. The same measurement could be achieved through an intensity and phase profile detection coupled with a computed scalar product, but without the stability and

the precision provided by direct experimental measurement of the overlap.

We produce stable input and output profiles using mode cleaning cavities operating as Gaussian mode selectors, locked to the desired resonating modes: $I(\vec{\rho}) = TEM_{m0}(\vec{\rho})$ and $O(\vec{\rho}) = TEM_{n0}(\vec{\rho})$. Phase plates are placed before the cavities to couple light from their input modes into the desired mode. The cavity is then locked to this mode.

A detailed schematic of the experiment can be found in Figure 7.9. To begin with, the light coming out of the laser is sent to a first mode cleaning cavity (Mc Leod), locked to the desired input mode $I(\vec{\rho}) = TEM_{m0}(\vec{\rho})$. Then, the output of this cavity is split in two using a half wave plate and a polarization beamsplitter. The vertical polarization is mode matched into a classical mode converter, another mode cleaning cavity (Mc Gonnagal), this time locked to the desired output mode $O(\vec{\rho}) = TEM_{n0}(\vec{\rho})$. This process is highly inefficient. After passing through Mc Gonnagal, this beam, still vertically polarized, is superposed with the horizontally polarized on another polarization beamsplitter. We use a half wave plate to swap the polarizations, so that at that point, the beam carries a mode $I(\vec{\rho})$ vertically polarized and a mode $O(\vec{\rho})$ horizontally polarized. We then use a succession of cylindrical and spherical lenses to mode match this beam into the UPMC.

In the UPMC, thanks to the polarization beamsplitters, only the vertically polarized light undergoes the mode conversion. The horizontally polarized light goes straight through. This means that the mode $I(\vec{\rho})$ is converted into $O'(\vec{\rho})$ while $O(\vec{\rho})$ remains untouched.

Because of the small tilt θ in the UPMC, at the output of the UPMC the vertical polarization is not perfectly aligned with the horizontal polarization, which went straight through the polarization beamsplitter. We use two polarizing Beamsplitters to align and superpose them. We then rotate the polarization by 45° and use a polarizer to interfere the two polarizations: the vertical polarization in the mode $O'(\vec{\rho})$ and the horizontal polarization in the mode $O(\vec{\rho})$.

We use the two polarizations of the beam of light for convenience: this way, the two modes share the same complex mode matching lenses used to prepare the beam for the UPMC, and there is no need to build it twice. Moreover, they make the alignment a step by step process.

Performance evaluation

The powers of the two output polarizations are balanced and a mirror mounted on a piezo electric transducer modulates the overall phase of the classically converted part of the beam, thus providing an interference signal on photodiode 3. We use a data acquisition

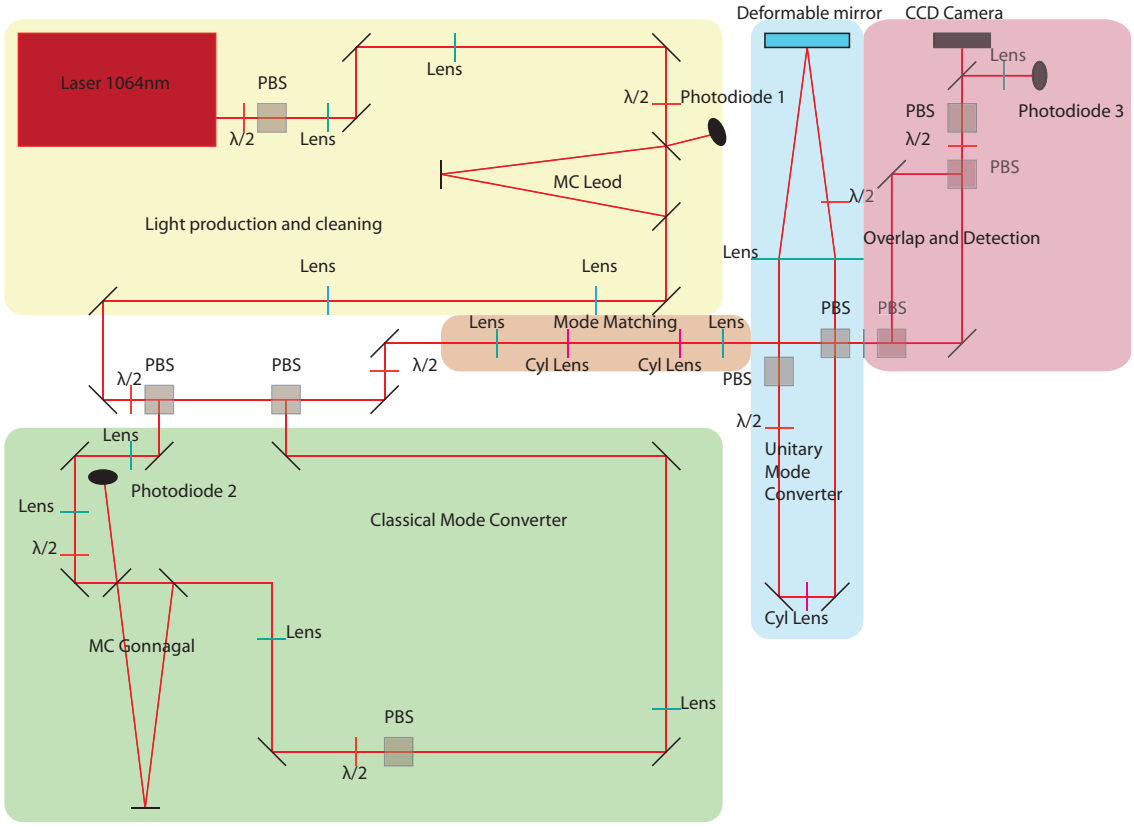

Figure 7.9: Detailed schematic of the experiment. The yellow zone represents the laser light production, the green zone the classical mode converter, the blue zone the UPMC and the red zone the detection stage.

card to record the interference signal and we derive the visibility v of this interference:

$$v = \frac{I_{max} - I_{min}}{I_{max} + I_{min}} \tag{7.1}$$

Where I_{max} and I_{min} are the maximum and minimum (respectively) of the light intensity on the detector. We have then simply $\alpha_1^2 = v^2$. Figure 7.10 presents such an interference signal.

Performance optimization

Since we cannot reliably send directly the right position $\vec{p}$ of the actuators to perform a given transform, we perform an optimization of $\vec{p}$ to maximize the visibility v: we move one actuator at a time, finding its optimal position before moving the next one. The order we move the actuators is random. This process is repeated as fast as is allowed by the settling time of the deformable mirror and the data acquisition process ($100Hz$). It is trivial to show that for a single reflection, such a sequential optimization will find the maximum v possible.

We stop this optimization process when the measured v stops increasing. For a typical three reflections optimization, this occurs after 10^5 overlap measurements. Power fluctu-

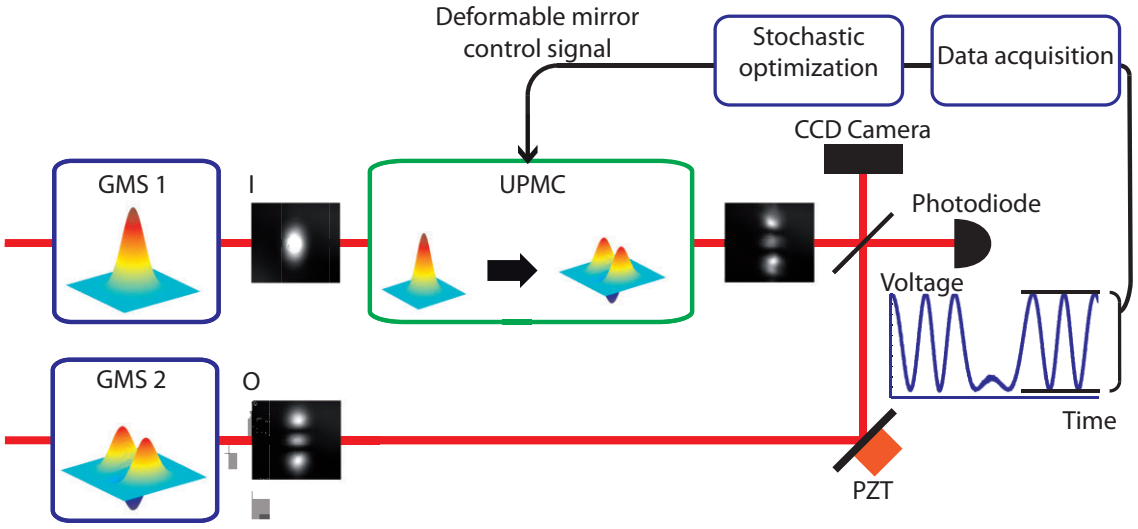

Figure 7.10: Functional schematic of the characterization process. Here $I = TEM_{00}$ and $O = TEM_{20}$. The desired output is phase modulated using the electroactuator PZT and overlapped with the output of the UPMC. The interference signal is then measured on a photodiode, and the intensity overlap is derived. Using the measured overlap, the stochastic optimization algorithm changes the control signal to all the pixels of the deformable mirror.

ations arising from the laser limit our ability to optimize very precisely the position $\vec{p}$, and make it redundant to introduce additional randomness in the optimization process. Repeating the optimization procedure consistently results in the same maximum overlap value, but with different membrane topographies.

The outcome of the optimization is the best v measured. When the best position $p_{\vec{final}}$ is found, we take another 40 interference traces, in a time frame of $4s$. The value recorded as the optimized conversion efficiency is then the square of the average of the visibilities computed on these 40 traces. Figure 7.11 presents a few traces of high visibility taken when $I(\vec{\rho}) = O(\vec{\rho}) = TEM_{00}$, for three reflections in the UPMC. The value measured, 0.994, shows the quality of the set-up alignment.

For repeated optimization procedures of the same transform, with the same number of reflections, the membrane topography was found to differ greatly, while the mode conversion efficiency was consistent. That is the fraction of power in the desired mode remains constant while the remaining power follows a random distribution. This can be explained by the high number of remaining degrees of freedom. When the maximum mode conversion efficiency was low, i.e. for small number of reflections, the shape of the optimized output mode differed from one optimization to another.

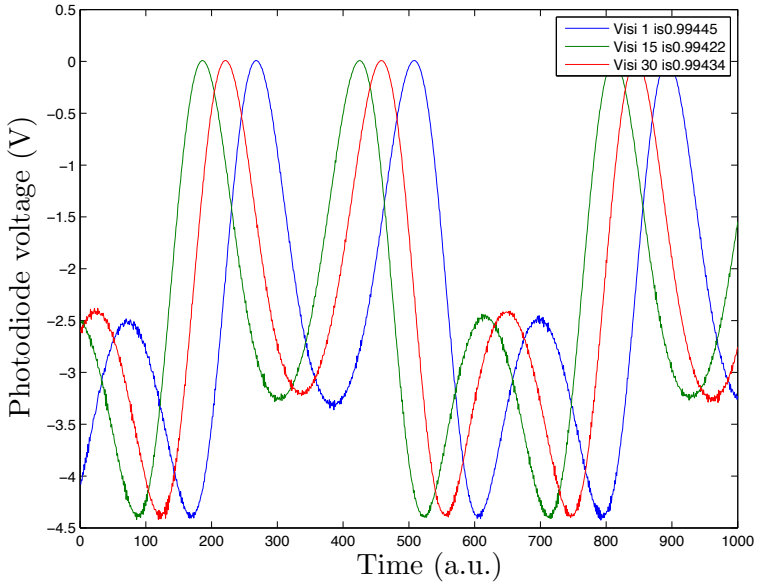

Figure 7.11: Interference signals obtained at the end of the optimization. These were taken for $I(\vec{\rho}) = O(\vec{\rho}) = TEM_{00}$. The three traces are recorded at different times, to test the stability of the measured visibility. For each trace, the electroactuator position move in a sinusoidal way, thus scanning the relative phase between the output of the UPMC and the reference mode. Since we have to modulate for all the optimization time, we choose a sine modulation for the electroactuator to avoid the high accelerations induced by linear scans.

7.2.2 The UPMC's mode conversion performances

We optimize the UPMC for different desired inputs and outputs, and different number of reflections. We find that its performances match the simulated results, and that the size of the deformable surface is the parameter limiting the number of modes it can efficiently manipulate.

Experimental results

For each desired transform, the mode cleaning cavities are locked to the desired input and output modes. Then, we choose the number of reflections the beam is given on the deformable mirror by sliding the half wave plates within the UPMC. Now, with the deformable mirror flat, we balance the powers between the output of the UPMC and the reference beam. We then proceed to optimize the membrane topography.

Fig. 7.12 presents the mode conversion efficiencies obtained after optimization for different transforms and for different numbers of reflections. As can be clearly seen in the figure, for all the transforms considered, the quality of the conversion consistently improves with the number of reflections allowed. This is in agreement with the fundamental idea underlying the UPMC that successive reflections on a deformable surface eventually lead to a perfect unitary transform.

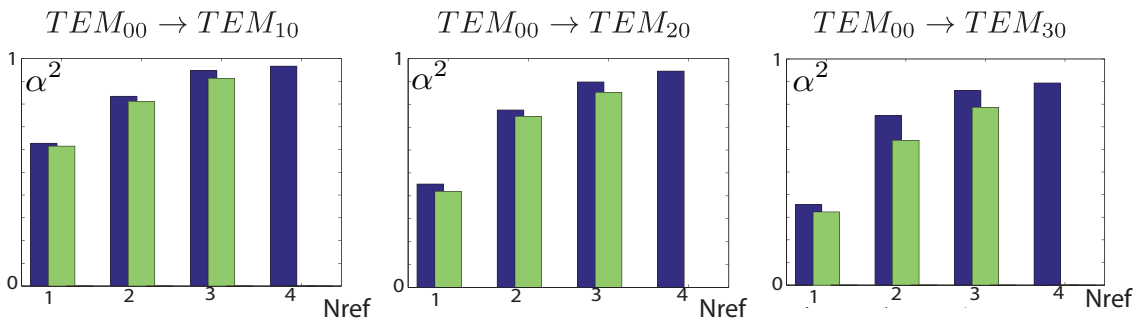

Figure 7.12: Measured mode conversion efficiency, α^2, for three different transformations (light green), compared to simulated results (dark blue). The number of reflections on the UPMC is varied.

In the case of the single mode transform, the value α^2 is the fraction of the power of the output mode effectively in the desired mode. For example, the value α^2 of 0.91 measured for the conversion $TEM_{00} \rightarrow TEM_{10}$ with three reflections on the deformable mirror means that 91% of the power of the UPMC's output is in the desired TEM_{10}. This value only reflects the power loss due to mode mismatch, and does not include the other sources of loss. Reverse transforms were also tested and for the transform $TEM_{10} \rightarrow TEM_{00}$ with 3 reflections the mode conversion efficiency is also 0.91.

Figure 7.13 presents snapshots of the output modes for the conversion $TEM_{00} \rightarrow TEM_{30}$. With an increased number of reflections, the spatial profile of the output visually comes closer to the desired profile.

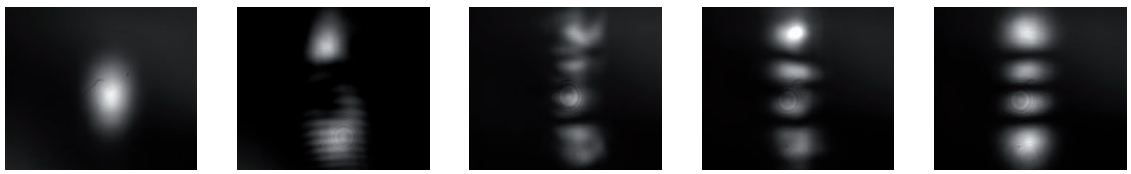

Figure 7.13: Stills from the CCD camera. These capture the shape of the output of the UPMC of a $TEM_{00} \rightarrow TEM_{30}$ conversion, with different numbers of reflections

Fig. 7.12 provides a comparison between the simulated and experimental UPMC. The good agreement between the two methods validates the model as a tool to explore further the capabilities of this experimental set-up. The limitations on the optimization speed of the experimental set-up compared to the computational simulations explain the small systematic difference between the results: a typical experimental optimization time allows for 10^5 trials. Computational tests involve typically 10^6 to 10^7 trials. By simulating the experimental optimization, we found that the 10^2 ratio explains the systematic difference.

Size matters

After the optimization is finished we run a set of local derivatives measurements: we modulate each actuator around its optimal position $\vec{p_{final}}$, and record the amplitude of the resulting variation of the visibility. The actuators with the biggest influence on the visibility are the ones where the light is most intense. Figure 7.14 presents the results of these measurements. They are accurate measures of where the light hits the deformable mirror. Moreover, the distribution of the light for the last reflection corresponds to the output spatial mode. In Figure 7.14, for three reflections, one can clearly see the three lobes of the TEM_{20} output mode.

The mode conversion efficiency for the transform $TEM_{00} \rightarrow TEM_{50}$, for three reflections in the UPMC, is $\alpha_1^2 = 0.60 \pm 0.01$; the quality of this transform is limited by the size of the beam on the deformable mirror. The optical set-up was chosen so that the energy of a TEM_{00} is spread over five actuators (see Figure 7.7), therefore a significant portion of the third reflection in the $TEM_{00} \rightarrow TEM_{50}$ transform (that tends to be the size of a TEM_{50}) hits the deformable mirror outside of the controllable membrane, as can be seen in Figure 7.15. This underlines the geometrical limit of this specific UPMC; it can only efficiently handle modes from TEM_{00} to TEM_{40}. Since the spot size of a TEM_{n0} mode scales as $\sqrt{n+1}$, an increased number of actuators would allow for the manipulation of more modes with the same precision.

As a conclusion, these results showed that the UPMC can perform single mode transform efficiently. Realistically, the capabilities of this UPMC are only limited by the number of reflections allowed and the number of pixels for each reflection. We found that three reflections on an array of 12 pixels are enough to perform single mode transforms with an efficiency better than 80% for the first 4 modes of the TEM basis.

7.3 Quantum performances of the UPMC

After the classical tests of the UPMC, we now proceed to use non-classical states of light, in this case squeezed states, to characterize the UPMC. Being able to manipulate the spatial profiles of co-propagating modes without changing their quantum properties is the key to being able to manipulate co-propagating multimode entanglement.

7.3.1 Spatial manipulations of quantum correlation

Transferring squeezing from one mode to another

Even if a full characterization of the UPMC performances as a multimode entanglement manipulator would require a complete set-up of copropagating squeezed modes and multi-pixel homodyne detection, it is possible to predict its performances considering only single mode manipulations. Indeed, there is nothing fundamentally different between manipulat-

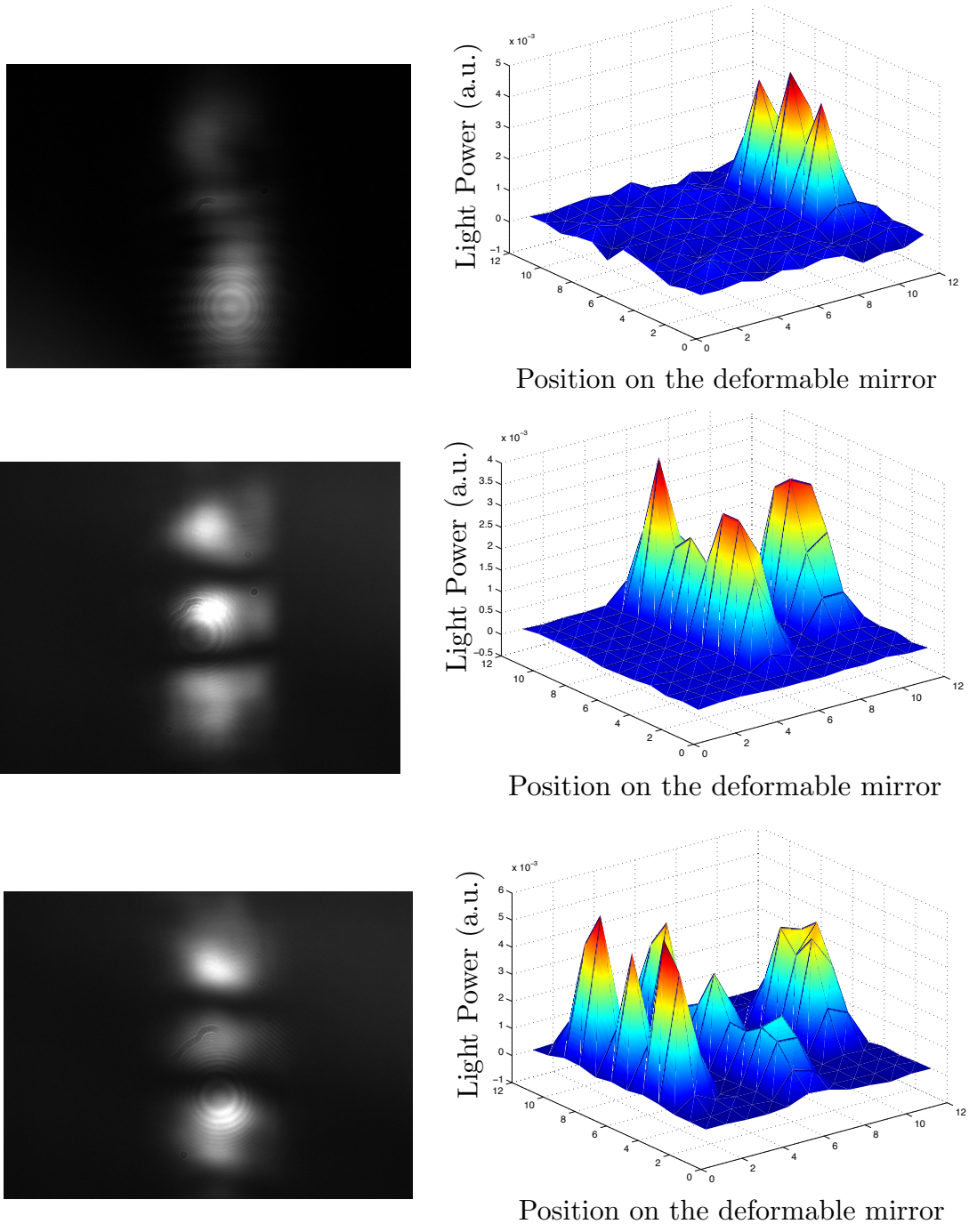

Figure 7.14: Light intensity distribution on the deformable surface on the right, snapshot of the output mode on the left. One reflection at the top, three reflections at the bottom. In the energy distribution graphs, the successive reflections take place from right to left, consistent with the UPMC's design presented in Figure 7.8

ing a single mode and manipulating several: the device remains the same, the alignment and components identical. We have simulated multimode manipulations with a UPMC, and checked that the model underlying these simulations was accurate by confronting it to classical results.

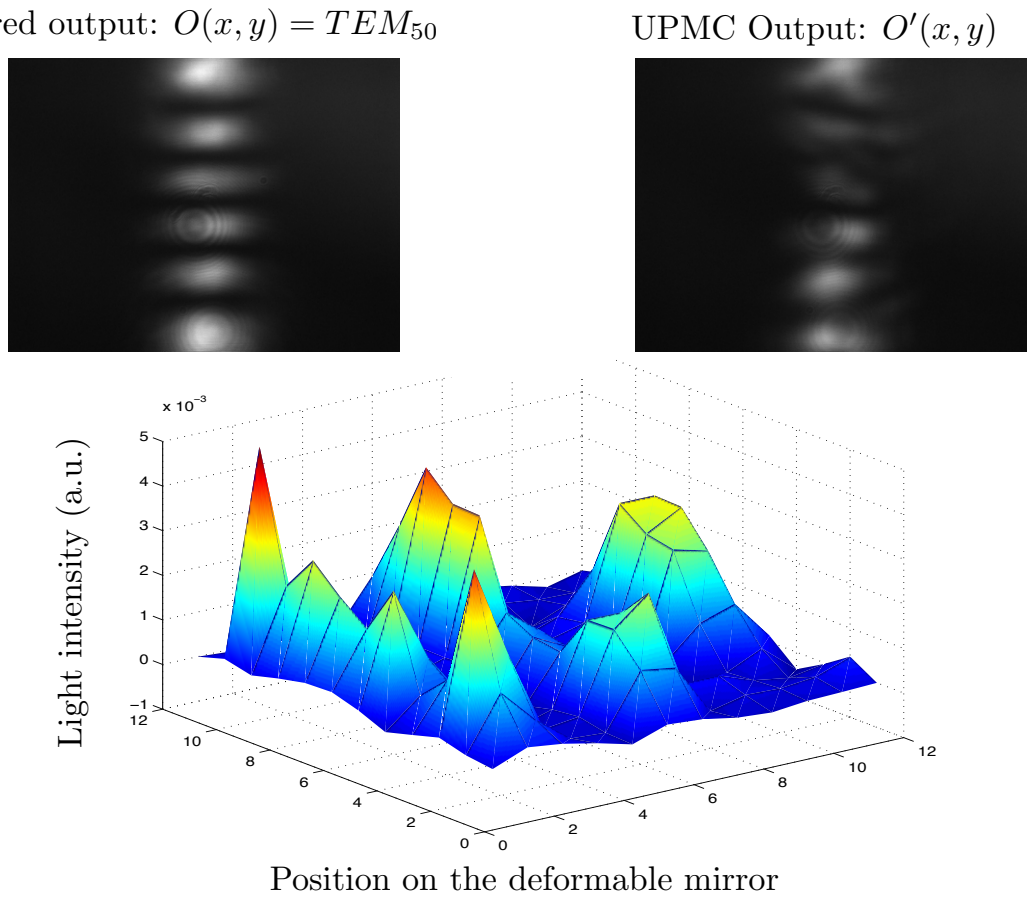

Figure 7.15: Light intensity distribution for a three reflection, $TEM_{00} \rightarrow TEM_{50}$ transform. The output profiles are presented above. The intensity distribution on the last reflection shows that a significant portion of the light does not hit the deformable mirror on the third reflection. No optimization can change that, since the desired output is bigger than the deformable mirror.

On the other hand, this model focused on the average field, without any consideration of noise characteristics. Using squeezed states, we can validate the abilities of the UPMC to manipulate continuous variable non-classical resources, based on noise properties. Moreover, transferring efficiently squeezed states from one spatial mode to another paves the way to more general quantum enhanced detections.

Characterization tools

We use squeezed states to characterize the UPMC. We produce squeezed states in an optical parametric amplifier (OPA) aligned in a bow-tie configuration. This OPA has been described earlier in 4.2.3. The squeezed light at the output of the OPA has the spatial profile of a TEM_{00}, and we want to characterize the ability of the UPMC to transform this TEM_{00} into another spatial mode without altering its quantum state. We use two separate homodyne detections (HD_1 and HD_2, as described in Fig. 7.16) to characterize the quantum state of the light before and after the UPMC. The local oscillator (LO_1)

for HD_1 is in the TEM_{00} mode that matches the output of the OPA. HD_2 uses a local oscillator (LO_2) in a different spatial mode that defines the desired output mode of the UPMC and is used to measure its quantum state.

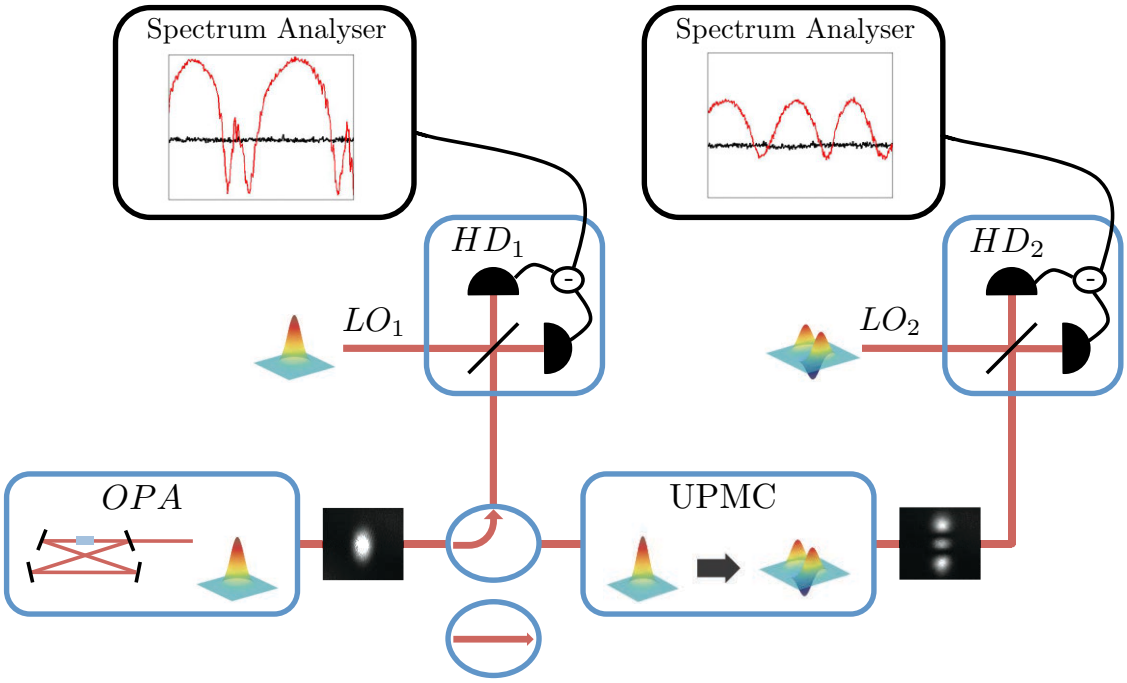

Figure 7.16: Functional schematic of the experiment. The output of the optical parametric amplifier (OPA), a squeezed state in the TEM_{00} mode, is either sent directly to be measured on the first homodyne detection HD_1 using a local oscillator in the TEM_{00} mode or sent through the UPMC. The UPMC changes the spatial profile of the light, in this specific example to a TEM_{20}. The squeezing levels in the TEM_{20} output mode are then measured using HD_2.

We use a high finesse mode cleaning cavity to produce a spatially stable LO_2. This cavity is seeded with a misaligned beam in order to lock it on resonance with a higher order TEM mode (TEM_{n0}). Using a such a cavity restricts the set of spatial transforms upon which to test the UPMC: the input is necessarily a TEM_{00} mode, and the output mode a TEM_{n0} produced by the mode cleaning cavity. Nonetheless, the results from this subset may then be generalized to predict the performance of the UPMC for all possible transforms.

A complete picture of this experiment can be found in Figure 7.17.

7.3.2 Experimental performances

Using the OPA, we send a squeezed mode into the UPMC, and evaluate how well the device transfers the squeezing to a different spatial mode. We find that the transfer efficiency is fully characterized by the squeezing variances of the input and output modes (the UPMC does not add noise), and that imperfect transfers are directly related to passive losses on

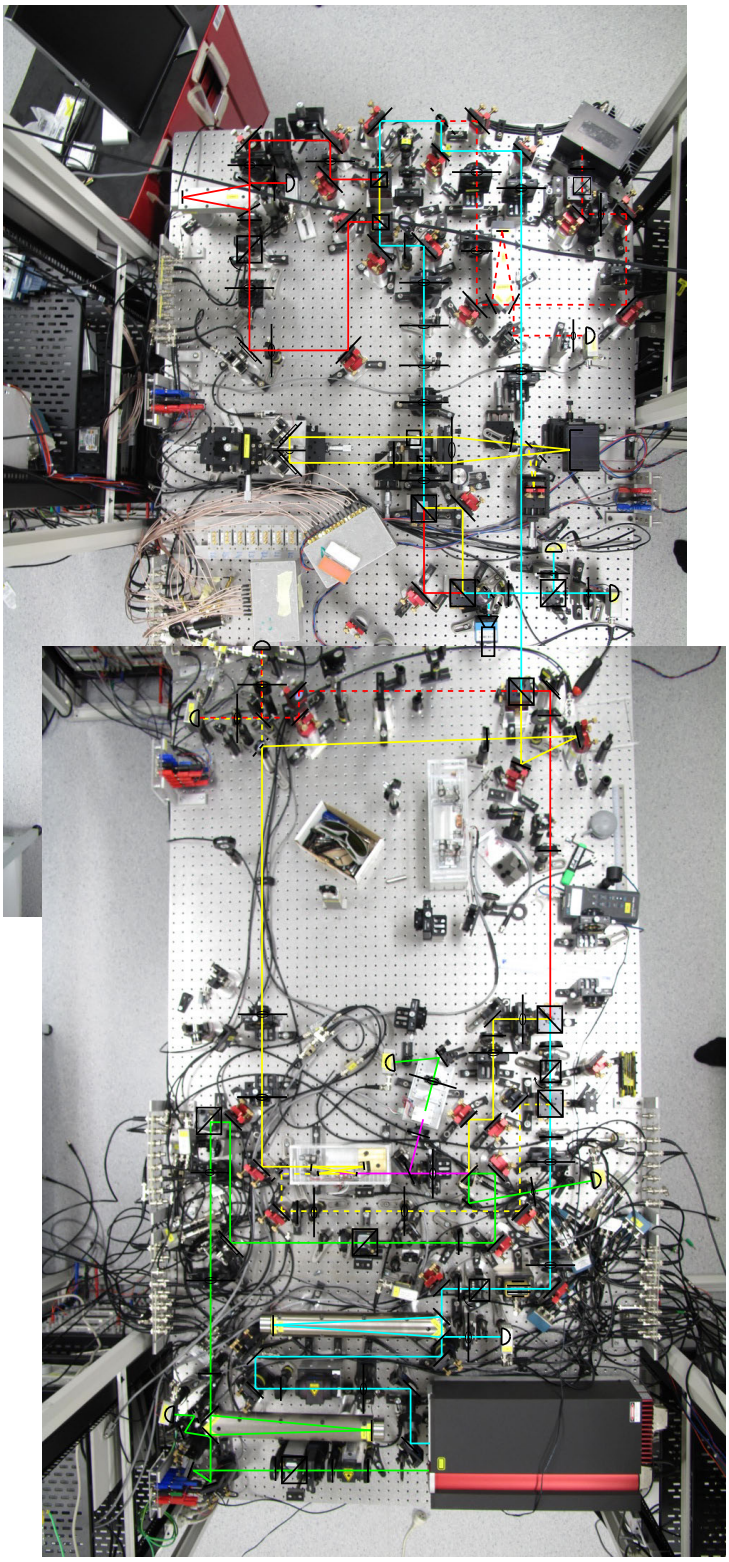

Figure 7.17: Composite picture of the experiment.

the optical components of the UPMC.

Measurements of the transferred squeezing

We test the UPMC for a range of transforms, using TEM_{00}, TEM_{10}, TEM_{20} and TEM_{30} modes as LO_2. First of all, we sent a coherent state, and checked that no addition of noise can be detected on HD_2 compared to HD_1 in the $1-6MHz$ bandwidth. We then send a squeezed state in the UPMC. We first characterize this state by measuring its squeezing and anti-squeezing variances on HD_1. Then, we measure these same variances on HD_2, to characterize the state after the UPMC. We measure the noise variance in a band of width $300kHz$ around the center frequency $2.7MHz$. Table 7.1 presents the variances measured on HD_1 and HD_2.

Table 7.1: Measured Variances before (HD_1) and after (HD_2) the UPMC for a range of transforms.

Output Mode:	TEM_{00}		TEM_{10}		TEM_{20}		TEM_{30}	
Homodyne	HD_1	HD_2	HD_1	HD_2	HD_1	HD_2	HD_1	HD_2
Squeezed quadrature, in dB	-5.1	-1.7	-5.0	-1.6	-4.9	-1.3	-5.0	-1.4
Anti-squeezed quadrature, in dB	6.3	4.4	6.4	4.4	6.3	3.3	6.6	4.0

As can be seen in Table 7.1, the UPMC is able to preserve squeezing when transforming the TEM_{00} input into any of the TEM_{n0} tested, from $n=0$ to $n=3$. This shows that the UPMC is able to transfer squeezing from a mode to another. When the UPMC is set to convert the output of the OPA to a TEM_{30}, the variance along the squeezed quadrature of the TEM_{30} is $1.4dB$ below the quantum noise limit. This is the first measurement of squeezing in such a high order mode. It shows that even this proof of principle UPMC gives access to high squeezing levels in complex spatial profiles. It is also noteworthy that the shape of the desired output mode seems to have a limited influence on the quality of the transform.

The influence of losses

In order to explain the difference of squeezing levels between HD_1 and HD_2, we measure the beam power at different points in the beam path. Overall, from the input to the output of the UPMC, we find 51% loss. Each reflection on the deformable mirror is responsible for a 4.2% loss; this value is consistent with the reflectivity of the gold membrane of the DM and the coatings used on the protective window. Thus, the three reflections on the deformable mirror introduce 12.1% losses. The polarizing beamsplitters each introduce 5% loss when used in transmission; accounting for a total 31% loss in the case of three reflections. Finally, the remaining 18% loss is consistent with the number of optical elements in the beam path and the specifications of their coatings. Additionally, because this proof of principle UPMC is limited to three reflections, the spatial profile of the output of the UPMC is not perfectly matched to LO_2. This mode mismatch is equivalent to an

additional loss, the value of which is derived from the visibility of the interference between the UPMC's output and LO_2.

We find that the differences between the quantum states measured before and after the UPMC can be accounted for by these power losses alone. Under this assumption, we use the measured noise variances to compute values of passive loss for each of the different transforms. In Fig. 7.18, we compare the losses calculated from these quantum measurements, to the losses in power we measured directly on the beam. As can be seen in Fig. 7.18, the two values are in good agreement, well within the error bars derived from the quantum measurements. This validates the assumption that the UPMC only introduces passive losses on the quantum state.

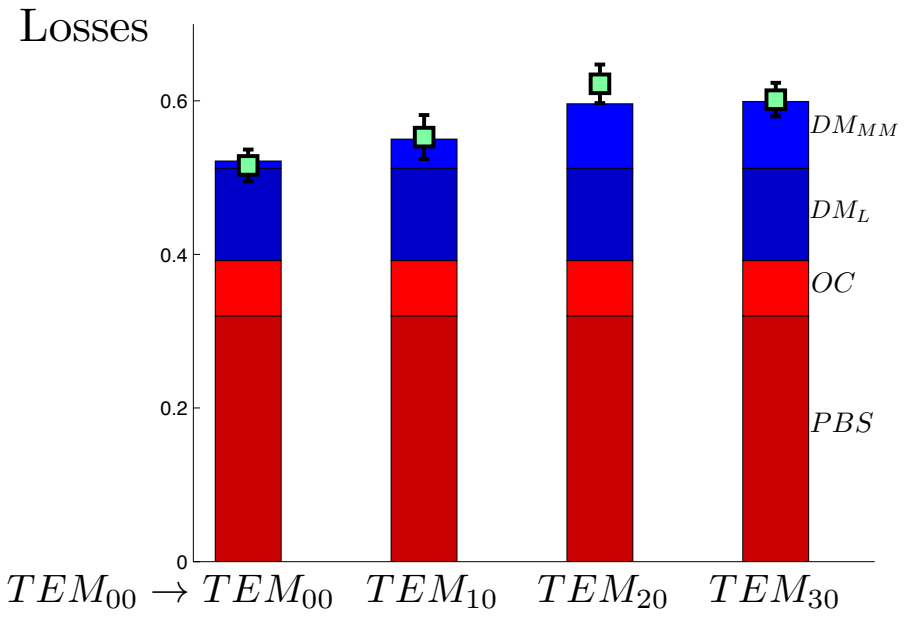

Figure 7.18: Comparison between the losses calculated from the quantum variance measurements and the losses in power, for different transformations of the spatial profile. PBS shows the losses from the polarizing beamsplitters and OC the losses from the other optical components. DM_L shows the losses from the reflections on the DM and DM_{MM} represents the loss due to the spatial profile mismatch. Finally, the squares represent the losses calculated from the quantum variance measurements.

As a conclusion, these results confirm that the UPMC can transform the spatial profile of the light while retaining its quantum properties, excluding passive losses introduced by its optical components. Convincingly, the UPMC does not add noise, and allows for high quality mode matching. It must be noted here that our device is a proof of principle UPMC. A lossless transform is indeed possible given access to higher quality optical components; there is nothing fundamental in the UPMC's design that destroys the quantum state of the light.

Part IV

Concluding remarks

Chapter 8

Case studies

We began this thesis with the presentation of two quantum related challenges: quantum enhanced detection and continuous variable quantum computing. For these challenges, complex spatial modes are either necessary or useful. Indeed, to improve a detection system using squeezed light, the light needs to be in the detection mode. To use the simplified set-up allowed by copropagating modes for quantum computation, we need to generate and manipulate multiple orthogonal squeezed modes within a single beam.
We presented a set of tools to address these challenges, in particular techniques to generate multiple squeezed modes within a beam in II, techniques to manipulate them in III and techniques to detect them simultaneously in 5. During the course of this work, we built each tool and characterized it experimentally (Fig. 4.9, Fig. 7.18 and Fig. 5.16). This gave us the ability to realistically assess the achievable performances of each of them.
In these concluding remarks, we present two case studies, one for quantum enhanced detection, the other for quantum computation. For each case, we combine the measured performances of each of our tools to estimate the performance of the overall system.

8.1 Quantum enhanced detection

8.1.1 Transferring squeezing into the detection mode

Our first case is quantum enhanced detection. As we introduced previously in 3.1.1, quantum enhanced detection involves shining a strong coherent beam (the probe beam) onto a physical system. Fluctuations of a real parameter p in this system entail changes in the output field envelope $\mathcal{E}(\vec{\rho}, p)$. From a detection of this output field, we can retrieve p. If we consider small variations of p around p_0, in the first order, the information on the value of p is carried in a single spatial mode u defined as

$$u(\vec{\rho}) = \frac{\left.\frac{\partial \mathcal{E}(\vec{\rho},p)}{\partial p}\right|_{p=p_0}}{\left\| \left.\frac{\partial \mathcal{E}(\vec{\rho},p)}{\partial p}\right|_{p=p_0} \right\|} \tag{8.1}$$

The shape of u thus depends on the interaction between the physical system we want to measure and the probe beam. An interesting property is that if the interaction is unitary, then u is orthogonal to $\mathcal{E}(\vec{\rho}, p_0)$. Otherwise, fluctuations of p would change the output power of the beam.

We measure p by detecting the amplitude quadrature of the field in mode u. An efficient method to do so is to perform an homodyne detection with the local oscillator in mode u. As presented in Fig. 5.5, if the detectors are good enough, and if we measure fluctuations of p above a certain frequency, the signal to noise ratio on the evaluation of p is limited by the quantum noise, and improving this ratio requires quantum noise manipulation. By using an amplitude squeezed light in mode u, the relevant quantum noise of the homodyne detection is reduced and we can detect p with an improved accuracy.

To achieve quantum enhanced detection, two steps are challenging. First of all, we need to be able to perform an homodyne detection on the mode u. To do so we have two options. The first option is simply to generate this mode u, and use it in a conventional homodyne detection set-up. This generation can use a UPMC (Fig. 7.10). Alternatively, we can use a multipixel homodyne detection (Fig. 5.7). In this case, we use the gains on the pixel recombinations to match the amplitude of mode u (Fig. 5.8). Additionally, a deformable surface might be required to match the local oscillator transverse phase to u's.

A second difficulty lies in the generation of amplitude squeezing in mode u at the homodyne detection. Since u does not necessarily correspond to a resonant mode in an OPA, the best option is to use a UPMC to convert the shape of a TEM_{00} squeezed beam into the desired mode. Then this mode can be used to enhance detection.

An interesting subtlety is that the squeezed mode needs to be superposed to the probe beam before the physical system. Indeed, if we were to superpose it afterwards, we would be replacing the light carrying our signal by the squeezed light, which does not improve the signal to noise ratio. When the interaction we want to measure is unitary, the orthogonality of $\mathcal{E}(\vec{\rho}, p_0)$ and u can be used to achieve such a lossless superposition. While the probe mode is transformed into $\mathcal{E}(\vec{\rho}, p_0)$ by the interaction, there is another mode u' which is transformed by the interaction into u. An example of these modes is presented in Fig. 8.2.

Since $\mathcal{E}(\vec{\rho}, p_0)$ and u are orthogonal and the interaction is unitary, u' and the probe mode are orthogonal too. We can use this property to superpose them, using for example the reflection on a locked cavity, as we presented in 4.3.1.

The complete scheme is synthesized in Fig. 8.1, in the simple case when choose to use a probe beam in the TEM_{00} mode. In this case, we make the probe go through a mode-matched cavity and bounce u' (orthogonal to the TEM_{00}) on the output coupler of

this cavity to achieve the superposition. In this reasoning, we did not take into account the fact that fluctuations of p around p_0 tend to couple light from u' into another mode than u. But in the case of small fluctuations of p this effect can be neglected.

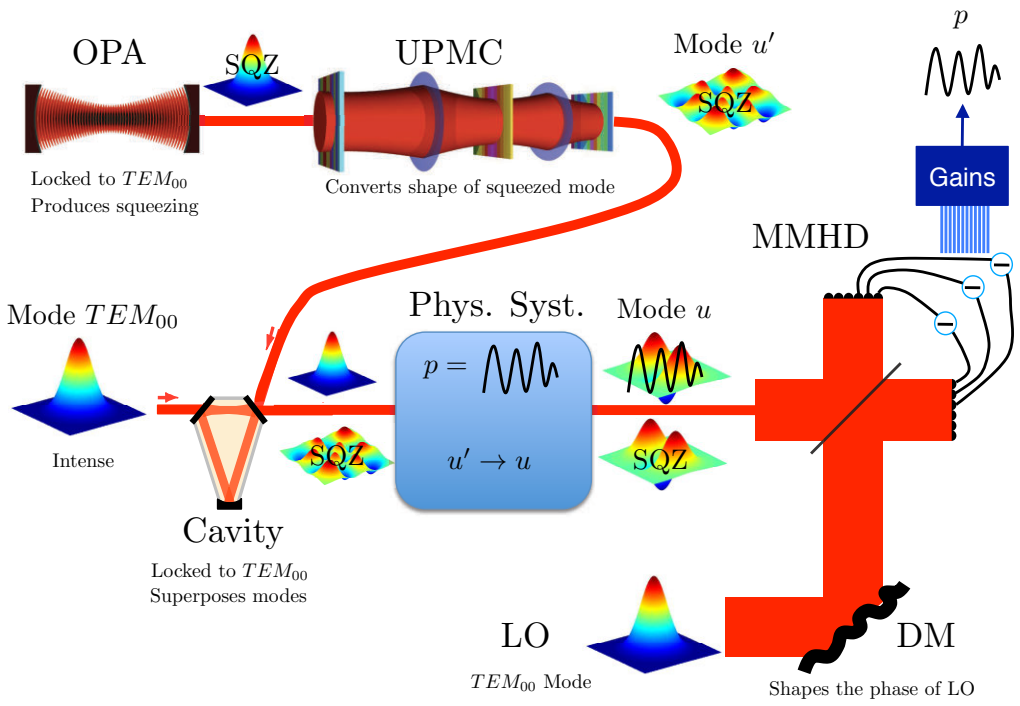

Figure 8.1: Schematic of a Quantum Enhanced Detection system. Squeezed light is produced efficiently by an OPA locked to the TEM_{00} mode. A UPMC converts the shape of this squeezed mode to u'. u' is then superposed losslessly to the bright probe beam in the TEM_{00} mode using a cavity. The multimode beam is shone onto the physical system, and fluctuations of the parameter p that we need to detect introduce fluctuations of the amplitude of u, while the physical system transforms u' in u, thus transferring the squeezing to the detection mode. We finally detect this beam with a multipixel homodyne detection. We use a deformable mirror in the local oscillator path to control the transverse phase profile of the detected mode, and the gains of the pixel recombination to control its transverse amplitude.

8.1.2 Example: detecting the movement of a small structure

Let us now present a practical situation, described in Fig. 8.2. We want to detect small lateral movements of a transparent glass filament (a hair) of diameter $d_h = 50\mu m$, with refractive index $n = 1.55$. We shine a laser beam on the hair, which diffracts the light. The position of the hair is thus encoded in the outgoing light. We image the hair onto our detection apparatus.

We choose to consider a hair so as to keep the problem one-dimensional. We want

to measure the displacement p of the hair along the transverse axis $\vec{x}$, around a position $p = 0$. We put the filament at the waist of a laser beam in the TEM_{00} mode. We assume the beam has a waist along $\vec{x}$ of d_h (its diameter is thus $2w_0 = 2d_h$). Fig. 8.2 presents the transverse profiles of the probe beam, of the average output mode $\mathcal{E}(x, p = 0)$, and of mode u' and u. u is the mode which contains all the information about the displacement of the hair p, while u' is the mode we need to squeezed before the hair so that u is squeezed at the output.

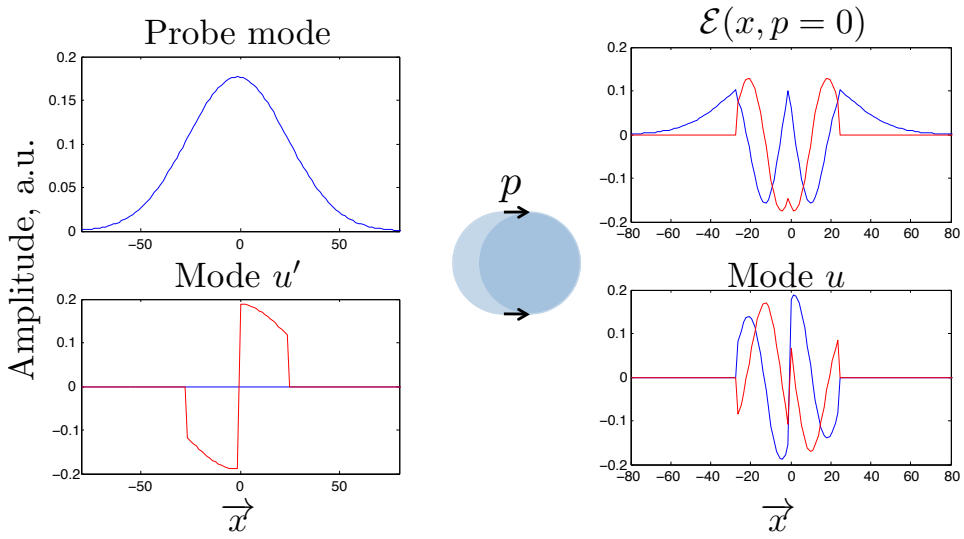

Figure 8.2: Transverse profiles of the different spatial modes involved in the problem: we shine a probe beam onto a transparent glass filament, and when the filament is at $p = 0$, the output mode is $\mathcal{E}(x, 0)$. When p fluctuates around $p = 0$, these fluctuations introduce amplitude fluctuations in mode u. Mode u' is the input mode in which we need to reduce the quantum noise (in the amplitude quadrature) in order to generate amplitude squeezing in the output mode u after the filament. The blue curve is the real part of the amplitude of the mode, and the red curve its imaginary part. All the modes are normalized.

We first study the detection efficiency. We use a multipixel homodyne detection, presented in Fig. 5.7, to detect the outgoing light. The local oscillator is in the TEM_{00} mode, the same as the probe beam. Different factors influence the detection efficiency: the quantum efficiency of the detectors, the losses on the protective window, the fill factor and the number of pixels we use. As far as the quantum efficiency, protective window losses and fill factor are concerned, they can be represented straight away as a loss coefficient for each process.

The intensity overlap α^2 between the optimal detection mode v_g and u depends on the number of pixels we use. Additionally, since the transverse phase of mode u is not constant, a phase shaping of the local oscillator (using a deformable mirror for instance) improves dramatically α^2. Fig. 8.3 shows the intensity overlap as a function of the number of pixels, in both cases: with or without the transverse phase shaping of the local oscillator. As we can see, because of the transverse phase of u, the transverse phase shaping is clearly needed. With this phase shaping, if we use 10 or more detection pixels, the intensity overlap is above 99%.

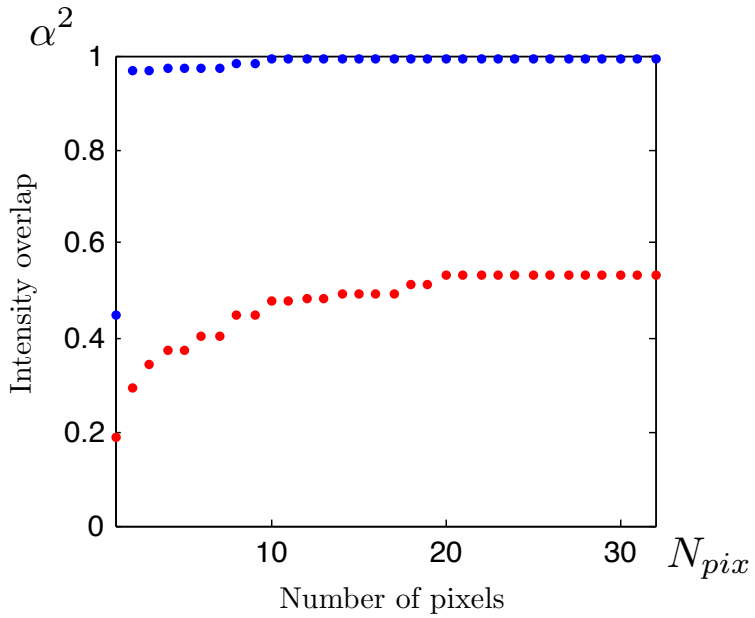

Figure 8.3: Intensity overlap α^2 between the optimal detection mode and u, as a function of the number of pixels used in the homodyne detection. We present two cases: in red we do not match the local oscillator transverse phase to u's, and in blue we use a deformable surface to match them.

We now want to improve the signal to noise ratio of the homodyne detection by using amplitude squeezed light in mode u. To do so, we produce amplitude squeezing in the TEM_{00} mode and then use a UPMC, as we presented in Fig. 7.8, to reshape the TEM_{00} into mode u', presented in Fig. 8.2.

Fig. 8.4 presents the intensity overlap between the output of the UPMC and mode u', as a function of the number of reflections on the deformable mirror. We compute these overlaps in two cases: the first case considers 12 actuators per reflections, as we have with our current mirror (Boston Micro-Machine Multi-DM). The second case considers 32 actuators per reflections, as can be found in the Kilo-DM, also from Boston Micro-Machine. Apart from the difference in number of pixels, the Kilo-DM and Multi-DM are identical devices. Adding more actuators per reflection improves the conversion efficiency.

While the UPMC improves the intensity overlap between its output mode and mode

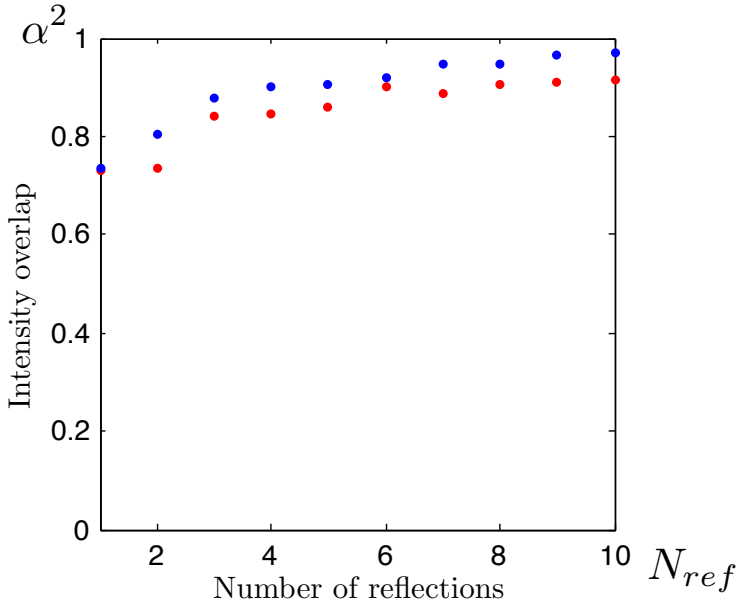

Figure 8.4: Intensity overlap α^2 between the output of the UPMC and the mode u', as a function of the number of reflections. In red with a Kilo-DM (12 actuators per reflections), in blue with the Kilo-DM (32 actuators per reflections)

u' for each additional reflection, they also subtract light: the reflection on the gold surface of the deformable mirror, the protective window and the conventional optical elements all introduce losses.

In Fig. 8.5 we combine these results to derive the quantum noise reduction we can realistically expect from the quantum enhancement for two set-ups. The first set-up "Today", considers a first version of the UPMC and multipixel homodyne detection. The second set-up "Tomorrow" presents the situation with realistically improved elements. The parameters for these two set-ups are presented in table 8.1

Table 8.1: Two realistic set-ups

Device	Parameter	Today	Tomorrow
OPA	Amplitude noise reduction	$-5dB$	$-6.5dB$
UPMC	Losses on DM surface	1% per loop	1% per loop
	Losses on protective window	4.2% per loop	0.5% per loop
	Losses on conventional optical elements	6.4% per loop	1% per loop
	Number of actuators	12 per ref.	32 per ref.
Multipixel Homodyne	Quantum efficiency	92%	95%
	Protective window losses	13%	0%
	Fill-factor	90%	90%
	Number of pixels	8	16

This case study allows us to conclude that enhancing detection using squeezed light

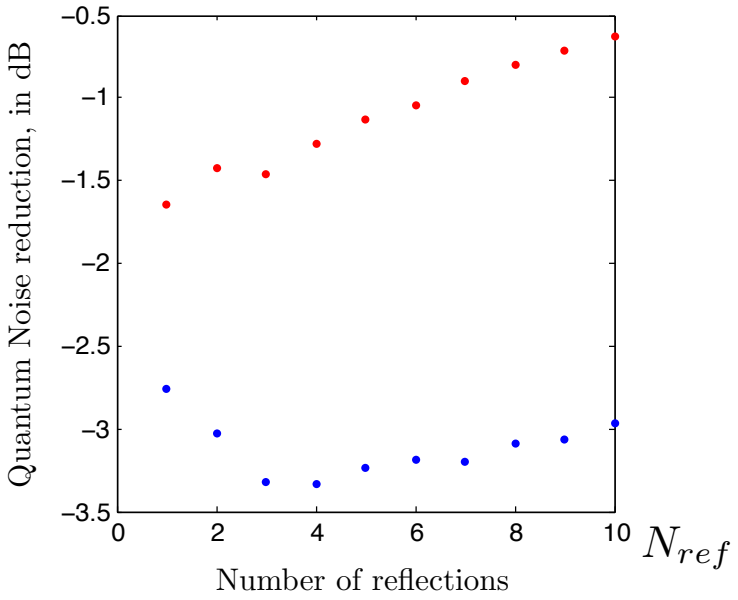

Figure 8.5: Overall predicted quantum noise reduction, in dB, for two realistic experimental set-ups. "Today" is in red, "Tomorrow" is in blue. We plot the quantum noise reduction, i.e. minus the improvement in signal to noise ratio, as a function of the number of reflections in the UPMC conversion. While today there is no gain in using multiple reflections, a in a more advanced set-up they become crucial, allowing for an improvement of $-0.6dB$ compared to the one reflection case, which is a phase only shaping of the squeezed mode.

is achievable. It involves all the components we presented in this thesis: the creation of a multimode beam, carrying the probe and the squeezed mode, the reshaping of the squeezed mode, to match the optimal detection mode, and finally the multipixel homodyne detection. Two important results should be taken out of this study: first of all that quantum enhancement can be used to improve the detection any small parameter. The methods we put forward here are applicable to any parameter p which introduce a variation in an output field $\mathcal{E}$. This is a significant difference compared to previous quantum enhancement systems.

A second result, shown clearly in Fig. 8.5, is that quantum enhancement is very sensitive to the quality of the optical set-up used. Not only do better optical components reduce losses, but they also allow for improved mode-matching thanks to the UPMC.

8.2 Cluster state computation

8.2.1 The cluster state model of quantum computation

Our second case study involves cluster state computation. We do not aim here at explaining the workings of a quantum computer based on cluster states. We merely present what is required to perform an algorithm with this method, and show how we can implement it with our copropagating modes. Cluster state computation is based on the principles

of one-way quantum computing: we first build a fixed, complex, multimode entangled state (here named cluster state). Then, the computation is performed using a sequence of classical detections on this state. In terms of quantum optics, this means that the main difficulty of cluster state computation is the creation of the multimode entangled state.

A multimode cluster state is defined by a graph. This graph, presented in Fig. 8.6, represents the entanglement relations between the different modes. Each circle is a mode, and the entanglement relation is defined by the connecting lines. For each mode i, we have:

$$\left\langle \Delta^2 \hat{p}_i - \sum_{j \in N_i} \hat{x}_j \right\rangle \to 0 \tag{8.2}$$

Where the set N_i is the set of modes j connected to mode i. For a cluster state to work perfectly, the variances need to be 0. But computations can still be performed with less than perfect variances ((Menicucci 06)). It entails a decrease in computation accuracy (which can be compensated by using more resources and specific error correcting algorithms).

We then perform classical detections on the different modes of the state to perform the computation. These detections can be homodyne, and in this case the computation specifies the local oscillator phases. Alternatively, detections can be more complex, involving for example avalanche photodiodes. We leave these last detections out of the scope of this work, and focus on protocols which can be implemented solely with homodyne detections.

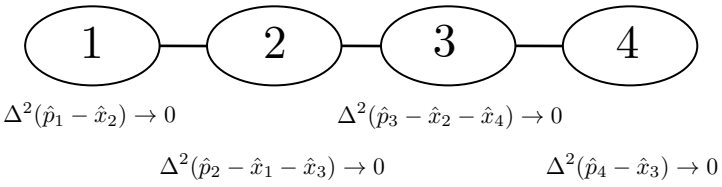

Figure 8.6: Representation of a 4-mode linear Cluster State, with the corresponding variance relations.

As presented in Fig. 3.3, our aim is to build the multimode cluster state between copropagating modes, instead of separate beams. To do so, we first generate a beam carrying multiple squeezed modes. This can be achieved using multiple bow-tie squeezers and phase plates, as presented in 4.3.1. Using locking loops, we control the relative phases of the superposed modes. We then use a UPMC to manipulate these modes in order to build the desired entanglement relation. Finally we detect these modes using a multipixel homodyne detection.

The physical operation we perform is controlled by the relative phases of the superposed modes, by the unitary transform performed by the UPMC and finally by the orthogonal

recombinations of the homodyne detection signals. Additionally, we can also shape the phase of the local oscillator. We can decompose this process into a succession of matrix product on the annihilation operators vector $\vec{\hat{a}}$. We find:

$$\vec{\hat{a}}_{det} = O\ D_{LO}\ U_T\ U_{UPMC}\ D_r\ \vec{\hat{a}}_{SQZ} \tag{8.3}$$

where $\vec{\hat{a}}_{SQZ}$ are the annihilation operators in the modes of the OPAs. D_r is the diagonal matrix which contains the relative phases of these modes and U_{UPMC} is the unitary matrix describing the action of the UPMC. Then, U_T is a unitary transfer matrix. It is the basis change matrix which converts the modes of the OPAs into pixel modes, which are more adapted to the multipixel homodyne detection. In the pixel basis, the local oscillator transverse phase profile is represented by a diagonal matrix D_{LO}. Finally, O is the orthogonal matrix describing the recombinations we perform on the output signals from the multipixel homodyne detection. This decomposition is synthesized in Fig. 8.7.

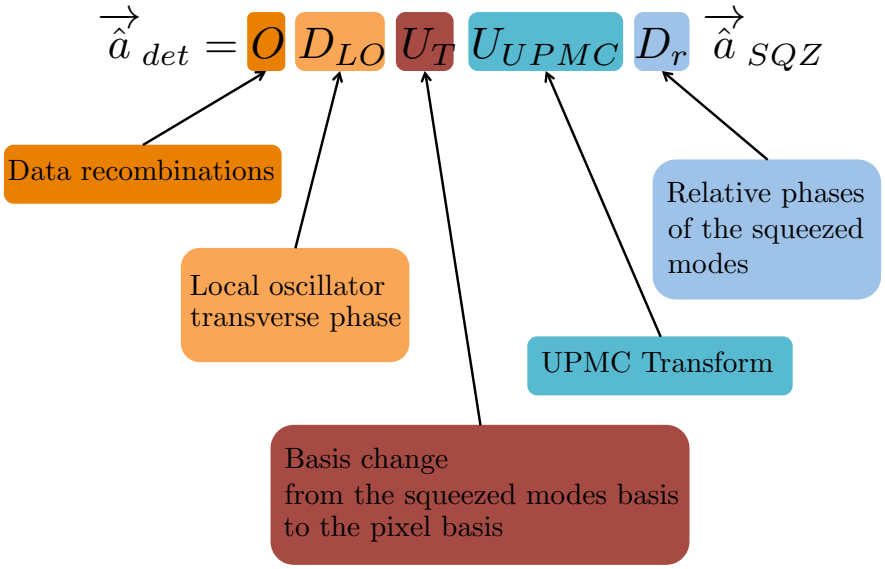

Figure 8.7: Decomposition of the degrees of freedom of our spatial modes manipulation and detection apparatus

The results of our multimode homodyne detection are the fluctuations of the amplitude quadratures $\vec{\hat{x}}_{det} = \vec{\hat{a}}_{det} + \vec{\hat{a}}^{\dagger}_{det}$.

From a theoretical point of view, as presented in 3.2.1, building a cluster states can be achieved using as many independent squeezed modes as there are circles in the graph. We then need to apply a unitary mixing U_{CS} to these modes, which depends on the graph we are building (the precise procedure to determine U_{CS} for a given graph is given in (Loock 07b)). Then, performing a computation requires the detection of the modes along specified quadratures. These quadratures correspond to the local oscillator phase of the

corresponding homodyne detection. These phases can be represented by a diagonal matrix D_C that we apply on the mixed modes. As a result, in order to perform a computation, we need to have:

$$\vec{\hat{a}}_{comp} = D_C U_{CS} \vec{\hat{a}}_{SQZ} \tag{8.4}$$

and measure the fluctuations of the amplitude quadratures $\vec{\hat{x}}_{comp}$. Depending on the computation we want to run on the cluster state, the matrix D_C of the local oscillator phase is different.

Comparing equations 8.3 and 8.4, we see that for any U_{CS} and any D_C, there is a set of matrices U_{UPMC}, D_r, D_{LO}, O we can choose so that $\vec{\hat{x}}_{comp} = \vec{\hat{x}}_{det}$. For example, $O = \mathbb{I}$, $D_{LO} = D_C$, $D_r = \mathbb{I}$ and $U_{UPMC} = U_T^{-1} U_{CS}$ is always a solution. But since the use of the UPMC adds losses, and D_{LO}, D_r and O do not add any, it is preferable to limit the use of U_{UPMC} by using the degrees of freedom in D_{LO}, D_r and O instead.

The last step of a cluster state computation is a correction on the last mode we need to detect. This correction depends on all the previous detections' results, and can be implemented by the addition of a coherent amplitude and phase modulated state on this last mode (Ukai 10). It is similar to the correction step in quantum teleportation (Furusawa 98). Like in the teleportation case, we need our electronics to perform the correction significantly faster than our frequencies of interests. In our case, with our squeezing frequencies between 2 and $5MHz$, such a correction is clearly achievable using broadband phase and amplitude modulators (such as the 4004-M and 4104-M, from New Focus).

In a multiple beam set-up, the correction is applied on the last beam by using a weakly reflective mirror. This mirror lets most of the last beam through, but with a strong enough correction beam, its weak reflection adds the desired correction. A similar scheme can be implemented in our co-propagating set-up. Instead of separate beams, we have orthogonal spatial modes. There is a specific spatial mode u_l which corresponds to the mode on which we need a correction. We use a weakly reflective mirror before the multipixel homodyne detection, and a strong enough correction beam in the mode u_l. The mirror introduces a small amount of losses onto all the modes, but adds the desired correction in mode u_l, as presented in Fig. 8.8. Such a scheme is exactly equivalent to a multiple beam set-up in which a small loss would be added before each homodyne detection. These losses can be reduced by using extremely weakly reflective mirrors, with the corresponding intense correction beam.

8.2.2 A four mode cluster state

Let us now present a practical application of this process. The goal is to build a 4 mode linear cluster state, similar to the one presented in (Yukawa 08a) (which was built with separate beams). For this cluster, which graph is presented in 8.6, the matrix U_{CS} defined

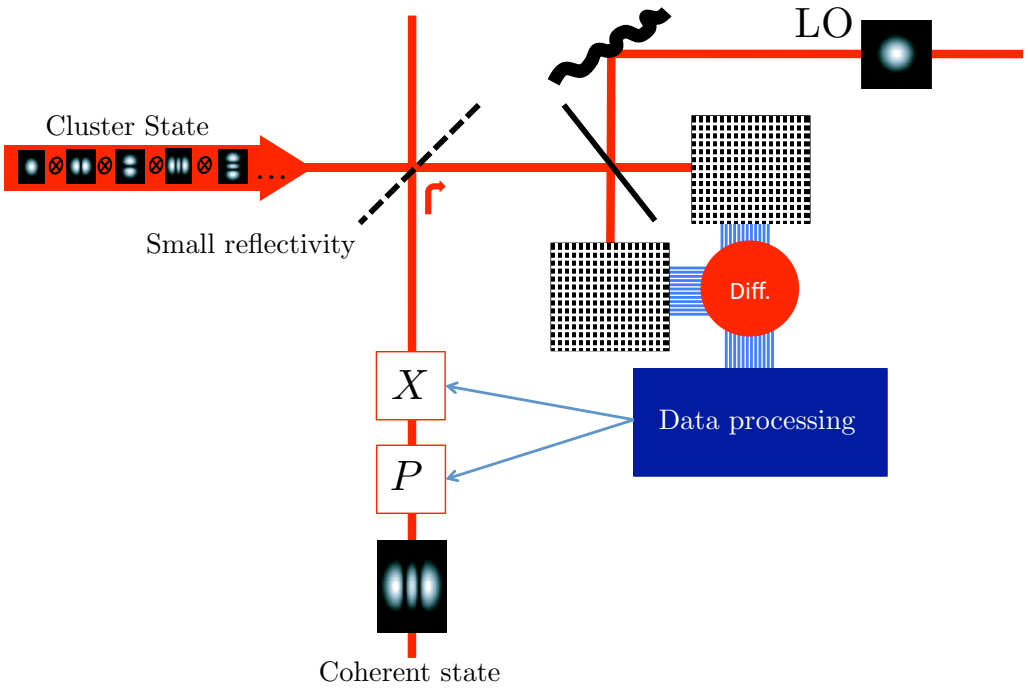

Figure 8.8: The cluster state computation is based on a succession of detections, and a final correction onto the last mode. This final mode can then be used in other parts of the system, or can be detected. In our case, it is detected using the same Multipixel Homodyne Detection. The correction process is a translation of the last mode in the phase space. This corresponds to the addition of a coherent field with the appropriate amplitude and phase. The amplitude (X) and phase (P) modulators are controlled by the results of the Multipixel Homodyne Detection.

by:

$$U_{CS} = \begin{pmatrix} \frac{i}{\sqrt{2}} & \frac{i}{\sqrt{10}} & -\frac{2}{\sqrt{10}} & 0 \\ -\frac{1}{\sqrt{2}} & \frac{1}{\sqrt{10}} & \frac{2i}{\sqrt{10}} & 0 \\ 0 & -\frac{2i}{\sqrt{10}} & -\frac{1}{\sqrt{10}} & -\frac{1}{\sqrt{2}} \\ 0 & \frac{2}{\sqrt{10}} & -\frac{i}{\sqrt{10}} & \frac{i}{\sqrt{2}} \end{pmatrix} \tag{8.5}$$

transforms four independent amplitude squeezed modes into a set of entangled modes with the variance relations specified by the graph 8.6.

We consider the case when we achieve the superposition of four squeezed beams using a succession of bow-tie optical parametric amplifiers, as presented in 4.3.1. We found experimentally that each time a beam undergoes such a superposition, we need to take into account additional losses introduced by the phase plate and the reflection on the cavity.

Considering that all the squeezed modes are generated using identical OPAs locked to the same TEM_{00} we can use a set of binary phase plates similar to the ones presented in

4.3.1 to achieve the superposition of the squeezed modes. The transfer matrix U_T between the squeezed modes and the pixel modes of the detection U_T can take the simple form:

$$U_T = \frac{1}{\sqrt{4}} \begin{pmatrix} 1 & 1 & 1 & 1 \\ 1 & 1 & -1 & -1 \\ 1 & -1 & 1 & -1 \\ 1 & -1 & -1 & 1 \end{pmatrix} \tag{8.6}$$

This simple form for U_T neglects the fact that the homodyne detection may involve more pixels, but could be expanded to include more modes and complete the basis. They are not needed here. Thanks to the binary phase plates, U_T is an orthogonal matrix: it does not involve any phase change.

As presented in (Ukai 10), such a linear cluster state can be used to perform any gaussian operation on an input quantum state. The desired operation is performed by choosing the matrix D_C's coefficients and the dependence of the classical correction on the homodyne detection results. We do not focus here on the classical correction. We evaluate the quality of our system on its ability to generate a cluster state with as low variances $\left\langle \Delta^2 \hat{p}_i - \sum_{j \in N_i} \hat{x}_j \right\rangle$ as possible, and for which the detection of $\vec{\hat{x}}_{det}$ performs the desired computation.

We find two very different cases. Consider first the case where we have:

$$D_{C1} = \begin{pmatrix} 1 & 0 & 0 & 0 \\ 0 & i & 0 & 0 \\ 0 & 0 & 1 & 0 \\ 0 & 0 & 0 & i \end{pmatrix} \tag{8.7}$$

This corresponds to measuring $\hat{x}_1$, $\hat{p}_2$, $\hat{x}_3$, and $\hat{p}_4$ simultaneously on the cluster state presented in 8.6. In this special case, we can find a matrix D_r which controls the relative phases in the original mode superposition so that there is an orthogonal matrix O which satisfy $D_{C1}U_{CS} = OU_TD$. There is no need for a UPMC.

A second, more general case is when there is no combination of matrices D_r, D_{LO} and O which would avoid the use of a UPMC. It is for example the case when D_{C2} is the identity matrix. In this case, finding the optimal combination of O and U_{UPMC} remains an open issue. As a rule of thumb, we found that apart from very specific transforms, the nature of U_{UPMC} does not matter much, and the overall efficiency α_n^2 of the UPMC depends on the number of modes we manipulate and the number of reflections we use.

As a result, we can predict the performances of our system in these two kinds of computations, for the two realistic set-ups "Today" and "Tomorrow". We complete these two models to account for the imperfect superposition: that each phase plate and reflection introduces an additional 12% loss in the case of "Today" and 1% loss in the case of "Tomor-

row". For the simple quantum computations, when there is no need for a UPMC, we find that the "Today" set-up yields a cluster state with all the variances $\left\langle \Delta^2 \hat{p}_i - \sum_{j \in N_i} \hat{x}_j \right\rangle$ at least $-1.8dB$ below the quantum noise level. The "Tomorrow" set-up, on the other hand, has them all at least $-4.5dB$ below the quantum noise level. When there is a need for the UPMC, Fig. 8.9 presents the maximum of the variances $\left\langle \Delta^2 \hat{p}_i - \sum_{j \in N_i} \hat{x}_j \right\rangle$ (compared to the quantum noise level) as a function of the number of reflections on the deformable mirror.

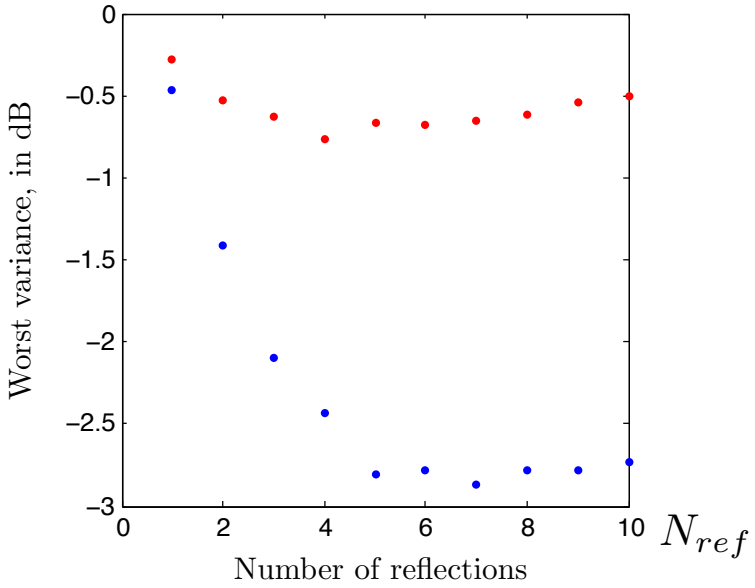

Figure 8.9: Maximum variance of all four combinations $\left\langle \Delta^2 \hat{p}_i - \sum_{j \in N_i} \hat{x}_j \right\rangle$ compared to their quantum noise limit, in dB, when the UPMC is needed to perform the computation. This worst variance is plotted as a function of the number of reflections allowed on the deformable mirror, for two different set-ups: "Today" in red, "Tomorrow" in blue. Comparing these values to the $-1.8dB$ and $-4.5dB$ (for "Today" and "Tomorrow", respectively) that we obtained for computations which do not involve the UPMC, we find that using the UPMC should clearly be avoided whenever possible, but that when it is necessary, a set-up of good quality ensures satisfying results.

As a conclusion, this second case study shows that the combination of a multimode beams, a UPMC and a multipixel homodyne detection can clearly be a building block for one-way quantum protocols, especially cluster states computations. It is a flexible option: a simple reprogramming of the UPMC changes the protocol performed by the device. On the other hand, efficient quantum computing with copropagating modes requires multiple reflections in a UPMC. The quality of its constituents becomes crucial.

Chapter 9

Conclusion

In this thesis, we presented the experimental implementation of a set of tools aimed at manipulating and detecting the quantum state of complex spatial modes. These tools corroborate our understanding of the spatial properties of quantum fields and give us the ability to engineer and detect any Gaussian state carried by any mode or set of modes.

We first presented different methods to generate a beam carrying multiple squeezed modes. We found that while degenerate OPAs were an attractive solution and could provide us with a beam carrying a few squeezed modes, building a fully degenerate OPA able to generate a high number of copropagating squeezed modes remains a challenge. On the other hand, a succession of single mode bow-tie OPAs and binary phase plates can be used to superpose a multiple squeezed modes on a beam. While such a scheme requires more resources than a degenerate OPA, which generates a multimode squeezed beam straight away, we found that single mode bow-tie OPAs are simpler to build than the degenerate OPA, and there is no theoretical limit on the number of modes we can superpose.

We can then use a UPMC, as we presented in 6.2.2, to turn this multimode squeezed beam into the desired multimode Gaussian state. While a UPMC can in theory perform this transformation perfectly, practical considerations such as losses and resource limitations obliged us to implement optimization algorithms to maximize the UPMC performance under these practical constraints. We showed experimentally that the computational model satisfyingly predicts the behaviour of the UPMC, and that it can indeed reshape at will the transverse shape of squeezed modes. The combination of a multimode squeezed beam generation and a UPMC is a flexible method to generate any multimode Gaussian state carried by copropagating modes.

In order to measure the outgoing multimode state, we designed and built a multipixel homodyne detection. By simply replacing the bucket photodiodes of a conventional homodyne detection by two photodiode arrays, and overcoming a few electronic challenges, we created an homodyne detection which can measure the amplitude of multiple copropagating modes simultaneously. The different linear recombinations of the multiple output signals from the multipixel homodyne detection correspond to as many different modes,

and we can set these linear recombinations to measure specific desired modes.

We presented in the concluding remarks two applications of these tools. The improvement of the detection of small spatial fluctuations of a light field is a well-known application of squeezing in higher order modes. Using the UPMC, we show that this improvement can be brought in for the detection of any small fluctuations, whatever its shape.
A second application of these tools is quantum computation. Our ability to generate any Gaussian state means we can build a cluster state, a fundamental resource for continuous variable quantum computing.

Future work on the quantum properties of transverse modes could include the experimental implementation of these two applications. A demonstration of detection improvement in a real system, for example the movements of a biological specimen, thanks to squeezing would bridge the gap between the quantum mechanical result and its application outside of its field. Such a demonstration would be facilitated by our ability to reconfigure the UPMC to adapt the squeezed mode to the complex, biological system. Another field of study is quantum computation. At the moment, the simplicity of the cluster states experimental set-ups which use multiple beams makes them the preferred option. However, the ability of multiple transverse modes to carry a very complex multimode state which can reconfigured with a press of a button is a strongly appealing alternative.

Bibliography

[Abas 83] G L Abas, V W S Chan & T K Yee. *Local-oscillator excess-noise suppression for homodyne and heterodyne detection.* Optics Letters, vol. 8, page 419, aug 1983. Cited p. 65

[Adesso 06] Gerardo Adesso, Alessio Serafini & Fabrizio Illuminati. *Multipartite entanglement in three-mode Gaussian states of continuous-variable systems: Quantification, sharing structure, and decoherence.* Physical Review A (Atomic, Molecular, and Optical Physics), vol. 73, no. 3, page 19, mar 2006. Cited p. 20, 35

[Alekseev 98] AN Alekseev, KN Alekseev, OS Borodavka, AV Volyar & YA Fridman. *Conversion of Hermite-Gaussian and Laguerre-Gaussian beams in an astigmatic optical system. 1. Experiment.* Technical Physics Letters, vol. 24, no. 9, pages 694–696, jan 1998. Cited p. 97

[Aoki 09a] Takao Aoki, Go Takahashi, Tadashi Kajiya, Jun-ichi Yoshikawa, Samuel L Braunstein, Peter van Loock & Akira Furusawa. *Quantum error correction beyond qubits.* Nature Physics, vol. 5, page 541, aug 2009. Cited p. 20, 34, 35

[Aoki 09b] Takao Aoki, Go Takahashi, Tadashi Kajiya, Jun-ichi Yoshikawa, Samuel L Braunstein, Peter van Loock & Akira Furusawa. *Quantum error correction beyond qubits.* Nature Physics, vol. 5, no. 8, pages 541–546, jun 2009. Cited p. 2

[Arvind 95] Arvind, B Dutta, N Mukunda & R Simon. *The real symplectic groups in quantum mechanics and optics.* Pramana, vol. 45, no. 6, pages 471–497, dec 1995. Cited p. 34, 35

[Bachor 03] Hans-Albert Bachor & Timothy C Ralph. A guide to experiments in quantum optics. Wiley-VCH, dec 2003. Cited p. 40, 56

[Bagnoud 04] V Bagnoud & JD Zuegel. *Independent phase and amplitude control of a laser beam by use of a single-phase-only spatial light modulator.* Optics Letters, vol. 29, no. 3, pages 295–297, jan 2004. Cited p. 118

[Balian 88] Roger Balian. *On the principles of quantum mechanics and the reduction of the wave packet.* American Journal of Physics, vol. 57, no. 11, page 1019, dec 1988. Cited p. 18

[Beck 01] M Beck, C Dorrer & I A Walmsley. *Joint Quantum Measurement Using Unbalanced Array Detection.* Physical Review Letters, vol. 87, page 253601, dec 2001. Cited p. 2, 20, 75

[Black 01] E D Black. *An introduction to Pound-Drever-Hall laser frequency stabilization.* American Journal of Physics, vol. 69, pages 79–87, 2001. Cited p. 45

[Borevich 81] Z I Borevich & S L Krupetskii. *Subgroups of the unitary group that contain the group of diagonal matrices.* Journal of Soviet Mathematics, vol. 17, no. 4, pages 1951–1959, nov 1981. Cited p. 105

[Bowen 03] Warwick Paul Bowen. *Experiments towards a Quantum Information Network with Squeezed Light and Entanglement.* PhD thesis, The Australian National University, oct 2003. Cited p. 40

[Braunstein 05] Samuel Braunstein. *Squeezing as an irreducible resource.* Physical Review A (Atomic, Molecular, and Optical Physics), vol. 71, no. 5, may 2005. Cited p. 34, 35

[C D Hobbs 99] Philip C D Hobbs. Building electro-optical systems: making it all work. Wiley, dec 1999. Cited p. 61, 62

[Chalopin 09] Benoît Chalopin. *Optique quantique multimode : des images aux impulsions.* PhD thesis, Université Pierre et Maire Curie, Université Pierre et Marie Curie - Paris VI, 2009. Cited p. 40, 54

[Chalopin 11] Benoît Chalopin, Francesco Scazza, Claude Fabre & Nicolas Treps. *Direct generation of a multi-transverse mode non-classical state of light.* Optics Express, vol. 19, no. 5, pages 4405–4410, feb 2011. Cited p. 54

[Childs 10] Andrew M Childs. *Quantum algorithms for algebraic problems.* Rev. Mod. Phys., vol. 82, no. 1, pages 1–52, jan 2010. Cited p. 30, 31, 33

[Cohen-Tannoudji 06] Claude Cohen-Tannoudji, Bernard Diu & Frank Laloe. Quantum Mechanics. Wiley, wiley edition, may 2006. Cited p. 1, 23

[Davidovich 96] Luiz Davidovich. *Sub-Poissonian processes in quantum optics.* Rev. Mod. Phys., vol. 68, no. 1, pages 127–173, jan 1996. Cited p. 25

[Dawes 01] A M Dawes & M Beck. *Simultaneous quantum-state measurements using array detection.* Physical Review A (Atomic, Molecular, and Optical Physics), vol. 63, no. 4, page 4, mar 2001. Cited p. 2, 75

[Dawes 03] A M Dawes & M Beck. *Mode optimization for quantum-state tomography with array detectors.* Physical Review A (Atomic, Molecular, and Optical Physics), vol. 67, no. 3, page 6, mar 2003. Cited p. 75

[de Gosson 06] M de Gosson. Symplectic geometry and quantum mechanics, volume 166. Birkhäuser, jan 2006. Cited p. 34

[Delaubert 06] V Delaubert, N Treps, M Lassen, C Harb, C Fabre, P K Lam & H-A Bachor. *TEM_10 homodyne detection as an optimal small-displacement and tilt-measurement scheme.* Physical Review A (Atomic, Molecular, and Optical Physics), vol. 74, no. 5, page 053823, jan 2006. Cited p. 2, 20, 29, 50, 92

[Delaubert 07a] V Delaubert, M Lassen, D R N Pulford, H-A Bachor & C C Harb. *Spatial mode discrimination using second harmonic generation*. Optics Express, vol. 15, no. 9, pages 5815–5826, 2007. Cited p. 40

[Delaubert 07b] Vincent Delaubert. *Quantum imaging with a small number of transverse modes*. PhD thesis, Australian National University, jan 2007. Cited p. 40, 42

[Delaubert 08] V Delaubert, N Treps, C Fabre, H-A Bachor & P Réfrégier. *Quantum limits in image processing*. EPL (Europhysics Letters), vol. 81, no. 4, page 44001, jan 2008. Cited p. 28, 29

[DiVincenzo 95] D P DiVincenzo. *Quantum Computation*. Science, vol. 270, no. 5234, pages 255–261, oct 1995. Cited p. 31

[Drever 83] R W P Drever, J L Hall, F V Kowalski, J Hough, G M Ford, A J Munley & H Ward. *Laser phase and frequency stabilization using an optical resonator*. Applied Physics B Photophysics and Laser Chemistry, vol. 31, no. 2, pages 97–105, jun 1983. Cited p. 45

[Duan 00] Lu-Ming Duan, G Giedke, J I Cirac & P Zoller. *Inseparability Criterion for Continuous Variable Systems*. Physical Review Letters, vol. 84, no. 12, pages 2722–2725, mar 2000. Cited p. 20, 23, 32, 92

[Eames 49] Thomas H Eames. *The Effect of Glasses for the Correction of Hypermetropia and Myopia on the Speed of Visual Perception of Objects and Words*. The Journal of Educational Research, vol. 42, mar 1949. Cited p. 1

[Ekert 91] Artur K Ekert. *Quantum cryptography based on Bell's theorem*. Physical Review Letters, vol. 67, no. 6, pages 661–663, aug 1991. Cited p. 30

[Fade 08] J Fade, N Treps, C Fabre & P Réfrégier. *Optimal precision of parameter estimation in images with local sub-Poissonian quantum fluctuations*. The European Physical Journal D-Atomic, vol. 50, pages 215–227, jan 2008. Cited p. 28, 29

[Fleck 80] M D Feit J A Fleck & Jr. *Computation of mode properties in optical fiber waveguides by a propagating beam method*. Applied Optics, vol. 19, no. 7, pages 1154–1164, apr 1980. Cited p. 7

[Furusawa 98] A Furusawa, J L Sørensen, S L Braunstein, C A Fuchs, H J Kimble & E S Polzik. *Unconditional Quantum Teleportation*. Science, vol. 282, no. 5389, pages 706–709, oct 1998. Cited p. 33, 148

[Gallion 09] Philippe Gallion, Francisco Mendieta & Shifeng Jiang. Progress in Optics, volume 52 of *Signal and Quantum Noise in Optical Communications and Cryptography*. Elsevier, 2009. Cited p. 1

[Glauber 65] RJ Glauber. *Optical Coherence and Photon Statistics*. Quantum Optics and Electronics, page 63, jan 1965. Cited p. 1, 24

[Gleyzes 07] Sébastien Gleyzes, Stefan Kuhr, Christine Guerlin, Julien Bernu, Samuel Deléglise, Ulrich Busk Hoff, Michel Brune, Jean-Michel Raimond & Serge Haroche. *Quantum jumps of light recording the birth*

and death of a photon in a cavity. Nature, vol. 446, no. 7133, pages 297–300, mar 2007. Cited p. 1

[Gottesman 01] Daniel Gottesman, Alexei Kitaev & John Preskill. *Encoding a qubit in an oscillator.* Physical Review A (Atomic, Molecular, and Optical Physics), vol. 64, no. 1, 2001. Cited p. 31

[Grosse 06] Nicolai Grosse, Warwick Bowen, Kirk Mckenzie & Ping Lam. *Harmonic Entanglement with Second-Order Nonlinearity.* Physical Review Letters, vol. 96, no. 6, page 4, feb 2006. Cited p. 20

[Grosshans 01] F Grosshans & P Grangier. *Continuous variable quantum cryptography using coherent states.* Physical Review Letters, vol. 88, no. 5, page 057902, dec 2001. Cited p. 20, 31

[Grynberg 10] Gilbert Grynberg, Alain Aspect & Claude Fabre. Introduction to Quantum Optics. From the Semi-classical Approach to Quantized Light. Cambridge University Press, Cambridge, sep 2010. Cited p. 1, 2, 18, 23

[Guerlin 07] Christine Guerlin, Julien Bernu, Samuel Del eacute glise, Cl eacute ment Sayrin, S eacute bastien Gleyzes, Stefan Kuhr, Michel Brune, Jean-Michel Raimond & Serge Haroche. *Progressive field-state collapse and quantum non-demolition photon counting.* Nature, vol. 448, no. 7156, pages 889–893, aug 2007. Cited p. 23

[Hage 08] Boris Hage, Aiko Samblowski, James DiGuglielmo, Alexander Franzen, Jarom iacute r Fiur aacute scaron ek & Roman Schnabel. *Preparation of distilled and purified continuous-variable entangled states.* Nature Physics, vol. 4, no. 12, pages 915–918, nov 2008. Cited p. 20

[Hage 10] Boris Hage, Aiko Samblowski & Roman Schnabel. *Towards Einstein-Podolsky-Rosen quantum channel multiplexing.* Physical Review A (Atomic, Molecular, and Optical Physics), vol. 81, no. 6, jun 2010. Cited p. 20, 40

[Haroche 06] Serge Haroche & Jean-Michel Raimond. Exploring the Quantum. Oxford University Press, Oxford, aug 2006. Cited p. 23

[Herschel 61] John Frederick William Herschel. *The telescope.* Encyclopedia Britannica, page 190, jan 1861. Cited p. 1

[Hsu 05] MTL Hsu, WP Bowen, N Treps & PK Lam. *Continuous-variable spatial entanglement for bright optical beams.* Physical Review A (Atomic, Molecular, and Optical Physics), vol. 72, no. 1, page 013802, jan 2005. Cited p. 91

[Hsu 10] Magnus T L Hsu, Joachim Knittel, Jean-Francois Morizur, Hans-A Bachor & Warwick P Bowen. *Optical pattern recognition via adaptive spatial homodyne detection.* Journal Of The Optical Society Of America A-Optics Image Science And Vision, vol. 27, no. 12, pages 2583–2587, dec 2010. Cited p. 59

[Hübel 10] Hannes Hübel, Deny R Hamel, Alessandro Fedrizzi, Sven Ramelow, Kevin J Resch & Thomas Jennewein. *Direct generation of photon triplets using cascaded photon-pair sources*. Nature, vol. 466, no. 7306, pages 601–603, jul 2010. Cited p. 23

[Ikramov 84] HD Ikramov. *Linear Algebra: Problems Book*. Victor Kamkin, jan 1984. Cited p. 106

[Janousek 08a] J Janousek, K Wagner, Jean-Francois Morizur, N Treps, P K Lam, C C Harb & H-A Bachor. *Optical entanglement of co-propagating modes*. Nature Photonics, vol. 3, no. 7, pages 399–402, dec 2008. Cited p. iv, 23, 47, 53, 75, 90, 96

[Janousek 08b] Jiri Janousek. *Investigation of non-classical light and its application in ultrasensitive measurements*. PhD thesis, Australian National University, DTU, ANU, feb 2008. Cited p. 40, 42, 44

[Knill 01] E Knill, R Laflamme & G J Milburn. *A scheme for efficient quantum computation with linear optics*. Nature, vol. 409, no. 6816, pages 46–52, jan 2001. Cited p. 23

[Krackhardt 92] Ulrich Krackhardt, Joseph N. Mait & Norbert Streibl. *Upper bound on the diffraction efficiency of phase-only fanout elements*. Applied Optics, vol. 31, no. 1, pages 27–37, jan 1992. Cited p. 113

[Lam 98] Ping Koy Lam. *Applications of Quantum Electro-Optic Control and Squeezed Light*. PhD thesis, The Australian National University, dec 1998. Cited p. 40

[Lam 99] P K Lam, T C Ralph, B C Buchler, D E McClelland, H-A Bachor & J Gao. *Optimization and transfer of vacuum squeezing from an optical parametric oscillator*. Journal of Optics B: Quantum and Semiclassical Optics, vol. 1, no. 4, pages 469–474, aug 1999. Cited p. 41

[Lassen 07] M Lassen, V Delaubert, J Janousek, K Wagner, H A Bachor, P K Lam, N Treps, P Buchhave, C Fabre & C C Harb. *Tools for Multimode Quantum Information: Modulation, Detection, and Spatial Quantum Correlations*. Physical Review Letters, vol. 98, no. 8, pages 083602–083604, 2007. Cited p. 2, 30, 37, 42, 59

[Lenstra 93] Arjen K Lenstra & Hendrik W Lenstra Jr., editeurs. Lecture Notes in Mathematics, volume 1554 of *A general number field sieve implementation*. Springer Berlin Heidelberg, 1993. Cited p. 31

[Lloyd 99] Seth Lloyd & Samuel L Braunstein. *Quantum Computation over Continuous Variables*. Physical Review Letters, vol. 82, no. 8, pages 1784–1787, feb 1999. Cited p. 31

[Loock 07a] Peter van Loock. *Examples of Gaussian cluster computation*. J. Opt. Soc. Am. B, vol. 24, no. 2, pages 340–346, 2007. Cited p. 34

[Loock 07b] Peter van Loock, Christian Weedbrook & Mile Gu. *Building Gaussian cluster states by linear optics*. Physical Review A (Atomic, Molecular, and Optical Physics), vol. 76, no. 3, page 032321, 2007. Cited p. 23, 33, 148

[Lüpken 92] Hermann Lüpken, Thorsten Peter, Frank Wyrowski & Olof Bryngdahl. *Phase Synthesis for Array Illuminator*. Optics Communications, vol. 91, no. 3-4, pages 163–167, jan 1992. Cited p. 113

[Mandel 95] Leonard Mandel & Emil Wolf. Optical Coherence and Quantum Optics . cambridge.org, Cambridge, cambridge university press edition, oct 1995. Cited p. 18, 23

[Masada 10] Genta Masada, Tsuyoshi Suzudo, Yasuhiro Satoh, Hideki Ishizuki, Takunori Taira & Akira Furusawa. *Efficient generation of highly squeezed light with periodically poled $MgO : LiNbO_3$*. Optics Express, vol. 18, no. 12, pages 13114–13121, jun 2010. Cited p. 41, 43

[Mckenzie 04] Kirk Mckenzie, Nicolai Grosse, Warwick Bowen, Stanley Whitcomb, Malcolm Gray, David McClelland & Ping Lam. *Squeezing in the Audio Gravitational-Wave Detection Band*. Physical Review Letters, vol. 93, no. 16, oct 2004. Cited p. 41

[Mehmet 10] Moritz Mehmet, Henning Vahlbruch, Nico Lastzka, Karsten Danzmann & Roman Schnabel. *Observation of squeezed states with strong photon-number oscillations*. Physical Review A (Atomic, Molecular, and Optical Physics), vol. 81, no. 1, jan 2010. Cited p. 26, 42

[Menicucci 06] Nicolas Menicucci, Peter van Loock, Mile Gu, Christian Weedbrook, Timothy Ralph & Michael Nielsen. *Universal Quantum Computation with Continuous-Variable Cluster States*. Physical Review Letters, vol. 97, no. 11, sep 2006. Cited p. 31, 33, 34, 146

[Menicucci 07] Nicolas C Menicucci, Steven T Flammia, Hussain Zaidi & Olivier Pfister. *Ultracompact generation of continuous-variable cluster states*. Physical Review A (Atomic, Molecular, and Optical Physics), vol. 76, no. 1, page 010302, 2007. Cited p. 34

[Menicucci 08] Nicolas C Menicucci, Steven T Flammia & Olivier Pfister. *One-Way Quantum Computing in the Optical Frequency Comb*. Physical Review Letters, vol. 101, no. 13, pages 130501–130504, 2008. Cited p. 34

[Mooij 99] J E Mooij. *Josephson Persistent-Current Qubit*. Science, vol. 285, no. 5430, pages 1036–1039, aug 1999. Cited p. 31

[Morizur 08] Jean-Francois Morizur, Massimiliano Colla & Hans-A Bachor. *Quantum noise detection: A portable and educational system*. American Journal of Physics, vol. 76, no. 11, pages 1022–1025, 2008. Cited p. iv, 1, 13

[Morizur 10a] Jean-Francois Morizur, S Armstrong, N Treps, J Janousek & H-A Bachor. *Spatial reshaping of a squeezed state of light*. The European Physical Journal D, vol. 60, pages 1–3, dec 2010. Cited p. v

[Morizur 10b] Jean-Francois Morizur, S Armstrong, N Treps, J Janousek & H-A Bachor. *Spatial reshaping of a squeezed state of light*. The European

Physical Journal D, vol. 61, no. 1, pages 237–239, dec 2010. Cited p. 26

[Morizur 10c] Jean-Francois Morizur, Lachlan Nicholls, Pu Jian, Seiji Armstrong, Nicolas Treps, Boris Hage, Magnus Hsu, Warwick Bowen, Jiri Janousek & Hans-A Bachor. *Programmable unitary spatial mode manipulation.* Journal Of The Optical Society Of America A-Optics Image Science And Vision, vol. 27, no. 11, pages 2524–2531, nov 2010. Cited p. v, 89, 90

[Nielsen 06] Michael A Nielsen. *Cluster-state quantum computation.* Reports on Mathematical Physics, vol. 57, no. 1, pages 147–161, 2006. Cited p. 33

[Potsaid 08] Benjamin Potsaid & John Ting-Yung Wen. *Design of Adaptive Optics Based Systems by Using MEMS Deformable Mirror Models.* International Journal Of Optomechatronics, vol. 2, no. 2, pages 104–125, jan 2008. Cited p. 118

[Raussendorf 01] Robert Raussendorf & Hans J Briegel. *A One-Way Quantum Computer.* Physical Review Letters, vol. 86, no. 22, pages 5188–5191, may 2001. Cited p. 33

[Reck 94] Michael Reck & Anton Zeilinger. *Experimental realization of any discrete unitary operator.* Physical Review Letters, vol. 73, no. 1, pages 58–61, jul 1994. Cited p. 36

[Reid 89] M D Reid. *Demonstration of the Einstein-Podolsky-Rosen paradox using nondegenerate parametric amplification.* Physical Review A - General Physics, vol. 40, page 913, jul 1989. Cited p. 32

[Roorda 02] A Roorda, F Romero-Borja, WJ Donnelly, H Queener, TJ Hebert & MCW Campbell. *Adaptive optics scanning laser ophthalmoscopy.* Optics Express, vol. 10, no. 9, pages 405–412, jan 2002. Cited p. 118

[Serre 02] Denis Serre. Matrices: theory and applications. Springer, jan 2002. Cited p. 11, 36, 95, 105

[Shirai 02] T Shirai. *Liquid-crystal adaptive optics based on feedback interferometry for high-resolution retinal imaging.* Applied Optics, vol. 41, no. 19, pages 4013–4023, jan 2002. Cited p. 118

[Shor 94] P.W. Shor. *Algorithms for quantum computation: discrete logarithms and factoring.* In 35th Annual Symposium on Foundations of Computer Science, pages 124–134, Santa Fe, nov 1994. AT&T Bell Labs., IEEE. Cited p. 31

[Shor 97] Peter W. Shor. *Polynomial-Time Algorithms for Prime Factorization and Discrete Logarithms on a Quantum Computer.* SIAM Journal on Computing, vol. 26, no. 5, pages 1484–1509, oct 1997. Cited p. 31

[Shor 00] Peter Shor & John Preskill. *Simple Proof of Security of the BB84 Quantum Key Distribution Protocol.* Physical Review Letters, vol. 85, no. 2, pages 441–444, jul 2000. Cited p. 30

[Siegman 86] Anthony E Siegman. Laser. University Science Books, jan 1986. Cited p. 1, 6, 8, 41

[Simon 88] R Simon, E Sudarshan & N Mukunda. *Gaussian pure states in quantum mechanics and the symplectic group.* Physical Review A (Atomic, Molecular, and Optical Physics), vol. 37, no. 8, pages 3028–3038, apr 1988. Cited p. 23, 56, 59

[Slusher 84] RE Slusher, LW Hollberg, Bi Yurke, JC Mertz & JF Valley. *Observation of squeezed states generated by four wave mixing in an optical cavity.* Physical Review Letters, vol. 55, no. 22, pages 2409–2412, dec 1984. Cited p. 1, 25

[Sterkenburgh 97] Tomas Sterkenburgh, Rolf Michael Michels, Peter Dress & Hilmar Franke. *Explicit finite-difference simulation of optical integrated devices on massive parallel computers.* Applied Optics, vol. 36, no. 6, pages 1191–1197, feb 1997. Cited p. 6

[Suzuki 06] Shigenari Suzuki, Hidehiro Yonezawa, Fumihiko Kannari, Masahide Sasaki & Akira Furusawa. *7dB quadrature squeezing at 860nm with periodically poled $KTiOPO_4$.* Applied Physics Letters, vol. 89, no. 6, page 061116, jan 2006. Cited p. 30, 43

[Takeno 07] Yuishi Takeno, Mitsuyoshi Yukawa, Hidehiro Yonezawa & Akira Furusawa. *Observation of -9 dB quadrature squeezing with improvement of phase stability in homodyne measurement.* Optics Express, vol. 15, no. 7, pages 4321–4327, apr 2007. Cited p. 30, 43, 45

[Tay 09] Jian Wei Tay, Michael A Taylor & Warwick P Bowen. *Sagnac-interferometer-based characterization of spatial light modulators.* Applied Optics, vol. 48, no. 12, pages 2236–2242, jan 2009. Cited p. 120

[Török 07] Peter Török & Fu-Jen Kao. Optical imaging and microscopy, volume 87. Springer, jan 2007. Cited p. 1, 28

[Treps 03] Nicolas Treps, Nicolai Grosse, Warwick Paul Bowen, Claude Fabre, Hans Bachor & Ping Koy Lam. *A Quantum Laser Pointer.* Science, vol. 301, no. 5635, pages 940–943, aug 2003. Cited p. 2, 28, 50, 75

[Treps 05] N Treps, V Delaubert, A Maître, J Courty & C Fabre. *Quantum noise in multipixel image processing.* Physical Review A (Atomic, Molecular, and Optical Physics), vol. 71, no. 1, jan 2005. Cited p. 2, 28

[Ukai 10] Ryuji Ukai, Noriaki Iwata, Yuji Shimokawa, Seiji C Armstrong, Alberto Politi, Jun-ichi Yoshikawa, Peter van Loock & Akira Furusawa. *Demonstration of unconditional one-way quantum computations for continuous variables.* Arxiv preprint quant-ph, vol. quant-ph, jan 2010. Cited p. 34, 56, 148, 150

[Vahlbruch 08] Henning Vahlbruch, Moritz Mehmet, Simon Chelkowski, Boris Hage, Alexander Franzen, Nico Lastzka, Stefan Goßler, Karsten Danzmann & Roman Schnabel. *Observation of Squeezed Light with 10-dB Quantum-Noise Reduction.* Physical Review Letters, vol. 100, no. 3, jan 2008. Cited p. 30, 41, 42

[van Loock 00] P van Loock & Samuel L Braunstein. *Multipartite Entanglement for Continuous Variables: A Quantum Teleportation Network*. Physical Review Letters, vol. 84, no. 15, pages 3482–3485, apr 2000. Cited p. 33

[Wagner 08] Katherine Wagner, Jiri Janousek, Vincent Delaubert, Hongxin Zou, Charles Harb, Nicolas Treps, Jean-Francois Morizur, Ping Koy Lam & Hans A Bachor. *Entangling the Spatial Properties of Laser Beams*. Science, vol. 321, no. 5888, pages 541–543, 2008. Cited p. 26, 30, 47, 90, 91, 92

[Walls 83] D Walls. *Squeezed states of light*. Nature, jan 1983. Cited p. 25

[Walls 08] D F Walls & Gerard J. Milburn. Quantum Optics. Springer, jan 2008. Cited p. 40

[Wu 86] Ling-An Wu, H Kimble, J Hall & Huifa Wu. *Generation of Squeezed States by Parametric Down Conversion*. Physical Review Letters, vol. 57, no. 20, pages 2520–2523, nov 1986. Cited p. 1, 41

[Wyrowski 91] Frank Wyrowski. *Upper bound of the diffraction efficiency of diffractive phase elements*. Optics Letters, vol. 16, no. 24, pages 1915–1917, jan 1991. Cited p. 108, 113

[Yee 66] Kane Yee. *Numerical solution of initial boundary value problems involving maxwell's equations in isotropic media*. Antennas and Propagation, IEEE Transactions on, vol. 14, no. 3, pages 302–307, may 1966. Cited p. 1, 6

[Yonezawa 04] Hidehiro Yonezawa, Takao Aoki & Akira Furusawa. *Demonstration of a quantum teleportation network for continuous variables*. Nature, vol. 431, no. 7007, pages 430–433, sep 2004. Cited p. 33

[Yonezawa 10] Hidehiro Yonezawa, Koyo Nagashima & Akira Furusawa. *Generation of squeezed light with a monolithic optical parametric oscillator: Simultaneous achievement of phase matching and cavity resonance by temperature control*. Optics Express, vol. 18, no. 19, pages 20143–20150, sep 2010. Cited p. 42

[Yukawa 08a] M Yukawa, R Ukai, P van Loock & A Furusawa. *Experimental generation of four-mode continuous-variable cluster states*. Physical Review A (Atomic, Molecular, and Optical Physics), vol. 78, page 012301, jan 2008. Cited p. 34, 35, 37, 149

[Yukawa 08b] Mitsuyoshi Yukawa, Hugo Benichi & Akira Furusawa. *High-fidelity continuous-variable quantum teleportation toward multistep quantum operations*. Physical Review A (Atomic, Molecular, and Optical Physics), vol. 77, no. 2, feb 2008. Cited p. 2

[Zhang 90] Wei-Min Zhang, Da Hsuan Feng & Robert Gilmore. *Coherent states: Theory and some applications*. Rev. Mod. Phys., vol. 62, no. 4, pages 867–927, oct 1990. Cited p. 24

[Zhang 08] Jing Zhang, Changde Xie & Kunchi Peng. *Continuous-variable telecloning with phase-conjugate inputs*. Physical Review A (Atomic, Molecular, and Optical Physics), vol. 77, no. 2, feb 2008. Cited p. 33

[Zhou 00] GG Zhou, XC Yuan, P Dowd, YL Lam & YC Chan. *Efficient method for evaluation of the diffraction efficiency upper bound of diffractive phase elements.* Optics Letters, vol. 25, no. 17, pages 1288–1290, jan 2000. Cited p. 113

Publications and Award

The results presented in this manuscript lead to the publication of several articles in peer-reviewed scientific journals and several public presentations in international conferences. Moreover, the UPMC and the ANU jointly filed a patent application to protect the intellectual property of a specific optimization method of the Unitary Programmable Mode Converter.

Publication

- Morizur, J. C., Colla, M., and Bachor, H. (2008). Quantum noise detection: A portable and educational system. American Journal of Physics, 76(11), 1022-1025
- Wagner, K., Janousek, J., Delaubert, V., Zou, H., Harb, C., Treps, N., Morizur, J. F., Lam, P.-K., and Bachor, H. (2008). Entangling the Spatial Properties of Laser Beams. Science, 321(5888), 541-543
- Janousek, J., Wagner, K., Morizur, J., Treps, N., Lam, P. K., Harb, C. C., and Bachor, H. (2008). Optical entanglement of co-propagating modes. Nature Photonics, 3(7), 399-402
- Morizur, J. C., Nicholls, L., Jian, P., Armstrong, S., Treps, N., Hage, B., Hsu, M., Bowen, W. P., Janousek, J., and Bachor, H. (2010). Programmable unitary spatial mode manipulation. Journal Of The Optical Society Of America A-Optics Image Science And Vision, 27(11), 2524-2531
- Hsu, M. T. L., Knittel, J., Morizur, J., Bachor, H., and Bowen, W. P. (2010). Optical pattern recognition via adaptive spatial homodyne detection. Journal Of The Optical Society Of America A-Optics Image Science And Vision, 27(12), 2583-2587
- Morizur, J., Armstrong, S., Treps, N., Janousek, J., and Bachor, H. (2010). Spatial reshaping of a squeezed state of light. The European Physical Journal D, 60, 1-3

Conferences

- Conference on Lasers and Electro-Optics / European Quantum Electronics Conference, Munich, 2009: Entangling spatial modes within a single beam

- Australian Conference on Optics Lasers and Spectroscopy, Adelaide, 2009: Quantum manipulations of spatial modes within a beam
- Conference on Lasers and Electro-Optics, San Jose, 2010: Experimental demonstration of computer reconfigurable multimode entanglement
- Advanced Imaging Techniques, Engelberg, 2010: Programmable unitary spatial modes manipulation
- Journées d'Imagerie Optique Non Conventionelle, Paris, 2011: Manipulation unitaire de modes spatiaux
- Conference on Lasers and Electro-Optics / European Quantum Electronics Conference, Munich, 2011: Spatial reshaping of a squeezed state of light
- International Conference on Quantum Information, Ottawa, 2011: Spatial reshaping of a squeezed state of light

Patent Application

During the course of this work, we developed a method to optimize a Unitary Programmable Mode Converter. This method is the object of the European patent application number 1046846, titled: "Method and system for configuring a device for correcting the effect of a medium on a light signal, method, device and system for correcting said effect.".

Award

This cotutelle project was awarded a Lavoisier Scholarship from the French Ministry of Foreign Affairs.